Investigation into the mechanism of a photoredox catalysed C(sp^3)–H functionalisation reaction in continuous flow

A Thesis Submitted by

Hannah Catherine Broderick

In partial fulfilment of the requirements for the degree of

Doctor of Philosophy

Department of Chemistry

Imperial College London

Molecular Sciences Research Hub

White City Campus

London W12 0BZ

United Kingdom

2023

Declarations

Declaration of Originality

I, Hannah Broderick, declare that this thesis and the work presented herein are my own as a result of my original research. Where I have referred to the published work of others, it is clearly attributed. Where this thesis is based on work done jointly with others, I have clearly acknowledged what is the contribution of others.

Copyright Declaration

The copyright of this thesis rests with the author. Unless otherwise indicated, its contents are licensed under a Creative Commons Attribution Non-Commercial 4.0 International Licence (CC BY-NC).

Under this licence, you may copy and redistribute the material in any medium or format. You may also create and distribute modified versions of the work. This is on the condition that: you credit the author and do not use it, or any derivative works, for a commercial purpose.

When reusing or sharing this work, ensure you make the licence terms clear to others by naming the licence and linking to the licence text. Where a work has been adapted, you should indicate that the work has been changed and describe those changes.

Please seek permission from the copyright holder for uses of this work that are not included in this licence or permitted under UK Copyright Law.

Acknowledgements

Firstly, I would like to thank Dr James Bull for the incredible opportunity to have been part of his group for the last four years, and for his tireless help, insight and direction with everything I have worked on during my PhD. I have learnt so much and had so many great experiences over the course of this project, and my time at Imperial has been a rich one as a result.

I would also like to thank Dr Phil Miller for his support and guidance, particularly in teaching me flow chemistry- this project would be very different without it. Many thanks to Dr Charles Romain for lending his expertise with computational chemistry, and whose contribution has helped to elevate this project in different and exciting ways.

I would like to thank the React CDT directors, in particular Professor Mimi Hii, for building an innovative and challenging course, and having me be a part of it. Many thanks also to Jinata Subba for always being a warm and helpful presence, and for organising many events across the CDT.

I would also like to thank all the members of the wonderful Bull group past and present who have shaped my time at Imperial. Special thanks to Joe for being a top tier fumehood partner, early morning company, and for always being able to cheer me up when my columns were terrible. Many thanks to Steph for the funny catch-ups, if only we had been in the same cohort sooner. Thank you also to Maryne for helping me get started with photochemistry, and to Sofia and Dani for all their help when I was starting in the group. Thanks to Seb, for imparting his hard-earned flow chemistry wisdom, and his flow kit. Thanks to Juan and George who have been with me all the way through my time in the Bull group, your work and dedication has been inspirational and I have learnt so much from you both. Many thanks to Hannan and Abi, my 'flow/light/bio' subgroup team, sharing tales of blue light and iridium chemistry, and also skittles. Many thanks to Ollie, for all your support and restorative hot-chocolate breaks. Many thanks to Freeman, not only for all the advice, laughs and help with electrochemistry- which was extensive- but also for all the snacks. Thanks to Carla and Nikki for being great fumehood neighbours, and to Matthew, Hikaru, Peerawat and Simon for your enthusiasm and energy, always helping a lab day to fly by. I look forward to following all your work and progress. It has been a pleasure working with you and I will miss you all.

Many thanks to Hannan, Freeman, Joe and Ollie for proofreading this thesis, I very much appreciate the time and diligence you put in to help me pull this into shape.

I am grateful to Corey Fulop for his help with NMR phasing issues and to Pete Haycock for running a sizable number of my NMR samples when things broke, and for always keeping the

NMR service working well. Thanks also to Lisa Haigh and Malgorzata Puchnarewicz for running all the mass spec analysis.

A big thank you to my fantastic CDT cohort, Aatikah, Josh, Linden, Matt and Sean. I could not have asked for more kind, hilarious and intelligent friends. Aatikah, thank you for being a wonderful friend ever since our interviews, and making me smile every day since.

Thank you to Alyssa for being an amazing friend for over 15 years, for your wisdom, encouragement and for always teaching me new and interesting things.

To Emma, Michael, Alice and my parents Mike and Gill. Thank you for all your support- even and especially if you might not have known what you were supporting! You have been an inspiration to me all my life and I owe this thesis in a large part to you.

Finally, a special thank you to my partner, Michael. Thank you for being my writing buddy while I put this together, for being on this PhD journey with me, for always believing in me and for all the tea. I look forward to our new chapter.

Abstract

Photoredox-catalysed C(sp^3)–H functionalisation is a powerful technique to access derivatized heterocycles with wide functional group tolerance. The kinetics of such reactions are currently poorly understood; orders in components are specific to variables including light intensity, catalyst, concentration, and setup. Flow chemistry can increase control over these variables and achieve higher surface-area-to-volume ratios, enhanced light penetration and improved reproducibility over batch counterparts. This thesis describes the development of a photoredox-catalysed C(sp^3)–H functionalisation reaction of *N*-aryl pyrrolidines with radical acceptors using batch and continuous flow approaches. Investigations into the reaction mechanism are described with a focus on understanding the kinetics of this system.

Section 2.1 describes the optimisation of the batch reaction. However this was found to be insufficiently reproducible for rigorous kinetic analysis, prompting translation to a continuous flow system to obtain kinetic profile data, presented in section 2.2. Mechanistic analysis of the reaction is presented in Section 2.3, including the application of VTNA to obtain a non-light-limited reaction regime used to study rates of different substrates, and to determine components in the apparent reaction rate law.

Kinetic experiments under the non-light-limited reaction conditions, alongside ex-situ analytical techniques, were used to determine that single electron transfer between *N*-aryl pyrrolidines and the iridium photocatalyst excited state was turnover-limiting. Investigating the effect of different reactants on reaction rate uncovered trends in the aryl substitution patterns of *N*-aryl pyrrolidines and different nitrogen heterocycles. This has deepened understanding into the chemistry of radical formation under iridium-catalysed photoredox conditions. Computational investigations sought to explain these trends in oxidation potentials, providing general insights into the formation of α-nitrogen radicals and the chemoselectivity of such transformations. This analysis is presented and discussed in section 2.4, culminating in a summary of the insights into this mechanism obtained throughout this work in the form of rate equations.

Contents

1. Introduction 12

1.1. C–H functionalisation 12

1.2. Photoredox catalysis for C–H functionalisation 13

1.2.1. General photoredox mechanisms 13

1.2.2. Strategies for photoredox catalysed C(sp^3)–H functionalisation 14

1.2.2.1. Oxidative iminium ion formation 14

1.2.2.2. Formation of α-aminoalkyl radicals 14

1.2.2.3. Single electron transfer (SET) methods of radical formation 16

1.2.2.4. Hydrogen atom transfer (HAT) methods of radical formation 20

1.2.2.5. Metallophotoredox strategies 21

1.3. Probing the mechanisms of photoredox reactions 24

1.3.1. U.V-vis spectroscopy 24

1.3.2. Cyclic Voltammetry 25

1.3.3. Luminescence quenching experiments (Stern-Volmer) 27

1.4. Kinetics of photoredox reactions 31

1.4.1. Key kinetic findings of photoredox systems 31

1.4.1.1. Effect of light intensity on reaction 31

1.4.1.2. Impact of catalyst concentration on rate 33

1.4.2. Ways to investigate the kinetics of photoredox systems 37

1.4.2.1. VTNA in reaction design 42

1.5. Conclusions 43

1.6. Project Aims 45

2. Results and discussion 47

2.1. Establishing and optimising a batch reaction 47

2.1.1. Developing a measurable batch reaction 47

2.1.2. Investigating reproducibility in the batch reactor 50

2.1.3. Optimisation of C(sp^3)–H functionalisation of aryl-pyrrolidines in batch 52

2.1.3.1. Control experiments 52

2.1.3.2. Discrete variable optimisation 52

2.1.4. Design of experiment modelling 60

2.1.4.1. Fractional factorial design 61

2.1.4.2. Custom DoE 65

2.1.5. Investigation into mono vs di addition formation 67

2.1.6. Sensitivity screen 69
2.1.7. Batch Reaction profile 71
2.2. Developing a continuous flow system 73
2.2.1. Optimisation in flow 73
2.2.1.1. Initial investigations into residence time 74
2.2.1.2. Flow reactor setup 74
2.2.2. Kinetic profiles 75
2.2.2.1. Reproducibility in flow 78
2.2.2.2. Kinetics of di-addition formation 79
2.3. Mechanistic analysis 81
2.3.1. Identifying orders in reaction components, and establishing non-light-limited reaction kinetics 81
2.3.2. Investigate catalyst quenching 87
2.3.2.1. Cyclic Voltammetry studies 88
2.3.2.2. Stern Volmer Luminescence Quenching Analysis 90
2.3.3. Same excess reactions 92
2.4. Trends in different substrates 96
2.4.1. Trends in aryl groups 97
2.4.1.1. Hammett analysis 100
2.4.1.2. Swain-Lupton analysis 101
2.4.2. Trends in heterocycles 103
2.4.2.1. Competition experiment 105
2.4.3. Computational experiments: what controls redox potentials? 106
2.4.4. Trends in acceptors 109
2.4.4.1. Experimental work 109
2.4.4.2. Kinetic isotope experiments 111
2.4.4.3. Computational analysis 113
2.4.5. Deriving a reaction rate law 116
3. Conclusions and future work 122
4. Experimental details and Characterisation data 125
4.1. General experimental considerations 125
4.2. Batch photoredox reactions 127
4.2.1. Batch photoredox reactor reaction set-up 127
4.2.2. Batch experimental detail 128
General procedure A for batch reactions with solid bases 128

Repeating standard conditions 131

4.3. Light Emission spectrum for Evoluchem 450 nm light source 132

4.4. UV-Vis spectra 133

4.5. General continuous flow experimental considerations 134

4.6. Flow reactor design details 134

4.7. Kinetic profiles 137

4.7.1. Calculation of kinetic profiles 138

4.7.2. VTNA experiments 139

4.7.3. Same excess experiments 151

4.7.4. Comparing different substrates 154

4.7.5. Competition experiment 155

4.7.6. Profiles to obtain reaction rate with different acceptors 156

4.7.7. Kinetic isotope experiments 157

4.8. Hammett analysis 163

4.9. Swain-Lupton analysis 163

4.10. Cyclic Voltammetry 164

4.11. Stern-Volmer luminescence quenching experiments 165

4.12. General computation considerations 167

4.13. Experimental details and compound characterisation 170

4.13.1. Substrate synthesis 170

4.13.2. C–H functionalisation product formation 176

5. References 197

6. Appendix 202

6.1. Cyclic voltammograms 202

6.2. Stern-Volmer graphs 209

Acronyms and Abbreviations

4CzIPN	1,2,3,5-Tetrakis(carbazole-9-yl)-4,6-dicyanobenzene
λ_{max}	Maximum wavelength of absorption
σ_p	Hammett constant
APCI	Atmospheric Pressure Chemical Ionisation
Ar	Aryl
aq.	Aqueous
BDE	Bond Dissociation Energy
BIPA	4-Biphenyl-L-alanine
Boc	tert-butyloxycarbonyl
bpy	2,2'-Bipyridine
bpz	2,2'-Bipyrazine
CAS	Chemical Abstracts Service
CFL	Compact Fluorescent Lamp
CV	Cyclic Voltammetry
cpcm	Conductor-like polarisable continuum model
DABCO	1,4-Diazabicyclo[2.2.2]octane
DBU	1,8-Diazabicyclo[5.4.0]undec-7-ene
DFT	Density-Functional Theory
DIPEA	*N*,*N*-Diisopropylethylamine
DoE	Design of Experiment
DMA	Dimethylacetamide
dmb	5,6-Dimethylbenzimidazole
dme	Dimethoxyethane
DMF	*N*,*N*-Dimethylformamide
DMSO	Dimethyl sulfoxide
DMT	1,4-dimethylterepthalate
DPA	9,10-Diphenylanthracene
d.r,	Diastereomeric ratio
dtbbpy	4,4'-Di-tert-butyl-2,2'-dipyridyl
EDA	Electron donor-acceptor
EI	Electron Ionisation
E_{ox}	Oxidation potential
equiv	Equivalents
E_{red}	Reduction potential

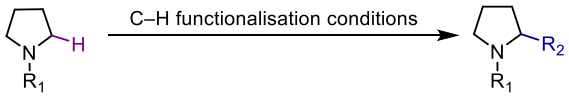
ESI	Electrospray Ionisation
ET	Energy Transfer
EWG	Electron Withdrawing Group
F	Field effects
Fc	Ferrocene
glyme	Dimethoxyethane
HAT	Hydrogen atom transfer
HOMO	Highest Occupied Molecular Orbital
HPLC	High-Performance Liquid Chromatography
HRMS	High Resolution Mass Spectrometry
I	Intensity OR current
ID	Internal Diameter
IR	Infrared
ISC	Intersystem crossing
KIE	Kinetic Isotope Effect
K_{SV}	Stern-Volmer quenching constant
k_q	Quenching rate
LED	Light Emitting Diode
LUMO	Lowest Unoccupied Molecular Orbital
Me	Methyl
MeCN	Acetonitrile
Mes-Acr	9-Mesityl-10-methylacridinium tetrafluoroborate
MeTHF	Methyl-tetrahydrofuran
mins	Minutes
MLCT	Metal-to-Ligand Charge Transfer
mp	Melting point
N-arylTHIQ	*N*-aryl tetrahydroisoquinoline
NBO	Natural Bond Orbital
N-BocMA	*N*-Boc-methylacrylate
NMP	*N*-methyl-2-pyrrolidone
NMR	Nuclear Magnetic Resonance
OD	Outer Diameter
OLED	Organic Light-Emitting Diode
SET	Single Electron Transfer
PC	Photocatalyst
PCET	Proton-Coupled Electron Transfer

PFA	Perfluoroalkoxy
Ph	Phenyl
pK_a	Negative logarithm of the acid dissociation constant Ka
ppm	Parts per million
ppy	2-Phenylpyridine
Q	Quencher
quat	Quaternary carbons
R	Resonance
rds	Rate-determining step
R_f	Retention factor
RPKA	Reaction Progress Kinetic Analysis
rpm	Revolutions per minute
rt	Room temperature
sat.	Saturated (referring to solutions)
SCE	Standard Calomel Electrode
TBME	*Tert*-Butyl Methyl Ether
TFA	Trifluoroacetic acid
THF	Tetrahydrofuran
TLC	Thin-Layer Chromatography
TMB	1,3,5-Trimethoxybenzene
t_R	Residence time
T_0	Excited-state lifetime
TS	Transition State
UV-vis	Ultraviolet-visible
v	Volume
V	Volts
VTNA	Variable Time Normalisation Analysis
w.r.t.	With respect to

1. Introduction

1.1. C–H functionalisation

C–H functionalisation is a reaction type which exchanges a C–H bond for a C–R bond, where R is any other atom (Scheme 1). By doing so, the complexity of the molecule can be increased, and functional groups installed at an otherwise inactive site.[1] When applied to nitrogen heterocycles, one of the most prevalent motifs in bioactive molecules,[2] C–H functionalisation allows synthesis of complex molecules without the need for *de novo* synthesis of the nitrogen heterocycle (Scheme 1).[3] This could be directly applied to increase throughput in a drug discovery programme to give rapid generation of new molecules, leverage heterocycle fragment libraries,[4] or provide late-stage functionalisation of high value molecules.[5]



Scheme 1: General scheme for C–H functionalisation of nitrogen heterocycles.

For C–H functionalisation to be suitable for application to nitrogen heterocycles, these reactions need to be functional group tolerant, allowing for complex molecules to be reacted without degradation. As C–H bonds are ubiquitous in organic molecules, these reactions also need to be selective and predictable in their selectivity, allowing a specific, known C–H bond to react over the many others present in the same molecule. An understanding of mechanism and kinetics of these reactions is therefore highly desirable to be able to predict how successful and reproducible a reaction of an unknown substrate will be.

There are several strategies for achieving C–H functionalisation, including metal-catalysed approaches leveraging either pre-installed[6] or transient[7] directing groups, or, more recently, radical methods utilising either visible light[8] or electrochemical methods.[9]

Over the last decade, the field of photoredox catalysis has exploded, with strategies to afford a wide variety of transformations, both existing and new, including several photoredox catalysed C–H functionalisation reactions reported for a wide range of substrates.[8] Photoredox catalysed reactions typically utilise ambient or near ambient temperatures, and use photoredox catalysts often capable of many turnovers with defined redox potentials. These milder methods contrast with many alternative C–H functionalisation strategies which can require high temperatures or harsh stoichiometric oxidants, or bases,[10] incompatible with many functional groups. As such, photoredox catalysis is an important reaction type with potential for application to industrial chemistry and late-stage functionalisation.[11] However,

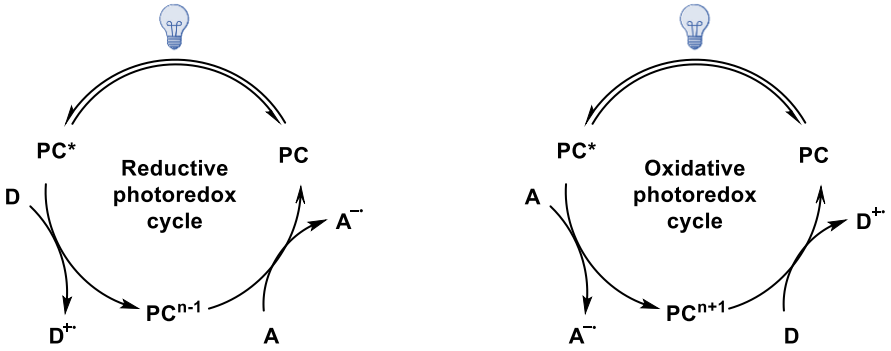
light-mediated reactions can be irreproducible, with reaction setups not necessarily standardised or rigorously described.[12] Furthermore, mechanistic investigation of light mediated reactions is complex; therefore, understanding of these reactions has often been limited, making it difficult to predict whether a molecule will be an effective substrate. Deeper mechanistic, and particularly kinetic, understanding of photoredox reactions is required to enable these reactions to be used more widely, and for industrial processes.[12,13]

This introduction will describe synthetic strategies for C–H functionalisation of nitrogen heterocycles using photoredox catalysis. Following this, the main techniques used to investigate the mechanisms of photoredox reactions will be presented, and the current literature on the kinetics of photoredox reactions summarised and illustrated with relevant examples.

1.2. Photoredox catalysis for C–H functionalisation

1.2.1. General photoredox mechanisms

Photoredox catalysis involves the irradiation of a photocatalyst (**PC,** Scheme 2) to form an excited state (**PC***) on absorption of a photon. The photocatalyst excited state is then able to act as a strong reductant or an oxidant, interacting with an electron donor (**D**) or acceptor (**A**) respectively to form a radical and the reduced ($\mathbf{PC^{n-1}}$) or oxidised ($\mathbf{PC^{n+1}}$) photocatalyst. The formed organic radical can then interact with other reactants, and the photocatalytic cycle is closed by the re-oxidation/-reduction of the catalyst by another component of the reaction (an electron acceptor, **A** for reductive photoredox cycles or electron donor **D** for oxidative photoredox cycles). This could be a sacrificial redox species, or a radical species generated in the reaction.



Scheme 2: General mechanism of A) reductive and B) oxidative photoredox catalysis.[14]

Such reactions have yielded a vast array of transformations, which has been expanded by combining with second and sometimes third modes of catalysis: most notably combination with transition metal and hydrogen atom transfer (HAT) catalysis which will be described in

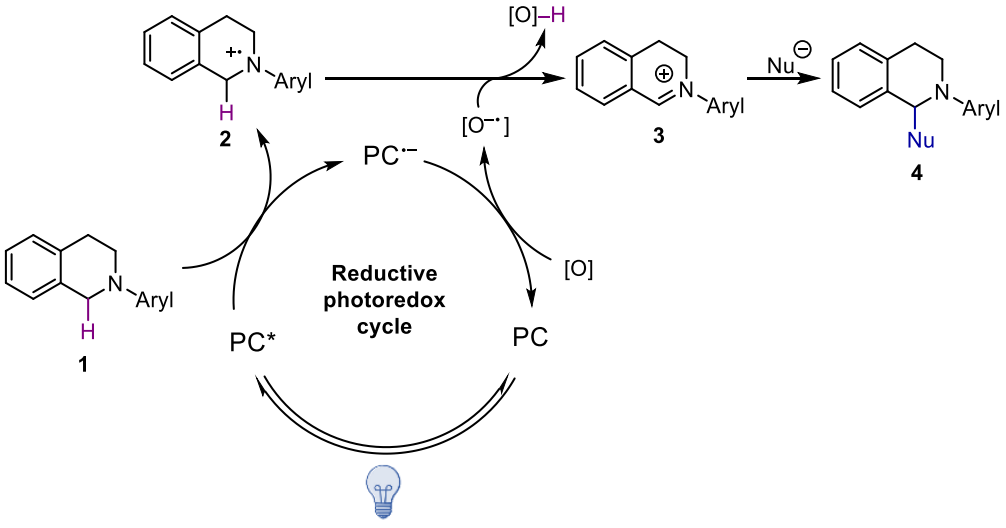
more detail throughout this chapter. The strategies described in the remainder of this section will relate to photoredox strategies for the C(sp^3)–H functionalisation of saturated nitrogen heterocycles.

1.2.2. Strategies for photoredox catalysed C(sp^3)–H functionalisation

There have been several methods to functionalise saturated nitrogen heterocycles through a variety of mechanisms. The two main strategies involve either formation of an iminium ion through photoredox catalysis, forming an electrophilic carbon centre, or formation of a carbon-centred radical.

1.2.2.1. Oxidative iminium ion formation

In 2010, Stevenson and co-workers described the generation of iminium ions from *N*-aryl tetrahydroisoquinolines (*N*-arylTHIQs) using photoredox catalysis, which could be trapped with nitronate nucleophiles (Scheme 3).[15] Several works expanded on this method to demonstrate trapping of the iminium ion with a range of nucleophiles, using the same general mechanism: single electron transfer between an excited state photocatalyst and *N*-arylTHIQ substrate **1** forms an amine radical cation **2**. Reaction with a terminal oxidant **[O]**, activated through reduction with the photocatalyst intermediate, forms iminium ion **3**, which is attacked by a nucleophile to obtain product **4**. The scope of heterocycles used in this approach was mostly limited to *N*-arylTHIQs or *N*-phenylpyrrolidines.[16]



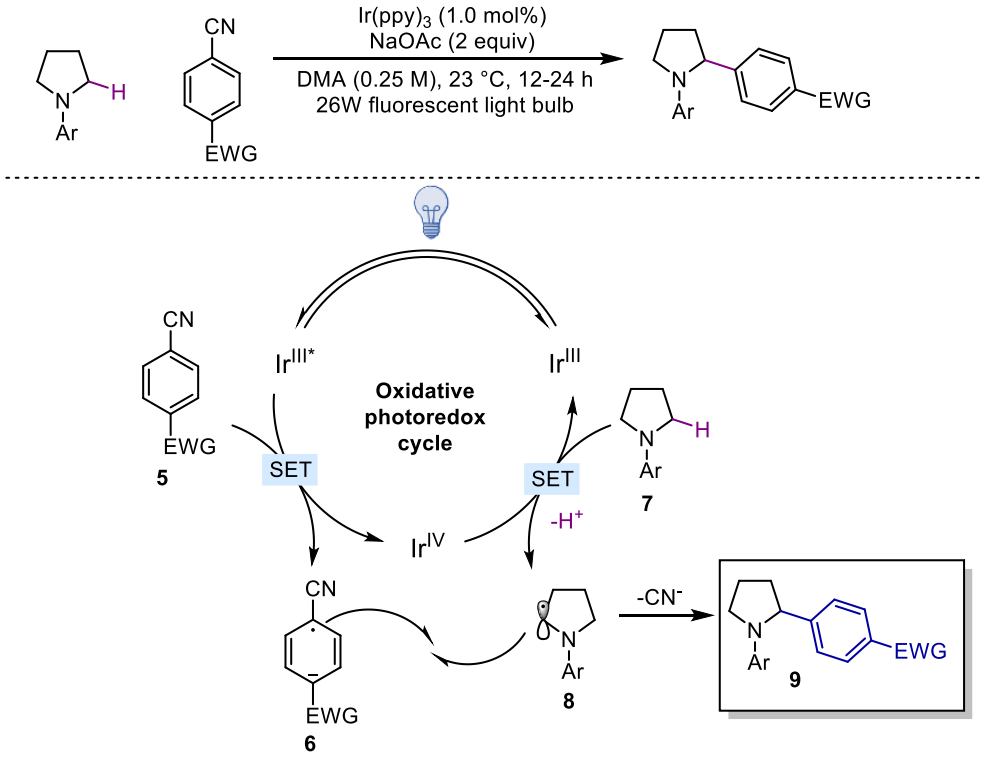
Scheme 3: C–H functionalisation of nitrogen heterocycles through iminium ion formation.[17]

1.2.2.2. Formation of α-aminoalkyl radicals

Using photoredox catalysis to form carbon-centred radicals on nitrogen heterocycles is a more versatile technique compared with iminium ion formation, with several strategies employed to

achieve C–H functionalisation. The first reported formation of an α-aminoalkyl radical formed using photoredox methods occurred in 2011, when MacMillan and co-workers achieved radical formation of *N*-arylpyrrolidines, such as compound **7**, through single electron transfer with an iridium-based photocatalyst to afford cyanoarylation of *N*-arylpyrrolidines (Scheme 4).[18] However, the reactivity between amines and cyanoarenes using light was first reported in 1980 by Ohashi and coworkers, who demonstrated the reaction of dicyanobenzenes with aliphatic amines under irradiation with a low-pressure mercury arc lamp in the absence of a photocatalyst.[19]

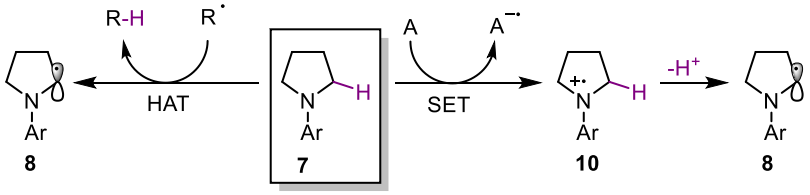
MacMillan's reaction was discovered using a high throughput workflow termed 'accelerated serendipity' to screen for new reactivity. This approach involved screening large numbers of reagents in a high-throughput, automated fashion. The proposed mechanism for this reaction involved visible light excitation of an iridium(III) catalyst, $Ir(ppy)_3$, which undergoes single electron transfer (SET) with electrophilic cyanoarene **5** to form reduced cyanoarene **6** (1,4-dicyanobenzene reduction potential −1.64 V vs SCE).[20] The iridium(IV) species is then reduced to the ground state Ir(III) through SET with aryl-pyrrolidine **7** (reduction potential +0.82 V vs SCE),[21] forming α-aminoalkyl radical **8** on deprotonation. The organic radicals generated through these two redox processes then couple with loss of cyanide to generate the arylated pyrrolidine **9**.



Scheme 4: Cyanoarylation of *N*-phenylpyrrolidines as described by MacMillan.[18]

The high yields for the cross-selective radical-radical coupling product **9** can be explained by the persistent radical effect.[22,23] Cyanoarene radicals are persistent anionic radicals,[24] slow to dimerise due to the kinetic barrier to overcome electrostatic repulsion. Conversely, nitrogen radicals are transient radicals and prone to homodimerization. As the photoredox cycle forms both cyanoarene and nitrogen radicals in one turnover, these radicals are generated at approximately equal rates. In the initial stages of the reaction, transient radicals are as likely to interact with persistent or transient radicals, meaning some radical homocoupling is likely to occur. This would lower the concentration of transient radical **8** relative to persistent radical **6**, which over the course of the reaction would increasingly favour formation of the cross-selective coupling product **9**.[25] Potential for homocoupling of the transient radical **8** may also explain why *N*-phenylpyrrolidine was used in this reaction in 3 equivalent excess.[26]

There have since been several approaches to the formation of carbon radicals on nitrogen heterocycles, which break down to two main strategies for radical formation. The first is single electron transfer (SET) between a more oxidising species and the substrate **7** to form an amine radical cation **10**. Formation of this radical cation increases the acidity of the protons at the α-position (aminium radical cations were estimated to have a pK_a 3–13),[27] and these can be readily deprotonated to form the α-aminoalkyl radical **8** (Scheme 5), as was the strategy employed in Scheme 4. The second approach uses a hydrogen atom transfer (HAT) reagent, which is usually activated either through direct excitation by visible or UV light[28] or through formation of a radical species formed by SET with a photocatalyst. The HAT reagent then directly abstracts a hydrogen radical from the amine substrate to form the α-aminoalkyl radical **8** directly (Scheme 5). These two mechanisms are complimentary, allowing for different reactivity.

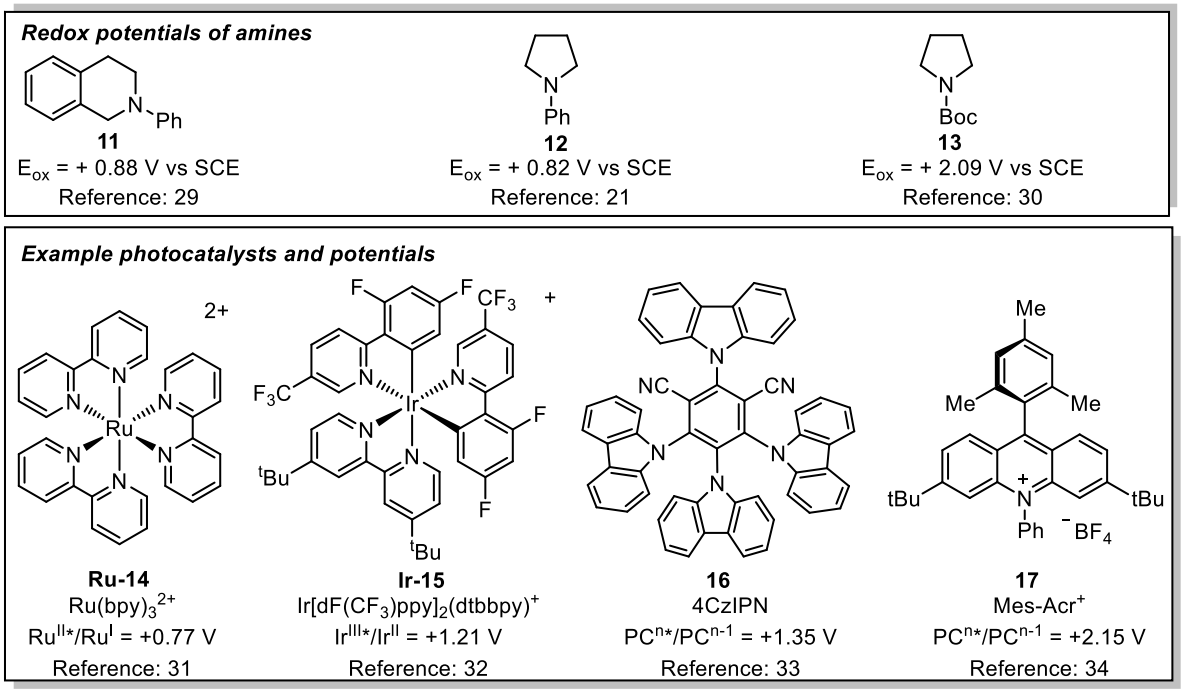


Scheme 5: Single electron transfer and hydrogen atom transfer strategies to from carbon centered radicals on nitrogen heterocycles.

1.2.2.3. Single electron transfer (SET) methods of radical formation

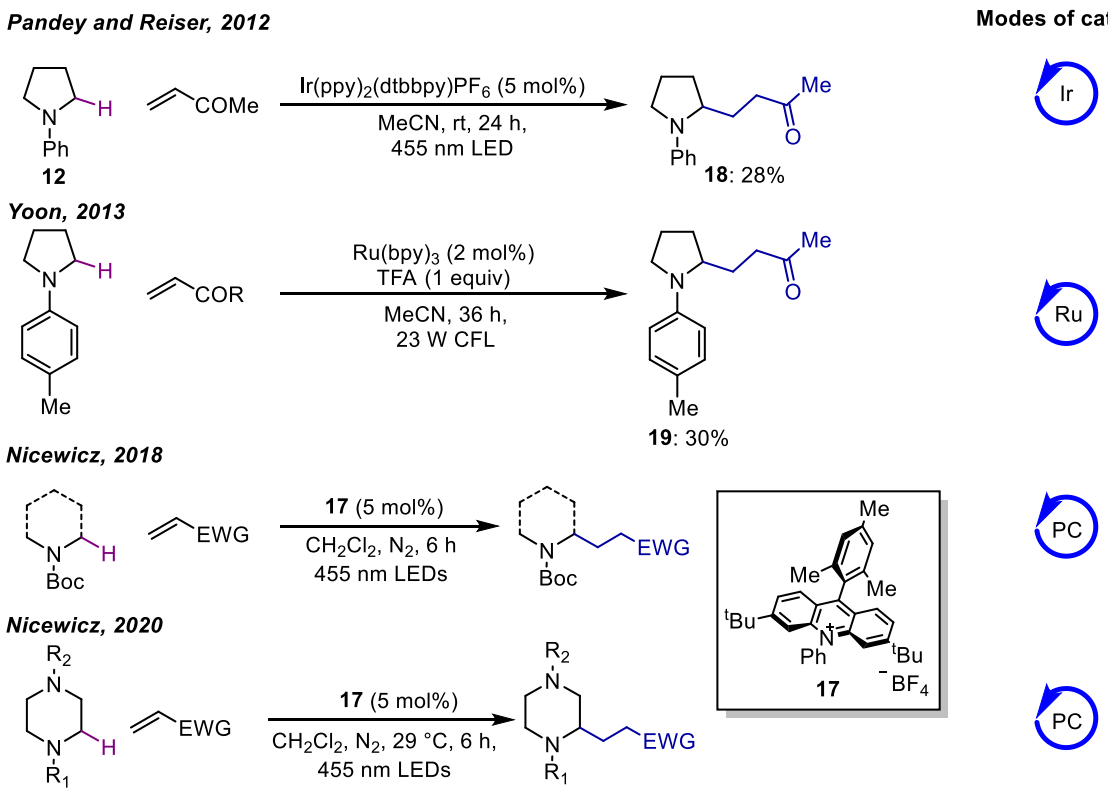
The substrate scope of SET methods is set directly by the relative redox potentials of the photocatalyst excited state and the substrate, with only certain nitrogen heterocycles compatible with this method. The most common photocatalysts are polypyridyl iridium and ruthenium complexes such as **14** and **15**, with oxidation potentials sufficient to oxidise *N*-aryl heterocycles (Scheme 6). Initial examples of these reactions consisted of substrates such as

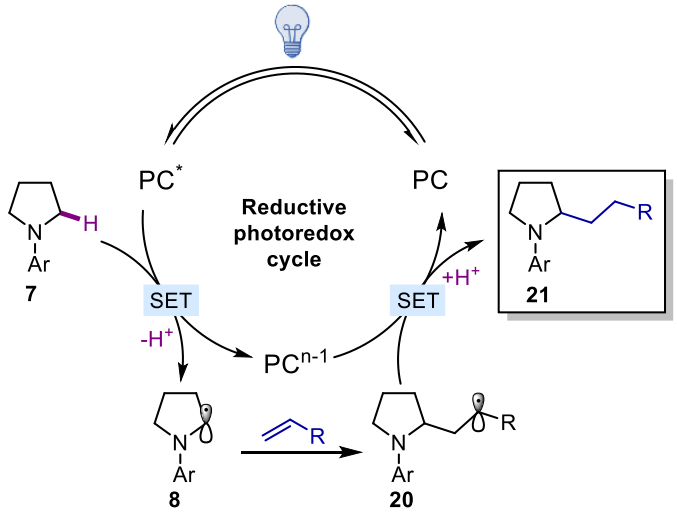
N-arylTHIQ **11** or *N*-aryl-pyrrolidine **12** with relatively low redox potentials. The generation of more bespoke catalysts such as **17** has allowed access to heterocycles with higher oxidation potentials such as *N*-Boc-pyrrolidine **13**.



Scheme 6: Redox potentials for different amine substrates and common photocatalysts. Redox potentials are given as V vs SCE.

In 2012, Reiser and co-workers reported the first photoredox catalysed C–H alkylation of nitrogen heterocycles, to functionalise mostly *N*-arylTHIQs and a single, low-yielding example using *N*-phenylpyrrolidine as a substrate (**17**, Scheme 7A). [35] This was a Giese-type reaction which behaved according to the general mechanism described in Scheme 7B: either an iridium or ruthenium photocatalyst was excited by absorption of visible light to form an excited state which underwent SET with amine heterocycle **12** to form an α-aminoalkyl radical **8** upon deprotonation.





Scheme 7: A) Examples of C–H functionlisation of nitrogen heterocycles using photoredox catalysis and B) the general mechanism for a single catalytic apporach.

The radical added into a radicophile to form the product radical **20**, which was reduced by the reduced catalyst intermediate and protonated to afford product **21** and regenerate the ground state photocatalyst.

A few examples using this strategy have afforded alkylation of azacycles, including an adaptation by Yoon in 2013 using TFA as a Brønsted acid co-catalyst to improve the efficiency of the strategy, obtaining higher yields of alkylated *N*-arylTHIQs using $Ru(bpy)_3$ than obtained

by the seminal work (Scheme 7A).[36] The authors proposed addition of acid to increase the rate of addition of the α-amine radical into the vinyl ketone acceptor, changing the rate determining step to a chain propagation mechanism. However, expansion of the strategy towards *N*-aryl azacycles more generally was limited, and only a single, low yielding example of an *N*-aryl-pyrrolidine, **19** in 30%, was achieved. The main reason for this low yield was likely a mismatch of redox potentials between the photocatalyst and substrate; excited $Ru(bpy)_3$ has a moderate oxidising power of +0.77 V vs SCE.

More recent approaches have sought to expand the oxidation potentials of photocatalysts to enable oxidation of substrates useful in medicinal chemistry, such as carbamate-protected azacycles. Particularly due to the high environmental and financial costs of iridium and ruthenium catalysts, new organic photocatalysts have been developed based on highly conjugated frameworks. In 2016, DiRocco and co-workers developed a series of acridinium-based catalysts with greater oxidising power than the first acridinium catalyst developed by Fukuzumi in 2014.[34] Notably, excited acridinium photocatalyst **17** (E^*_{red} = +2.15 V) was used by the Nicewicz group for alkylation of Boc-protected nitrogen heterocycles of a variety of ring sizes (4–6, Scheme 7A).[37] Expanding on this work, in 2020 the same group applied this methodology to the alkylation of differently *N*-protected piperazines, developing a predictive method to determine the selectivity of the reaction with respect to each of the α-nitrogen positions (Scheme 7A).[38] Site-selectivity was explained and predicted using natural population analysis[39],[40] to determine the relative change in electron density between the neutral molecule and radical cation at each of the nitrogen centres.

In 2012, Adachi and co-workers developed a series of organic light emitting diodes (OLEDs) with cyanoarene cores.[33] Additional organic photocatalysts containing variations of the on the cyanoarene scaffold were generated by Zeitler and co-workers, in 2018.[41] These have so far been used in as organic photocatalysts in several photoredox transformations,[42] and, in increasing the redox ranges accessible by organic photocatalysts, may provide promise in accessing azacycles with higher oxidation potentials.

Despite the difference in photocatalysts employed, the elementary steps of reaction: excitation of the photocatalyst, oxidation by one reaction component, and reduction by another, remain consistent across these examples. Developing an understanding of the kinetics of these steps would be powerful for aiding design of efficient photoredox reactions at a variety of reaction scales. More complex mechanistic approaches to photocatalytic reactions all employ these core steps, with modifications either in the formation of the heterocycle radical, or subsequent radical reactivity. The rest of this section will describe common modifications to the simple photoredox mechanism to achieve more diverse reactivity.

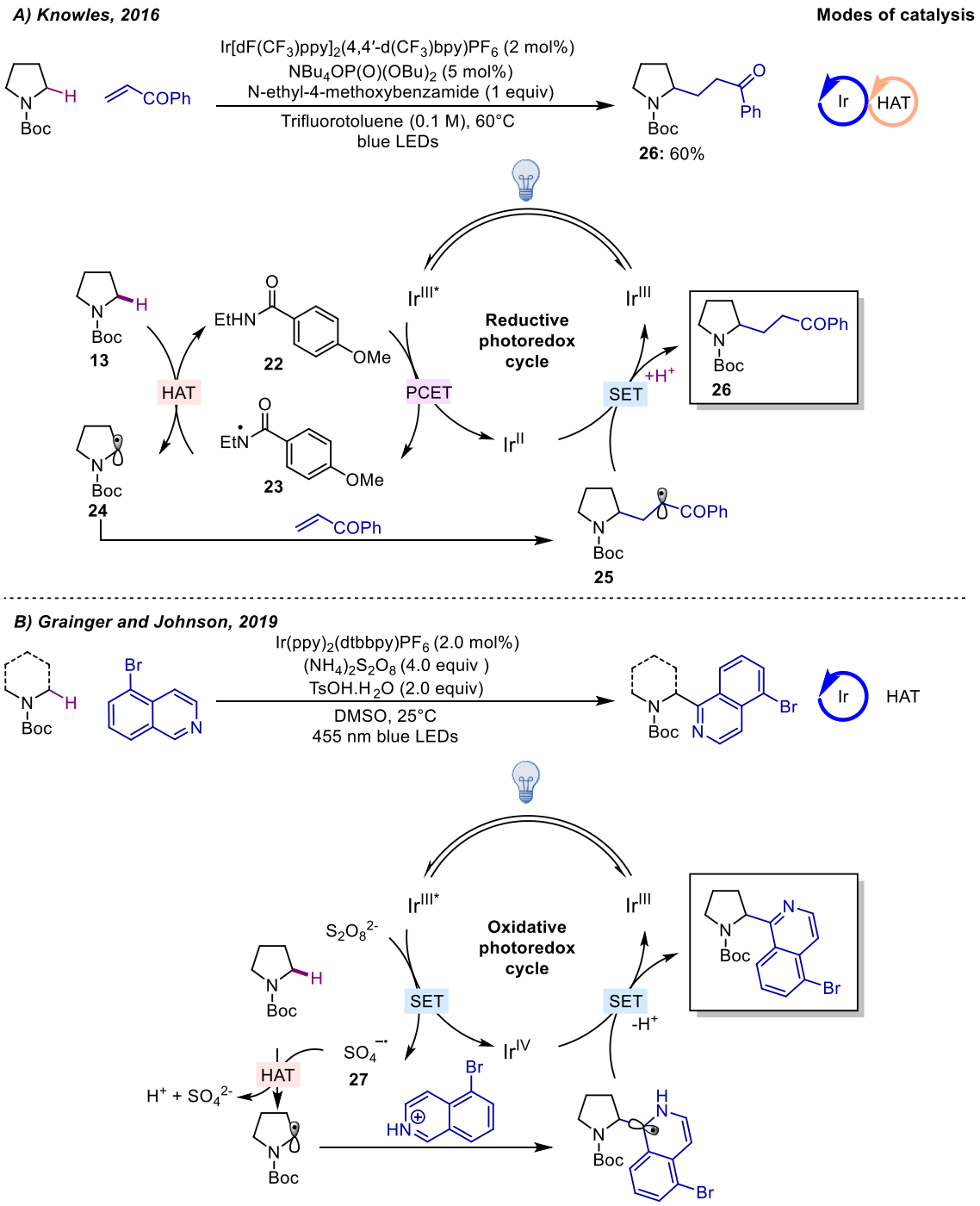
1.2.2.4. Hydrogen atom transfer (HAT) methods of radical formation

Another approach to achieve the α-aminoalkyl radical formation of heterocycles with higher oxidation potentials is hydrogen atom transfer. Rather than the substrate scope being determined by redox potentials, HAT dependson the bond enthalpy of the C–H bond to be broken, which is largely governed by polarity, as well as steric effects. In these strategies, photoredox catalysts are often used to activate the HAT reagent through SET, with the resulting radical able to abstract a hydrogen atom from the nitrogen heterocycle to form a carbon-centred radical at the most hydridic position, usually an α-heteroatom C–H bond. The most hydridic position in a molecule is also dependent on the electrophilicity of the resulting HAT radical. Selected examples of combined photoredox/HAT strategies to achieve C–H functionalisation of nitrogen heterocycles are presented in Scheme 8.

In 2016, Knowles and co-workers reported an alkylation reaction using an excited state iridium catalyst to activate benzamide **22**, generating heterocycle radical **23** through a proposed concerted proton and electron transfer from the substrate to a phosphate base and iridium catalyst respectively, (proton-coupled electron transfer, PCET) Scheme 8a).[43] Radical **23** then acts as a hydrogen atom transfer agent to obtain the α-aminoalkyl radical of *N*-Boc-pyrrolidine **24**. Radical **24** could then add into the acceptor to form product radical **25**, which was reduced and protonated to afford product **26**, closing the catalytic cycle in the same way as in the general mechanism for alkylation depicted in Scheme 7B. This reaction was mainly used to functionalise *N*-alkyl amides, with a single nitrogen heterocycle example **26** reported in the scope.

A photoredox/HAT strategy was also used by Grainger, Johnson and co-workers at Astex in 2019 to achieve arylation of nitrogen heterocycles through a Minisci-type reaction, developed using a high-throughput workflow (Scheme 8B).[44] The main difference in this mechanism to that of Knowles was in formation of the amine radical; this work used a persulfate ion as a stoichiometric HAT agent, activated by oxidative SET with the iridium photocatalyst to form sulfate radical **27**.

These two examples exemplify HAT as a strategy for the generation of carbon radicals from nitrogen heterocycles with high oxidation potentials, allowing greater scope of heterocycles to be used in photoredox reactions than with direct electron transfer. HAT agents can be optimised for different photocatalysts and C–H bonds, increasing the utility of photosynthetic transformations.

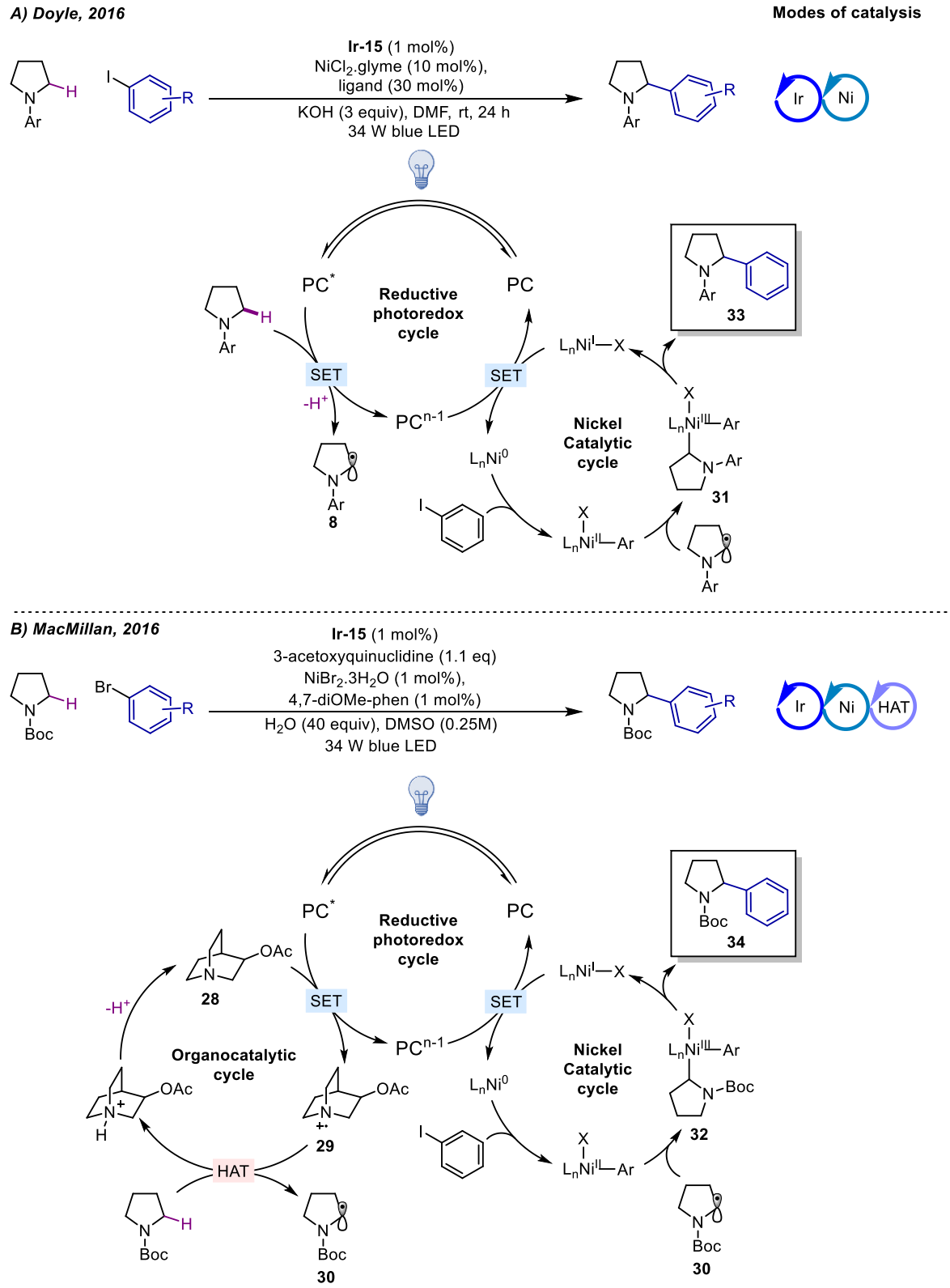


Scheme 8: Selected photoredox catalysed C–H functionalisations using combined photoredox and HAT catalysis strategies.

1.2.2.5. Metallophotoredox strategies

A key development in photoredox catalysis has been combining radical generation with transition metal catalysis, termed 'metallophotoredox', which has allowed expansion of the transformations possible using α-aminoalkyl radicals. In 2016, reports came from the groups of both Doyle and MacMillan respectively to achieve C(sp^3–H) arylation of nitrogen

heterocycles (Scheme 9A and B). Decarboxylative methods using metallophotoredox had previously been reported in a collaboration between Doyle and MacMillan and coworkers.[45]



Scheme 9: Examples of metallophotoredox mechanisms as described by A) Doyle[34] and B) MacMillan.[35]

These strategies had many similarities, both utilising nickel catalytic cycles to couple nitrogen heterocycle radicals and aryl halides, but differed in their generation of these heterocycle radicals: Doyle's example used direct SET between the iridium photocatalyst and *N*-aryl-heterocycles,[46] whilst MacMillan's example utilised a nominally catalytic HAT agent in the form of 3-acetoxyquinuclidine **28**, activated by SET with the excited state photocatalyst to form radical cation **29**.[47]

In these approaches, α-aminoalkyl radicals **8** and **30** are generated by methods discussed previously, either SET (Scheme 9A) or HAT (Scheme 9B), initiated from interaction with the photocatalyst excited state. To close the photocatalytic cycle and regenerate the ground state photocatalyst, a nickel(I) complex is reduced to Ni(0). Aryl or alkyl halides can then oxidatively add in to the nickel(0) complex, which can then be oxidised further by addition of the generated α-aminoalkyl radical to form a Ni(III) complex (**31** and **32**). Reductive elimination then affords the product (**33** and **34**) and a Ni(I) complex, closing the nickel catalytic cycle.

Metallophotoredox approaches have since been used to achieve several interesting coupling transformations, greatly widening the scope of achievable reactions.[48] Of note was the expansion of the triple-catalytic cycle approach described in Scheme 9B to achieve couplings of carbamate protected heterocycles with alkyl bromides.[49] Alternative transition metals including copper and palladium have also been used in place of nickel in similar transformations.[36]

Whist there have been many mechanistically distinct photoredox reactions of varying complexity to achieve C–H functionalisation of nitrogen heterocycles, there have been few mechanistic studies in this area. Photoredox reaction mechanisms are typically difficult to determine, and despite a decade of innovative synthetic strategy and a surging uptake of visible-light based methods, there have been few systematic studies on the underlying chemical properties, and in particular kinetics, of such mechanisms. This includes studies on the more mechanistically simple, single catalytic cycle reactions. Limitations on the utility of photoredox methods have become reproducibility, scale-up, and selectivity - factors which require focused and extensive mechanistic understanding. Light-promoted radical reactions contain several differences compared with two-electron chemistry which complicates mechanistic experimentation, and over the last 5 years has there been increasing research into detailed mechanistic analysis for photoredox catalysis. However, few publications pertain to C–H functionalisation of nitrogen heterocycles.[50,51] A deeper understanding of the fundamental chemistry of such reactions could therefore enable more intelligent design and greater usage of photoredox reactions for a variety of scales.

This thesis aims to investigate the mechanism of a single catalytic cycle reaction to uncover insights into the kinetics and selectivity of photoredox reactions. The main techniques used for investigating the mechanisms of photoredox reactions will therefore be discussed in the next section, both the methods used and key uses of these methods in mechanistic analysis.

1.3. Probing the mechanisms of photoredox reactions

One of the difficulties in mechanistic analysis is that the kinetics of the photoredox reaction is intrinsic to the reaction set-up, therefore any photophysical measurements taken out of the reactor must be critically evaluated to determine their relevance to the reaction. This section will therefore describe *in situ* techniques, particularly relating to kinetic analysis, and *ex situ* photophysical techniques, separately in this section. Both types of methods are important to give holistic reaction analysis.

1.3.1. UV-vis spectroscopy

Spectroscopic methods are useful for choosing which wavelengths of light to use with different photocatalysts. Photocatalysts have maximum wavelengths of absorption, λ_{max}, related usually to a metal-to-ligand charge transfer event in the case of transition metal photocatalysts. Choosing a light wavelength which matches the maximum wavelength of absorbance of the photocatalyst absorbance may be desirable. UV-vis spectroscopy can be used to determine the photocatalyst λ_{max}. Other reaction species may absorb light at the same wavelength which could reduce reaction efficiency or lead to undesirable side-reactivity/degradation; therefore, the wavelengths at the catalyst λ_{max} may not be the most productive.[26]

The most efficient photocatalytic reactions from an energy standpoint are ones in which the solution, and therefore the catalyst, are uniformly irradiated, and one in which there is no excess light transmittance through the solution. UV-Vis spectroscopy can be used to determine the absorbance of the solution, which is controlled by the Beer-Lambert law (equation 1). Absorbance is related to transmittance through equation 2.

$$A = \varepsilon c l \quad (1)$$

$$A = -\log T \quad (2)$$

UV-vis spectroscopy can also be used to determine which components in a reaction are capable of acting as electron transfer or energy transfer agents, such as when electron donor-acceptor (EDA) complexes could be active in a reaction mechanism.[26] If the UV-Vis spectrum of a combination of reagents differs from that of the individual components added together,

especially if there is a new absorption peak within the wavelength range of lights used for photoredox reactions, this can indicate formation of an encounter complex in the reaction mixture. The most common of this type of complex is an EDA complex, which can induce single electron transfer or energy transfer on irradiation.[52] UV-vis spectroscopy can therefore be used for mechanistic investigations of photochemical reactions.

1.3.2. Cyclic Voltammetry

Cyclic voltammetry is an electrochemical technique which allows determination of the redox potential of a given material. Redox potentials are a thermodynamic descriptor of the tendency for a material to gain or lose electrons, and therefore describe the feasibility for SET between two species to occur. This is most usually expressed as in the Nernst equation (equation 3), where n is the number of electrons transferred in the reaction, F is the Faraday constant (96500 coulombs.mol^{-1}), and ΔE the change in cell potential.

For photoredox reactions in which the photocatalyst excited state interacts with a quencher, the Rehm-Weller equation can describe the energy change in terms of redox potentials (equation 4).[53] The ΔG of electron transfer from an electron donor (D) to an electron acceptor (A) is related to the difference in oxidation $E^0_{D^{\cdot+}/D}$ and reduction $E^0_{A/A^{\cdot-}}$ potentials of these components respectively. E^* is the excited-state energy of the catalyst, e is the unit electrical charge and $\Delta E_{Coulombic}$ describes the Coulombic attraction, or work done to bring the electron donor and acceptor complexes together. In most organic reactions, Coulombic attraction is assumed to be negligible, so the Nernst and Rehm-Weller expressions can be condensed to equation 5.[53,54]

$$\Delta G_0 = -nF\Delta E \quad (3)$$

$$\Delta G_{ET} = e[E^0_{D^{\cdot+}/D} - E^0_{A/A^{\cdot-}}] - E^* + \Delta E_{Coulombic} \quad (4)$$

$$\Delta G_{ET} = -nF(E^0_{D^{\cdot+}/D} - E^0_{A/A^{\cdot-}} - E^*) \quad (5)$$

For a reaction to be favourable, ΔG should be less than 0. Therefore, for a SET reaction to be feasible by reductive quenching, the oxidation potential of the substrate must be of a lower magnitude than the reduction potential of the catalyst. Redox potentials are therefore a useful metric to determine which substrates are likely to productively interact in single electron processes.

Cyclic voltammetry (CV) allows the redox potential of a compound to be determined. It is an electrochemical method which involves applying a potential across an electrochemical cell containing a sample of the molecule to be studied. The cell potential is scanned between set

values at a constant rate, and the resulting current is recorded.[55] Redox events are visible as 'waves' of current peaks. For compounds with reversible oxidation/reduction potentials, two waves of opposing sign are observed at different potentials: an oxidation and a reduction (Figure 1a). For a reversible reaction, the $E_{1/2}$ describes the potential halfway between the peak oxidation and peak reduction potential. This has been described as the most reproducible and standard measurement used to present redox potentials of photocatalysts.[56]

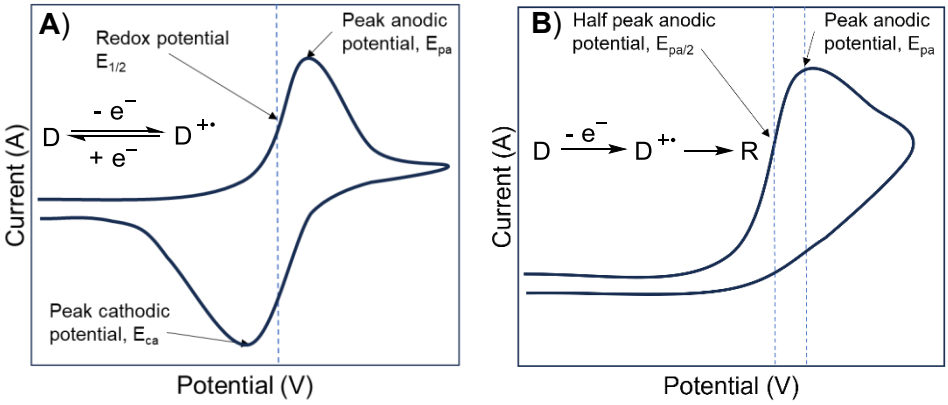


Figure 1: Schematic of a A) reversible CV wave and B) irreversible oxidation.[41,57,43]

Several organic molecules undergo irreversible electron transfer, where a chemical step follows the electron transfer step preventing reversible redox events. This chemical step could be a deprotonation, rearrangement, or decomposition (Figure 1B). For example, some of the most common synthetic photoredox methods employ redox active esters or carboxylic acid radical precursors. In both cases, single electron transfer is accompanied with a rapid irreversible fragmentation to form the desired radical species.

Due to the lack of a comparative reversible single electron transfer, it is difficult to report redox potentials of molecules such as this in the traditional $E_{1/2}$ manner using cyclic voltammetry, and therefore either peak anodic potentials (E_{pa})[41] or half peak anodic potentials ($E_{pa/2}$) values[54] are reported instead. It is notable that the E_{pa} and $E_{pa/2}$ values are both subject to variation based on the setup of the cyclic voltammetry experiment, particularly the scan rate. CV analysis is therefore more useful as a comparative rather than absolute method when obtaining redox potentials of substrates with irreversible electron transfers.

In 2016, Nicewicz and co-workers published the redox potentials ($E_{pa/2}$) for over 180 organic molecules, obtained both experimentally from cyclic voltammetry data and using DFT measurements.[54] This provided organic chemists with a framework with which to compare the likely reactivity of several substrates in photoredox reactions, by comparing with the redox potentials of photocatalysts. In 2023, Stirling and co-workers developed both DFT and

machine learning methods to predict the redox potentials of excited state organic photocatalysts, enabling the expansion of the dataset of photocatalysts.[58] Furthermore, redox potentials are often used to help identify feasible substrate interactions in deciphering mechanisms of photoredox reactions.

1.3.3. Luminescence quenching experiments (Stern-Volmer)

One of the most common methods to investigate photoredox reaction mechanisms is Stern-Volmer luminescence quenching. Stern-Volmer analysis provides information on how the excited state photocatalyst interacts with other reaction components, particularly which reaction component the photocatalyst excited state is quenched by and the rate constant of that process.[14,59]

The rate of photocatalyst quenching is related to the processes of photon absorbance and excited state decay. On absorption of a photon, an electron in the HOMO of the photocatalyst is promoted from a ground state ($\mathbf{S_0}$) to a singlet excited state ($\mathbf{S_1}$, Figure 2). From here, the electron can either decay back to the ground state in a radiative manner as fluorescence, or undergo intersystem crossing (ISC), a non-radiative process, to form a triplet excited state ($\mathbf{T_1}$).[26,60] Intersystem crossing is typically required for photocatalysis as for metal photocatalysts the triplet excited state is usually much longer lived than the singlet excited state (μs vs ns). For organic photocatalysts this is not always the case, and S_1 can be the more persistent photocatalyst state.[61] From the triplet state, the electron can either decay back to the ground state through phosphorescence or interact with a molecule either through energy transfer or single electron transfer- allowing a chemical transformation to occur. The excited state lifetimes of commercial catalysts are usually known in a given solvent.[14]

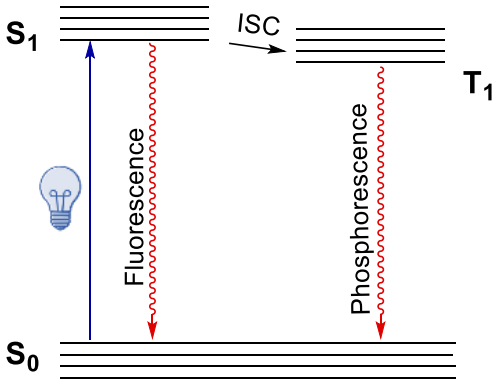


Figure 2: Jablonski diagram.

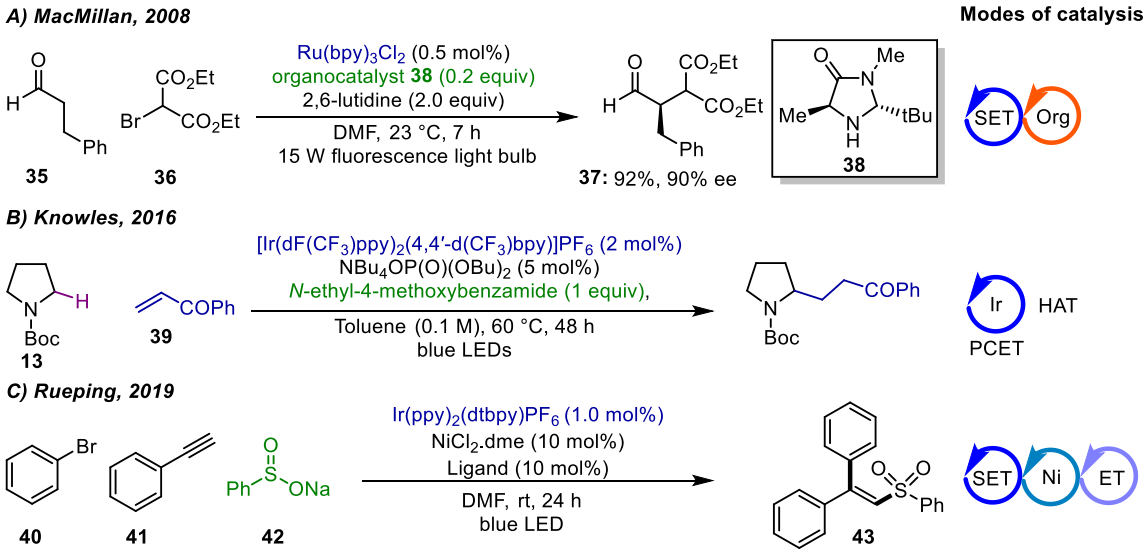
To obtain the rate of catalyst quenching by a particular reaction component, the luminescence emission spectrum of a solution of photocatalyst is recorded, and the intensity of this emission recorded as I_0. A portion of the reaction component to be tested, the quencher Q, is then added to the photocatalyst solution, and the spectrum is re-recorded, giving I. This is completed over several different concentrations of Q. If the tested compound undergoes electron or energy transfer with the photocatalyst excited state, the solution emission intensity will decrease as concentration increases.

Plotting a graph of I_0/I against [Q] allows determination of both the quenching constant K_{SV} via equation 6 and, if the catalyst excited state lifetime τ_0 is known, also the rate constant for quenching k_q, via equation 7.

$$\frac{I_0}{I} = 1 + K_{SV}[Q] \quad (6)$$

$$K_{SV} = k_q.\tau_{0.} \quad (7)$$

Stern-Volmer studies have been used in many photoredox investigations to determine the species responsible for quenching the catalyst excited state in new reaction types, and is regularly referenced in communications and reviews on investigating reaction excited states.[26,60] In 2008, MacMillan and co-workers developed a reaction to afford enantioenriched α-alkylated aldehydes **37** from aldehydes **35** and racemic α-bromocarbonyls **36** in a complex reaction mixture using photoredox and organocatalysis (Scheme 10A).[62] The authors used luminescence quenching to determine that the amine organocatalyst **38,** rather than the expected bromoalkane **36,** was interacting with the excited state of $[Ru(bpy)_3]^{2+}$. In 2016, Knowles and co-workers used Stern-Volmer analysis to identify a proton-coupled electron transfer mechanism in the remote C(sp^3)–H alkylation of amides and *N*-Boc-pyrrolidine **13** with Michael acceptors **39**, observing that the amines only quenched the catalyst in the presence of base (Scheme 10B).[43]



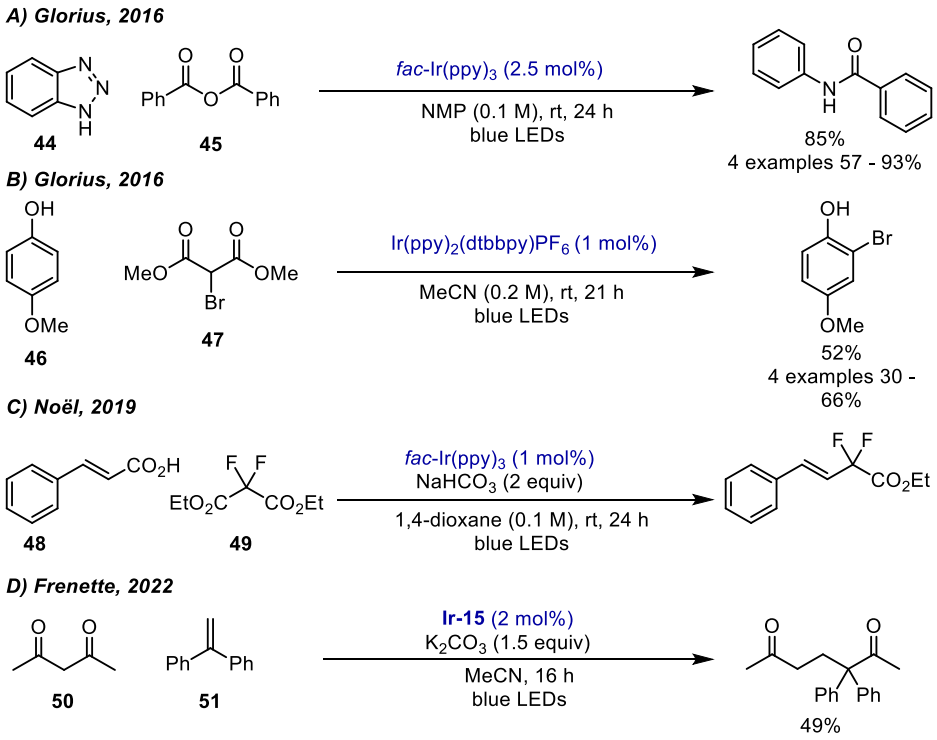
Scheme 10: Selected examples using luminescence quenching to gain mechanistic understanding in photoredox examples. In each case the catalyst quencher is coloured in green.

In 2019, Rueping and co-workers used Stern-Volmer studies to identify sulfinate salts **42** as the catalyst quencher in a synthetic strategy using single electron transfer, energy transfer and nickel catalysis to afford stereodefined olefins **43** (Scheme 10C) from alkyl bromides **40** and alkynes **41**.[63] Furthermore, emission spectra of different tested catalysts were used to rationalise different rates of isomerisation in the products and identify that the rate of isomerisation was linked to the triplet-triplet energy transfer. Hence, the authors were able to switch reaction selectivity from *E* to *Z* by choosing photocatalysts based on the triplet state energy.

Due to the widespread use of luminescence quenching experiments and the degree of information obtained by these studies, high-throughput and computational methods for Stern-Volmer analysis have been used to screen for new substrates in photoredox reactions. In 2016, Glorius and co-workers developed a screening platform in which 100 acetonitrile-soluble organic compounds were rapidly screened for a reduction in fluorescence emission intensity of a solution of photocatalyst which would signify interaction with the photocatalyst excited state.[64] This allowed identifications of hits which were optimised to obtain novel reactions: benzotriazoles **44** with anhydride **45** and phenols **46** with alkyl bromides **47** using iridium photocatalysis (Scheme 11A and B).

Furthermore, in 2019, Noël and co-workers developed a fully automated continuous flow platform to perform Stern-Volmer analysis and extract k_q data.[65] This was applied to a known reaction, the decarboxylation of cinnamic acid **48** with fluoroalkane **49**,[66] to investigate the

catalyst quenching (Scheme 11C). Interestingly, the E/Z mixture of cinnamate quenched the catalyst at approximately twice the rate of fluoroalkane **49**; however, the *trans*-cinnamate quenched at a lower rate than the **49**. Due to the presence of base in this reaction, the cinnamate was assumed to be the *trans*-diastereomer. Therefore, with a higher k_q and lower reduction potential, the authors proposed fluoroalkane **49** oxidatively quenched the $Ir(ppy)_3$ catalyst in the first step of this reaction.



Scheme 11: Novel photocatalytic reactions identified by Stern-Volmer screening methods.

Frenette and co-workers took this idea further in 2022, developing a computational model to predict successful substrates in photoredox reactions using quenching rate constants obtained by Stern-Volmer experiments.[67] The authors noted that the kinetics of photoredox reactions were crucial for the success of these reactions, and often difficult to predict. Using one of the most widely used photoredox catalysts, $Ir[dF(CF_3)ppy]_2(dtbbpy)PF_6$ (**Ir-15**), rate constants for 49 quenchers representing a variety of molecules (mostly amines and phenols, but also more diverse substrates including trifluoroborate salts and thiols) were experimentally determined. This dataset was used to obtain a model using DFT calculations to predict quenching constants. Two models were developed for this, using either ionisation energies or redox potentials of potential quenchers respectively to predict k_q. The authors noted that ionisation energies were better predictors of quenching rate than redox potentials, although there was good agreement with both models. The authors were able to predict novel photoredox substrates and developed the novel reaction of diketone 2,4-pentanedione **50** and

1,1-diphenylethylene **51** based on the computational model (Scheme 11D). This work indicated the importance of understanding the kinetics and not solely redox potentials for successful reaction.

In 2022, Cresswell and Euser and co-workers developed a microreactor approach for Stern-Volmer analysis using optofluidic hollow-core photonic crystal fibres, allowing analysis to be performed on nanolitre solutions.[68] This work demonstrated that quantitative analysis could be achieved with a 10^4 reduction of volume compared to standard cuvette analysis, limiting waste of expensive photocatalysts. This method supported conclusions obtained from Stern-Volmer analysis in batch, regarding a photocatalytic HAT approach to hydroaminoalkylation of acrylates with primary alkylamines. This example will be discussed in detail in section 1.4.2.

These selected examples demonstrate the utility of the Stern-Volmer luminescence quenching experiments and are one tool chemists can use to probe the excited state interaction between the catalyst and quencher. Crucially, unlike redox potentials, luminescence quenching techniques can be used to understand the rate of single electron transfer from a catalyst excited state, i.e., the rate of quenching. However, this experiment is undertaken in a fluorescence spectrophotometer, containing a different light source and often pathlength compared to the synthetic reaction. Therefore, it is perhaps most useful for comparative kinetics between different reaction components or substrates.

1.4. Kinetics of photoredox reactions

While Stern-Volmer and cyclic voltammetry studies can provide useful methods to investigate reaction mechanisms, the rate of photoredox reactions is very particular to the concentrations of components, features of the light source and reaction setup. Complete investigation of the kinetics of photoredox reactions, and therefore full understanding of the reaction mechanism, requires *in situ* reaction analysis. This next section will discuss methods to obtain kinetic information on photoredox reactions, as well as key findings from kinetic studies reported in the literature.

1.4.1. Key kinetic findings of photoredox systems

1.4.1.1. Effect of light intensity on reaction

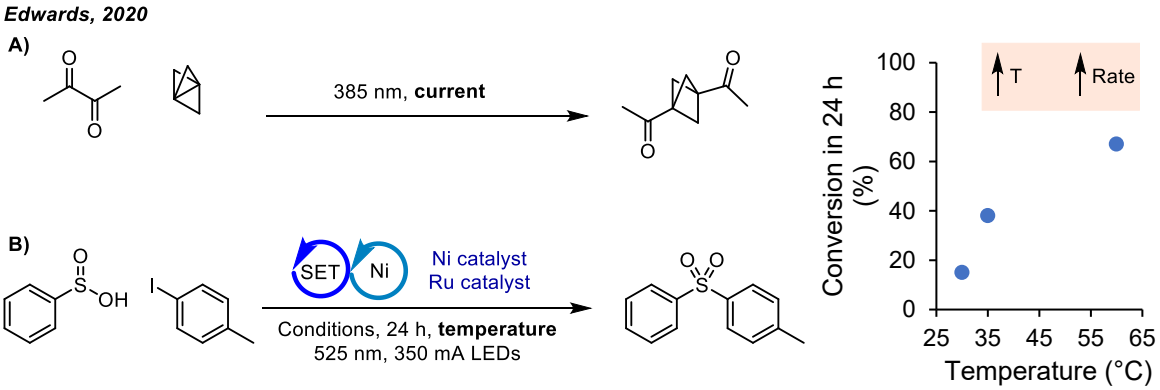
Light is a energy source essential for effective photoredox catalysis- a photon is required to interact with a molecule of photocatalyst to form the excited state. As such, light influences reaction rate. There are a few features it is useful to consider when discussing the kinetics of photoredox reactions.

1. Photon flux: number of photons reaching a specific unit of area per second.[69]
2. Quantum yield (φ): the ratio between photons of light absorbed and molecules of product formed.[70]

Photon flux and quantum yield are features which are not only specific to a reaction, but to the reaction set-up. Detailed kinetic analysis is required to determine the role of light intensity, and therefore photon flux, in the particular reaction and system being studied. This is not without challenges, as the concentration of light is so set-up specific: to the power, wavelength and distance of the light source from the reaction mixture, to the thickness and curvature of the vessel, and the surface-area to volume ratio of the reaction mixture itself. As such, reactions can be difficult to reproduce between different laboratories, and there have been several calls from industry for standardisation or full reporting of reaction setups to mitigate for this.[12]

In 2019, Bloh proposed several rate equations to describe homogeneous photoredox catalysis using rate law derivations and mathematical models.[71] Of note, reaction rate was described in relation to substrate concentration. Bloh proposed that for reactions in which light intensity was relatively low, two kinetic regimes would be present throughout the reaction. The first would be when substrate concentration is high, rate would be governed by the rate of photon absorption and quantum yield, therefore by the concentration of photocatalyst and light intensity. As substrate concentration decreases, the rate may shift to first order kinetics with respect to substrate and the excited state of the photocatalyst. There have been a few detailed studies of the kinetics of photoreactions, investigating these effects and these will be discussed throughout this section.

In designing a scalable photochemical reactor, Edwards and co-workers at GSK demonstrated that increasing the power of the LEDs in the reactor increased the rate of a Norrish I reaction, but only to a point beyond which no rate increase was observed (Scheme 12A).[72] At low light intensities, the reaction was photon-limited and the rate increased with light intensity, and above 800 mA, excitation of the photosensitised substrate was not rate limiting, and there was no dependency on light.



Scheme 12: Investigations into yield change with light. For reaction B, the 60 ° C point is an isolated yield rather than %conversion.

Furthermore, using the same scalable platform, Edwards and co-workers investigated the dependency of a combined photoredox and nickel catalysed cross coupling reaction (Scheme 12B), in one of the first investigations into the effect of temperature on photoredox reactions. The authors were able to exploit features of their developed photoreactor including a thermoelectric cooling unit and internal temperature probe to both set and measure the real temperature of photoredox reactions. Setting the current and wavelengths of the reactor allowed decoupling of the rate contributions of light and temperature, and allowed the authors to determine a rate dependence on temperature (Scheme 12C). This implied that a thermally governed process was rate-limiting, proposed to be the oxidative addition into the nickel complex. By contrast, under photon-limited conditions the excitation of photocatalyst by light would likely be temperature independent.

As has been described in some examples throughout this section already, flow chemistry is frequently employed to enable photoredox reactivity. Flow reactors typically enable higher photon flux through a solution due to allowing for much smaller pathlengths than typical batch equipment, vials or glass vessels.[73] Consequently, flow photoreactions are often much faster than the same reaction in batch.[74,75] Additionally, the flexibility of flow chemistry allows a reactor to be designed for a particular reaction, providing more possibilities for optimisation than batch including reactor volumes, pathlengths, flow rates and distance from a light source. Along with optimisation, flow chemistry setups can also enable more reproducible methods for scaling up reactions due to this flexibility.[13]

1.4.1.2. Impact of catalyst concentration on rate

Whilst light sources are clearly important in photoredox reactions, photons interact with photocatalysts and therefore the concentration of the photocatalyst is important. Investigations

into the impact of catalyst concentration on reaction rate have unveiled a few key considerations.

In 2017, Wittenburger and co-workers at Abbvie investigated the rate of oxidation of 9,10-diphenylanthracene **52** using a photoflow reactor (Figure 3A) and consequently proposed several heuristics for designing photo-flow reactors based on their findings.[76] These heuristics included:

1. Assuming a continuous light intensity, increasing reaction concentration should increase the rate of product formation.
2. Increasing catalyst concentration should increase reaction rate, up to physical limitations.

Whilst the first heuristic is perhaps intuitive, the second hints at an important phenomenon in photoredox reactions: rate dependence on catalyst is only linear to a point, with limitations being due to catalyst light absorbance according to the Beer-Lambert law.

An earlier photoflow study is useful for exemplifying this limitation. In 2012, Gagne and co-workers were investigating photocatalyst loading when designing a flow reactor for photoredox mediated synthesis of *C*-glycosides (Figure 3B).[77] In this instance, increasing the concentration of the $[Ru(dmb)_3]^{2+}$ photocatalyst decreased the rate of reaction, which was directly contradicted by the Abbvie heuristic. Rate was found to be correlated to the transmittance of light through the reaction mixture as described by the Beer-Lambert law (equations 1, 2 and 8).

$$L = \frac{-\log(T)}{\varepsilon c} \tag{8}$$

Photocatalysts are highly light-absorbing species with often known extinction coefficients, meaning the absorbance of a reaction mixture is proportional to the concentration of photocatalyst in solution. This also means that the distance light travels through a reaction solution is proportional to the concentration of photocatalyst in solution, assuming no other reaction components absorb the incident light. Higher catalyst loadings can therefore reduce the distance of light penetration through the reaction solution, meaning the distribution of active, excited-state catalyst is not uniform and the rate of reaction decreases as a result. The effect of photocatalyst concentration on reaction rate is therefore not linear throughout all photocatalyst loadings.

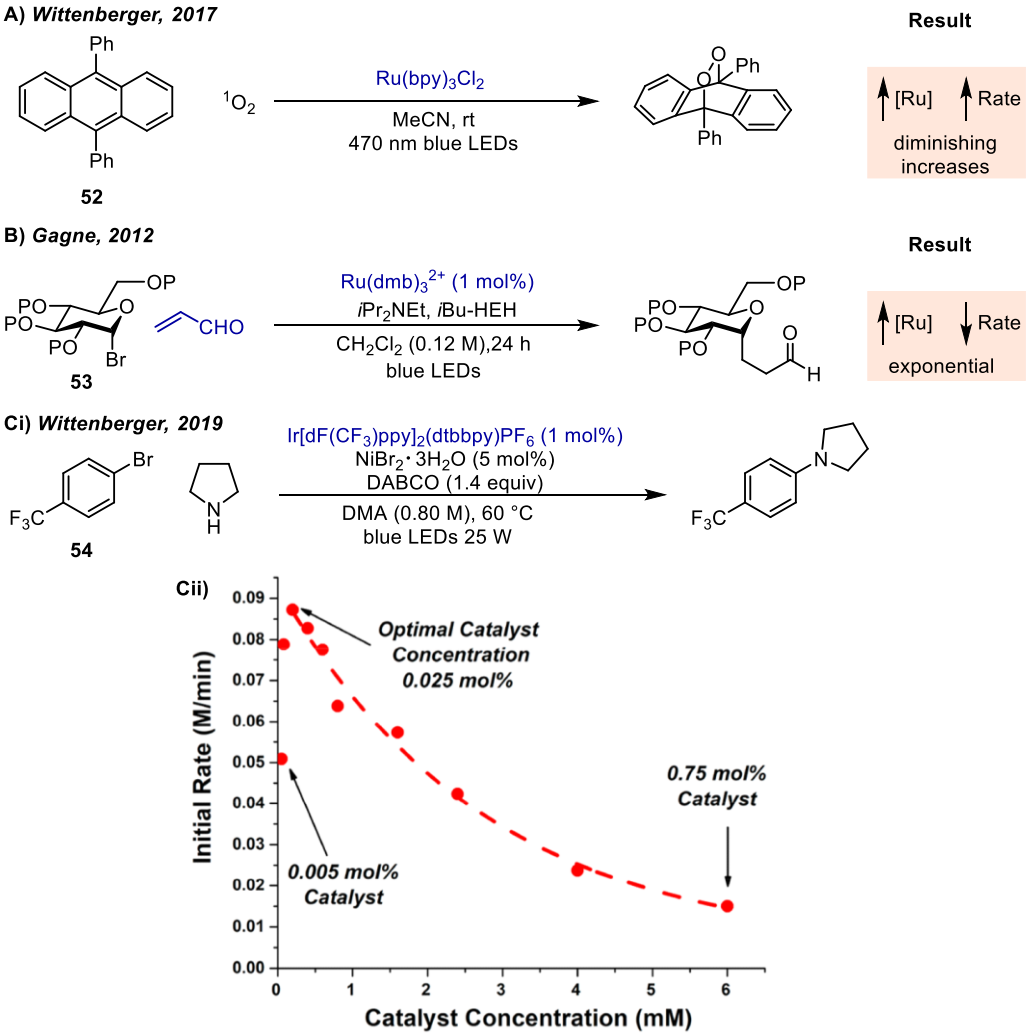


Figure 3: Investigations into the effect of catalyst concentration on rate as reported by A) Wittenberger and co-workers in 2017, B) Gagne and co-workers in 2012, and C) Wittenberger and co-workers in 2019. Graph reproduced directly from Wittenberger and co-workers, 2019.[78]

A detailed 2019 study from Abbvie showed how catalyst loading affects reaction rate through two different effects (Figure 3C).[78] Wittenberger and co-workers were developing a flow chemistry platform for scaling photochemical reactions using a dual photoredox/nickel catalysed C–N coupling reaction, first reported by MacMillan and Buchwald in collaboration with Merck,[79] as a model reaction (Figure 3Ci). Investigation into the kinetics of the batch reaction showed apparent zero-order until conversion reached 81%, and above this conversion level, rate became dependent on the concentrations of photocatalyst, nickel catalyst and aryl bromide **54**. This is consistent with the reaction being light-limited until the starting material dropped below 20%, at which point the turnover limiting step shifted to one involving the substrates and photocatalyst.

The authors then investigated the effect of photocatalyst concentration on initial reaction rate (Figure 3Cii), finding there was an optimal catalyst concentration below which the rate was slower due to conventional effects of catalyst concentration, namely that catalyst concentration is rate limiting and increasing catalyst concentration correspondingly increases reaction rate. Above this optimal concentration, the rate decreased exponentially in accordance with the Beer-Lambert law, due to non-productive light absorption from excess catalyst decreasing light penetration through the reaction mixture- the same effect as described by Gagne. When investigating the effect of varying concentration of the same photocatalyst in a different reaction, a photoredox/nickel catalysed C–C reaction, a different optimal catalyst concentration was identified. Abbvie later leveraged these principles and further mechanistic investigation to design and conduct a commercial scale photoredox reaction obtaining over 500 kg intermediate.[80] This highlights an important implication for chemists: the optimal catalyst concentration for a photoredox reaction is specific to a particular reaction and setup.

Additionally, in 2020, Naber and colleagues at Merck used the concept of 'photon equivalents' to scale up the same C–N coupling reaction in plug-flow (Figure 4).[81]

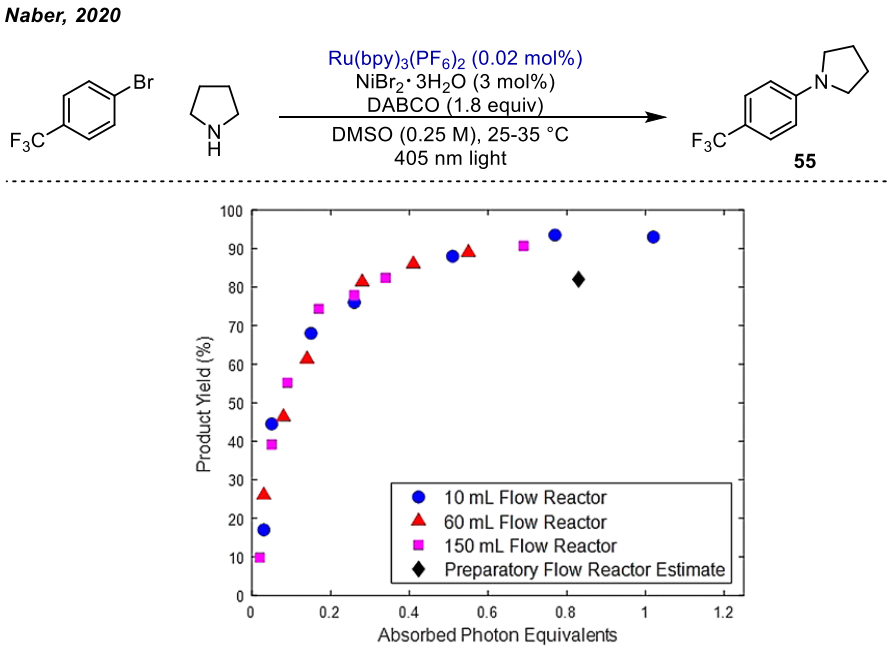


Figure 4: Scale-up considerations for photochemistry. Graph reproduced directly from Naber and co-workers.[81]

Photon equivalents were defined as 'the ratio of absorbed photons to aryl bromide for a given time of irradiation'.[81] The authors checked the reaction was not photon-limited by ensuring transmittance throughout the reactor at different reactor diameters. The absorbed photons per unit time was calculated, then converted into photon equivalents. The reaction was run in three

reactors of different sizes and the yield plotted against photon equivalents for each reactor. These three graphs overlayed well and provided predictive conditions for scaling the reaction to a preparative reactor, a 3.5 L plug-flow reactor. The reaction broadly complied with predictions, achieving 10 kg/d of the phenyl-pyrrolidine product **55** and demonstrated the importance of understanding light intensity and related parameters when scaling up flow reactions.

The consequences of these investigations for the organic chemist are that the outcome of photoredox reactions is directly dependent on the reaction set-up, and the interplay of light, substrate concentration and reactor geometry have significant impact on the kinetic regime of the reaction, and therefore outcome. Particularly important is that each reaction has an optimal catalyst concentration, depending on which set-up is being used. Several parameters can be used to optimise photoredox reactions, and investigation into reaction set-up, and vessel pathlength provide additional opportunities to tune a reaction outcome for a variety of reaction scales.

1.4.2. Ways to investigate the kinetics of photoredox systems

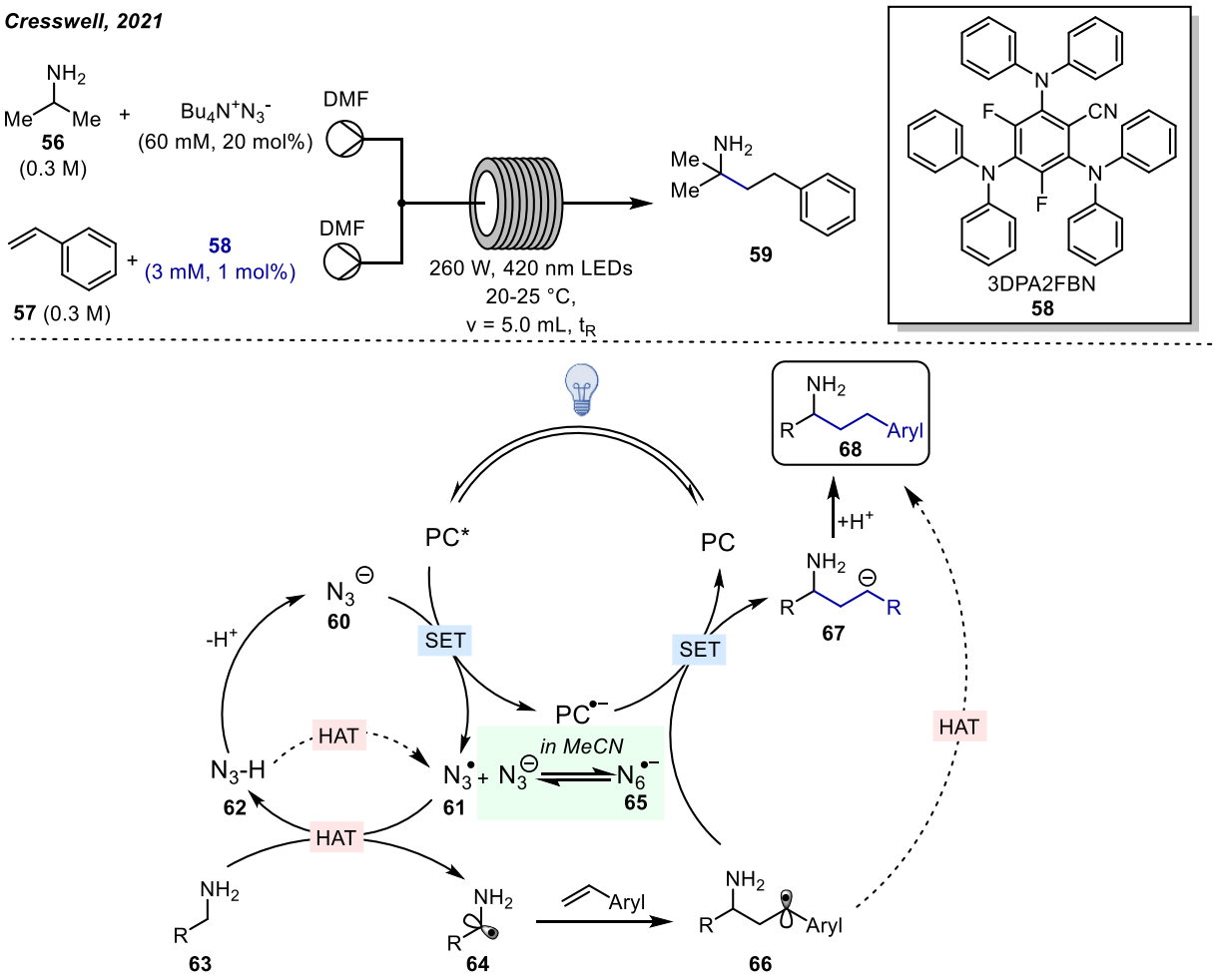
The above sections have described how light intensity is important and can affect photoredox reactions. This section will outline studies aiming to gain kinetic insight into the chemistry of the reaction i.e. the remaining steps not involved with light absorption.

Along with photoredox-specific kinetic considerations, there are a few techniques which have been established to investigate the kinetics of photoredox reactions. Blackmond developed reaction profile kinetic analysis (RPKA), a form of visual kinetic analysis which allows determination of useful information regarding reaction progression. ‘Same excess’ experiments can be used to identify any catalyst degradation or product inhibition using concentration against time profiles.[82,83] Orders in reaction components can be determined using ‘different excess’ experiments. Burés developed a version of this technique using the concept of ‘different excess’ experiments, using concentration against a normalised time axis to determine the order in reaction components- a technique called ‘variable time normalisation analysis’.[84,85]

Since their introduction, these visual kinetic analysis methods have increased the amount of information chemists have been able to extract from kinetic data. This has been true also in the field of photoredox, where there have been some limited examples of investigations using RPKA or VTNA analysis to obtain information regarding photocatalytic cycles. These methods have been used to identify orders in reaction components to support mechanistic hypotheses,

been used to determine whether a reaction is photon-limited and to guide formation of non-light-limited reactions. These investigations will be described in the remainder of this section.

In 2021, Cresswell and co-workers reported the use of VTNA as applied to a photoredox reaction, to investigate the mechanism of a novel photocatalytic hydroaminoalkylation of styrenes **57** with primary alkylamines **56** (Scheme 13).[86]



Scheme 13: Hydroaminoalkylation of styrenes with primary alkylamines reported by Cresswell and co-workers, and proposed mechanism.[70,71]

Stern-Volmer luminescence quenching studies confirmed that azide anion **60** quenched photocatalyst **58** excited state to afford azidyl radical **61**, and redox potentials were used to rationalise selective quenching by the azide anion over the amine substrate **63**. Azidyl radical **61** could therefore act as a hydrogen atom transfer (HAT) agent to form the α-aminoalkyl radical **64**. Detailed further work using transient absorption spectroscopy in collaboration with Orr-Ewing and co-workers revealed further insight into the HAT reagent; when this reaction is

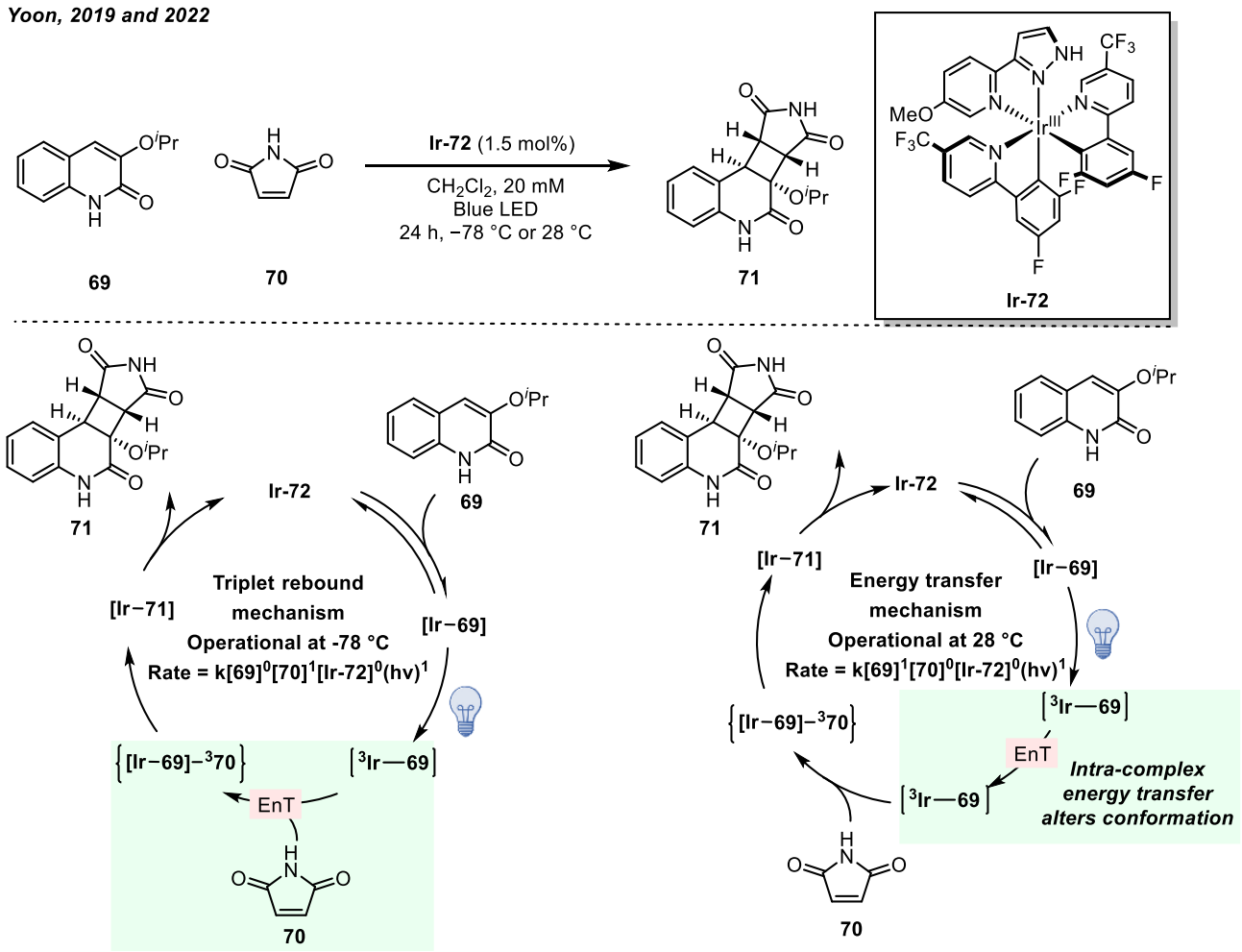
performed in acetonitrile as the standard solvent, the azidyl radical rapidly complexed with the more abundant azide anion to form radical anion **65** (Scheme 13, green box).[61] This was shown to be a reversible reaction which modulated the concentration of reactive azidyl anion in solution. From here, the mechanism followed photoredox catalysed Giese-type chemistry; alkyl radical **64** added into a radicophile, forming product radical **66** which was reduced to anion **67** and protonated to form the neutral product **68**.

Quantum yield measurements to determine the likelihood of a radical chain mechanism were undertaken using ferrioxalate actinometry. A ratio of 0.31 photons absorbed to molecules generated suggested a partial radical chain mechanism between protonated azide **62** and product radical **66**. The reaction was then adapted to a continuous flow process to prove effective scale-up of the reaction synthesis, but also to enable automated VTNA analysis. Different excess experiments were performed for each component of the catalyst, which was zero order in every reaction component except styrene **57**. This indicated that the reaction rate was limited by either addition of amine radical **64** into the acceptor, or reduction of product radical **66**.

In 2019, Yoon and co-workers reported a [2 + 2] cycloaddition reaction between quinolone **69** and maleimide **70** using iridium complex **Ir-72** as an enantioselective triplet sensitiser (Scheme 14).[87] Stern-Volmer analysis, transient absorption spectroscopy, kinetic experiments, and DFT calculations were employed to determine that this reaction proceeded by a novel mode of asymmetric catalysis, where enantioselectivity was conferred between excited state species with no significant ground state pre-association. The resting state of the catalyst was found to complex with the quinolone, adopting a geometry in which energy transfer to maleimide **70** became preferable upon complex excitation. The enantioselective bond-forming step could then occur between the triplet state maleimide and quinolone bound to the chiral iridium complex. This mechanism was termed 'triplet rebound' (Scheme 14, left mechanism). An additional paper in 2022 by the same group investigated this mechanism further using VTNA by LED-NMR.[88] LED-NMR allows *in situ* NMR data collection, which has been very beneficial to investigating photoredox mechanisms through kinetic analysis.[1,89,54,90] Here, the authors used different excess VTNA experiments to find the rate law for the reaction under LED-NMR conditions at two different temperatures, −78 °C and 28 °C. At −78 °C the reaction was found to be first order with respect to **70** and light power (correlated with light intensity), and zero order with respect to photocatalyst (**Ir-72**) and maleimide (**69**): rate = $k[\mathbf{69}]^0[\mathbf{70}]^1[\mathbf{Ir\text{-}72}]^0(hv)^1$.

[1] The LED-NMR device consists of a simple circuit using fibreoptic cable connected to LEDs to irradiate a sample within the NMR spectrometer. Several mechanistic insights for photoredox reactions have been gained using this method since its introduction.

The use of variable power LEDs in this setup allowed the identification of a 'first order in light', and the conclusion that the reaction was photon-limited. At 28 °C the first order dependence was switched to give first order in quinolone **69** rather than maleimide **70**: rate = k[**69**]^{1}[**70**]^{0}[**Ir-72**]^{0}(hv)^{1}. This change in orders belied a change in mechanism at different temperatures.



Scheme 14: VTNA studies using LED-NMR determined different mechanisms under different temperatures as reported by Yoon and co-workers.[87,88] Rate determining steps are highlighted in green boxes. 'EnT' denotes energy transfer.

Interestingly, when conducting this reaction in batch using initial rates analysis and a different light source, the reaction was found to be first order in catalyst, and therefore not photon-limited. Consequent DFT studies led to the conclusion that, at ambient temperatures, energy transfer between the complexed chiral photocatalyst and quinolone was rate-determining; however, at −78 °C, the complex could not adopt the conformation needed to undergo energy transfer, and instead the rate-determining energy transfer was bimolecular, between the iridium-quinolone complex and maleimide. This research demonstrated how set-

up specific not only the rate of photoreactions can be, but also the mechanism. VTNA experimentation is a powerful way to identify whether a reaction is photon-limited, and therefore to ensure correct interpretations about the mechanism can be uncovered.

Lloyd-Jones and co-workers also used LED-NMR in combination with visual kinetic analysis to investigate the kinetics of a dual photoredox/nickel catalysed cross-electrophile coupling reaction using aryl bromide **73** and alkyl bromide **74** to obtain coupled product **75** (Figure 5).[91]

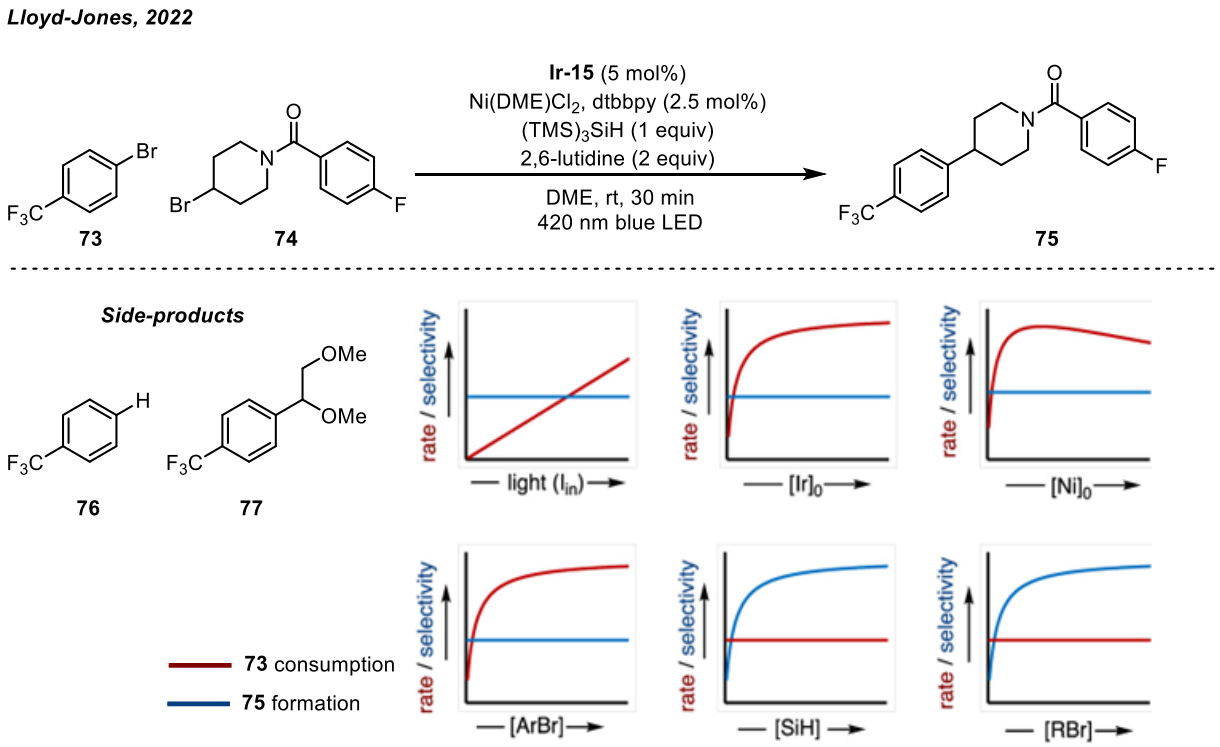
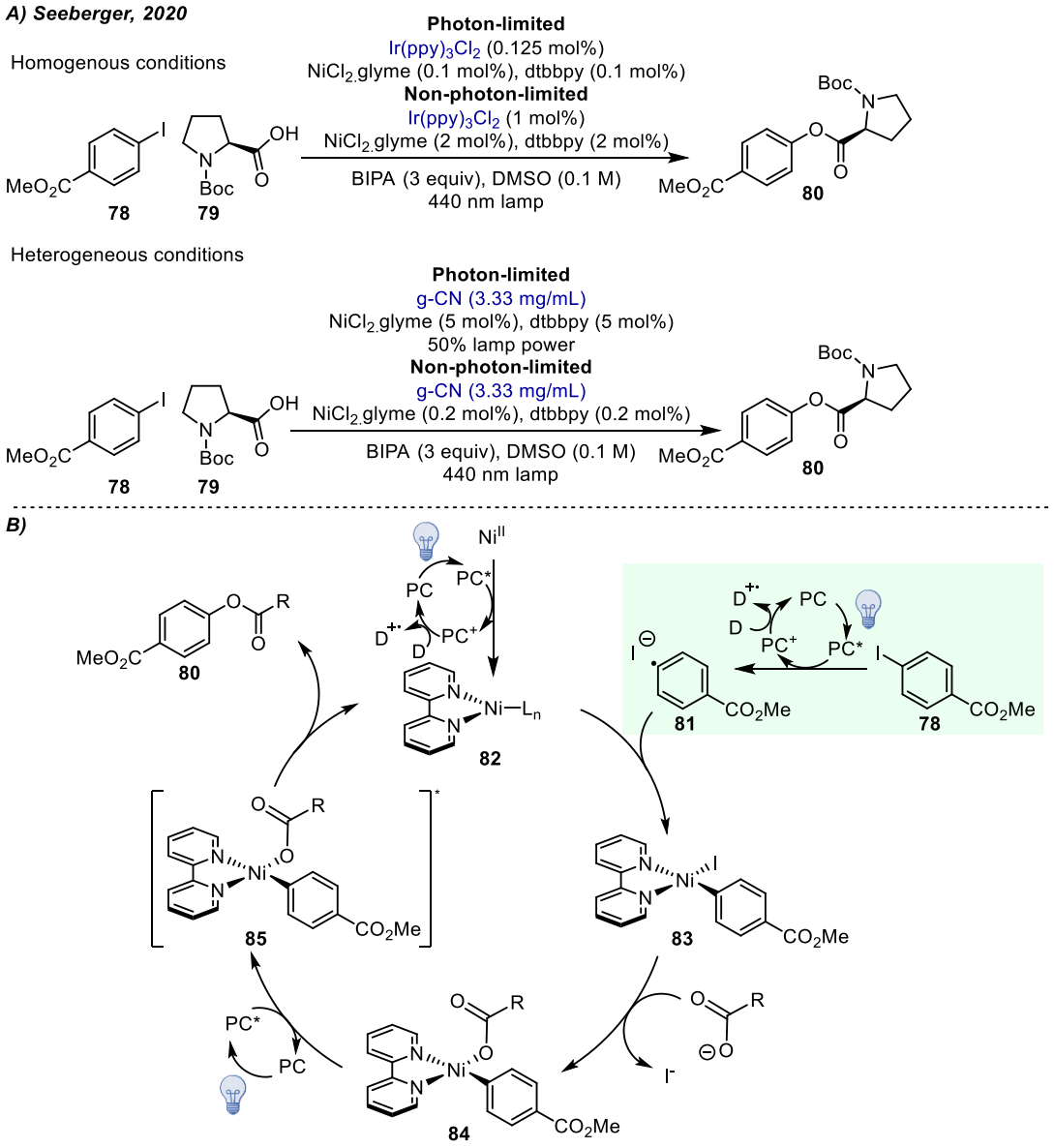


Figure 5: Rate vs selectivity controlling reaction components. Graphs reproduced directly from Lloyd-Jones and co-workers.[91]

Visual kinetic analysis was used to determine the variation of product and side-product formation ratios on changing each component in the reaction mixture. Light, photocatalyst, aryl bromide and nickel complex concentrations determined the rate of aryl bromide consumption, whilst silane and alkyl bromide were selectivity-determining, affecting the distribution of products and side-products. The rate of desired product formation was therefore a combination of the rate and selectivity-determining steps. As has been found in other studies, increasing the concentration of photocatalyst and nickel complex did not necessarily increase the rate of reaction due to limitations from the Beer-Lambert law. The authors used the information to develop a kinetic model to describe the behaviour of this reaction. The data and accurately predicted the kinetics of several different substrates.

1.4.2.1. VTNA in reaction design

VTNA has also been used to guide the design of photoredox systems for mechanistic analysis. In 2020, Seeberger and coworkers compared the *O*-arylation of a metallophotoredox catalysed cross-coupling reaction with heterogeneous (graphitic carbon nitride, g-CN) and homogeneous ($Ir(ppy)_3$) catalysts under both photon-limited and photon-unlimited systems (Scheme 15).[92]



Scheme 15: VTNA investigation into photon-limited and unlimited conditions for the coupling of carboxylic acids and aryl halides using A) homogeneous and heterogeneous photoredox catalysis. B) proposed mechanism following kinetic studies.[77] Green box indicates new mechanistic insight.

The mechanism for the metallophotoredox coupling of carboxylic acids with aryl halides had been proposed in 2017 by MacMillan and co-workers.[93] The authors demonstrated, using UV-Vis and Stern-Volmer studies, that reductive elimination from the nickel(II) complex **84** was induced with visible light following formation of an excited state nickel(II) complex **85**.

Seeberger and co-workers used kinetic experiments to guide the development of non-photon-limited systems through changing the concentration of the reaction and Ni catalyst and confirming by determining the orders in different reaction components using VTNA. Different orders were found when using the heterogeneous and homogeneous catalysts. When using the heterogeneous conditions, there was a partial order in aryl halide, whereas when using the homogeneous system, all components were zero order except a first-order in the nickel catalyst. Furthermore, the reaction rate when using the g-CN heterogeneous catalyst changed based on which aryl halide was used; the reaction was faster when using an aryl iodide than an aryl bromide, whilst the iridium homogeneous catalyst had no such substrate rate dependency.

Through Stern-Volmer quenching studies, the aryl halide **78** was found to be quenched by the photocatalyst, likely resulting in aryl halide reduction to aryl radical **81**. The g-CN heterogeneous catalyst had a lower reduction potential than the corresponding iridium $Ir(ppy)_3$ catalyst which, combined with the kinetic data, allowed the authors to propose that there was a direct single electron transfer to the aryl halide from the excited heterogenous photocatalyst, which had not previously been identified (Scheme 15B, green box). The formed radical **81** was then proposed to undergo oxidative addition with nickel complex **82** to generate complex **83**. An electron donor proposed to be the BIPA amine base can then regenerate the ground state photocatalyst. However, the oxidation states of the nickel species involved in this mechanism could not be confirmed by the authors, requiring further investigation to elucidate.

Under less reducing, heterogeneous catalysis conditions, aryl halide reduction had an impact on the reaction rate. This extra photocatalytic interaction also explained the scope limitations for this reaction to electron-poor aryl halides. These could be more easily reduced and therefore gave higher yields in the reactions with both catalysts than corresponding electron-rich aryl halides. Comparison of photon-limited and photon-unlimited systems were crucial in this analysis for separating the contribution of the nickel and photocatalytic cycles to the rate.

1.5. Conclusions

The kinetics of light dependent reactions are intrinsically linked to reaction setup, and the photophysical properties of catalysts. As such, the optimal catalyst concentration for the

reactor is unique to each photoreaction, and when investigating kinetics of these reactions, focused efforts must be made to achieve a regime under which valuable conclusions from the work can be drawn.

Few kinetic studies have been conducted on C–H functionalisation of nitrogen heterocycles. There are several methods available which have been applied to other photoredox systems in the last few years including visual kinetic analysis, fluorescence quenching analysis and cyclic voltammetry. A holistic review of the mechanism is required taking into consideration the photophysics of the system as described by the Beer-Lambert law, and therefore the geometry of the vessel the reaction is conducted in, to determine what the reaction's limitation to light is. This must be understood and, in some cases, overcome to enable conclusions to be drawn regarding the chemistry and mechanism of the system. Even among more well-established approaches to C(sp^3)–H functionalisation there are many questions left unanswered about the proposed mechanisms of reactions.

1.6. Project Aims

Saturated heterocycles are desirable motifs present in a wide range of pharmaceutical and agrochemical agents, and functionalisation of the heterocycle core allows construction of interesting, potentially bioactive molecules with increased 3D character. The aim of the work contained in this thesis was to increase mechanistic understanding of a photoredox reaction of saturated heterocycles and to determine trends in selectivity for this reaction towards different substrates (Figure 6). The first aim was therefore to develop a high yielding reaction. A requirement for the reaction was to have a single catalytic cycle, and for it to be able to be readily replicated in other laboratories. Therefore, the reaction would be first developed in batch, and the reaction reproducibility investigated (Figure 6A). A Giese-type addition of saturated nitrogen heterocycles to Michael acceptors was chosen, related to initial work by Pandey and Reiser, and Nicewicz and co-workers (section 1.2.2.3).[27,30]

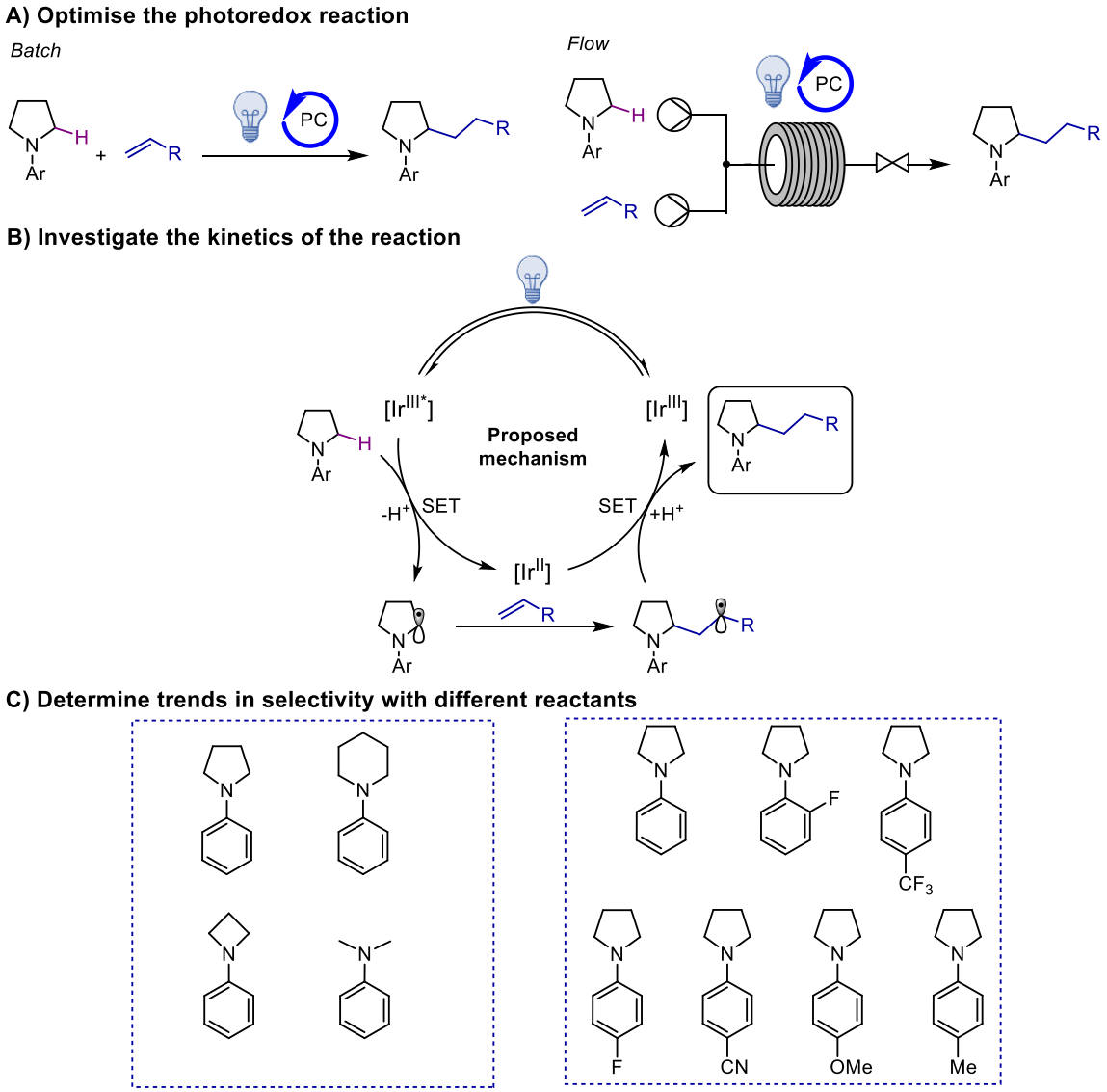


Figure 6: Summary of project aims.

For kinetic experimentation to be possible, it would be necessary for the reaction to be measurable, reproducible, and complete over a reasonable timeframe, i.e., to be able to complete a reaction profile within a day. The reaction would therefore also be developed to be suitable for kinetic analysis, for which flow photochemistry was envisaged and employed.

Once a suitable reaction had been developed, the next aim would be to gain mechanistic insight into the reaction. A key aim of this section would be to ensure the reaction would be non-light-limited, or at least one in which the rate dependence on light intensity was negligible. This would be essential for allowing investigation into how the different substrates affected the reaction- effects which would most likely be masked if the turnover determining step was excitation of the catalyst. The reaction mechanism would then be investigated using several experiments and techniques, including visual kinetic analysis to determine orders in reaction components, cyclic voltammetry to determine redox potentials and Stern-Volmer analysis to determine which reaction components can quench the excited state of the iridium catalyst and the comparative rates at which these occur (Figure 6B).

The final aim was to gain insight into what controls the kinetics and therefore selectivity of the reaction with respect to different reagents (Figure 6C). An increase in predictive power for how well different nitrogen heterocycles or anilines would behave in this reaction would increase the use of the reaction for medicinal chemists.

A combination of experimental and computational approaches were envisaged to investigate trends in both the saturated heterocycle size and substitution of the N–aryl group, as well as the effects of different electron acceptors on reaction rate. Using this data, a kinetic model of the photoredox reaction would be presented.

To summarise, the key aims were:

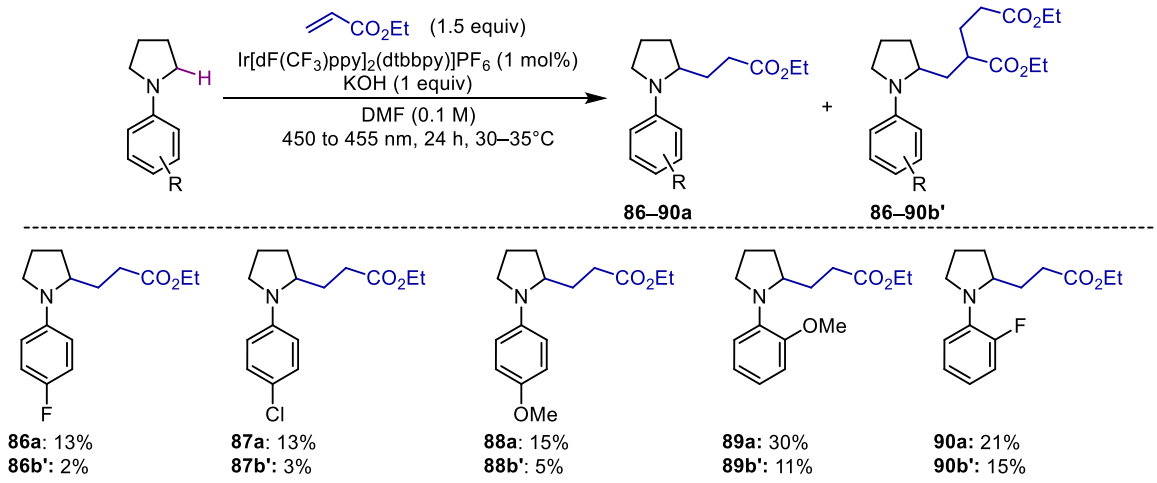
1. Development of a photoredox catalysed Giese-type reaction of nitrogen heterocycles with Michael acceptors using batch and continuous flow set-ups.
2. Development of a measurable, non-light-limited flow setup for the reaction.
3. Identification of trends in reaction outcome using different reagents and causes of these trends.
4. Holistic interpretation of reaction kinetics and presentation of a kinetic model.

2. Results and discussion

2.1. Establishing and optimising a batch reaction

2.1.1. Developing a measurable batch reaction

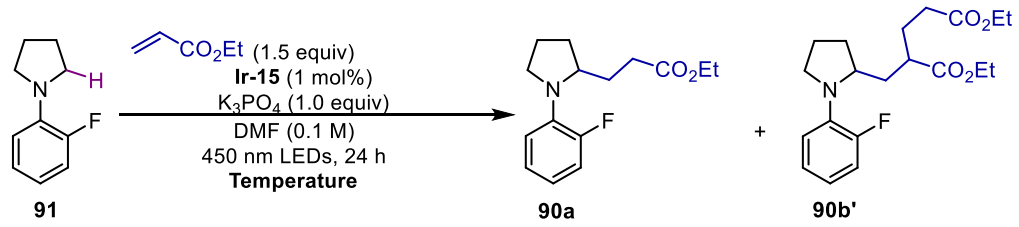
The first aim was to develop a C(sp^3)–H functionalisation reaction. The desired features of this reaction included that it be a C(sp^3)–H alkylation reaction of a saturated nitrogen heterocycle with one mode of catalysis. The Giese-type reaction of *N*-aryl-pyrrolidines provided a positive starting point. Previous work in the group found that this reaction produced two products when reacted with ethyl acrylate, a mono alkylated product (**a**) and a 1:2 telomer product (**b'**, Scheme 16).[17] The mono and telomer products did not give distinct peaks in ^{1}H NMR spectra of the crude reaction mixture, complicating quantitative analysis, which would have severely limited the throughput of work in reaction optimisation, and kinetic experiments. By examining alternative substrates, *N*-(2-fluorophenyl)pyrrolidine was found to give mono- and telomer products with distinct ^{19}F signals (**90a** and **90b'**, Scheme 16).



Scheme 16: Previous work on this reaction using ethyl acrylate.[17] Reactions run on 0.3 mmol scale, isolated yields given.

The reaction of *N*-(2-fluorophenyl)pyrrolidine with ethyl acrylate was therefore taken as the starting point in this work. A recirculating water bath was attached to a Hepatochem photoreactor, allowing temperature to be controlled and maintained constant over the course of the reaction. A temperature of 40 °C was chosen due to a brief temperature screen indicating this was highest yielding temperature for total product formation (Table 1).

Table 1: Reaction temperature screen.



Entry	Reaction temperature (°C)	Total yield of 90a + 90b' (%)
1	30	67
2	40	69
3	50	57

Yields calculated by ^{1}H NMR using 4,4'-difluorobiphenyl as internal standard. There was no resolution of **90a** and **90b'** in this spectrum. Reported reaction temperatures were the temperatures of the water bath rather than internal reaction temperature.

Analytical methods were also investigated further, with efforts focused primarily on NMR methods as these were most readily available. Due to the presence of separable fluorine peaks in the ^{19}F NMR spectra, a quantitative ^{19}F NMR method was attempted using fluorinated internal standards. However, using trifluorotoluene and 4,4'-difluorobiphenyl **92** as internal standards resulted in ^{19}F NMR spectra where the peaks of the product and internal standard could not be brought into the same phase (Figure 7), leading to inaccuracies with the yield determination.

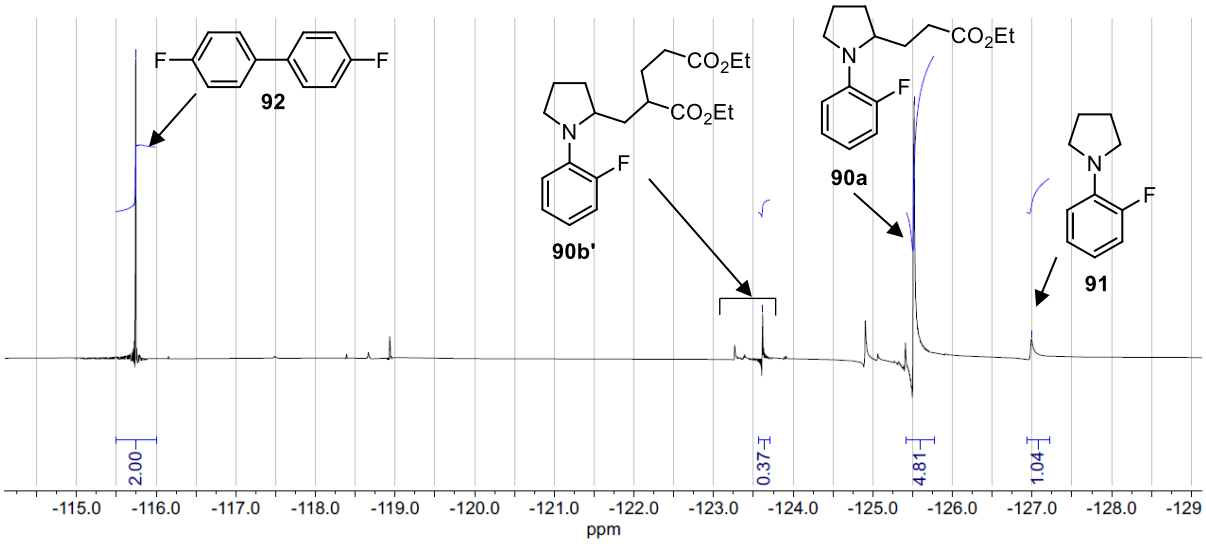
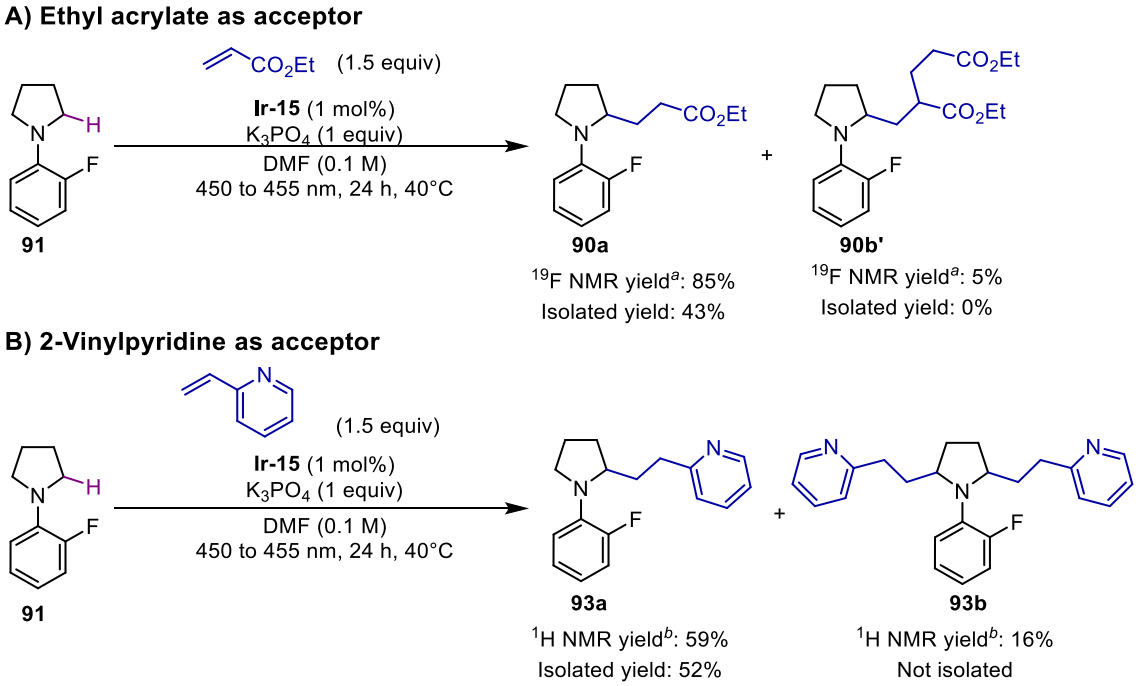


Figure 7: ^{19}F NMR spectrum of crude reaction mixture.

It was thought that interference of the Teflon™ lining of the NMR probe during analysis was the source of the problems with phasing in the −110 to −130 ppm region of the ^{19}F NMR spectrum. Several ^{19}F NMR experiments using variable pulse delays, and different internal

standards were attempted to resolve this issue but were unsuccessful based on large differences between the ^{19}F NMR and isolated yields as noted in Scheme 17A.[2]



Scheme 17: Comparison between NMR reaction yields and isolated methods using A) ethyl acrylate and B) 2-vinylpyridine acceptors. Reactions performed on a 0.2 mmol scale. [a] Yield determined by ^{19}F NMR method with 20 s delay using hexafluorobenzene as internal standard. [b]Yields determined by ^{1}H NMR spectroscopy with 30 s delay using 1,3,5-trimethoxybenzene as internal standard.

Changing the acceptor from ethyl acrylate to 2-vinylpyridine resulted in a reaction with a mono product **93a** and a different, symmetrical di-addition product **93b** (Scheme 17B). Vinylpyridines were found to be under-represented acceptors in the photoredox Giese literature compared to styrenes or acrylates,[94,95] and their reaction with heterocycles had the potential to afford interesting new molecules. Happily, when using 2-vinylpyridine as an acceptor, the substrates and products were distinguishable from each other in the ^{1}H NMR spectrum of the reaction mixture, allowing for quantitative ^{1}H NMR analysis and giving a more general analytical method also applicable to reactions with non-fluorinated substrates. The reaction as described in Scheme 17B was therefore chosen for further development and optimisation.

This di-addition product **93b** was formed as a mixture of diastereomers in a 70:30 ratio of major to minor, with the major product characterised as the *trans*-product through a

[2] ^{19}F NMR experiments were developed and conducted by Corey Fulop.

combination of ^{1}H NMR analysis and analogy to literature compounds.[96,97] The mono-alkylation product **93a** presumably re-enters the reaction mechanism in place of the starting material, undergoing SET to form a second α-amino carbon radical. Conversely, the branched telomer product **90b'** observed with ethyl acrylate as acceptor could form from addition of either the product radical or anion into another molecule of ethyl acrylate. In a a similar photoredox system a telomer di-addition product with ethyl acrylate was found to be formed by addition of the enolate radical into a second equivalent of ethyl acrylate, and did not require further interaction with a photocatalyst.[98]

2.1.2. Investigating reproducibility in the batch reactor

Photoredox reactions can be notoriously irreproducible. Therefore, prior to conducting the reaction optimisation, the reproducibility of the reaction in the chosen setup, a Hepatochem photoreactor, was investigated.[99] Both the reproducibility between different positions in the reaction (labelled A to H, Figure 8), and between runs in the same position run on different occasions were investigated. For this section, vial positions will be referred to as indicated in the schematic in Figure 8.

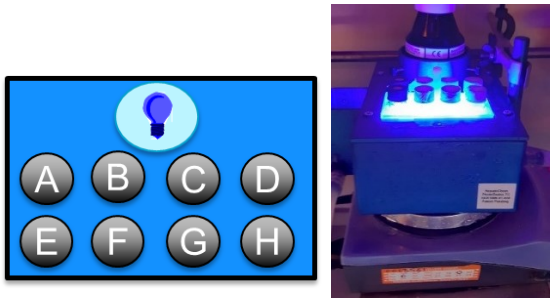


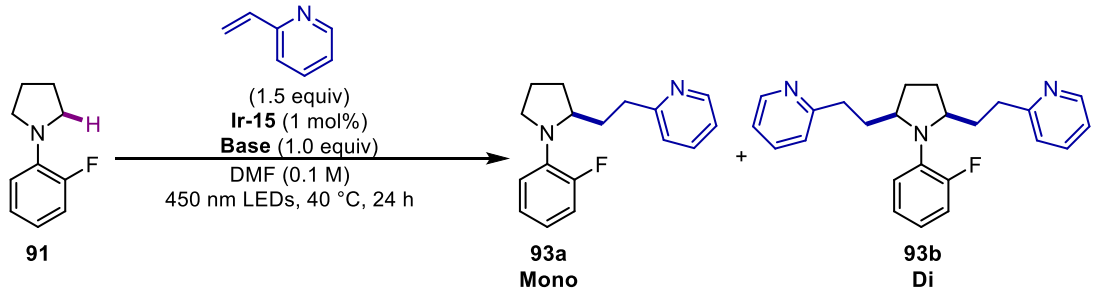
Figure 8: Schematic (left) and photograph (right) of Hepatochem temperature controlled photoreactor showing reaction vial positions.

Reactions were made up in stock solutions and portioned out into vials to be tested in different positions in the reactor. The initial reaction using potassium phosphate tribasic gave yields with considerable variation across the photoreactor (Table 2). Recent work by Swierk and co-workers investigating the cyanoarylation of *N*-phenylpyrrolidines, as described by MacMillan and co-workers and depicted in Scheme 4,[18] demonstrated that the presence of an insoluble base in a photochemical reaction can cause scattering of incident light, reducing quantum yield.[51] The authors found that deprotonation of the *N*-phenylpyrrolidine radical cation was the slowest reaction step under these conditions, but that the reaction rate was limited by light scattering and other non-productive light absorbing processes.

In this photoredox alkylation work, potassium phosphate was insoluble in the reaction mixture, therefore the size of K_3PO_4 crystals were likely inconsistent and therefore the difference in

surface area in contact with solution may have led to variability in the reaction. Exchanging to an organic soluble base was consequently investigated in an attempt to remove this variable. Changing to a homogeneous reaction solution was desirable as it would also facilitate transfer of this reaction to flow for subsequent kinetic investigations.

Table 2: Testing reproducibility in the photoreactor.



Reactor position	Yield (%)								
	K_3PO_4			DBU run 1			DBU run 2		
	Mono 93a	Di 93b	Total 93a+93b	Mono 93a	Di 93b	Total 93a+93b	Mono 93a	Di 93b	Total 93a+93b
A	-	-	-	56	27	83	63	25	87
B	36	7	43	5	41	46	60	46	103
C	-	-	-	52	35	87	52	48	101
D	69	6	75	68	7	75	69	11	80
E	66	15	81	27	27	54	57	14	70
F	-	-	-	68	17	85	64	22	86
G	75	22	97	63	22	85	73	24	97
H	-	-	-	67	7	81	60	13	72
Mean Average	62	13	74	51	23	75	62	25	87
Standard deviation	15.1	6.5	19.6	21.5	11.5	14.7	6.2	13.4	11.8

Reactions performed on 0.1 mmol scale. Yields calculated by ^{1}H NMR with 20 s delay using 1,3,5-trimethoxybenzene as internal standard.

The reproducibility of the reaction was investigated across all 8 vials of the photoreactor using an organic soluble base, DBU. This reaction was conducted twice: the first run gave lower consistency than using K_3PO_4, with the yield in position B in particular having decreased from 36 to 5%. However, a repeat using DBU as base gave much greater consistency across the reactor, with a standard deviation of 6.2 vs 21.5 across the 8 reactions (Table 2, DBU run 2). The variability of results obtained in the same reactor positions indicated that there was no particular position bias to the results, but that there were still occasional issues with reproducibility in the batch reaction using soluble or insoluble bases. However, due to the greater amenability of homogenous reaction mixtures to continuous flow, soluble bases were chosen for investigation moving forward. To address potential irreproducibility in the

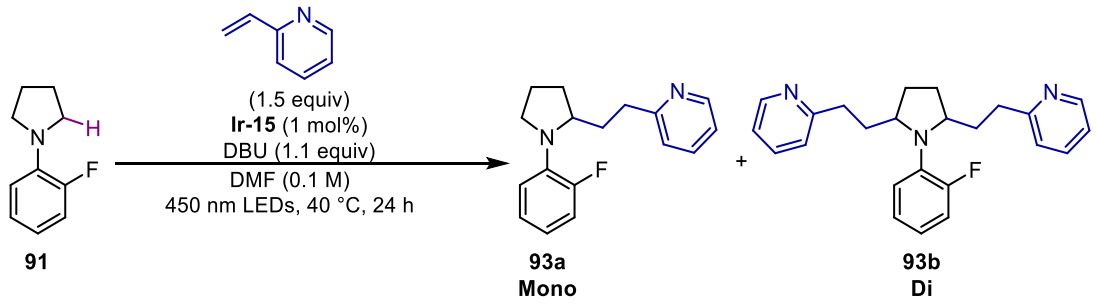
optimisation, all discrete variable investigations were conducted in duplicate, with optimisation focused on selecting for both reproducibility and yield.

2.1.3. Optimisation of C(sp^3)–H functionalisation of aryl-pyrrolidines in batch

2.1.3.1. Control experiments

Ahead of the reaction optimisation, control experiments were conducted to determine the requirement for each component (Table 3). As expected, the reaction required the presence of photocatalyst and visible light. Interestingly, the reaction worked in the absence of an added base but with a much lower yield than in the presence of base. Therefore a base screen was included in the reaction optimisation.

Table 3: Control experiments.



Entry	Change from standard conditions	Average yield (%)[a]		
		Mono 93a	Di 93b	Total 93a + 93b
1	None[b]	59	16	75
2	No base	15	0	15
3	No photocatalyst	0	0	0
4	No light	0	0	0

[a]Reactions conducted on 0.2 mmol scale. Yields calculated by ^{1}H NMR with 20 s delay using 1,3,5-trimethoxybenzene as internal standard. [b]Yields given as an average of 4 samples.

2.1.3.2. Discrete variable optimisation

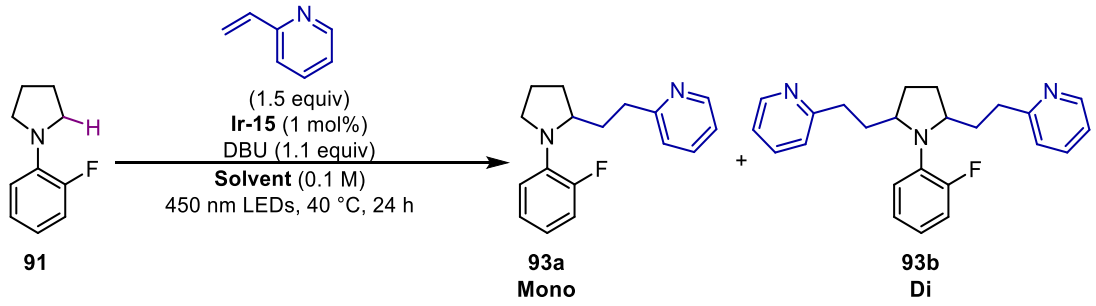
Whilst good conversion was observed following the reproducibility screen, we aimed to optimise the reaction yield for mono-alkylation product formation, and for reaction reproducibility. The latter meant that a factor would be considered less favourably if there was large variability between samples. Discrete reaction variables were investigated first, and were performed in duplicate with yield and range data reported in each case.

Solvent screen

Several solvents with a range of properties were tested in the reaction mixture (Table 4). These were initially performed on 0.1 mmol scale; however, this proved practically challenging to

conduct and raised concerns with reaction consistency (entries 1–3). The scale of the test reactions was increased to 0.2 mmol for the remaining screen (entries 4–12). As photoredox reactions are known to be sensitive to scale, the reaction with DMF was performed at both scales to allow comparison with each set of solvents (entries 1 and 4).

Table 4: Solvent screen.



Entry	Solvent	Reaction scale (mmol)	93a Yield range[a,c] (%)	Average yield (%)[a,b]		
				Mono 93a	Di 93b	Total 93a+93b
1	DMF	0.1	4	50	32	82
2	Acetonitrile	0.1	11	49	52	101
3	DMSO	0.1	14	44	35	79
4	DMF	0.2	10	59	17	76
5	CH_2Cl_2	0.2	1	58	7	65
6	THF[d]	0.2	34	35	6	41
7	TBME	0.2	2	9	0	9
8	1,4-Dioxane	0.2	19	34	3	37
9	MeTHF	0.2	7	48	4	52
10	Chlorobenzene	0.2	6	33	3	36
11	Toluene	0.2	33	38	4	42
12	Trifluorotoluene	0.2	1	46	4	50

[a]Yields determined by ^{1}H NMR spectroscopy with 20 s delay using 1,3,5-trimethoxybenzene as internal standard. [b]Yields given as a mean average of 2 results. [c]Range given as sample 1 yield **93a** – sample 2 yield **93a** for each pair of results. [d]Results given as an average of four samples, in two samples this formed an insoluble gum.

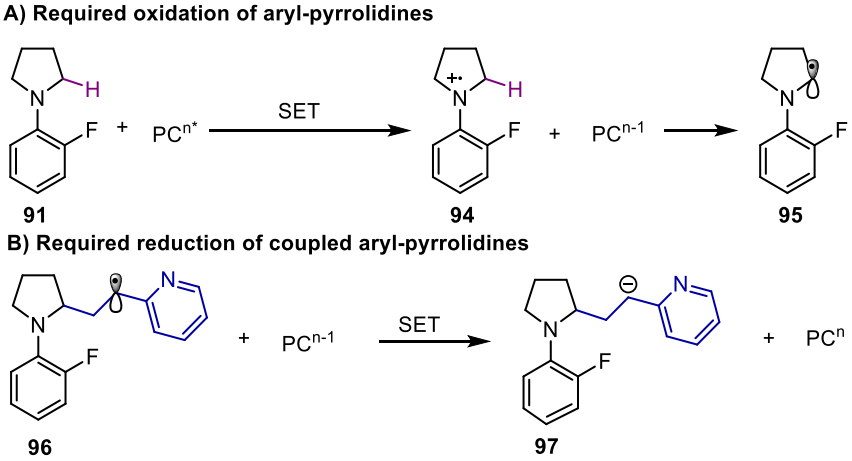
DMF was found to give the highest yield of **93a** at both 0.1 and 0.2 mmol scales, and the results had good agreement at both scales. Dichloromethane and acetonitrile also gave good yields in this reaction, which may be desirable due to lower boiling points, and in the case of acetonitrile, provide a less environmentally damaging and less toxic alternative to DMF or dichloromethane. DMF and dichloromethane were selected for further study due to better selectivity for the mono-alkylation product **93a**. Ether solvents THF, *tert*-butyl methyl ether (TBME) and 1,4-dioxane resulted in low yields (entries 6–8), although MeTHF performed better and with good selectivity (entry 11). No alkylation of ether solvents was observed.

Aromatic solvents such as toluene and chlorobenzene resulted in low yields (35 and 33% average yields, entries 10 and 11).

As CH_2Cl_2 gave comparable yields to DMF, greater mono selectivity and was much easier to handle, particularly in terms of solvent removal, some of the further optimisation reactions in this chapter were conducted using CH_2Cl_2 as the solvent. However, it was found that there was occasional broadening of signals in the ^1H NMR spectrum when using dichloromethane which was not observed when using DMF as solvent, and following repeat reactions in both solvents, DMF was ultimately chosen as the reaction solvent.

Photocatalyst screen

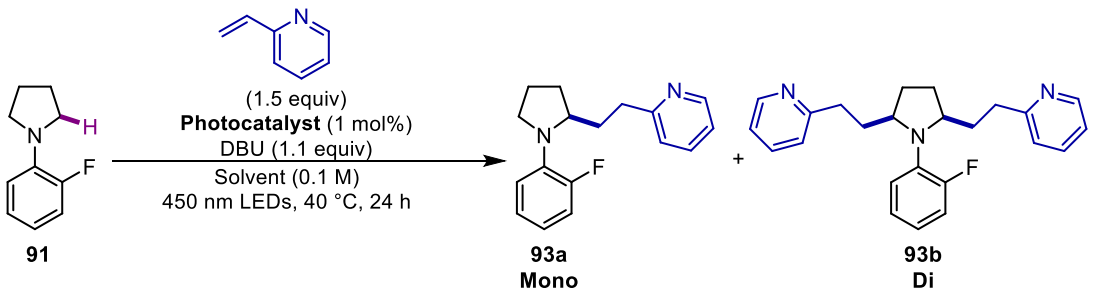
For this reaction to be productive, two redox events are required: first oxidation of pyrrolidine **91** to the aminium radical cation **94,** then deprotonation to obtain α-aminoalkyl radical **95** (Scheme 18A), involving reduction of the photocatalyst excited state PC^{n*}/PC^{n-1}. The second is reduction of the coupled product to the corresponding anion (Scheme 18B), involving oxidation of the photocatalyst reduced state PC^{n}/PC^{n-1}. The oxidation potential of related substrate N-phenylpyrrolidine **12** has been reported as +0.82 V vs SCE,[30] meaning a photocatalyst with a more positive redox potential was required for productive reaction.



Scheme 18: Redox steps in the photoredox catalysed alkylation of pyrrolidines.

A screen of photocatalysts of varying redox potentials provided information not only on the optimal catalyst for this system (Table 5), but also information on the redox potentials required to successfully perform both redox events (Figure 9). Initial screens were performed in CH_2Cl_2, with the remainder conducted in DMF when this was found to be a more suitable solvent. The result of the catalyst in entry 4 was replicated in DMF for more accurate comparison between photocatalysts.

Table 5: Photocatalyst screen.



Entry	Photocatalyst	$E_{1/2}$ (PC^{n*}/PC^{n-1}) (V)[100,101]	$E_{1/2}$ PC^{n}/PC^{n-1} (V)[100,101]	λ_{max} (nm)	Solvent	Yield range[b] (%)	Average yield (%)[a]		
							93a	93b	93a+b
1	2,4,6-Triphenylpyrylium tetrafluoroborate **98**	+2.30	−0.35	417	CH_2Cl_2	0	0	0	0
2	Mes-Acr$^+$ **99**	+2.06	−0.57	430	CH_2Cl_2	0	0	0	0
3	$Ru(bpz)PF_6$ **Ru-100**	+1.45	−0.80	443	CH_2Cl_2	0	0	0	0
4	$Ir[dF(CF_3)ppy]_2(dtbbpy)PF_6$ **Ir-15**	+1.21	−1.37	380	CH_2Cl_2	1	58	7	65
5					DMF	10	59	17	76
6	Eosin Y **101**	+0.78	−1.06	539	DMF	5	11	1	12
7	$Ru(bpy)_3(PF_6)_2$ **Ru-14**	+0.77	−1.33	452	DMF	0	23	0	23
8	$Ir(ppy)_3$, **Ir-102**	+0.31	−2.19	347	DMF	17	14	3	17
9	4CzIPN **16**[25,102,103]	+1.35	−1.21	391	DMF	5	50	38	88
10	$Ir[dF(Me)ppy]_2(dtbbpy)PF_6$	+0.92	−1.44	360[104]	DMF	8	46	50	96

[a]Reactions performed on 0.2 mmol scale. Yields calculated by ^{1}H NMR with 20 s delay using 1,3,5-trimethoxybenzene as internal standard. Yields given as an average of 2 results. All potentials are given in volts versus the saturated calomel electrode (V vs SCE). [b]Range given as sample 1 yield **93a** – sample 2 yield **93a** for each pair of results.

Productive reaction was only observed for photocatalysts with excited state reduction potentials of +0.77 V or higher (Figure 9A), with low yields observed for $Ru(bpy)_3(PF_6)_2$ (**Ru-100**, Table 5, entry 7). This was consistent with the expected oxidation potential for **91** as discussed above. Similarly, productive reaction was only observed using photocatalysts with more negative standard reduction potentials than −1.06 V between the ground state and reduced state (Figure 9B). The catalyst therefore needed to be capable of satisfying both criteria to be successful in this reaction. As the chemical structures of many catalysts lend themselves to being more highly oxidising *or* reducing, this left relatively few catalysts capable of generating good yields in this reaction. Heteroleptic transition metal ruthenium or iridium-based catalysts allow facile redox tunability which has, for several years, allowed these compounds to have wider redox ranges than their organic counterparts, particularly greater reducing power.

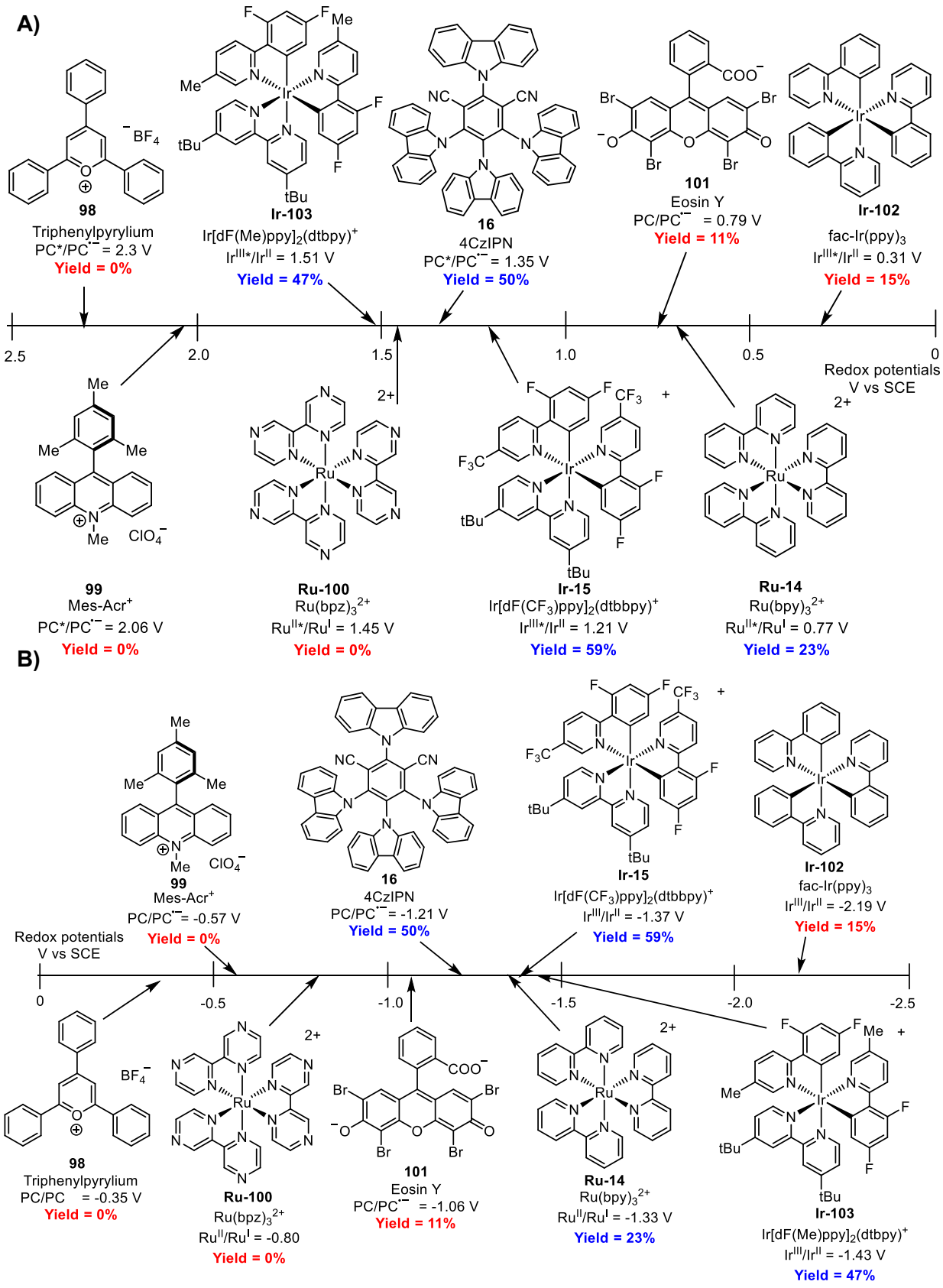


Figure 9: Standard reduction potentials of A) photocatalyst excited states to reduce states and B) ground state to reduced state, with associated reaction yields. Yields reported in blue if reaction occurred with a yield above 20%, red if not.

Organic photocatalysts **98**, **99** and **101** were not productive in this reaction, likely due to being insufficiently reducing in the PC^{n-1} state (Table 5, entries 1,2 and 5). However, more recently, organic photocatalysts with broader redox ranges able to be both oxidising and more reducing have been developed, with 4CzIPN being demonstrated to work in a range of transformations.[105] As iridium and ruthenium based photocatalysts are expensive and made from precious metals which it is environmentally damaging to obtain,[106] it is encouraging to have improved organic photocatalysts as alternatives. Furthermore, 4CzIPN pleasingly worked in this reaction to afford excellent overall yield, but was not selected as the solvent moving forward due to its lower selectivity for **93a** over **93b** compared with **Ir-15**. $Ir[dF(Me)ppy]_2(dtbbpy)PF_6$ also gave good yields in this reaction, with almost complete total conversion of amine to combined products. **Ir-15** gave the highest yield of **93a** under the tested conditions, and therefore was chosen as the photocatalyst used in future studies.

Light wavelength is also a factor in how efficient a photocatalyst can be in a reaction. Each catalyst has a walevelength which it absorbs most strongly at (λ_{max}), that enables the transition of the catalyst from the ground to excited state. Matching the wavelength of light to the λ_{max} maximises the efficiency of light absorption, thereby maximising the proportion of catalyst in the excited state, though this may not correlate to yield. LEDs with 450 nm maxima were used in the catalyst screen. These LEDs were not monochromatic, but instead emit light wavelengths on a bell curve between 400 and 500 nm, with a maximum at 450 nm. Consequently, catalysts with λ_{max} values away from this range, such as Eosin Y and $Ir(ppy)_3$ (Table 5**,** entries 6 and 8), may have given lower yields due to a mismatch of catalyst and wavelength of light used. However, as these catalysts are both not strongly oxidising, further investigation into these catalysts was not deemed necessary.

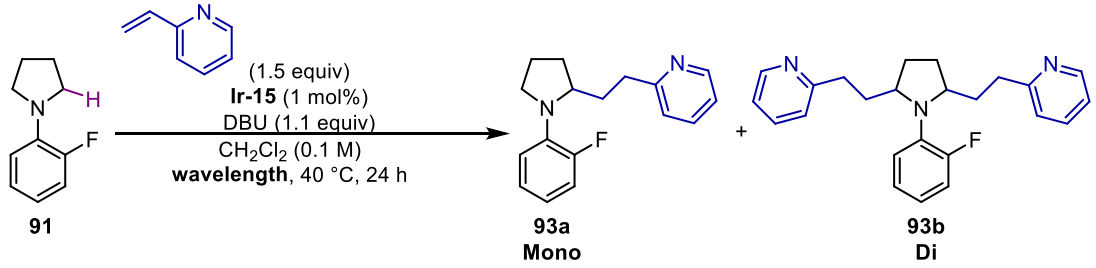
The optimal catalyst for this system was found to be $Ir[dF(CF_3)ppy]_2(dtbbpy)PF_6$ (**Ir-15**, Table 5, entry 10). This catalyst has been prevalent in the literature for generating α-amino radials[46,47] and therefore we believed further investigations would allow insight into a commonly used photocatalyst.

Wavelength screen

The optimal catalyst following the solvent screen, **Ir-15,** has a λ_{max} at 380 nm, therefore shorter wavelengths LEDs closer to 380 nm were hypothesised to give higher yields. Different wavelengths of light were then investigated (Table 6). Contrary to our initial hypothesis, in general shortening the wavelength reduced the level of mono-alkylation and increased the level of di-alkylation whilst keeping the overall yield similar (Table 6). The variability in yields may also be due to differences in light intensities, as this could not be standardised with the setups available- the 427 nm wavelength light in particular resulted in much lower overall

yields. Furthermore, as the λ_{max} of the LEDs became closer to UV, it is possible that absorption by reaction components other than the catalyst, particularly aromatic components, may reduce the effective intensity, or decrease light penetration through the vial. The 450 nm LEDs which gave the highest yields of mono and overall product were therefore chosen for further optimisation.

Table 6: Effect of changing light wavelength on the yield of reaction.



Entry	Light wavelength (nm)	Yield range (%)[b]	Average yield (%)[a]		
			Mono 93a	Di 93b	Total 93a + 93b
1	450	10	59	17	76
2	440	7	45	21	66
3	427	2	37	4	40
4	390	2	38	30	68

[a]Reactions conducted on a 0.2 mmol scale. Yields calculated by ^{1}H NMR with 20 s delay using 1,3,5-trimethoxybenzene as internal standard. Yields given as an average of 2 results. [b]Range given as sample 1 yield **93a** – sample 2 yield **93a** for each pair of results.

The UV-Vis absorbance spectrum of catalyst **Ir-15** had an absorbance band corresponding to the metal-to-ligand charge transfer event of the catalyst (MLCT) at 380 nm, the same as the literature recorded value (orange line, Figure 10). The irradiance of the 450 nm LEDs (maximum yielding tested light wavelength, Table 6) is overlayed in blue.

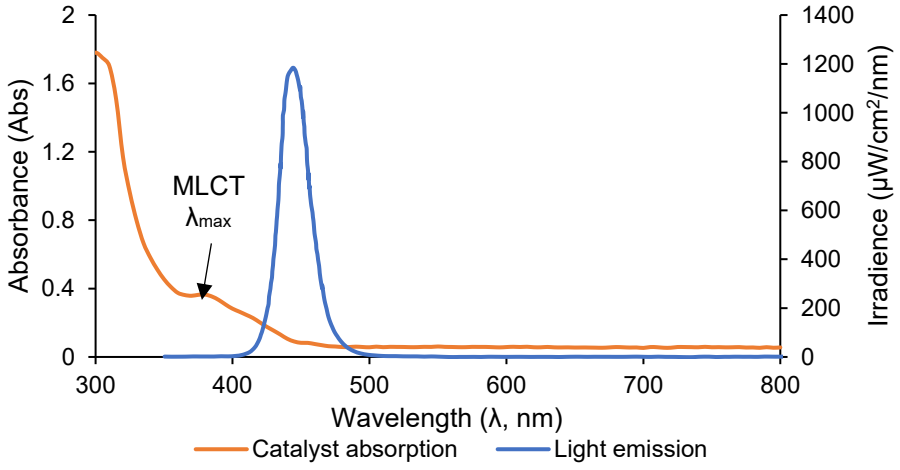


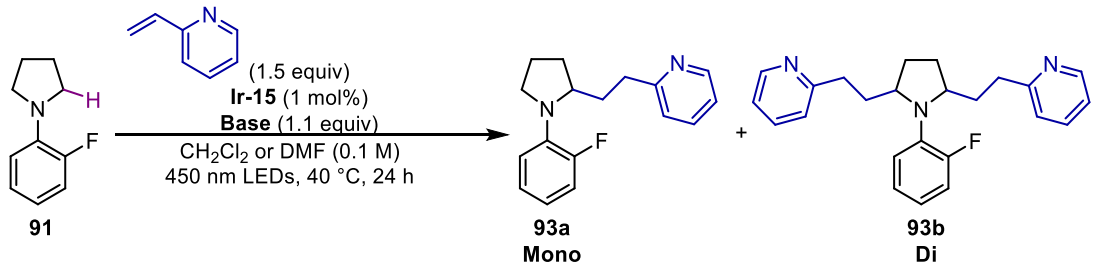
Figure 10: Overlay of UV-Vis absorption spectrum of **Ir-15** (orange trace, 0.05 mM in DCM) and wavelengths of light emitted by the 450 nm blue LED light source (blue trace).[107]

Despite a slight mismatch between the maximum wavelength of catalyst absorption and LED emission, there are wavelengths at which the LED emission and catalyst absorbance overlap to achieve excitation of the catalyst. Barner-Kowollik and co-workers also found that the photochemical activity of chromophores is often red-shifted compared to the UV-Vis λ_{max},[108] which we see here with longer wavelengths giving better yields.

Base screen

Whilst the reaction is in principle catalytic in base, control experiments demonstrated the yield was much lower in the absence of an added base (15%, Table 3, entry 2). The substrates themselves could however act as a base, and allow some reactivity even without an additional base. Additionally, for ease of transfer to flow and to minimise potential light scattering, a homogenous reaction mixture was desirable. Therefore, bases expected to be soluble in the reaction mixture were screened (Table 7).

Table 7: Screen of organic-soluble bases.



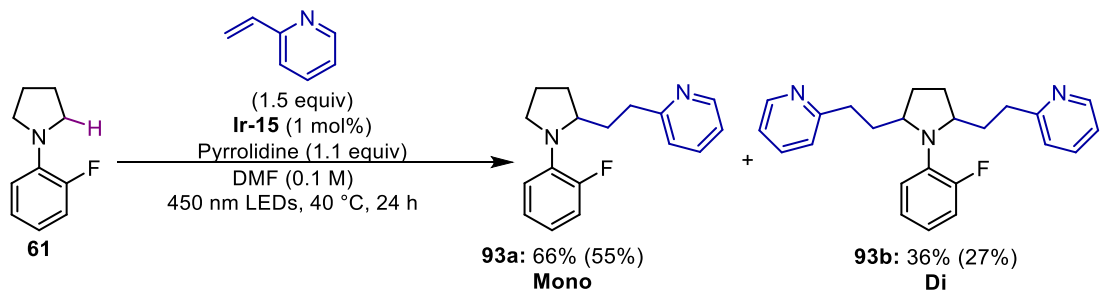
Entry	Base	Solvent	pK_a in MeCN[109]	Range (%)[b]	Average yield (%)[a]		
					Mono 93a	Di 93b	Total 93a+b
1	Piperidine	CH_2Cl_2	19.4	18	56	46	102
2	DBU	CH_2Cl_2	24.3	10	50	20	63
3	2,6-Lutidine	CH_2Cl_2	14.2	2	12	0	12
4	Tetrabutylammonium acetate	CH_2Cl_2	Unknown	1	38	23	61
5	KOtBu[c]	CH_2Cl_2	NA	0	0	0	0
6	NEt_3	CH_2Cl_2	18.8	2	23	2	25
7	DABCO[c]	CH_2Cl_2	18.3[110]	4	38	ND[d]	ND[d]
8	DIPEA	CH_2Cl_2	17.8	0	0	0	0
9	None	DMF	-	0	15	0	15
10	Piperidine	DMF	19.4	18[e]	53[e]	50[e]	103[e]
11	DABCO	DMF	18.3		47	10	57
12	Pyrrolidine	DMF	19.6	7	61[e]	47[e]	107[e]

[a]Reactions conducted on 0.2 mmol scale. Yields calculated by ^{1}H NMR with 20 s delay using 1,3,5-trimethoxybenzene as internal standard. [b]Range given as sample 1 yield **93a** – sample 2 yield **93a** for each pair of results. [c]Bases resulted in heterogeneous reaction mixtures due to insolubility. [d]Di-addition yield could not be determined due to overlapping signals in the ^{1}H NMR. [e]Yields given as an average of 4 samples.

Using piperidine in CH_2Cl_2 the reaction was found to proceed to full conversion (Table 7, entry 1). Therefore, when translating to DMF, piperidine and pyrrolidine were tested and the results of 4 runs was averaged to increase confidence in the differences in these results, with all results lying with 10% range for pyrrolidine. The reaction with DABCO was repeated in DMF (entry 12) due to insolubility in CH_2Cl_2 (entry 8), which improved the yield from 38–47%. There was no correlation observed between strength of these bases (pK_a in acetonitrile) and the yield obtained for this reaction. The highest yielding base for this reaction was pyrrolidine, which also gave clean, easily interpreted ^{1}H NMR spectra in DMF due to its volatility. This was therefore chosen as the base with which to continue optimisation of this reaction.

The role of the base in the reaction was unclear at this point; the oxidation potential of pyrroldine had been noted as 0.85 V vs SCE in MeCN compared with + 0.82 V vs SCE in MeCN for *N*-phenylpyrrolidine.[30] Therefore, it was possible, whilst unprecedented, that pyrrolidine may have interacted with the excited photocatalyst to become a HAT agent. Further investigation into the role of the base will be discussed in section 2.3.2.2.

This optimisation of discrete variables gave the reaction conditions in Scheme 19. Whilst this reaction reached full conversion, further investigation of continuous reaction variables was desirable for two reasons: 1) to understand the impact of reaction variables on the outcome of the reaction, to understand which factors needed to be controlled for reproducible reactions, and 2) to optimise for increased mono-alkylated **93a** selectivity.



Scheme 19: Discrete variable optimisation. Yields determined by ^{1}H NMR using 1,3,5-trimethoxybenzene as an internal standard. Isolated yields are given in parentheses.

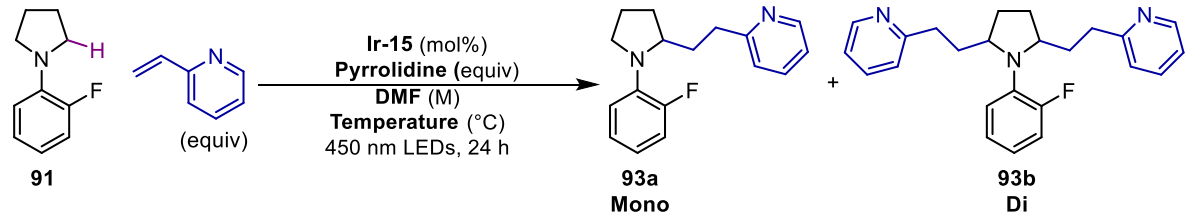
2.1.4. Design of experiment modelling

Design of experiment (DoE) modelling was then used to optimise the continuous variables in this reaction, aiming for maximum yield of mono-alkylated **93a**. These models were designed using JMP Pro v16 DoE software. From this section forwards, unless otherwise specified, reactions were no longer run in duplicate: repeats and error analysis were built into the DoE models to account for potential reaction variability.

2.1.4.1. Fractional factorial design

A fractional factorial DoE design was constructed to determine which of the many continuous variables affected the reaction outcome. Five factors were chosen to be studied: concentration, temperature, catalyst loading, base equivalents and acceptor equivalents (Table 8). The fractional factorial design used was a screening model based on a 2^{5-1} design which would allow analysis of the contribution of each of the 5 factors (variables) to the model as well as all 2-factor interactions, but no higher order interactions. This model therefore allows wide screening with a relatively small number of experiments, but lacks the resolution required for a full, accurate, response surface diagram. Due to observing variable reproducibility with this reaction, four centre-point repeats were built into the model.

Table 8: Design and yield of fractional factorial DoE.



Entry	Base (equiv)	Ir-15 (mol%)	Concentration (M)	Temperature (°C)	Vinyl pyridine (equiv)	Yield mono 93a, (%)
1	1.5	0.5	0.3	50	1.1	63
2	0.5	0.5	0.3	25	1.1	62
3	0.5	0.5	0.3	50	2.0	11
4	0.5	1.5	0.3	25	2.0	36
5	0.5	1.5	0.07	50	2.0	20
6	0.5	0.5	0.07	50	1.1	65
7	1.5	1.5	0.3	25	1.1	58
8	1.5	0.5	0.3	25	2.0	62
9	1	1	0.18	38	1.6	54
10	1.5	0.5	0.07	50	2.0	67
11	1.5	1.5	0.07	50	1.1	59
12	1	1	0.18	38	1.6	58
13	1	1	0.18	38	1.6	58
14	1.5	1.5	0.07	25	2.0	63
15	1	1	0.18	38	1.6	58
16	0.5	0.5	0.07	25	2.0	45
17	0.5	1.5	0.3	50	1.1	67
18	1.5	0.5	0.07	25	1.1	57
19	0.5	1.5	0.07	25	1.1	61
20	1.5	1.5	0.3	50	2.0	60

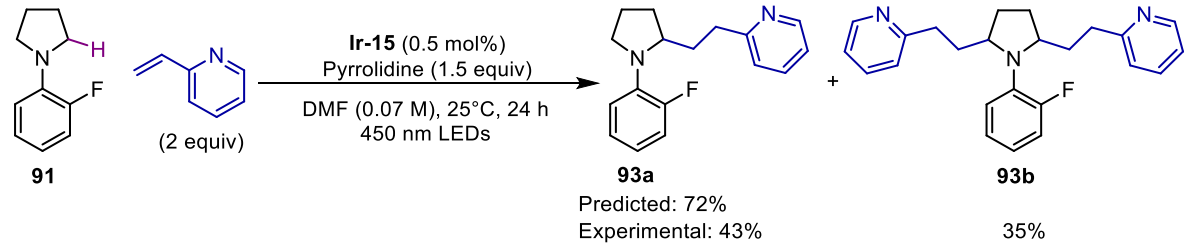
Reactions performed on 0.2 mmol scale. Yields determined by ^{1}H NMR using 1,3,5-trimethoxybenzene as an internal standard.

A second order interaction between pyrrolidine and 2-vinylpyridine equivalents was the factor which had the largest impact on the yield of **93a**, followed by the primary effects from these factors respectively (Table 9). Temperature, catalyst, and solvent concentration had non-significant primary interactions, with some 2nd order effects having a low impact on reaction yield.

Table 9: Effect summary output from DoE analysis

Source	LogWorth	PValue
Amount of base*Amount of 2-vinylpyridine	5.940	0.00000
Amount of 2-vinylpyridine(1.1,2)	5.113	0.00001 ^
Amount of base(0.5,1.5)	4.929	0.00001 ^
Temperature*Amount of 2-vinylpyridine	2.736	0.00184
Amount of catalyst*Solvent concentration	2.272	0.00535
Amount of base*Temperature	2.081	0.00831
Temperature(25,50)	1.206	0.06224 ^
Solvent concentration(0.067,0.3)	0.551	0.28124 ^
Amount of catalyst(0.5,1.5)	0.214	0.61129 ^

The maximum yield predicted by the model was 72% using pyrrolidine (1.5 equiv), iridium photocatalyst (0.5 mol%), DMF (0.07 M), and 2-vinylpyridine (2 equiv), with the reaction run at a temperature of 25 °C. These conditions were therefore attempted to determine whether the model had accurately predicted the yield (Scheme 20).

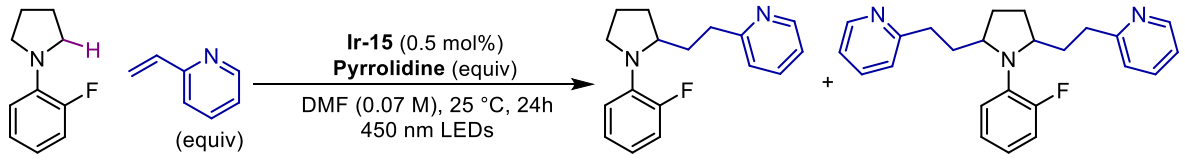


Scheme 20: Maximum predicted yield from screening DoE. Yields determined by ^{1}H NMR using 1,3,5-trimethoxybenzene as an internal standard.

The yield obtained for this experiment was much lower than the predicted and previously obtained yields of 72% and 67% respectively (Scheme 20). However, as this was a screening model rather than a model designed to optimise for yield, it is unsurprising the predicted yields were not very accurate. As the model predicted a strong effect of the two-factor interaction between 2-vinylpyridine and base, both 2-vinylpyridine and pyrrolidine equivalents were investigated in more detail ahead of a more focused DoE design (Table 10). The reaction concentration, temperature and catalyst loading were kept as described in the predicted maximum conditions.

At equivalents of pyrrolidine at or below 1.1 equiv, changing the 2-vinylpyridine loading only slightly affected the reaction yields. At 1.5 equiv pyrrolidine, the amount of 2-vinylpyridine required to achieve the same yield of product was much larger than at lower base loadings. Increasing the amount of base in the reaction beyond 1.1 equivalents therefore had a detrimental effect on mono-alkylated **93a** yield which could only be mitigated by increasing amounts of 2-vinylpyridine in the reaction, an undesirable change. It was unclear what had caused this reduction in yields, no evidence was seen for the reaction between pyrrolidine and 2-vinylpyridine.

Table 10: Investigating the interaction between 2-vinylpyridine and pyrrolidine.



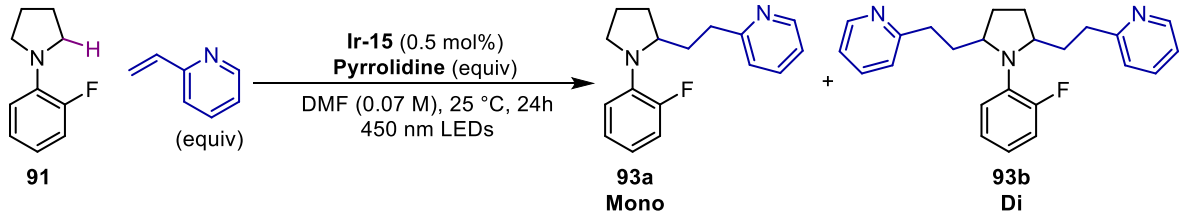
91 **93a Mono** **93b Di**

Entry	Base (equiv)	Vinyl pyridine (equiv)	Yield (%)		
			93a, Mono	93b, Di	93a+b, Total
1		1.1	64	9	64
2	0.5	1.6	66	10	66
3		2.0	63	12	63
4		1.1	57	6	57
5	1.1	1.6	66	11	66
6		2.0	62	12	62
7		1.1	31	1	31
8	1.5	1.6	25	1	25
9		2.0	59	19	59

Reactions performed on 0.2 mmol scale. Yields determined by ^{1}H NMR using 1,3,5–trimethoxybenzene as an internal standard.

Increasing the equivalents of pyrrolidine or 2-vinylpyridine in combinations beyond the limits of the screening DoE model did not improve the yield of **93a** further (Table 11), but instead tended to give increased yields of **93b**. Therefore, an upper limit of 2 equivalents of both 2-vinylpyridine and pyrrolidine was chosen for investigation in the second, custom DoE.

Table 11: Exploring the limits of useful pyrrolidine and 2-vinylpyridine equivalents.



Mono 93a (%)		Pyrrolidine			
		1.5	**2**	**2.5**	**3**
2-Vinylpyridine (equiv)	**2**		65	65	62
	2.5	42	63	45	43
	3	59	38	45	63

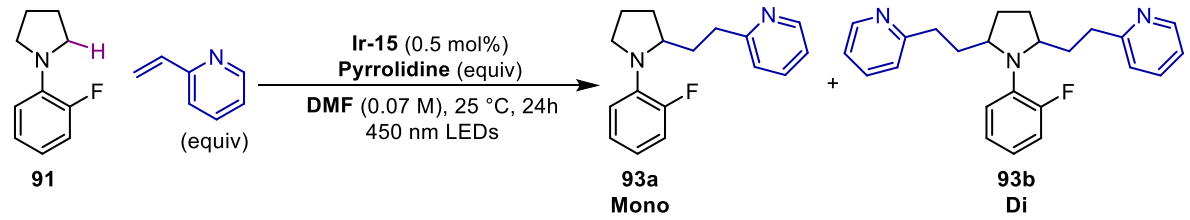
Di 93b (%)		Pyrrolidine			
		1.5	**2**	**2.5**	**3**
2-Vinylpyridine (equiv)	**2**		18	12	10
	2.5	34	14	5	42
	3	17	42	35	18

Reactions performed on 0.2 mmol scale. Yields determined by ^{1}H NMR using 1,3,5–trimethoxybenzene as an internal standard.

2.1.4.2. Custom DoE

A custom design model was then used to investigate three factors with consideration of all higher order interactions: concentration, base loading, and 2-vinylpyridine loading (Table 12). Concentration was selected due to previous investigations showing a strong concentration dependence for reaction concentration.

Table 12: Custom DoE data.



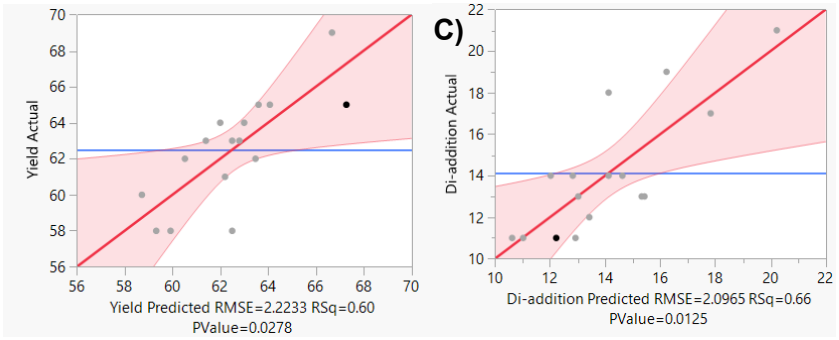
Entry	Pyrrolidine (equiv)	2-Vinylpyridine (equiv)	Concentration (M)	Yield (%)		
				Mono 93a	Di 93b	Total 93a+b
1	0.7	1.5	0.20	58	17	75
2	0.5	1.3	0.10	65	14	79
3	0.3	1.1	0.10	58	12	70
4	0.7	1.5	0.10	65	11	76
5	0.5	1.5	0.15	64	19	82
6	0.3	1.5	0.10	69	14	83
7	0.3	1.1	0.20	62	13	75
8	0.3	1.5	0.20	60	21	81
9	0.5	1.1	0.15	64	14	78
10	0.3	1.3	0.15	61	13	74
11	0.5	1.3	0.15	63	14	77
12	0.5	1.3	0.20	63	13	76
13	0.5	1.3	0.15	58	18	76
14	0.7	1.1	0.10	62	11	73
15	0.7	1.1	0.20	65	11	76
16	0.7	1.3	0.15	63	11	74

Reactions performed on 0.2 mmol scale. Yields determined by ^{1}H NMR using 1,3,5-trimethoxybenzene as an internal standard.

The model generated from this data identified the second order interaction between 2-vinylpyridine and concentration to have the most significant impact on the reaction output, with the loading of 2-vinylpyridine found to be another significant factor (Figure 11A). The actual-by-predicted yield plots for the correlation with mono and di products respectively show there is a large degree of error in this model, indicated by the pink shading, and the confidence for this model was low (Figure 11B and 11C). This shows that, despite concentrated efforts to increase reproducibility in this reaction system, there was still a fair degree of variability in this batch reaction. This would make the batch reaction an unsuitable method for undertaking kinetic analysis which requires reliable, reproducible data.

A)

Source	LogWorth	PValue
2-Vinylpyridine*Concentration	2.424	0.00377
2-Vinylpyridine(1.1,1.5)	2.048	0.00896
Concentration(0.1,0.2)	1.121	0.07571
Pyrrolidine(0.3,0.7)	1.010	0.09767



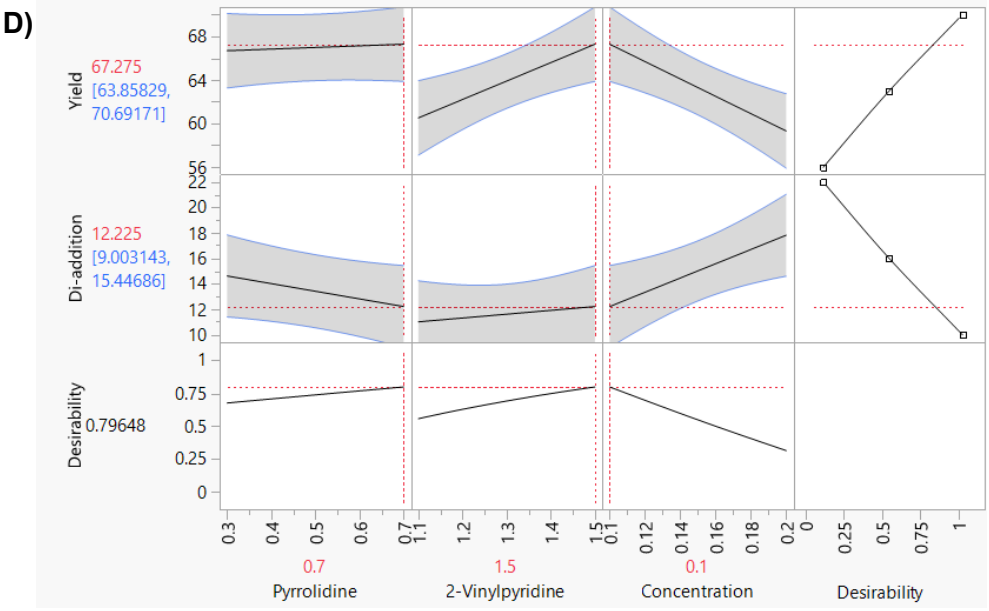
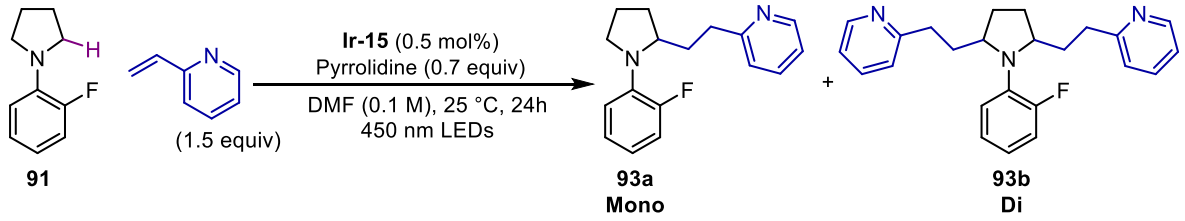


Figure 11: Output data from custom DoE. a) Effect summary showing significant factors. Actual-by-predicted plots for b) mono and c) di products. d) Prediction profiler with desirability maximised for mono **93a** yield and minimised for di **93b** yield.

The model also provided predicted conditions for the maximum mono **93a** and minimum di **93b** product yields (Figure 11D). When tested experimentally, there was excellent agreement between the predicted and the experimentally determined yields (Table 13, entries 1 and 2). The prediction profiler depicted a trend where mono **93a** increased with reduced concentrations, up to the limit of the DoE. Additional experiments were therefore conducted at lower concentrations of 0.08 and 0.07 M; however, this decreased **93a** and increased **93b** product formation - the opposite of the desired outcome (Table 13, entries 3 and 4). The DoE optimised conditions were therefore determined to be the optimal conditions for this reaction as a batch procedure.

Table 13: Validating custom DoE.



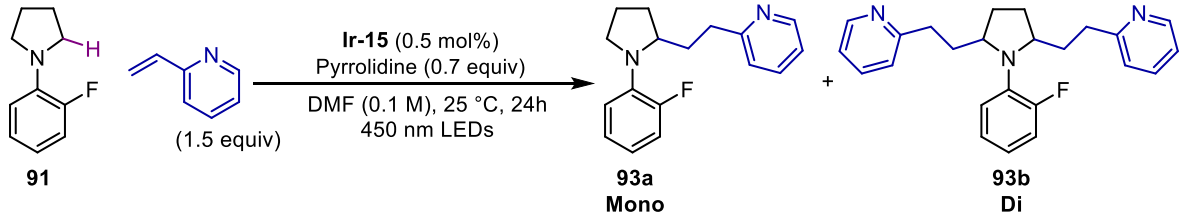
Entry	Change from given conditions	Yield (%)		
		Mono 93a	Di 93b	Total 93a+b
1	DoE predicted conditions	69	14	83
2	None	65	11	76
3	0.08 M concentration	46	28	74
4	0.07 M concentration	52	25	77

Reactions performed on 0.2 mmol scale. Yields determined by ^{1}H NMR using 1,3,5-trimethoxybenzene as an internal standard.

2.1.5. Investigation into mono vs di addition formation

An investigation into how the ratio of **93a**:**93b** product changes was conducted (Table 14). Longer reaction times and re-charges of 2-vinylpyridine and iridium photocatalyst increased the formation of di product **93b**, thereby reducing the yield of mono-alkylation.

Table 14: Investigation into factors affecting di-alkylation.



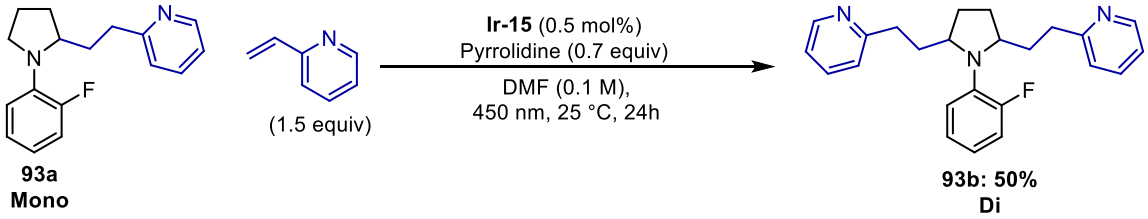
Entry	Change from given conditions	Yield (%)		
		Mono 93a	Di 93b	Total 93a+b
1	None	65	11	76
2	Longer time reaction (40 h)	46	33	79
3[a]	Re-charge of 2-Vinylpyridine	39	51	89
4[b]	Re-charge of Iridium photocatalyst	47	50	97

Reactions performed on 0.2 mmol scale. Yields determined by ^{1}H NMR using 1,3,5-trimethoxybenzene as an internal standard. [a]Re-charge of 0.5 equiv 2-vinylpyridine added after 24 h reaction, then reaction continued until 40 h total reaction time. [b]Re-charge of 0.5 mol% **Ir-15** added after 18 h reaction, reaction continued until 40 h total reaction time.

Recharging the photocatalyst gave the greatest total yield, leading to almost full conversion. This indicated that there may be some catalyst deactivation in the standard reaction preventing

full conversion, which was overcome by a catalyst recharge. This was investigated further using same excess experiments in section 2.3.3.

It was also of interest to understand formation of the di-addition product alone. As such, mono-alkylated **93a** was used in the reaction as the starting material (Scheme 21).

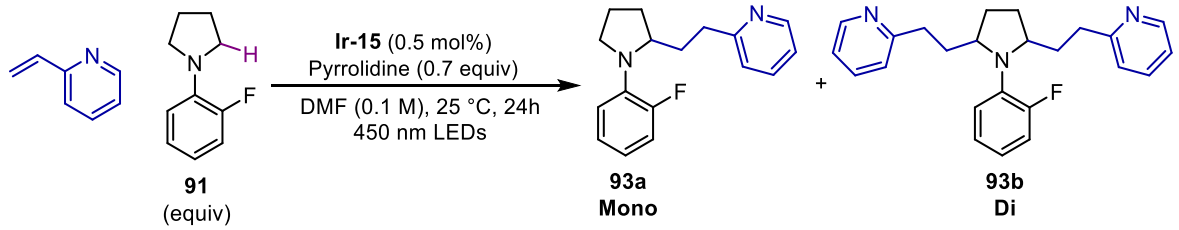


Scheme 21: Using mono alkylated **93a** as substrate.

The conversion of this reaction was lower than when using the standard substrate **91** (50% vs 76% total yield, Scheme 21). No further products were formed in this reaction - no telomer branched side chain products or functionalisation of the remaining α-nitrogen C−H bonds. As it would be expected that the tertiary alkyl radical would be more stable than the secondary, the absence of the additional α-nitrogen functionalisation is perhaps due to steric effects preventing further additions of a tertiary α-amine radical into 2-vinylpyridine to form a quaternary pyrrolidine centre. Further mechanistic experiments were undertaken and are presented in section 2.3 of this thesis onwards.

Many C–H functionalisation reactions are reported with amines as the limiting reagents, as it is often difficult to obtain high conversion of the radical forming species. The amine was chosen as the limiting reagent in this work as it was likely to be the more valuable reagent in complex molecules. It was of interest, however, to understand how the reaction behaves with the alkene as limiting reagent instead in situations using a more valuable acceptor (Table 15).

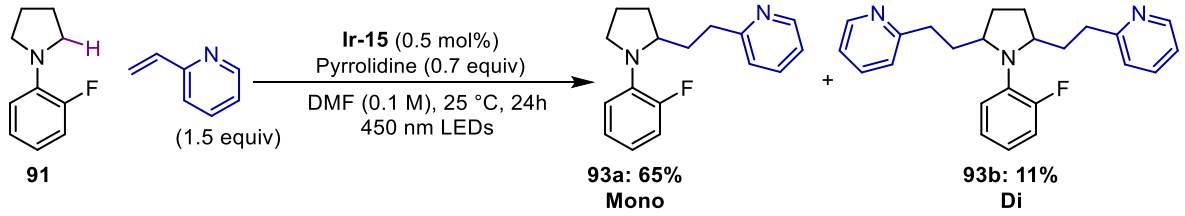
Table 15: Using amine substrate in excess.



Entry	Equivalents 91 (eqiuv)	Yield mono 93a (%)	Yield di 93b (%)	2-vinylpyridine reacted (%)
1	0.7	65	13	91
2	2.0	86	9	104
3	1.5	80	14	108
4	1.0	61	19	99

Reactions performed on 0.2 mmol scale. Yields determined by ^{1}H NMR using 1,3,5-trimethoxybenzene as an internal standard. Di-alkylation product **93b** yield was calculated with respect to the amount of amine, rather than the limiting 2-vinylpyridine acceptor. Entry 1 is the standard conditions.

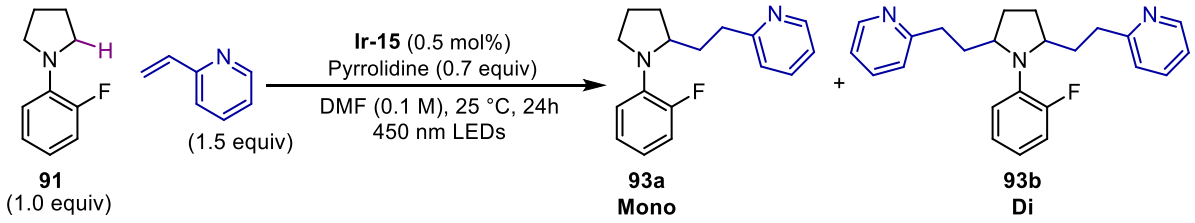
Whilst having a 1:1 ratio of amine to acceptor caused no discernible difference in yields to the standard conditions, increasing the amine loading to 1.5 or 2.0 equiv **91** gave high yields of over 80%. This means if the alkene is considered more valuable than the amine, these different reaction conditions could be used to achieve higher conversions. However, because of the value of heterocycle fragments and our interest in them in this work, the reaction was carried forward with the optimised conditions described in Scheme 22.



Scheme 22: Batch optimised conditions.

2.1.6. Sensitivity screen

A perceived lack of reaction reproducibility can limit the uptake of photoredox reactions. As such, a focused investigation into the causes of reaction variability was valuable. For this, we conducted a sensitivity screen based on a similar screen developed by Glorius and coworkers.[111] The results are depicted in both tabulated and graphical form in in Figure 12.



A)

Entry	Change from given conditions	Yield (%)		
		93a	93b	93a+b
1	None	65	11	76
2	High concentration (0.11 M)	61	20	81
3	Low concentration (0.09 M)	47	52	99
4	High O_2 (under air)	58	20	78
5	Moderate O_2 (no sparge)	55	26	81
6	High H_2O (+ 20 µL water)	61	13	74
7	High temperature (35 ºC)	51	49	100
8	Shorter wavelength (440 nm)	47	47	94

B)

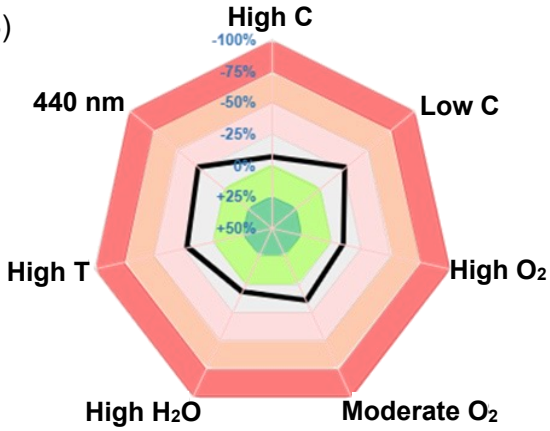


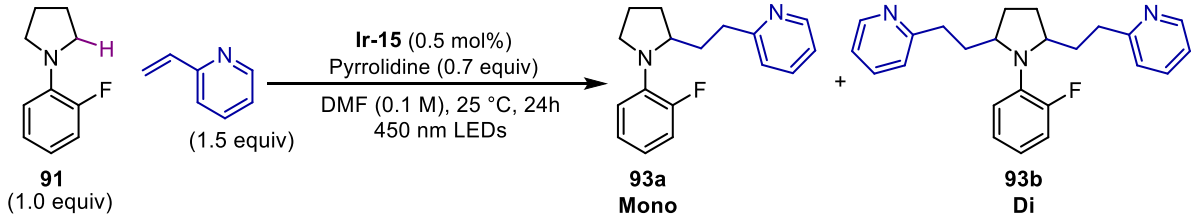
Figure 12: Sensitivity screen results as A) a table and B) radar diagram. Reactions performed on 0.2 mmol scale. Yields determined by ^{1}H NMR using 1,3,5-trimethoxybenzene as an internal standard. In the radar diagram the black line represents the percentage change in yield when changing each of the variables on the diagram coordinates.

Pleasingly, there was no tested condition in which the reaction failed, instead showing tolerance of a range of conditions including the presence of water and oxygen. Increasing the reaction temperature, lowering concentration and using shorter light wavelengths had the largest negative impact on the mono-alkylated **93a** yield, although this varied the reaction outcome by less than 20% at these larger changes, and resulted in greater di-alkylated **93b** reactivity rather than failed reaction. It was surprising that temperature impacted the reaction when the DoE screening had identified little impact on yield. Temperature may be more difficult to control than reaction concentration depending on the set-up available: using a recirculating bath as in this experiment will have controlled the temperature more consistently than setups using fans for example. The main outcome of this experiment showed that the reaction is tolerant and robust to many of the changes which could occur if the set-up were to be translated to a different user. This gives a level of confidence that good yields of product should be obtained when reproducing this reaction.

2.1.7. Batch Reaction profile

A sampling procedure was developed to determine whether it would be possible to gain accurate and reliable reaction profile data in batch, using an *in situ* internal standard which would remain inert through the reaction. 1,3,5-Trimethoxybenzene (TMB) was unsuitable due to its degradation throughout the reaction (Table 16, entry 1), resulting in calculated yields of over 190%.

Table 16: Results of internal standard screen.

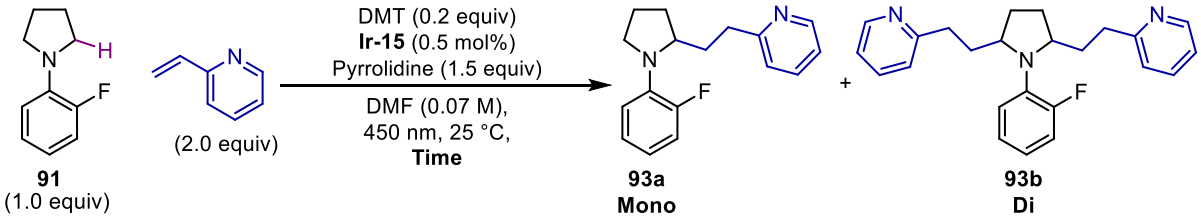


Entry	Internal standard	Yield determined by internal standard (%)	Yield determined by TMB (%)	Yield difference (%)	Potential internal standard?
1	TMB	190	-	-	X
2	DMT	64	58	6	✓

Reactions were conducted on a 0.2 mmol scale. Yields determined by ^{1}H NMR using specified internal standard.

Good agreement was found between yields calculated using 1,4-dimethylterepthalate (DMT) as an internal standard added to the reaction mixture at the beginning of the reaction, and that calculated using TMB as an internal standard added to the crude product after work-up.

The reaction profile was then attempted using both a sampling procedure where 0.2 mL aliquots were taken from the reaction at different timepoints, and using individual reactions which were worked up at the same timepoints (Figure 13). These reactions were set up at the same scale, 0.2 mmol **91**, using stock solutions. This experiment was conducted using the best predicted conditions found from the fractional factorial DoE (Scheme 20), not the final optimised conditions.



A)

Entry	Time (h)	Sample/Individual reaction	Yield 93a (%)
1	2	Sample	13
		Individual	26
2	4	Sample	30
		Individual	40
3	6	Sample	44
		Individual	51
4	21	Sample	62
		Individual	47
5	24	Sample	59
		Individual	61

B)

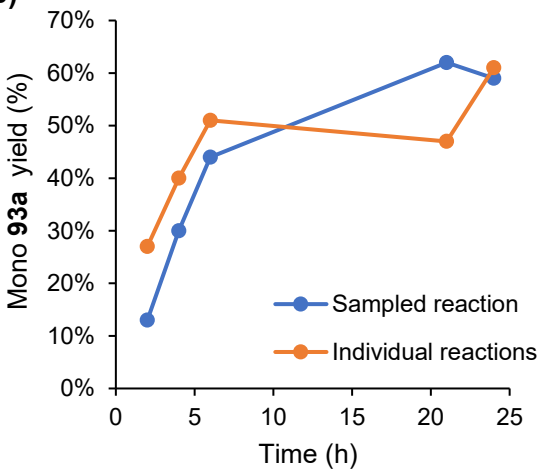


Figure 13: A) Results of sampled and individual reactions at different time points. Yields calculated by ^{1}H NMR with a 20 s delay using 1,4-dimethyl terephthalate as an internal standard. B) Profile of the reaction over time, with data collected from one sampled reaction and individual reactions worked up at each timepoint.

The sampled reaction had a greater consistency between timepoints than that of the individual reactions. These profiles showed that the reaction to form mono-alkylated **93a** was complete within 20 h. However, the variation between one sampled reaction and repeat reactions observed, ca. 10% yield, confirmed that this batch sampling procedure would not be sufficient to compare reaction profiles with confidence. Due to the variability and long reaction times present in the batch profile procedure, investigations were instead focused on developing a flow chemistry procedure.

2.2. Developing a continuous flow system

Using flow reactors to perform photoredox reactions has been one of the most effective solutions for both maximising reaction efficiency and scaling reactions. Flow chemistry setups typically allow for more consistent light irradiation and higher surface area to volume ratios when compared with batch reactors.[13] Furthermore, flow reactors have enabled kinetic analysis of photoredox systems leading to mechanistic insight.[70] Therefore, a flow reaction setup was investigated. The aim of this section was to generate a flow system which could be used for kinetic analysis, and therefore was optimised for conversion but not throughput of material. The requirements for this system were that it allowed sufficient reactor output for sample analysis, and that a complete reaction profile could be obtained over the course of a day.

2.2.1. Optimisation in flow

The flow setup was modified from the existing Hepatochem photoredox reactor. The vial holder was removed from the reactor well and replaced with a coil of PFA tubing (I.D. 1 mm) wrapped around a test-tube (Figure 14). The cavity containing the coil of tubing was connected to a recirculating unit, maintaining a flow of water at a set temperature through the reactor (for further experimental detail see section 4.6). The coil was connected at one end to a syringe pump, and a 5 psi back-pressure regulator at the other end to act as a check valve.

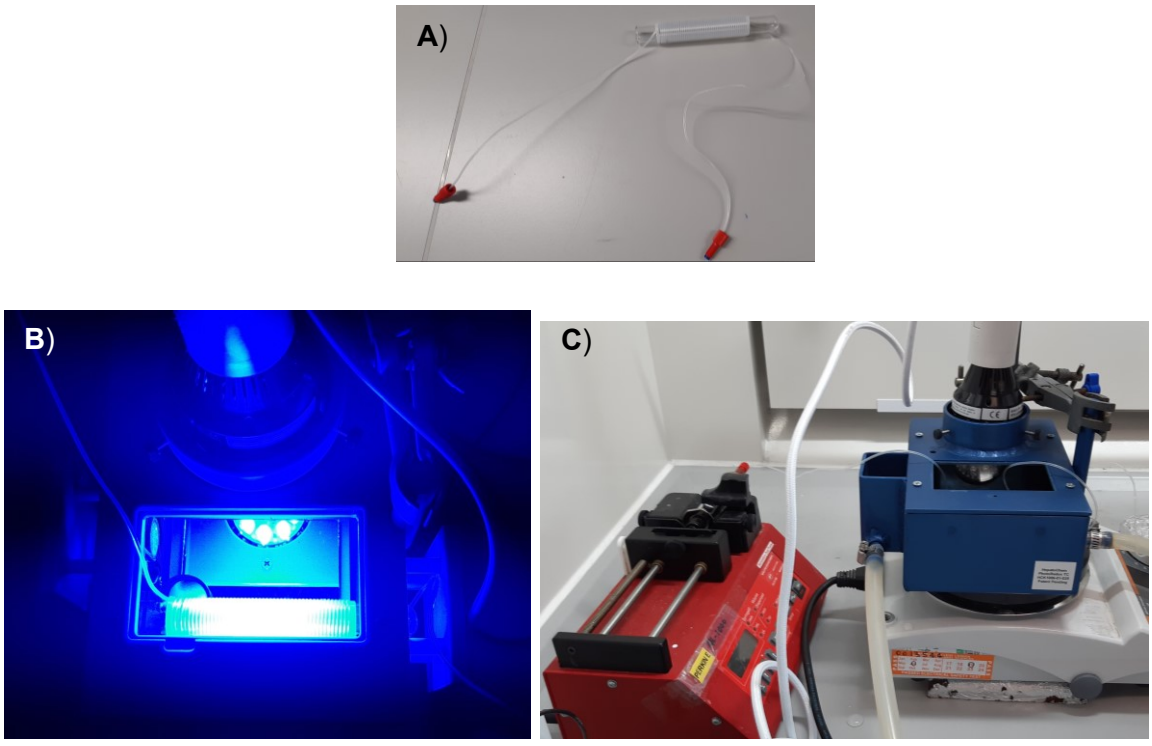


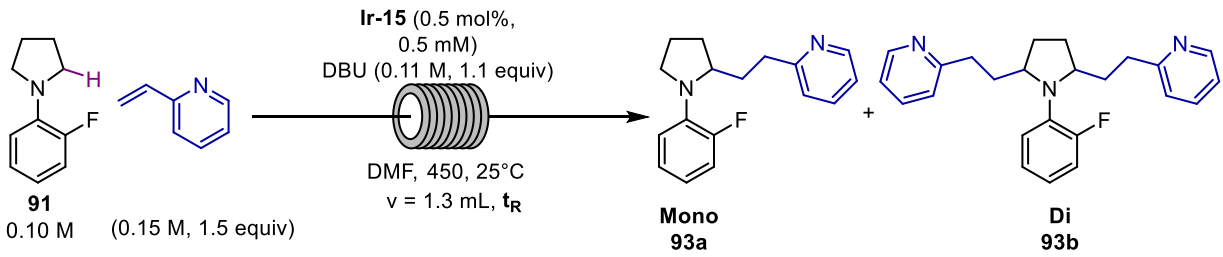
Figure 14: A) coil of tubing B) coil of tubing inside the photoreactor C) the complete setup.

See experimental section 4.6 for further detail on the continuous flow system setup.

2.2.1.1. Initial investigations into residence time

Happily, the reaction translated well into flow and showed good conversion with a 1 h residence time, much faster than the comparable batch reaction (Table 17). While conversion to **93a** over 30 mins residence time (t_R) was lower than over 60 mins, the reaction was selective for mono-alkylation at 30 mins t_R and would achieve higher throughput than the higher conversion 60 min reaction. Doubling the t_R from 60 to 120 mins only increased di-alkylation.

Table 17: Results of reaction using a flow reactor at different residence times, t_R. The residence time was adjusted by changing the flow rate through the reactor.



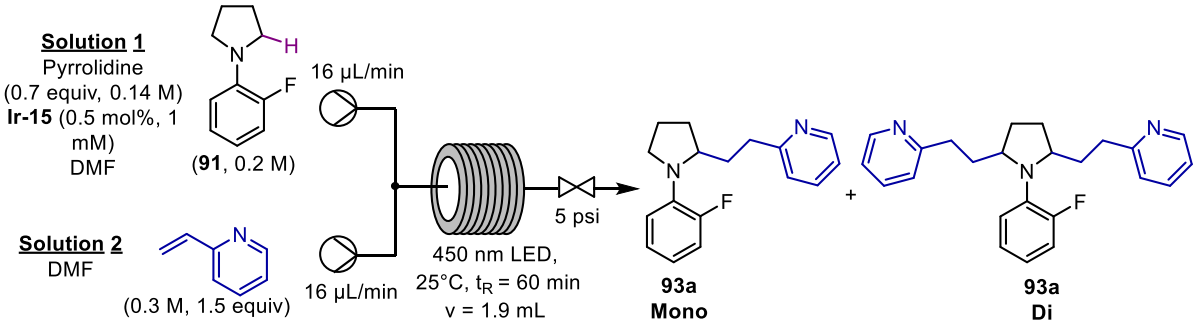
Entry	Residence time, t_R (min)	Flow rate (µL/min)	Yield (%)			Mono 93a throughput in 24 h (mg)
			Mono 93a	Di 93b	Total 93a+b	
1	Batch 1 h[a]	N/A	19	0	19	-
2	30	43	33	0	33	322
3	60	22	55	3	58	289
4	120	11	56	12	68	135

Reaction output collected for 30 min per sample. [a]Reaction conducted on 0.2 mmol scale. Yields determined by ^{1}H NMR using 1,3,5-trimethoxybenzene as an internal standard. Yields are an average of three consecutive samples collected after a purge of two reactor volumes.

2.2.1.2. Flow reactor setup

The first modification from the initial flow experiments was to split the reaction mixture into two input streams, one with the amine substrate, the other with the acceptor (Table 18). This was to allow flexibility to change either of these streams mid-reaction for more efficient scope generation. The yield was slightly improved by this alteration (Table 18, entry 1). A similar yield was seen when changing the feed solutions to include the photocatalyst and pyrrolidine within solution 2.

Table 18: Reaction optimisation of flow parameters.



Entry	Change from given conditions	Yield (%)		
		Mono	Di	Total
1	None	64[b]	11[b]	75[b]
2	Using 2 x 450 nm lights, dimethyl terephthalate added to solution 1 as standard	69	11	80
3	[Ir] catalyst and pyrrolidine in solution 2 instead of 1	61	10	71
4	Reactor volume 1.0 mL, flow rate 8.3 µL[b]	69	9	78

[a]Yields determined by ^{1}H NMR using 1,4-dimethyl terephthalate as an internal standard. Yields are an average of 3 samples following 2 reactor volume purge. [b]Yields calculated by by ^{1}H NMR with a 20 s delay using 1,3,5-trimethoxybenzene as an internal standard, yield given is an average of 3 samples at steady state.

Crucially, DMT could be added into solution 1 as an inert internal standard to allow the reaction to be monitored without having to add a standard to an individual sample (Table 18, entry 2). This both reduced the volume of samples required for analysis (from 0.6 mL to ca. 200 µL) and increased the accuracy of yield calculations. Decreasing the reactor volume to 1.0 mL from 1.9 mL also reduced the amount of material required for each experiment without impacting the reaction yield.

2.2.2. Kinetic profiles

At this point, the reactor design and sampling were considered robust enough to attempt a reaction profile. The reaction was analysed at eight residence times by changing the flow rate. Happily, a consistent profile was obtained with minimal variation between three consecutive samples (Figure 15). Di-alkylated **93b** product did not form until 20 min residence time, then formed slowly up to 60 min residence time.

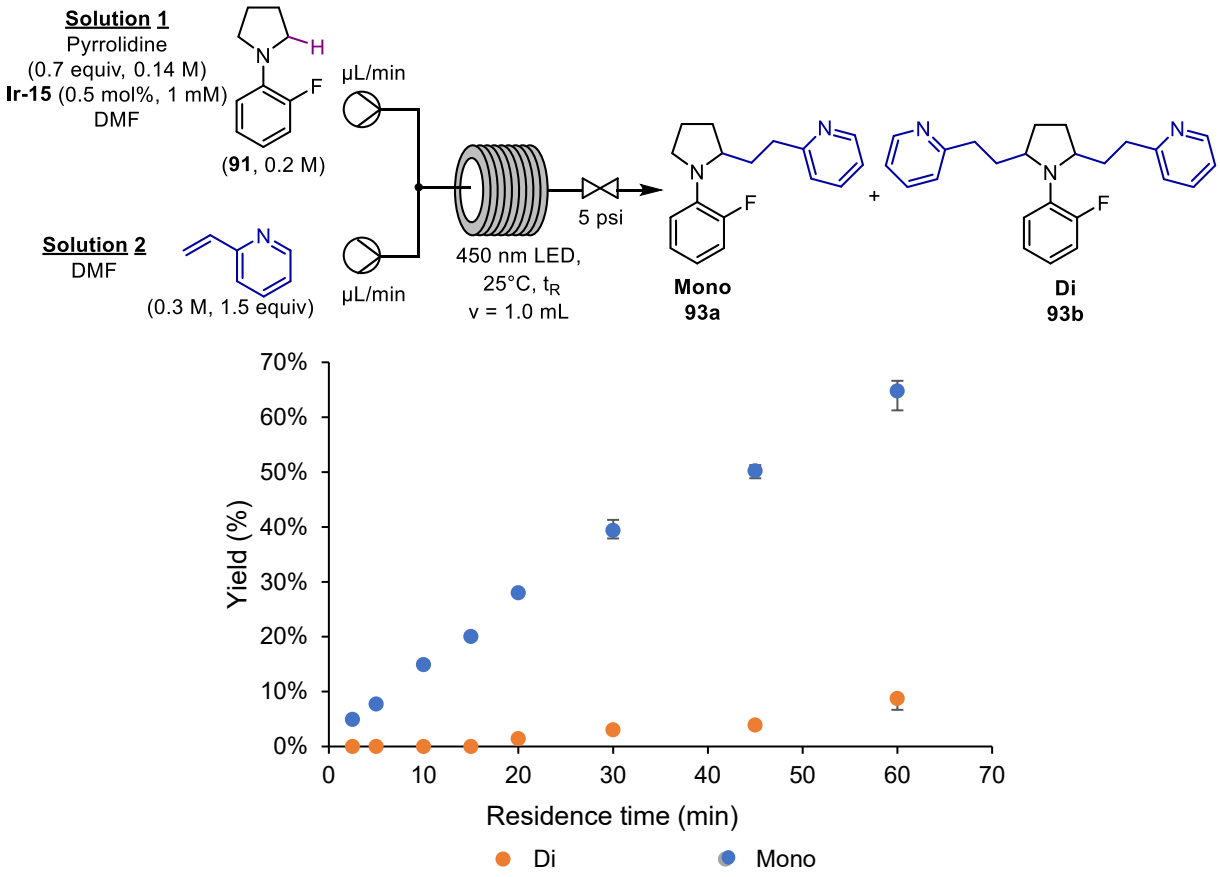


Figure 15: Profile of reaction showing product and di-addition formation using 1 x 450 nm light and temperature controlled at 25 °C. Points given as an average of 3 samples collected for each residence time, range shown in error bars.

Increasing the temperature from 25 °C to 45 °C increased the rate of reaction slightly (Figure 16A), suggesting the reaction was not entirely controlled by light intensity. Light intensity was then investigated by adding more lights around the reactor, which unsurprisingly increased the reaction rate (Figure 16B). No more than 3 lights could fit around this reactor setup, so this highest light intensity setup was used for further experimentation.

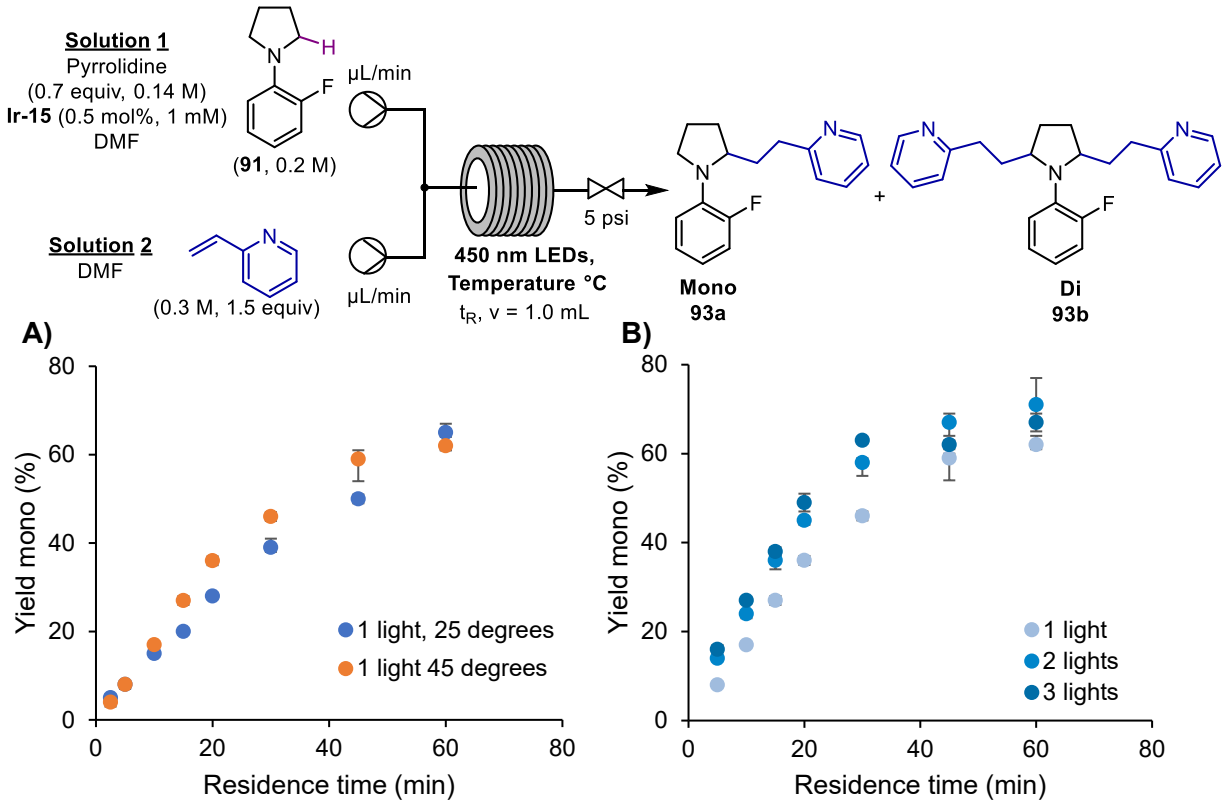
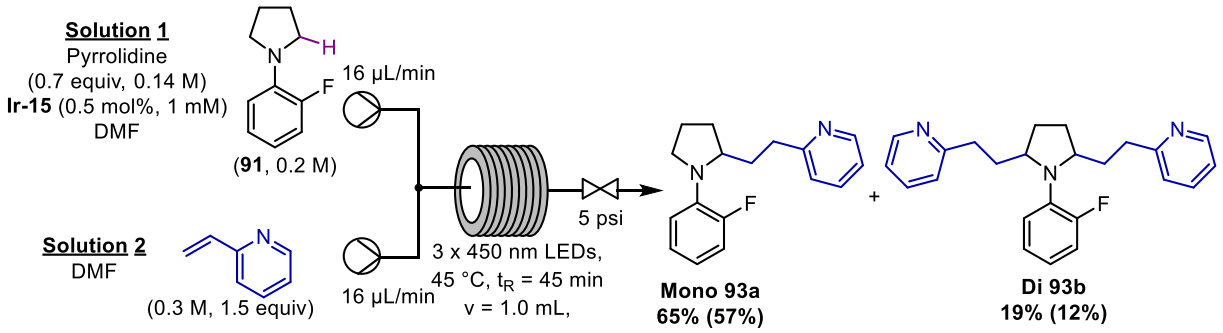


Figure 16: Effect of A) temperature and B) light intensity of the profile at different light intensities. Error bars have been plotted using the maximum and minimum values of three consecutive samples of flow output.

The conditions detailed in Scheme 23 were therefore taken forward as the standard conditions for kinetic analysis method development.



Scheme 23: Selected standard reaction. Yields determined by ^{1}H NMR using 1,4-dimethyl terephthalate as an internal standard, yield is given as an average of 3 samples following a 2 reactor volume purge. Yields in parentheses are isolated yields.

2.2.2.1. Reproducibility in flow

The reproducibility of the reaction under standard conditions was then investigated by analysing three complete reaction profiles. This was to gain understanding of the error associated with the profiles and determine the confidence with which conclusions could be drawn from this kinetic analysis (Figure 17).

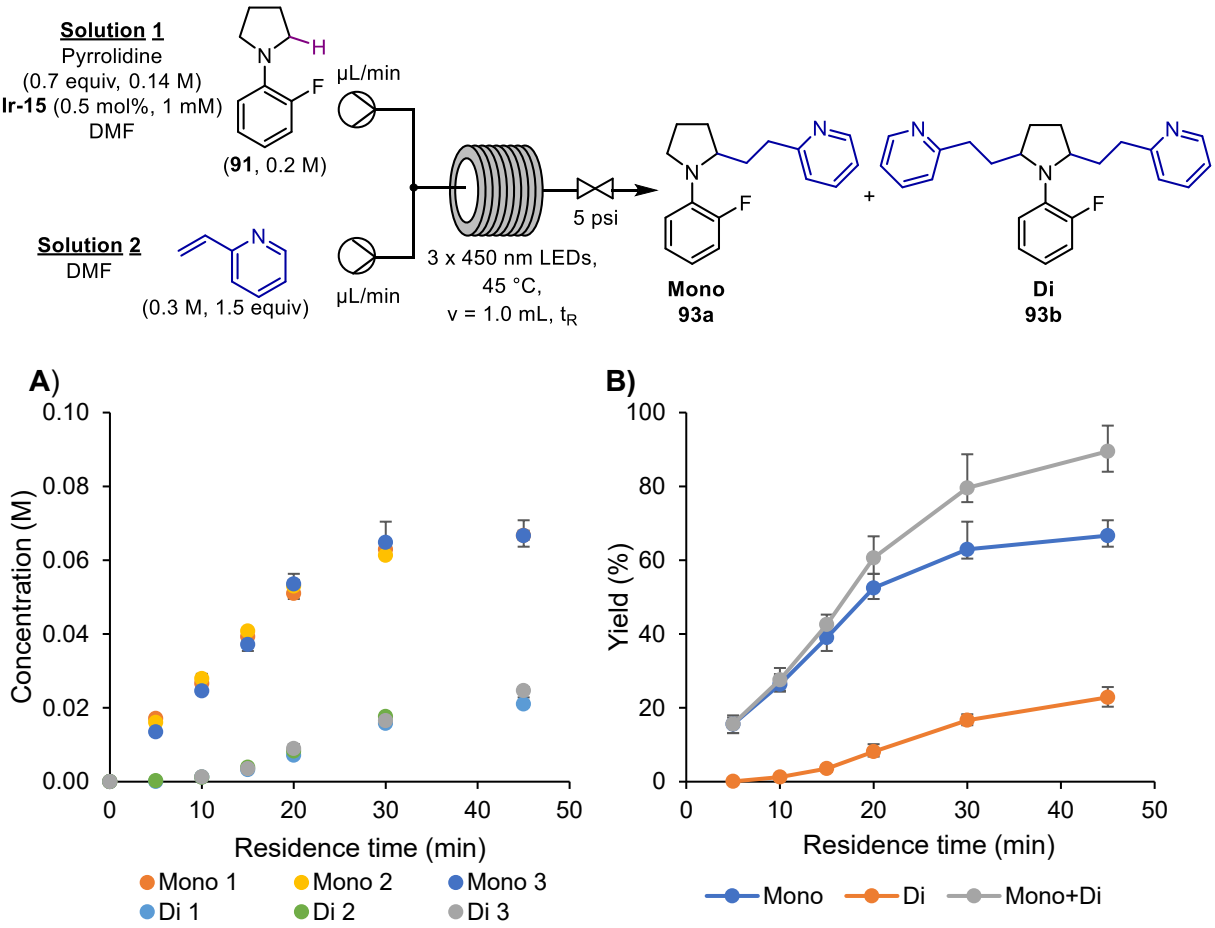


Figure 17: Control profile variability. A) three overlayed individual control reaction profiles. Yields given as an average of three consecutive samples of flow output, calculated using ^{1}H NMR with a 10 s delay vs DMT. B) Averaged profiles. Yields given as an average of 3 samples × 3 profiles, calculated using ^{1}H NMR with a 10 s delay vs DMT. Ranges of the samples given as error bars. Note 45 min timepoint is an average of 6 samples.

The good agreement of these profiles showed this was a suitable and reproducible system for examining the kinetics of the reaction. However, on repeating this control profile several months later (Repeat 1, Figure 18) it was clear this profile had a reduced rate compared to the original control (Figure 17B = Control, Figure 18). The profile was re-run with a newly synthesised batch of starting material (Repeat 2, Figure 18), which overlayed the slower Repeat 1 profile. This indicated that the difference in reaction profile was not a feature of the

batch of starting material, but more likely a change in the set-up over time causing a change in the light intensity of the reactor- either dimming of the lights over time or adjusting of the lights to slightly different positions, causing a reduction in rate. The consistency of the newer profiles with each other was reassuring, and to mitigate for the potential for profile variation over time, it was decided that the control profile be repeated periodically. Results of changes in the profiles were deemed comparable if the control profiles run before and after them overlayed. This allowed confident comparison between different systems, for example when using different substrates.

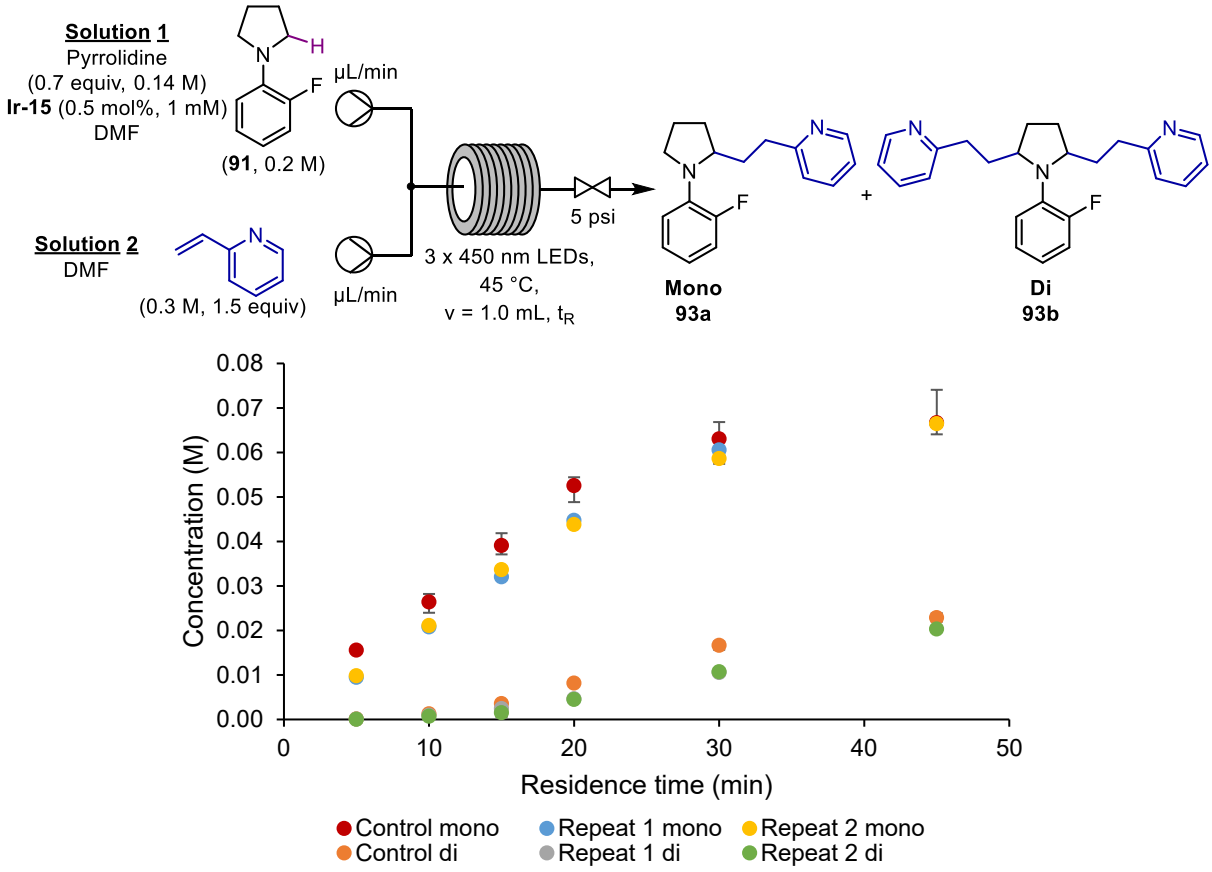


Figure 18: Experiments conducted to determine the cause of control profile inconsistency for the reaction. Repeat 1 and repeat 2 profiles were considered to overlay and be distinct from the control profile.

2.2.2.2. Kinetics of di-addition formation

From the control profiles in Figures 17 and 18 it was clear that the rate of formation of di-alkylated **93b** was much slower than that of mono-alkylated **93a**, up to the end timepoint of the profile. The comparative rates of formation of **93a** and **93b** addition were then investigated by measuring the profile of formation of the di-alkylated product **93b** from mono-alkylated **93a** (Figure 19A).

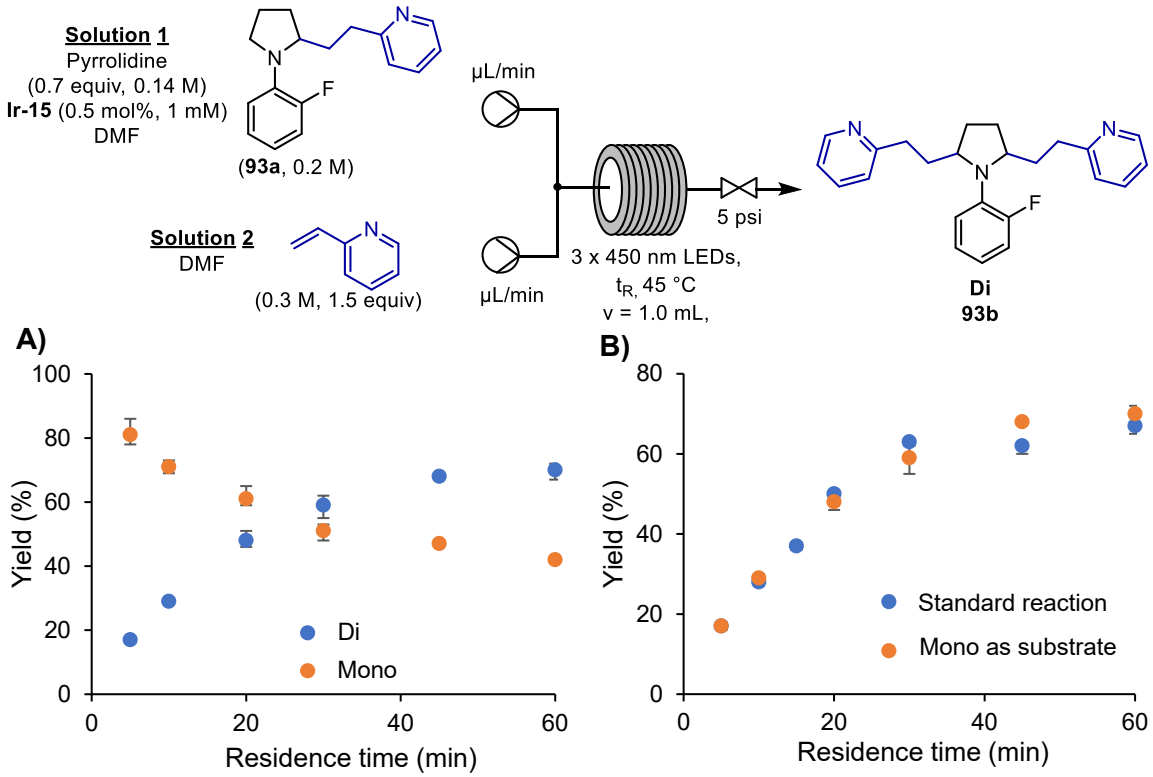


Figure 19: A) Profile of the reaction using **93a** as starting material. B) Overlay of the formation of **93a** from **91** (blue trace), and formation of **93b** from **93a** (orange trace).

The rate of formation of **93b** from **93a** overlayed completely with the standard profile formation of **93a** (Figure 19B). While the standard reaction does not result in 100% mono-alkylated due to the formation of **93b**, when the reaction is performed with **93a** as the substrate, the formation of **93b** does not react to completion despite not forming any further products. It suggests the di-alkylated product could cause reaction inhibition, which will be discussed further in section 2.3.3. It has the potential to quench the photocatalyst excited state, and if no further reaction occurs, this could stall the reaction by preventing catalyst turnover.

2.3. Mechanistic analysis

This section will describe investigations into understanding the mechanism of the developed reaction, and will discuss the techniques which will be used in comparing different reaction setups, including:

1. Orders in reaction components and identification of light independent kinetics
2. Cyclic voltammetry studies to identify redox potentials of reaction substrates
3. Stern-Volmer analysis to determine interactions of the catalyst excited states
4. Same excess reactions to identify any product inhibition or catalyst deactivation

2.3.1. Identifying orders in reaction components, and establishing non-light-limited reaction kinetics

One of the key challenges in this project was to develop a photoredox reaction in which the kinetics were not limited by light intensity, to allow comparisons with different substrates to provide information on the underlying reaction chemistry. Variable time normalisation analysis (VTNA), a technique developed by Burés to determine orders in reaction components, was first applied. As discussed in the introduction, section 1.4.2, VTNA and other visual kinetic analysis techniques have been used to determine the dependence of a reaction on light intensity. This was therefore a starting point for our mechanistic research.

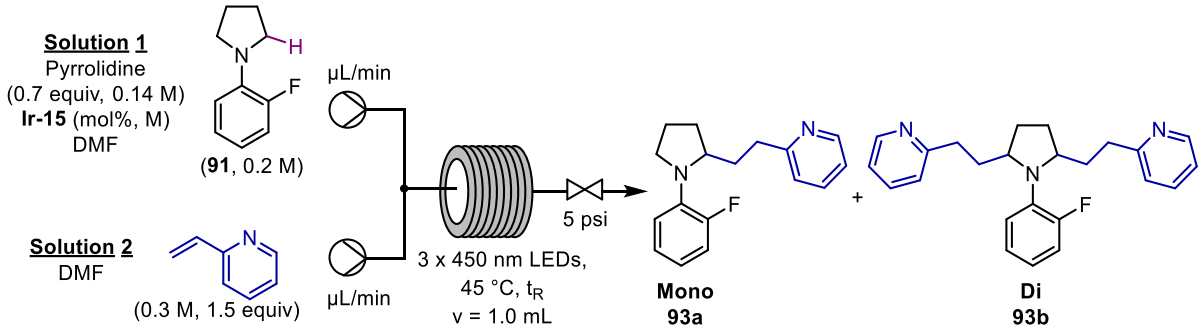
Different excess VTNA involves running at least two reaction profiles, one control reaction profile, then a second which is identical to the first except in the concentration of one component. The time axis of the profile is then adjusted according to the VTNA equation (equation 9)[84]. The exponent of the equation α is determined by the researcher as being the number at which both profiles overlay, and this signifies the order in the component for which the concentration was varied. Usually, a third profile is run with a different concentration again of this component to increase confidence in the determined order.

$$\int_{t=0}^{t=n} [A]^{\alpha} dt = \sum_{i=1}^{n} \left(\frac{[A]_i + [A]_{i-1}}{2} \right)^{\alpha} (t_i - t_{i-1}) \qquad (9)$$

To determine the order in catalyst, data for three reaction profiles was collected (Table 19). For each profile, four outputs were assessed: mono-alkylated **93a** formation, di-alkylated **93b** formation, total product formation (**93a+b**), and (mono **93a** + (2 × di **93b**)) formation (to account for the fact that any di-addition material had gone through the reaction cycle twice). In each instance, the order was the same by every output, with **93b** formation presumably too low to have too much of an impact on the profile relative to mono-alkylation. The standard conditions

were the conditions optimised in section 2.2 (Table 19, Profile 1). For simplicity, only the concentrations of mono-alkylated **93a** are presented here in Table 19.

Table 19: Results of VTNA for catalyst concentration.



Residence time (min)	Mono 93a concentration (M)		
	Profile 1 Catalyst = 0.25 mol%	**Profile 2** Catalyst = 0.50 mol%	**Profile 3** Catalyst = 0.75 mol%
5	0.009	0.016	0.016
10	0.020	0.027	0.033
15	0.033	0.039	0.050
20	0.046	0.053	0.062
30	0.059	0.063	0.066
45	0.064	0.068	0.069

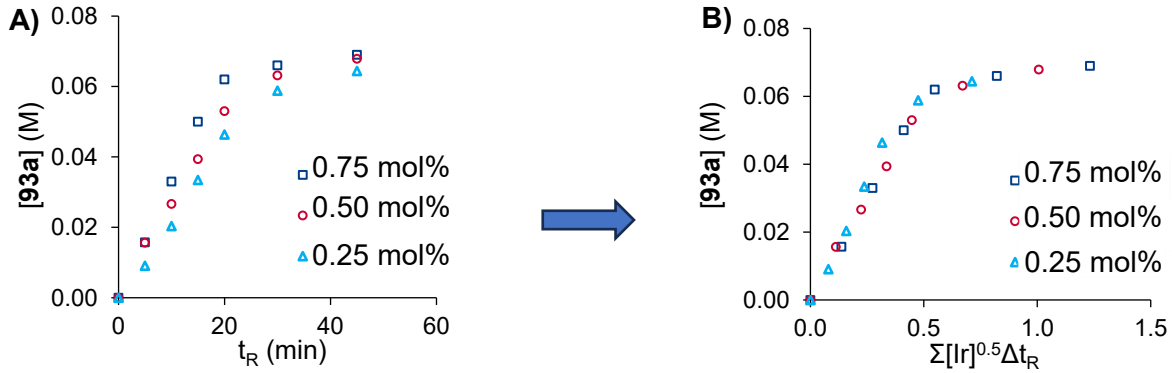


Figure 20: VTNA analysis to determine order in catalyst. A) mono **93a** formation against residence time and B) mono **93a** formation against normalised time, with α set to 0.5. Yields given as an average of three consecutive samples of flow output, calculated using ^{1}H NMR with a 10 s delay vs DMT.

The profiles were then fitted using the time normalisation equation, starting with the order in catalyst set to zero, which indicates no normalisation applied and the x-axis is equal to residence time. As can be seen in Figure 20A, the profiles do not overlay when the order in catalyst is set to zero. The exponent was then varied until the profiles overlayed, and 0.5 was found to give the best overlay (Figure 20B). This analysis was conducted for each reaction components find the order with respect to that component (Figure 21). The orders are summarised in Figure 22.

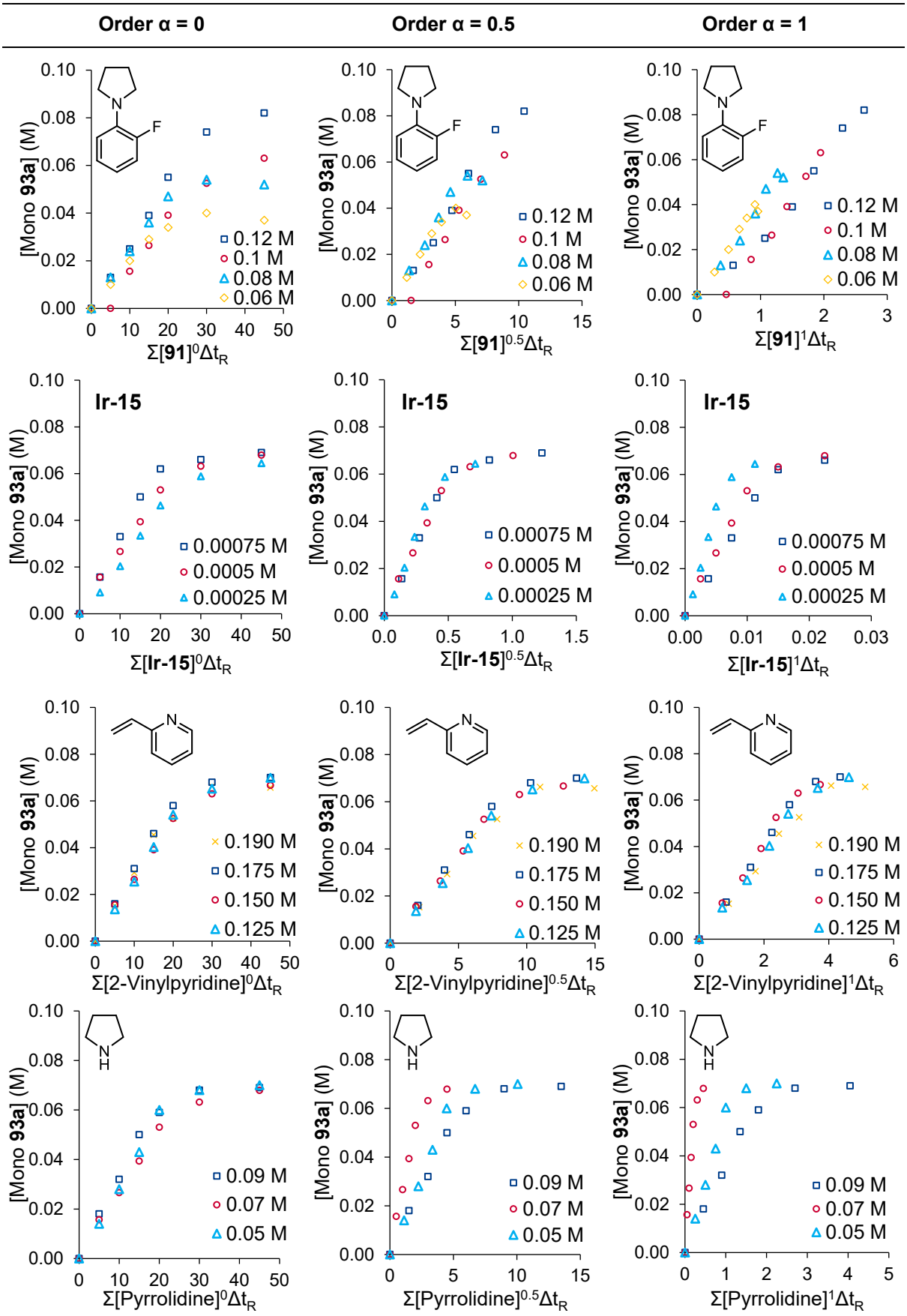
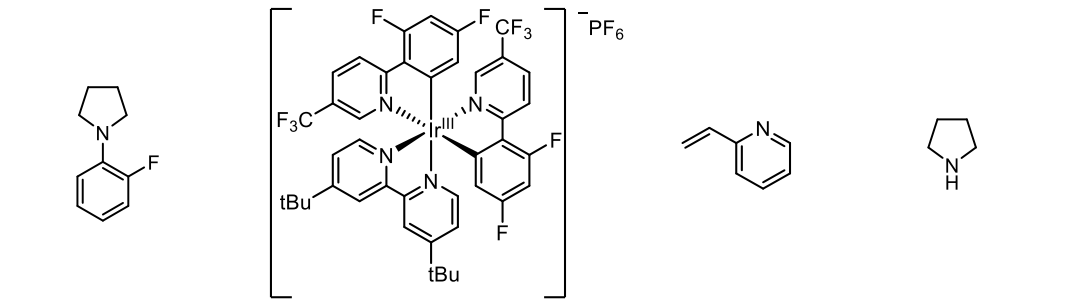


Figure 21: Time normalised VTNA plots for all reaction components at 0.1 M reaction concentration w.r.t. **91** as standard reaction, with orders of α = 0, 0.5 and 1.



Best overlay α = 0.5 Best overlay α = 0.5 Best overlay α = 0 Best overlay α = 0

Figure 22: Orders in reaction components for reaction concentration 0.1 M w.r.t. **91**.

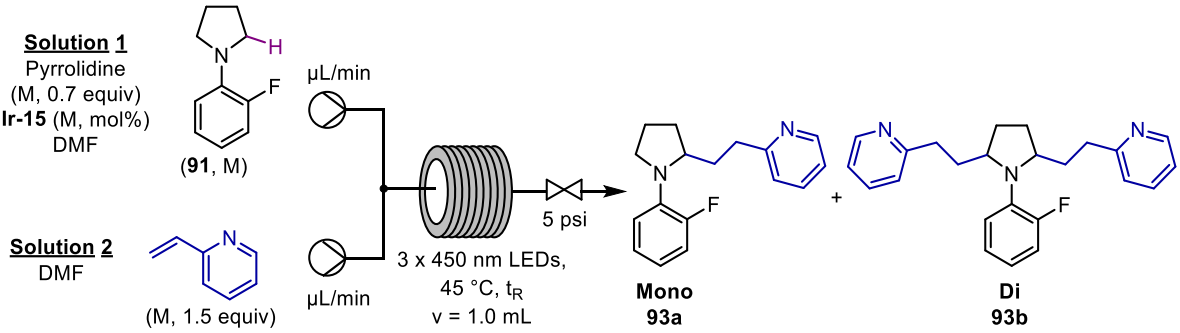
The results of this VTNA analysis provided a lot of interesting information. The orders for **[Ir]** and the amine substrate were a positive value in a 1:1 ratio, indicating the k_{obs} included a bimolecular step in the mechanism involving both substrate **91** and the catalyst (Figure 22). The single electron transfer (SET) event between **Ir-15** and **91** satisfies this criterion. The non-integer order was consistent with there being a change of kinetic regime during the reaction, and the observed 0.5 order was thought to be due to an average of two regimes, one where the reaction was first order with respect to these components, and a period where the reaction was zero order with respect to these components. As discussed in the introduction section 1.4.1, many homogeneous photoredox reactions are initially light-limited with rate only dependent on light intensity, before the kinetics shift to first order in substrate once the substrate concentration sufficiently decreases. This phenomenon could explain the partial orders seen in Figure 21.[71] Furthermore, an observed zero order in base and 2-vinylpyridine (Figures 21 and 22) indicated that steps after the SET including deprotonation, addition into the acceptor and re-protonation were not turnover limiting.

Taking this light-limited system as a starting point, VTNA was used to guide the development of light-independent conditions. This investigation looked at the effect of both reaction concentration and catalyst loading on the orders of photocatalyst and amine substrate **91**. As described in the introduction, work by Wittenberger and coworkers at Abbvie had demonstrated that catalyst concentration had a marked and two-effect impact on reaction rate.[78] In this situation, catalyst concentration could therefore could influence the light dependence of the reaction. Additionally, as the light intensity around the reactor could not be increased, lowering the concentration of the reaction could act as an indirect way of increasing photon equivalents.

Table 20 and Figure 23 describe the results of this investigation. Profiles were recorded using 3 catalyst loadings at each of 3 reaction concentrations. The order in **Ir-15** at each of these concentrations was determined by VTNA analysis, overlaying two of the profiles at each

concentration. For each concentration and catalyst loading, a profile was compared with a different excess profile. These profiles were overlayed using VTNA analysis to determine the order in the amine substrate.

Table 20: Summary of orders in iridium catalyst and *N*-(2-fluorophenyl)pyrrolidine at different reaction concentrations and catalyst loadings.



Reaction Concentration (M)	Ir-15 loading	Order in Ir-15	Order in 91[a]
High 0.1	High (1.0 mol%	– 0.2	0.0[b]
	Medium (0.5 mol%)	0.3	0.4
	Low (0.3 mol%)		1.0
Medium 0.05	High (1.0 mol%)	0.3	0.5
	Medium (0.5 mol%)	1.0	0.5
	Low (0.3 mol%)		0.8
Low 0.03	High (1.0 mol%)	0.4	0.5
	Medium (0.5 mol%)	0.9	1.0
	Low (0.3 mol%)		1.0

[a]Order in **91** was determined by comparing a profile at each catalyst loading to one taken at 0.8% concentration. Orders have been found by VTNA analysis of profile data, obtained using ^{1}H NMR with a 10 s delay using 1,4-dimethyl terephthalate as an internal standard. [b]Profile at 0.10 M concentration compared with one at 0.12 M to obtain order in starting material.

While it is difficult to give definitive values for a non-integer reaction order with a visually comparative technique such as VTNA, it was clear that lowering reaction concentration increased the orders of both amine substrate **91** and iridium photocatalyst **Ir-15** to 1st order (Table 20, Figure 23).

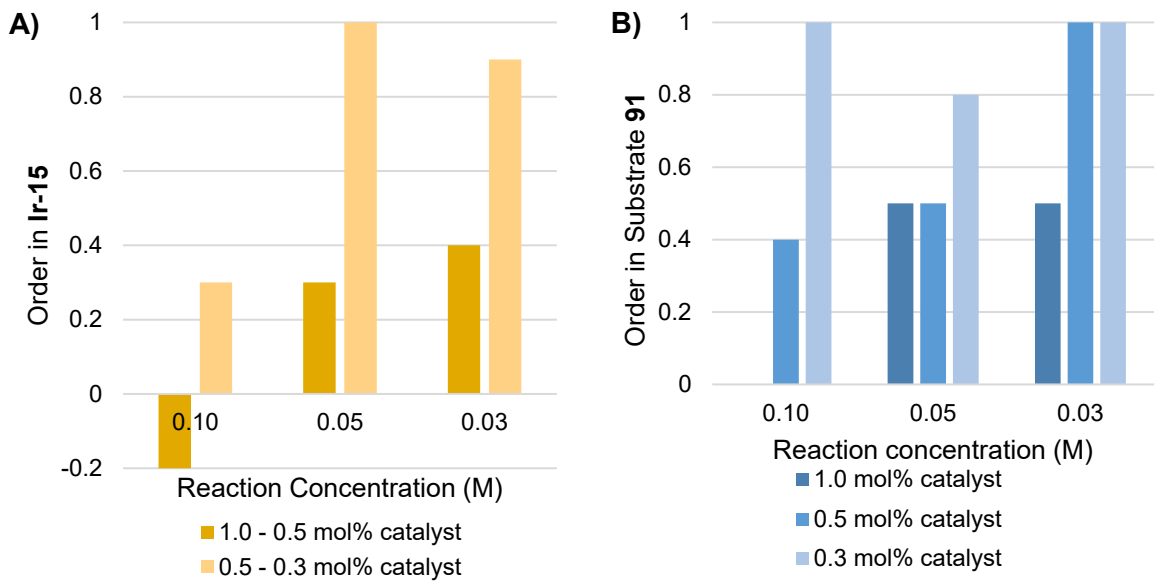


Figure 23: Summary of orders in A) iridium catalyst and B) *N*-(2-fluorophenyl)pyrrolidine found at different reaction concentrations and catalyst loadings.

Further interesting observations included that at high catalyst loadings of 1 mol% and 0.1 M reaction, the order in catalyst became negative, whilst the yield in substrate **91** was 0. This is likely due to the light absorbing properties of the catalyst. The Beer-Lambert law (equation 1) states that light absorbance is proportional to the concentration of the light absorbing species, assuming the pathlength stays constant as in a situation with a fixed diameter reactor.

Therefore, having higher catalyst concentration increases absorbance of light and could reduce transmittance through the reactor, leading to dark spots, thereby decreasing the reaction rate and consequently the value for the order in catalyst and amine. The negative value for the order in Figure 23a indicates a reduction in rate on increasing the catalyst loading from 0.5 to 1 mol%, which highlights this effect most clearly. Contrastingly, there is no negative order associated with the amine substrate as this species does not absorb 450 nm light (determined by UV-Vis, section 4.4); therefore, substrate **91** concentration does not negatively impact the reaction rate at higher concentrations.

Conditions under which orders in both the photocatalyst and substrate were 1, indicating non-light-limited conditions, were achieved: 0.03 M reaction concentration with a catalyst loading of 0.5 mol%.

The orders in pyrrolidine and 2-vinylpyridine were re-tested under these non-light-limited conditions and found to still be zero (Figure 24), suggesting the turnover limiting step of this reaction to be the SET between the catalyst excited state and the aryl-pyrrolidine substrate, and the reaction kinetics were independent of light intensity.

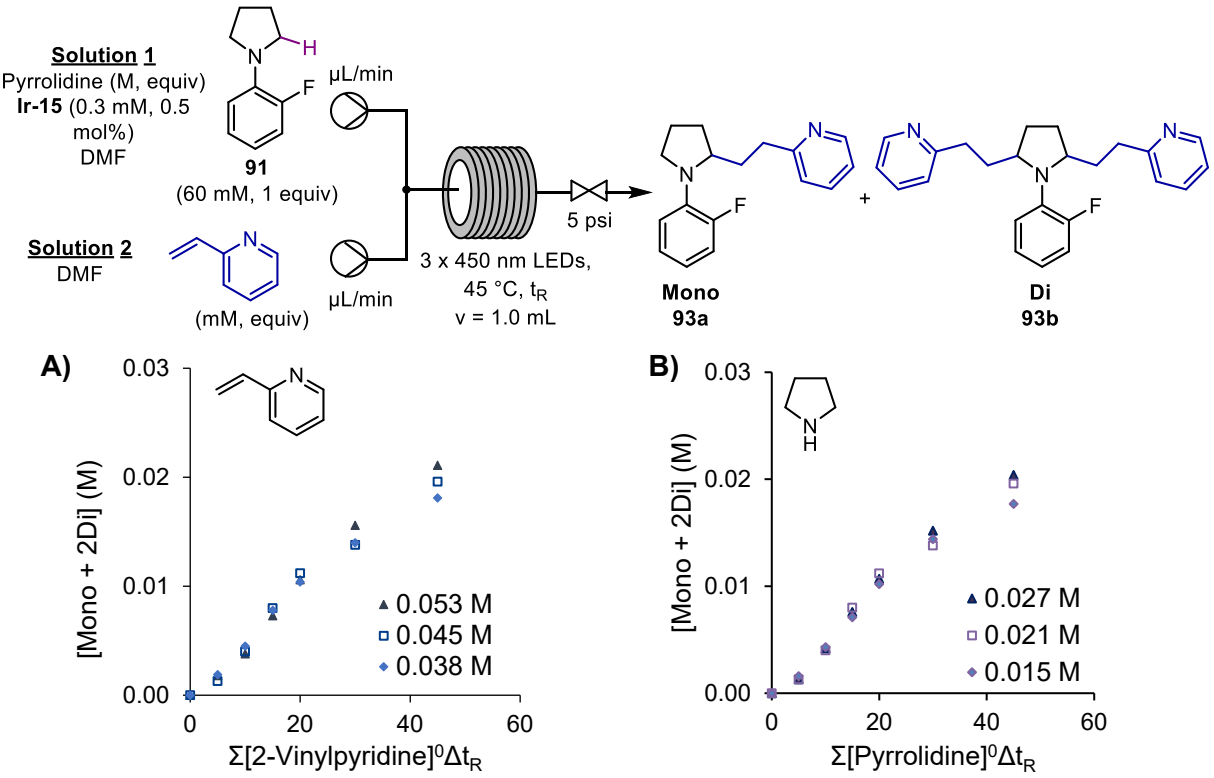


Figure 24: Different excess VTNA anlaysis analysis to determine orders in A) 2-vinylpyridine and B) pyrrolidine. The value of α giving the best overlay is presented in each case.

The power law, or apparent rate law, for the non-light-limited conditions is described in equation 10.

$$rate = k[\boldsymbol{Ir\text{-}15}]^1[\mathbf{91}]^1 \qquad (10)$$

These non-light-limited conditions were consequently used to investigate the effect of different substrates on reaction rate, which will be discussed in section 2.4. Having determined that SET was likely to be turnover limiting for this reaction, the kinetics of this step were investigated using cyclic voltammetry and Stern-Volmer luminescence quenching analysis.

2.3.2. Investigate catalyst quenching

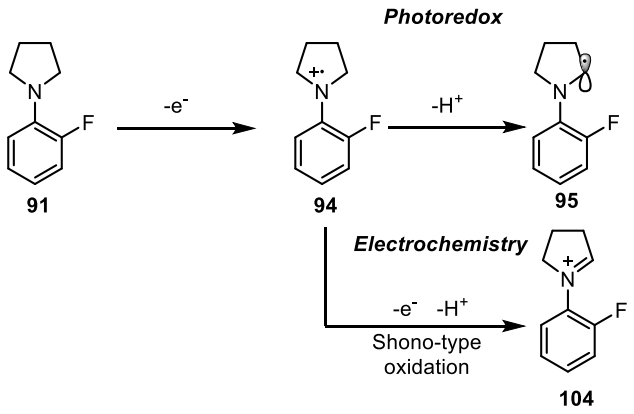
VTNA and kinetic profiling provide important, directly applicable data on the reaction kinetics, and are powerful techniques for this reason. As described in the introduction, cyclic voltammetry and Stern-Volmer luminescence quenching experiments are *ex situ* analytical techniques which can provide information on the interaction between the photocatalyst and substrates (sections 1.3.2 and 1.3.3 respectively). These techniques are most useful for comparisons between reaction components rather than absolute kinetic information. Due to the specificity of the kinetics to the reaction set-up and light intensity, the exact reaction

conditions could not be replicated within the cuvette or potentiostat required for these analyses.

2.3.2.1. Cyclic Voltammetry studies

As introduced in section 1.3.2, cyclic voltammetry (CV) is an electrochemical technique which allows determination of the redox potential of a given material, a useful metric to determine which substrates are likely to interact in single electron processes. In the photoredox processes being investigated in this thesis, the aryl-pyrrolidine substrate must have a less positive reduction potential than the excited photocatalyst (**Ir-15** $E_{1/2}^{III*/II}$ = + 1.21 V vs SCE) in order to be efficiently oxidised. However, it is also important to consider the ways in which electrochemical processes differ from photoredox processes.

Pertinent to this work is the propensity for electrochemical systems to undergo a Shono-type two-electron oxidation of amines to form iminium ions such as **104**,[112] whereas simple photoredox systems typically only permit single electron oxidation. This is due to it being statistically improbable that a generated amine radical will interact with a second molecule of excited photocatalyst, necessary for a second oxidation event to occur, before deprotonation (Scheme 24). Conversely, in electrochemistry, oxidation occurs at the surface of an electrode at which multiple redox events may occur before a molecule diffuses away, dependent on current. Luo and co-workers found that under electrochemical systems, two-electron oxidation is often the preferred pathway for product generation in amine functionalisation.[113] CV experiments were therefore conducted to determine whether valuable information regarding patterns in oxidation potentials could be obtained for this photoredox process.



Scheme 24: One or two electron oxidation possible with electrochemical set up to give either a carbon-centred radical (one electron oxidation), or imine cation (two electron, Shono-type oxidation).

Cyclic voltammetry was first performed on substrate **91** to determine whether this peak represented a single or two-electron transfer. In this instance, the voltammogram was measured with an equimolar amount of **91** and ferrocene present in the solution to be tested (Figure 25A). The peak current of the amine $I_{substrate}$ was double that of the peak current of the ferrocene oxidation wave $I_{ferrocene}$, indicating a two-electron oxidation. Scan rate experiments were undertaken to see if the reversible one-electron oxidation could be observed for the *N*-arylpyrrolidine substrate **91** (Figure 25B). Increasing the scan rate shortens the time at which the substrate is in the oxidised vs reduced state, thereby reducing the time available for the oxidised substrate to undergo an irreversible chemical reaction and perhaps allowing the reversible wave to be seen.

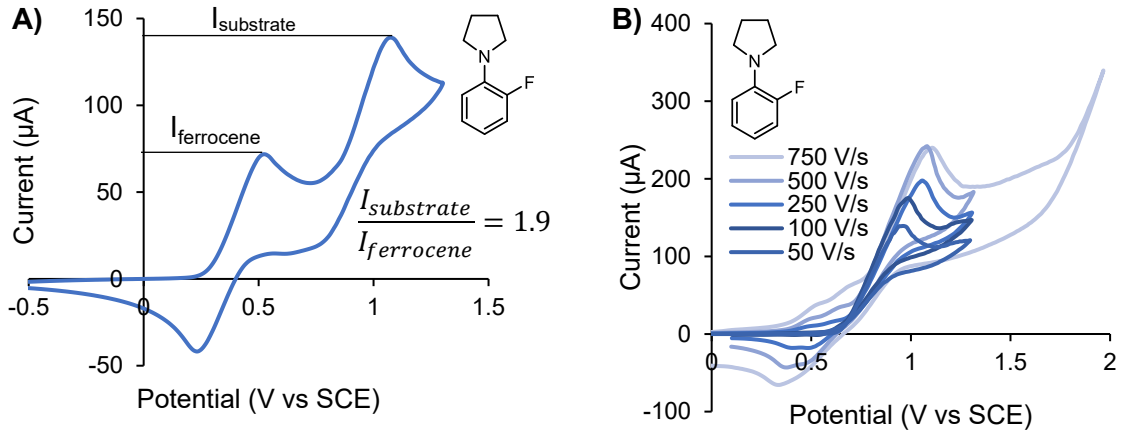


Figure 25: Cyclic voltammograms of A) *N*-(2-fluorophenyl)pyrrolidine **91** and ferrocene at 100 mV/s scan rate B) substrate **91** at different scan rates.

Above a scan rate of 250 mV/s a reversible reduction wave began to appear, likely to be the reduction peak associated with a reversible one-electron oxidation. As no new oxidation peak appeared, it is likely that the observed irreversible two-electron oxidation wave overlayed with the one electron oxidation, and therefore that determining the redox potentials of the amine substrates by cyclic voltammogram would be a useful measurement by which to compare the oxidation potentials of different substrates as an approximation to the one electron oxidation potential. Due to the possibility of the second electron oxidation event affecting the absolute redox potentials observed, the obtained redox potentials were considered useful as a comparative method between substrates. As the observed waves were irreversible, peak anodic potentials E_{pa} results were given.

Oxidation potentials for all reaction components were determined using cyclic voltammetry (Table 21). Aryl-pyrrolidine containing substrates (entries 1-3, Table 21) each showed a single, irreversible oxidation peak of similar potentials, within the range feasible to be oxidised by the

excited photocatalyst. Of note was that the di-product had the lowest oxidation potential of all reaction components.

Table 21: Values at which the peak current was recorded for irreversible oxidation peaks

Entry	Analyte	E_{pa} (V vs SCE)
	Ir catalyst (Ir^{III*}/Ir^{II})	+1.21 ($E_{1/2}$)[32]
1	*N*-(2-flurorophenyl)pyrrolidine	+1.13
2	Mono	+1.11
3	Di	+1.01
4	Pyrrolidine	None
5	2-Vinylpyridine	None

Measured using 5 mM concentration of analyte in 0.1 M solution of $LiClO_4$ in DMF, from –0.5 to +1.5 V using 100 mV/s scan rate.

2-Vinylpyridine were not redox-active over the redox window analysed (−0.5 to +1.5 to V). Interestingly, under these experimental conditions, the pyrrolidine base, was also not redox-active, which was unexpected when compared with literature values (1.09 V vs SCE in acetonitrile).[114]The discrepancy in results could have been caused by the use of lithium perchlorate as an electrolyte; if the lithium ions had complexed with the pyrrolidine this may have raised the oxidation potential and led to an unrepresentative cyclic voltammogram. Stern Volmer quenching was therefore investigated to determine whether pyrrolidine was redox active in this reaction (section 2.3.2.2).

2.3.2.2. Stern-Volmer Luminescence Quenching Analysis

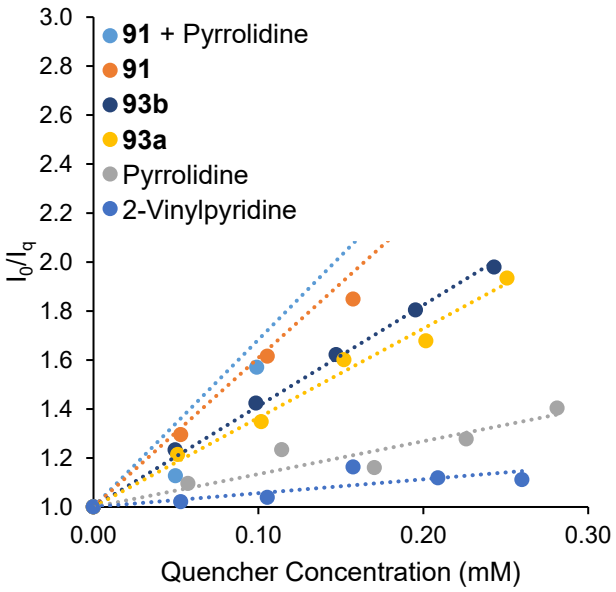
Stern-Volmer quenching analysis is a method to identify which components can quench the excited state of the photocatalyst,[59] and has been used to support proposed mechanisms for a range of photoredox reactions (see 1.3.3). To determine which components of the reaction can quench the excited state of the iridium photocatalyst, each of the reaction components were tested as potential quenchers, Q. First, the luminescence emission spectrum of a solution of photocatalyst was obtained using a fluorescence spectrophotometer, and the maximum emission intensity recorded (I_0). One reaction component was then added portion-wise to this solution, and the maximum intensity (I) recorded after each addition, at each concentration of quencher $[Q]$. A graph of $\frac{I_0}{I}$ against $[Q]$ allowed determination of the Stern Volmer constant K_{SV} for each reaction component (equation 11, Figure 26). K_{SV} is related to the kinetic constant of quenching k_q according to equation (12, where τ_0 refers to the excited-state lifetime in the absence of quencher. τ_0 is a known constant for most commercial photocatalysts- for this catalyst **Ir-15**, τ_0 = 2.3 μs.[24]

$$\frac{I_0}{I} = 1 + K_{SV}[Q] \quad (11)$$

$$K_{SV} = k_q \tau_0 \quad (12)$$

There are two potential quenching modes for molecules interacting with photocatalysts: electron transfer or energy transfer. Förster and Dexter energy transfer are potential methods of energy transfer which could account for quenching of the catalyst. Förster energy requires overlap between the absorption band of the substrate and the emission band of the iridium catalyst to be feasible,[115] which UV-Vis spectra of the substrates and luminescence spectrum of the catalyst have shown to be absent in this (see experimental 4.4). Dexter energy transfer, or triplet energy transfer, occurs between the triplet excited state of a photocatalyst and a substrate, and involves simultaneous electron transfer between these substrates. One electron is donated from the lowest unoccupied molecular orbital (LUMO) of the donor, and one electron is accepted from the highest occupied molecular orbital (HOMO) of the acceptor (Figure 1B). Instead of forming a radical, the excited triplet state of the acceptor is formed, re-forming the photocatalyst ground state.[116] The **Ir-15** iridium catalyst in this reaction has been shown to undergo Dexter energy transfer with styrene substrates in [2+2] cycloadditions,[100] and with diazirines in MicroMap cell proximity labelling studies.[115] However, the triplet state of N-aryl amines is not expected to be within the energy window feasible for triplet energy transfer from photocatalysts. Furthermore, the catalyst is sufficiently oxidising to undergo SET with *N*-phenylpyrrolidines, and other photocatalysts with similar redox windows to this catalyst did give productive reactivity, it is unlikely that energy transfer is having a major contribution to the quenching of this catalyst, and we assumed that the change in quenching rate is due to SET between photocatalyst **Ir-15** and the quencher in each case.

Every aryl-pyrrolidine containing component of the reaction was able to quench the photocatalyst: the amine substrate **91**, mono-alkylated **93a** and di-alkylated **93b** (Figure 26), which is consistent with the obtained redox potentials. The quenching constants for these compounds are comparable to those observed for other anilines in the literature quenching the same catalyst (4-bromoaniline $k_q = 3.40 \times 10^9$ $M^{-1}s^{-1}$).[67] The amine substrate quenched the catalyst roughly twice the rate of mono-alkylated **93a**. This was initially not predicted, as the reaction under light-limited conditions showed an overlay in rate of formation using **91** and **93a** as substrate respectively (Figure 19); however, a repeat under the new light-limited conditions showed that the rate of formation using **93a** as substrate was indeed slower than the reaction with **91** as substrate (results discussed in upcoming section 2.3.3), highlighting the importance of using the non-light-limited conditions to uncover substrate dependent changes in rate.



B)

Component	K_{SV} (mM^{-1})	k_q ($\times 10^9$, $M^{-1}s^{-1}$)	R^2
91	6.1	2.7	0.99
Di **93b**	4.1	1.8	1.00
Mono **93a**	3.6	1.6	0.99
Pyrrolidine	1.3	0.6	0.88
2-Vinylpyridine	0.6	0.3	0.65
91 + Pyrrolidine	6.8	3.0	0.98

Figure 26: Stern-Volmer luminescence quenching analysis, concentration of photocatalyst solution used was 0.05 mM. A) Collected data. B) Stern-Volmer quenching constants derived from experimental data and photocatalyst τ_0 = 2.3 μs.[32] R^2 value has been given to inform the significance of the correlation.

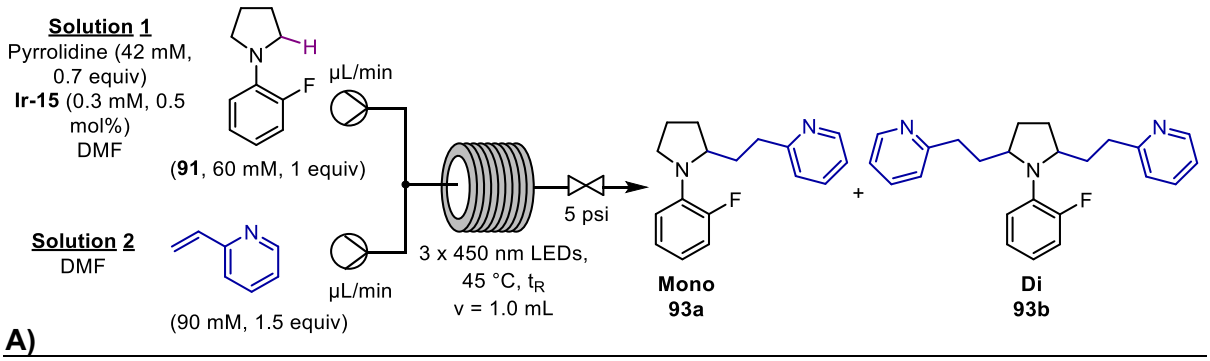
Furthermore, **93b** can quench the catalyst at a very similar rate to **93a** yet forms no further products in the reaction. This could potentially provide a mechanism for product inhibition (Figure 26B, entries 2 and 3). This could explain why the reaction using mono **93a** as a substrate does not go to completion (Figure 19). Adding pyrrolidine (0.7 equiv) to **91** did not increase the rate of quenching above the sum of the pyrrolidine and amine rates, suggesting the base is not involved in this SET process (Figure 26B, entry 1). 2-Vinylpyridine and pyrrolidine were not effective quenchers of the photocatalyst as is consistent with the proposed mechanism, giving low k_q values (Figure 26).

2.3.3. Same excess reactions

Same excess analysis was used to determine whether there was product inhibition or catalyst deactivation in the reaction using the light independent conditions. Same excess analysis is another visual kinetic analysis technique developed by Blackmond in the form of reaction profile kinetic analysis, or RPKA, using whole profile reaction rates to determine whether a reaction component was preventing the reaction from continuing to completion. Same excess experiments involve recording one reaction profile using standard reaction conditions. Then, a second profile is collected in which the starting concentrations of all reaction components match those seen at a specific timepoint of the researchers choosing, in the absence of product(s). The profiles are then overlayed to determine whether there is a difference in rate,

with the only difference between the profiles being catalyst turnover and concentration of product(s). If the second profile is faster than the standard profile, then there is likely either catalyst degradation or product inhibition occurring in the reaction. If so, a third profile identical to the second but with product(s) added in at the appropriate concentration to match the standard profile, can be used to distinguish between the causes of reaction deceleration.[84]

In this instance, the standard reaction profile at 10 min in had 25 mmol concentration of starting material, and 5 mmol of **93a**. A same excess profile was run using the concentrations of reaction components matching those seen in the control profile at 10 min residence time, in the absence of product (Figure 27).



A)

Reaction component	Starting Concentration (mM) Control profile	Same excess Time-shift 10 min
N-(2-fluorophenyl)pyrrolidine **91**	30	25
2-Vinylpyridine	45	40
Ir-15	15	15
Pyrrolidine base	21	21

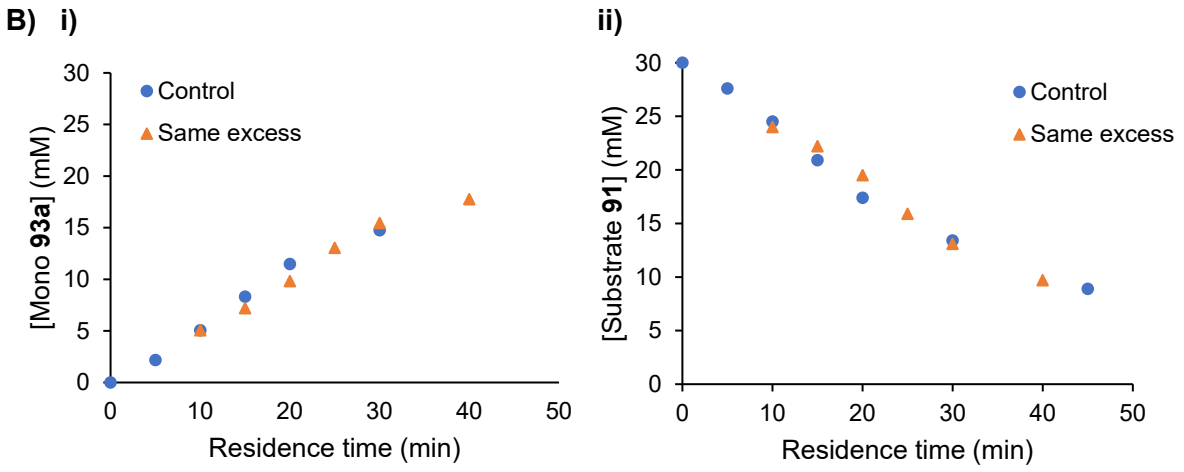


Figure 27: Same excess analysis A) Concentrations of reaction components in same excess analysis. B) Results for same excess experiment showing i) formation of mono-alkylated **93a** and ii) consumption of amine substrate **91**. Note, 30 mM = initial concentration of **91**.

The standard profile and same excess profile overlayed well (Figure 27B). This indicated there was no product inhibition or catalyst degradation over the course of the reaction. However, it was unclear why the reaction using **93a** as a starting material did not go to completion. It was hypothesised that the di product **93b** might inhibit the reaction. Cyclic voltammetry and Stern-Volmer analysis confirmed that the **93b** did quench the catalyst, and flow reactions using **93a** as substrate identified no further substrate formation other than **93b**. This could stall the catalytic cycle, preventing oxidation of the catalyst back to the active Ir^{III} ground state. Therefore, the same excess analysis was repeated on the reaction using mono **93a** as the substrate (Figure 28).

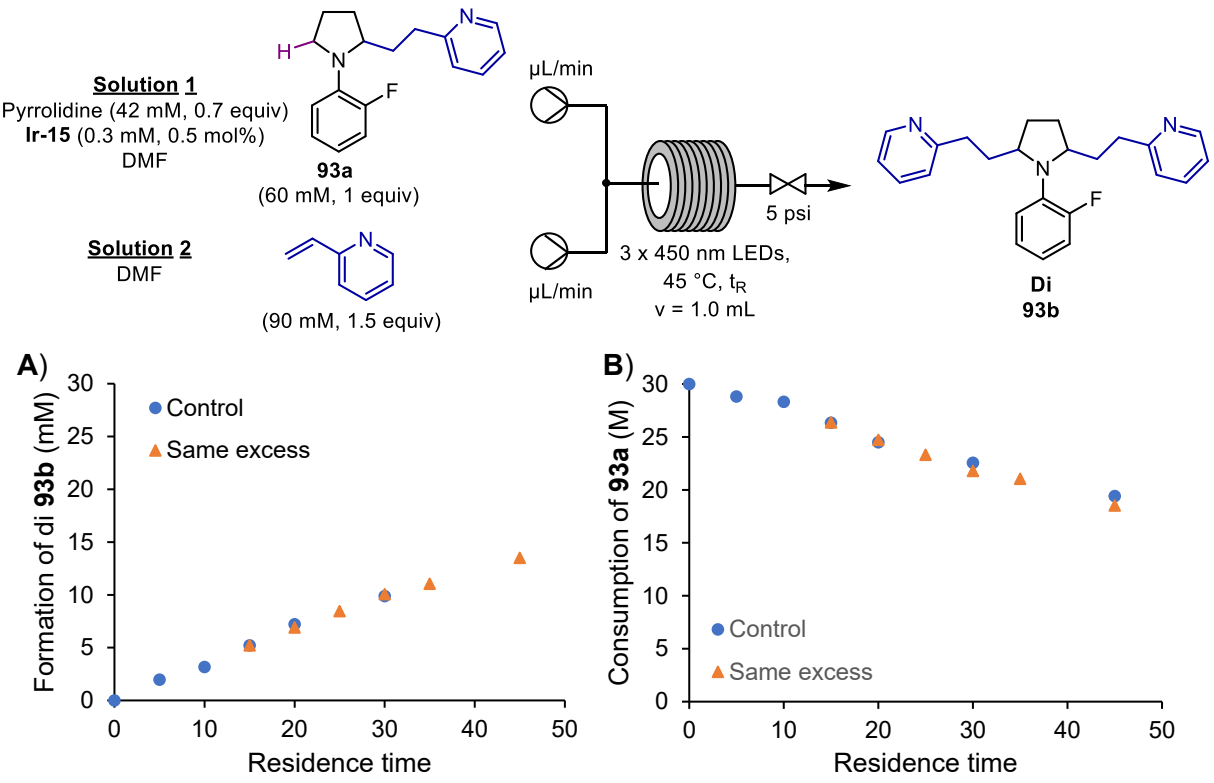


Figure 28: Same excess analysis for formation of di. Time-shift of 15 mins plotting A) formation of di product **93b**, and B) consumption of starting material **93a.**

No product inhibition was observed using this reaction; however, this time the rate of formation of di-alkylated **93b** was much slower than the rate of formation of mono **93a**, which was consistent with the Stern-Volmer data showing a reduced rate of catalyst quenching for **93a** than substrate **91**. It was possible that product inhibition was not identified due to the slow reaction, meaning the residence times used in this reaction were a small fraction of the timeframe of the overall reaction, meaning inhibition was not observed.

The same excess analysis also showed that over the standard reaction used, there was no product inhibition or catalyst degradation significantly impacting the reaction rate. The profiles using the mono **93a** (Figure 28) as substrate also showed that di product **93b** formation was much slower than the reaction to form mono product **93a**, even when no other substrate is present in the reaction. This shows the selectivity for the mono product and shows that for this substrate, di product **93b** is minor compared to mono product **93a** formation.

2.4. Trends in different substrates

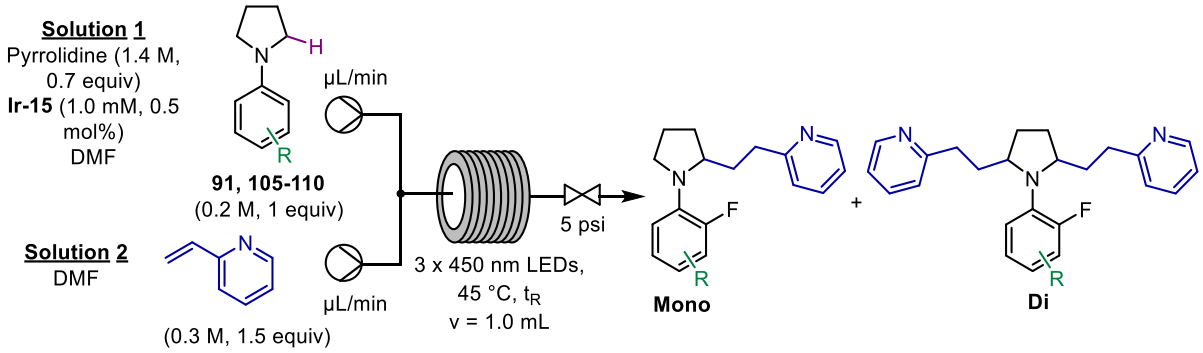
Several pieces of information were used to investigate the trends in different compounds. For each substrate, the yield was obtained using 0.1 M reaction concentration conditions to obtain material to be characterised. Reaction profiles were collected using the light-independent reaction conditions as described in 2.4.1 to compare the rates of the reaction with different substrates. Redox potentials were measured by cyclic voltammetry to allow identification of any trends in redox potentials. Stern-Volmer luminescence quenching analysis was performed to represent the kinetics of SET more accurately as relates to catalyst quenching compared with the electrochemical cyclic voltammetry method.

To compare reaction rates with substrates that may have higher levels of di-addition product 93b formation than the standard reaction, rates have been determined with respect to the rate of (mono + (2 × di)) formation. Due to the low levels of di-addition product formed early in the reaction, it was assumed that formation of the di-addition product was from two complete catalytic cycles being required, rather than an internal HAT mechanism between the formed mono-alkylated product radical and the second α-aminoalkyl radical. An internal HAT mechanism would not be concentration dependent, whereas in all profiles with tested substrates, formation of di-addition product did not start before around 30% mono-product had been made. Therefore, the rate of (mono + (2 × di)) product formation was considered to be the best metric to describe the reactivity of this system, with two complete rounds of the catalytic cycle required to obtain the di-alkylated product, and one for the mono-alkylated product**.** This approach was first taken to investigate trends in substrate aryl group.

2.4.1. Trends in aryl groups

N-Aryl pyrrolidine substrates with variable substituents on the aryl ring were investigated to determine the reaction yield, quenching constant, reaction rate under non-light limited conditions, and redox potentials. The results of these investigations are described in Table 22, ordered by redox potential.

Table 22: Data for different aryl groups.



Substrate	R group	Yield (%)[a]			k_q (10^9, $M^{-1}.s^{-1}$)	Rate (a+2b) (mM/min)[b]	E_{pa} (V vs SCE)
		Mono	Di	Total			
Ir-15		-	-	-	-	-	+1.21[c]
105	4-Me	68	17	85	4.0	1.23	+0.75
106	H	36	44	80	3.2	1.55	+0.93
107	4-F	61	6	77	2.8	1.02	+0.93
91	2-F	57	12	69	2.3	0.79	+1.13
108	4-CF_3	22	0	22	1.7	0.23	+1.53
109	4-OMe	34	1	35	2.6	0.54	+0.56, +1.10
110	4-CN	12	0	12	1.4	0.17	> + 2.0 V

[a]Isolated yields. [b]Rate of formation of (mono + 2di) products given. Rate extracted from profiles using 0 to 20 min as described in section 4.7.4. [c]Redox potential is standard reduction potential for $Ir^{III}*/Ir^{II}$, $E_{1/2}$.

With the exception of substrate **109**, R = OMe (Table 22, entry 7), k_q and redox potentials of the substrates correlated with isolated yields. As the differences in electronics of the aryl group would have a much greater effect on the first SET event in the reaction rather than the second, it supported the conclusions from the VTNA that reaction rate was dependent on the SET between excited state photocatalyst and amine substrate to form the amine radical cation.

To interpret the correlations more closely, graphs depicting the linear regression associated with reaction rates, Stern-Volmer quenching rates and redox potentials were plotted. Firstly, there was a negative correlation obtained between the measured substrate oxidation potentials measured and the quenching rate obtained by Stern-Volmer analysis (Figure 29A,

R^2 = 0.87). Stern-Volmer quenching analysis is notoriously difficult to reproduce, so it was pleasing to see this correlation.

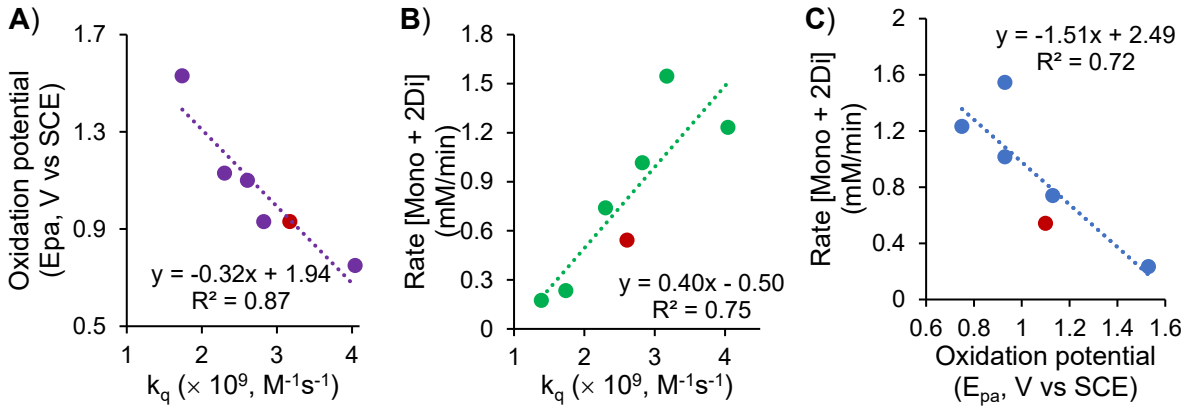


Figure 29: Linear correlations between A) oxidation potential and quenching rate k_q, B) reaction rate and k_q and C) reaction rate and oxidation potential. R = CN was not included in graphs A and C due to oxidation potential not being present within the tested range. Data for substrate R = OMe is highlighted in red in each graph.

The rate of reaction was positively correlated with k_q, and negatively correlated with the redox potential. Substrates with higher oxidation potentials are thermodynamically less favoured to do the single electron transfer according to the Nernst equation (see discussion section 1.3.2). As found by Frenette and co-workers, k_q obtained by Stern-Volmer analysis was a slightly better predictor for reaction rate than redox potentials (R^2 = 0.75 vs 0.72).[51] This is perhaps unsurprising as k_q, like reaction rate, is a kinetic descriptor whilst redox potentials are a thermodynamic quantity. However, the high correlation between redox potentials and quenching constants depicted in Figure 29A demonstrates that these properties are linked, with higher redox potentials resulting in slower rates of catalyst quenching.

Substrate **109**, R = OMe had a lower rate and isolated yield than expected from the quenching rate and redox potential data obtained. The cyclic voltammogram of this compound indicated some interesting aspects: there were two distinct oxidation events for this species, a reversible peak at $E_{½}$ +0.45 V, and a second, irreversible peak at +1.10 V, rather than just the single, irreversible peak observed for other substrates (Figure 30).

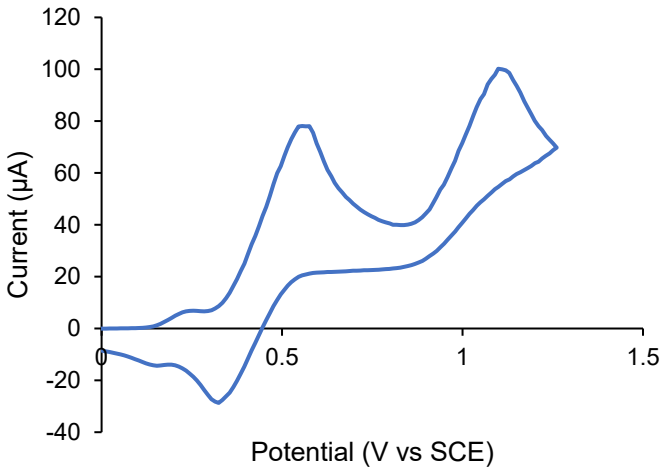
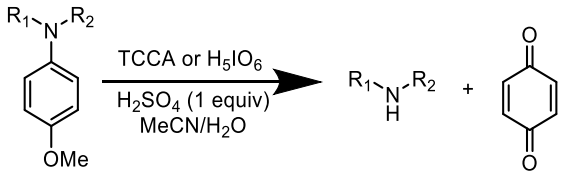


Figure 30: CV of *N*-(4-Methoxyphenyl)pyrrolidine **109.**

The irreversible peak was expected to be the relevant redox event for this reaction. Presence of a second, reversible wave indicated there could be a competing redox process for this substrate in the reaction. For example, Rutjes and coworkers described the oxidative removal of a PMP group as benzoquinone, a potential degradation pathway.[117]



Scheme 25: Proposed method of aniline deprotection.[117]

It is possible that whilst a certain degree of productive reaction occurred, there may have been some degradation of the product throughout the reaction, or a competing oxidation event causing lower yields than expected. As both oxidation events were within the range of the photocatalyst, the reaction could have become stalled by catalyst quenching promoting a non-productive SET event, from which it may not have been possible to re-oxidise the catalyst and close the photoredox catalysis cycle. Removing this datapoint from graphs in Figure 29B and C increased the R^2 value by 0.05 and 0.08 respectively. Despite the lower rate, however, it was still possible to achieve useful quantities of the *para*-methoxy substrate, with good selectivity for mono-alkylated product obtained (34% mono to 1% di).

2.4.1.1. Hammett analysis

Having determined that the rate of reaction was correlated to the redox potentials of the substrates, it was hypothesised that redox potentials may be correlated with Hammett substituents, σ (Figure 31).

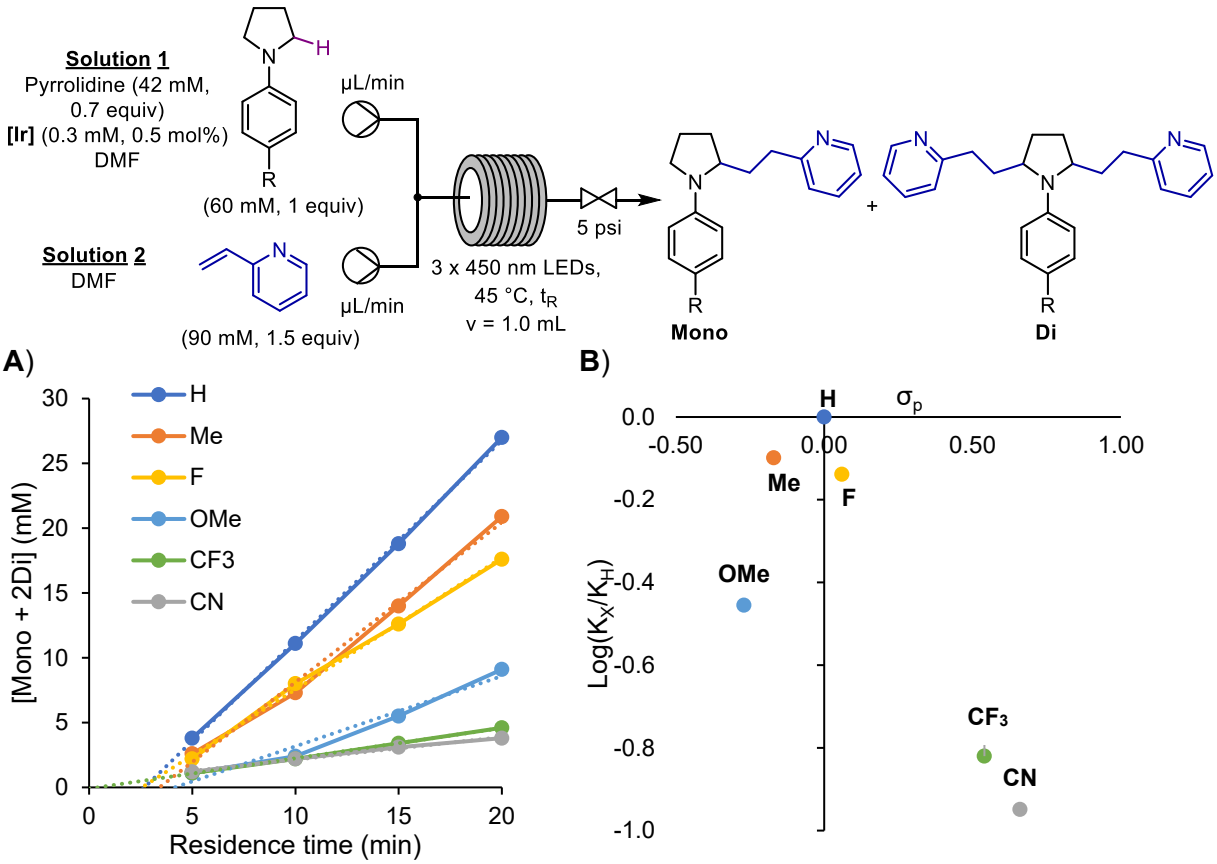


Figure 31: Hammett analysis. A) Profiles depicting product formation (concentration of mono + (2 × di) of differently *para*-substituted substrates. B) Hammett plot using kinetic data.[118]

An interesting trend was observed in the Hammett analysis of this data; reaction rate was highly correlated with Hammett σ_p values when the σ_p values were positive, i.e. electron-poor substrates gave slower reactions (Figure 31B, $R^2 = 0.64$ including all datapoints vs $R^2 = 0.99$ for $\sigma_p > 0$). However, for electron-donating Me and OMe substrates, the trend was reversed and these gave lower rates of product formation. The fastest substrate was the unsubstituted aniline. When σ+ constants, as described by Brown and Okamato,[119] were used in place of σ values, the shape of the Hammett plot was very similar, with no improved correlation. Non-linear Hammett plots, particularly convex plots, can denote a change in mechanism in a reaction, or could denote that a measured rate constant may be due more than one step.[120] In this instance, the rate of quenching was fastest when R = Me; therefore, this trend does not appear to be explained by trends in SET rates. However, radicals can be stabilised by electron-

withdrawing or electron-donating groups. It is therefore possible that σ_p values at the extremes of the tested points, for example OMe and CF_3/CN, the formed radical is sufficiently stable to slow down addition into the acceptor, and the overall rate, and the non-linear Hammett plot is a result of a change in rate-determining step. Alternatively, treating OMe as an outlier due to its different redox properties as described above, the substrates still have a good correlation (R^2 = 0.94 without OMe). It is difficult to draw conclusions regarding substrates with negative σ_p values with only OMe and Me substrates tested. Expanded examples using electron donating substituents would allow more definitive analysis. Using σ^+ constants in place of σ constants

2.4.1.2. Swain-Lupton analysis

As Hammett parameters were not fully correlated with this reaction, we turned to another linear free energy correlation method using Swain-Lupton parameters.[121] Swain-Lupton parameters were used by Colbran and co-workers to predict the $Co^{III/II}$ redox potentials of tuned cobalt complexes, where the authors found poor correlation with Hammett parameters.[122] Analysis using Swain-Lupton parameters involves regression analysis to solve the Swain-Lupton equation 13. This is performed by a regression analysis using the predictor under investigation, oxidation potential for example, and the field F and resonance R constants for each substituent to obtain coefficients f and r.[101] Field and resonance constants for a range of substituents were described by Taft and co-workers.[118] The resulting f and r coefficients can be simplified into value α according to equation 14 to give equation 15. Plotting the predictor of interest against the Swain-Lupton equation 15 allows determination of the extent of correlation.

$$\sigma = fF - rR \quad (13)$$

$$\alpha = f/r \quad (14)$$

$$\sigma = \alpha F - R \quad (15)$$

Correlations with Swain-Lupton constants as described above were performed for each metric: rate, quenching constant and redox potential. In each case, the linear regression was performed using all substrates analysed in Table 23, with the exception of R= OMe which has been discussed to be an outlier. Results for this analysis are presented in Figure 32, with trend lines given without incorporation of the 4-OMe substrate. For reference, the value for the 4-OMe substrate has been added to each graph in Figure 32 in red.

The Swain-Lupton parameters correlated well with quenching rates and redox potentials, giving high R^2 values of 0.99 and 1.00 respectively. The correlation was less strong with

reaction rates, and correlated similarly as well as the Hammett parameters had (R^2 = 0.87 vs 0.94). In each case, the *para*-methoxy substrate was a significant outlier that did not match the trends of the other substrates.

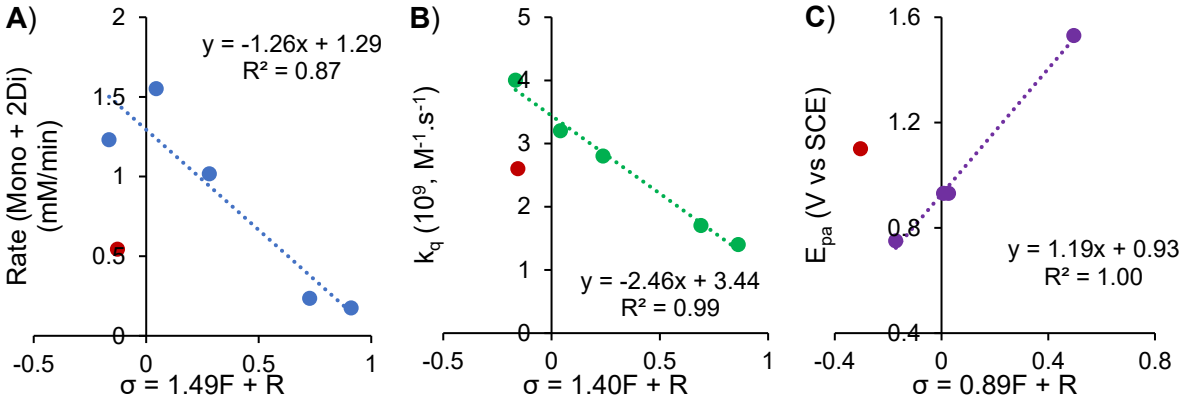


Figure 32: Correlation of experimentally determined parameters A) reaction rate, B) Stern-Volmer quenching constant, and C) oxidation potentials of substrates measured by cyclic voltammetry with compounds **105** to **110** against Swain-Lupton parameters. Results for R = OMe substrate are given in red in each graph.

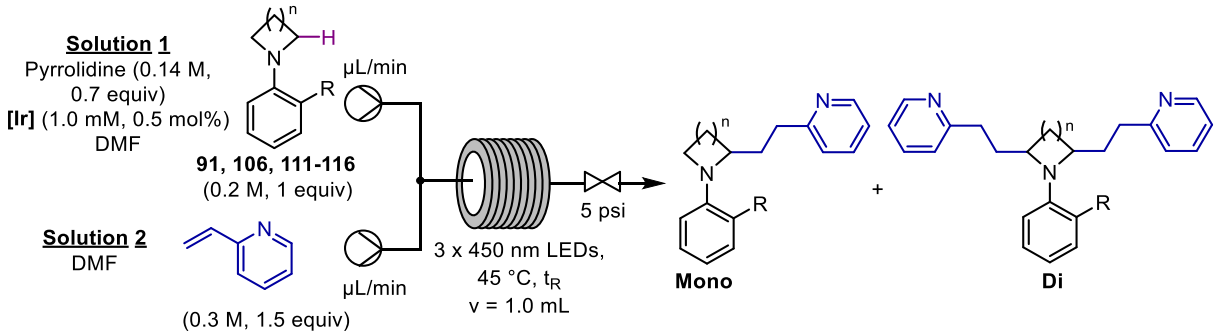
The f and r coefficients were variable across these linear regression models. The contribution from field effects was more significant than resonance in the case of rate and k_q, but not redox potentials. The linear regression model did not correlate as highly for reaction rate as with the redox potential and quenching rate k_q, which indicates other experimental effects, perhaps a steric component, influence the rate of the reaction which are not captured by the Swain-Lupton parameters.

The Hammett and Swain-Lupton analyses together shows that rate is well correlated and to a limited extent predictable using *N*-arylpyrrolidines with electron-ithdrawing substituents at the *para* position. Substrates with additional redox events within the scope of the reaction, such as with a *para*-methoxy substituent, do not match the observed trends. These results demonstrate that the kinetics of this C–H functionalisation reaction are affected by the electronics of the aryl group substituents and, in particular for electron-withdrawing groups, these rates trend with redox potentials and quenching rates. This supports the conclusions so far that SET to the *N*-arylpyrrolidine substrate is turnover limiting for substituents with negative Hammett constants σ_p.

2.4.2. Trends in heterocycles

Trends in nitrogen heterocycles were investigated in the same way as the aryl group substituents (Table 23). All tested heterocycles gave productive reactions, with the exception of aryl-morpholine.

Table 23: Data for different heterocycles.



Substrate	R group	Ring size	Yield (%)[a]			k_q (10^9, $M^{-1}.s^{-1}$)	Rate (a+2b) (mM/min)[b]	E_{pa} (V vs SCE)
			Mono	Di	Total			
		Ir catalyst	-	-	-	-	-	+1.21[c]
91	F	5	57	12	69	2.3	0.79	+1.13
111	F	4	49	8	57	2.0	0.40	+1.27
112	F	6	18	4	22	1.1	0.12	+1.39
113	F	6-morpholine	0	0	0	0.7	-	+1.27
106	H	5	36	44	80	3.2	1.55	+0.93
114	H	$N(Me)_2$[d]	-	52	-	3.3	1.76	+1.17
115	H	4	44	31	75	2.6	1.27	+1.22
116	H	6	35	15	50	2.3	0.57	+1.55

[a]Isolated yields given. [b]Rate of formation of (mono + 2di) products given. Rate extracted from profiles using 0 to 20 min as described in section 4.7.4. [c] Redox potential is standard reduction potential for $Ir^{III}*/Ir^{II}$, $E_{1/2}$. [d]Mono product was not isolated cleanly therefore no yield determined.

This analysis showed a clear trend in reaction profiles for the different heterocycles (Figure 33). Using both unsubstituted aryl-heterocycles, and 2-fluoro substituted aryl-heterocycles, substrate ring size had a strong effect on reaction kinetics in the order of ring size fastest to slowest: 5 > 4 > 6. As with the variation of aryl groups, with the exception of *N*-arylmorpholine **113**, the oxidation potentials of substrates with different ring sizes were correlated to the quenching rate k_q, and consequently reaction rate was correlated to the redox potentials and k_q.

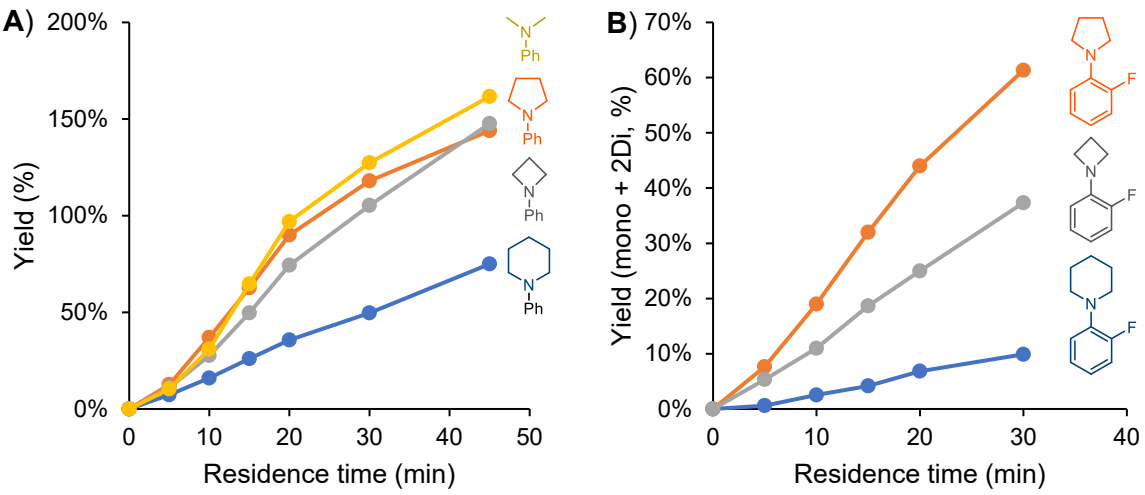


Figure 33: Profiles depicting product formation (concentration of mono + (2 × di)) of substrates with different ring sizes using either A) phenyl ring or B) 2-fluorophenyl ring.

Interestingly however, these correlations held true only when substrates with the same aryl group and different ring sizes were compared, and two linear trends were observed for the correlation between oxidation potential and k_q, and rate and redox potential: one for the *ortho*-fluoro substrates **91**, **111** and **112**, and one for the unsubstituted anilines **106**, **114**–**116** (Figure 34).

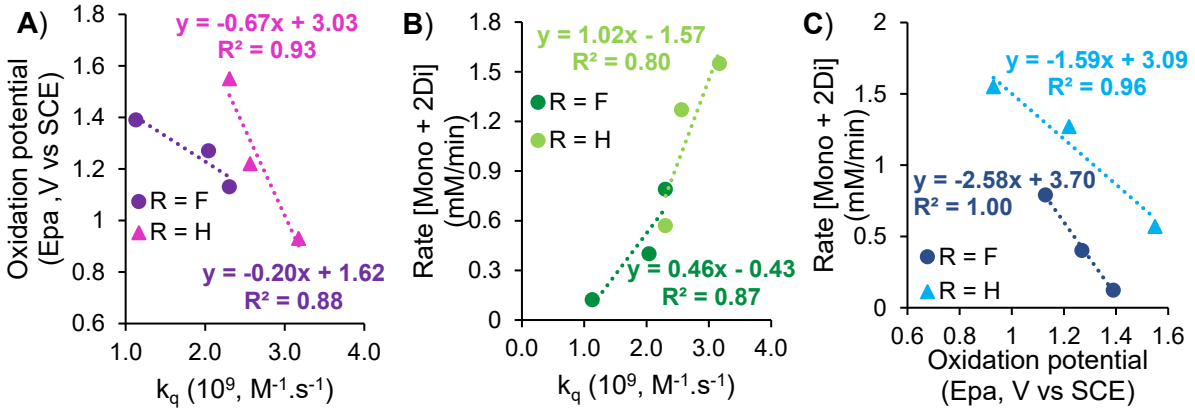


Figure 34: Linear correlations between A) oxidation potential and quenching rate k_q, B) reaction rate and k_q and C) reaction rate and oxidation potential, using heterocycle ring sizes 4, 5 and 6.

In each instance, the rates for different ring sizes trended the same way: with the fastest 5-membered pyrrolidine having the fastest k_q and lowest redox potential, then 4-membered azetidine, and the slowest 6-membered piperidine. The presence of two trends rather than a consistent correlation between redox potentials and k_q values (Figure 34A), or reaction rate and redox potentials respectively (Figure 34C), indicates that redox potentials on their own

are insufficient to predict reaction rate for this reaction. Contrastingly, reaction rate and k_q were more strongly correlated, and a plot including all datapoints from both aryl groups gave a linear regression R^2 value of 0.84. This indicates that is information in the k_q value which more readily describes reaction rate than redox potentials, and provides a means to determine trends between substrates. This also supports the SET between photocatalyst and amine substrate being turnover limiting.

2.4.2.1. Competition experiment

A competition experiment was undertaken to determine whether the differences in rate seen with different substrates translated to selectivity in product formation. Both *N*-arylpyrrolidine **91** and *N*-arylazetidine **111** were present in the reaction mixture in equimolar concentrations at the beginning of the reaction. The reaction profile is depicted in Figure 35.

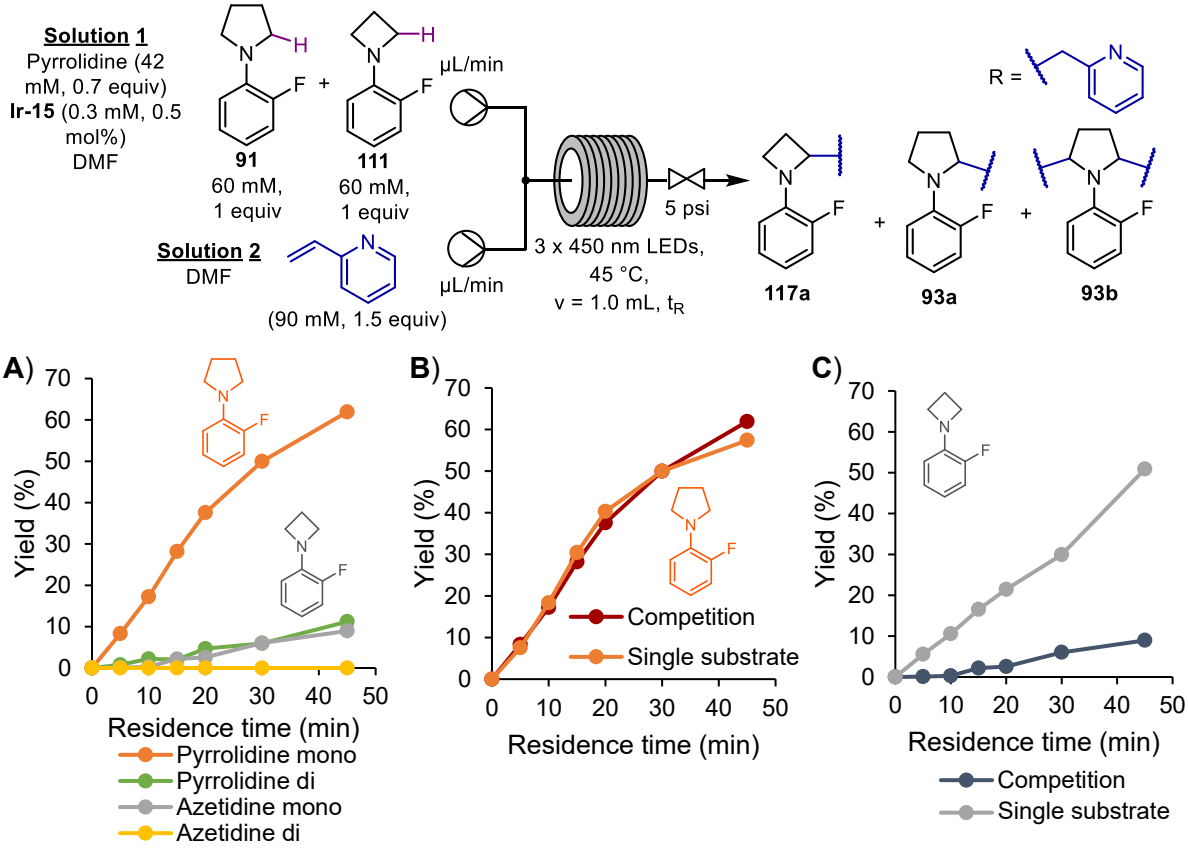


Figure 35: A) Competition experiment between phenyl pyrrolidine and azetidine. Difference in rate of formation of mono product in the competition experiment and when only B) substrate **91** and C) substrate **111** were present in the reaction mixture.

The rate of formation of the pyrrolidine product **93a** was much greater than that of any other products, with ratio of 60:10:10 **93a**:**93b**:**117a** (Figure 35A). This shows a marked degree of selectivity for the faster reacting substrate **91** over slower **111**. The rate of the pyrrolidine mono

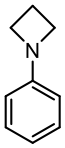
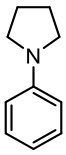
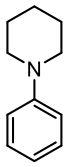
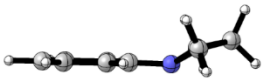
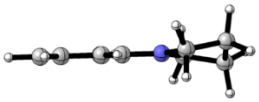
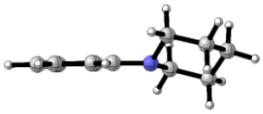
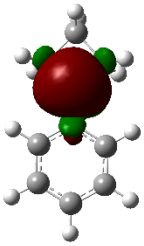
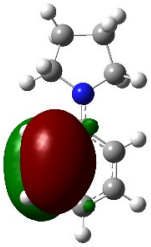
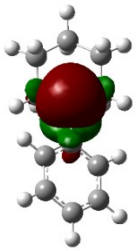
product **93a** formation in the competition experiment matched that observed when there were no other substrates present in the reaction mixture (Figure 35B) whilst the rate of formation of the azetidine product **117a** and **117b** was drastically reduced compared to when it was the only substrate (Figure 35C). This experiment demonstrates how important understanding the kinetics of reactions is for understanding selectivity, and shows how substrates reacting in isolation may behave very differently when there are multiple substrates in the same mixture.

2.4.3. Computational experiments: what controls redox potentials?

To gain a better understanding of the trends observed experimentally, computational studies were carried out in collaboration with C. Romain, who conducted all computational experiments, and analysed by myself and J. Bull. DFT calculations were carried out at ωB97XD/def2TZVP (cpcm = DMF) at level of theory.

To highlight the role of the *N*-heterocycle size (i.e. 4, 5 and 6-membered rings), three model compounds were considered: azetidine **115**, piperidine **106** and pyrrolidine **116**. Energy minimised geometries were determined for each structure with summary data in Table 24.

Table 24: Analysis of the energy minimised structures of neutral substrates.

Ring size	4  115 Azetidine	5  106 Pyrrolidine	6[a]  116 Piperidine
Molecular geometry of the optimised structure			
N Pyramidalisation (°)[b]	343.6	360.0	345.9
NBO analysis			
N–C bond length (Å)	1.37	1.36	1.40
Ionisation potential (eV)[c]	5.52	5.24	5.64

All geometry optimisations were carried out at wB97xD/Def2-TZVP (cpcm=DMF) level of theory. [a]Only the equatorial conformation has been considered. [b]Sum of the angles formed by the nitrogen atom connected to the three adjacent carbon atoms. [c]Calculated in the gas phase.

Only the most stable conformers were considered for each compound. One immediately noticeable aspect of these structures was the change of geometry of the heterocycle nitrogen (Table 24), with the pyrrolidine featuring almost a flat structure (i.e. the sum of the three angles formed by the nitrogen atom connected to the three carbons is almost 360 °).

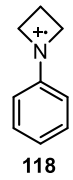
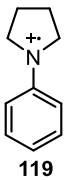
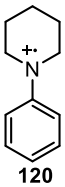
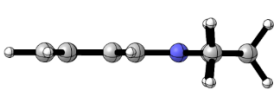
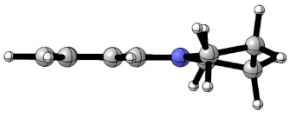
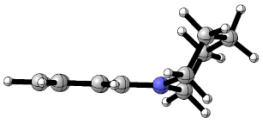
The degree of nitrogen pyramidalisation changed substantially between the 5-membered ring and azetidine or piperidine. The 5-membered pyrrolidine was virtually planar throughout the molecule, demonstrating an almost trigonal planar sp^2 nitrogen hybridisation. Moving to phenylazetidine and ultimately phenylpiperidine, the geometry around the nitrogen centre became more pyramidal. This increase in pyramidalisation correlates with an increase in C_{aryl}–N bond length, which together describes the increase in sp^3 character. A similar trend was observed by Bottini and Nash with regards to trends in 'resonance energy' for different *N*-phenylheterocycles, analysed by UV spectroscopy.[123]

These factors, together with the shape of the molecules, indicate a change in hybridisation of the nitrogen lone pair when changing ring size; the more planar the molecule, the more delocalised the nitrogen lone pair is into the aryl system, and the shorter the N-aryl bond

length. NBO analysis supported this explanation; no ‘lone-pair’ was observed on nitrogen for *N*-phenylpyrrolidine **106**, with electron density instead localised on the aryl group. The N-aryl bond was observed as almost a full double bond (antibonding character prevented formal double-bond assignment). The observed decrease in ionisation energy could be explained by delocalisation of the nitrogen lone pair into the aryl system, which would increase the energy of these electrons, and consequently decrease the energy required to remove one. Whilst ionisation energy is a thermodynamic descriptor, the trends in rates of these substrates observed experimentally correlate with these trends in heterocycle structure, suggesting that rate is, to an extent, controlled by the structure and bonding of the ground state nitrogen heterocycles.

Energy minimisation analysis was completed for the amine radical cations (Table 25) and for the carboncentred radicals (Table 26). The trends observed for both radical states were different to that observed for the neutral substrates: trends in N–C bond lengths increased from 4 < 5 < 6 membered rings.

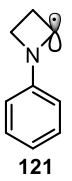
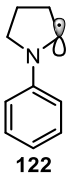
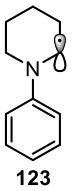
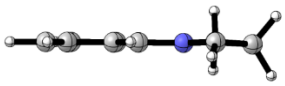
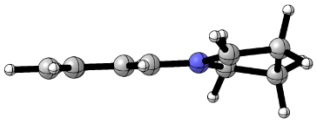
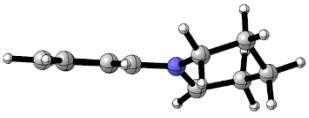
Table 25: Energy minimised structures of radical cations of each substrate.

Ring size	4  118 Azetidine	5  119 Pyrrolidine	6  120 Piperidine
			
N–C bond length (Å)	1.33	1.34	1.35
Wiberg bond index	1.37	1.36	1.34
Spin density N (e)	0.45	0.47	0.48

Note: data for piperidine has been included in the chair equatorial conformation.

Spin density on the nitrogen for the radial cations and carbon for the alkyl radicals also increased in the order of 4 < 5 < 6 membered rings. This order did not match any trends in reaction rates or catalyst quenching rates.

Table 26: Energy minimised structures of carbon centred radicals of each substrate

Ring size	4  121 Azetidine	5  122 Pyrrolidine	6  123 Piperidine
			
N–C bond length (Å)	1.37	1.38	1.39
Wiberg bond index	1.12	1.11	1.09
Spin density CH (e)	0.75	0.76	0.78

Note: data for piperidine has been included in the chair equatorial conformation.

2.4.4. Trends in acceptors

2.4.4.1. Experimental work

Given the data above with different *N*-heterocycle substrates, indicating that SET between the excited state photocatalyst and amine substrate was turnover-limiting, changing the acceptor was not initially expected to impact the reaction rate. However, on testing different acceptors,

it was immediately apparent that the reaction proceeded with vastly different experimental reaction rates depending on the acceptor used (Figure 36). *N*-Boc-methylacrylate (*N*-BocMA) formed the mono product as two diastereomers, whilst ethyl acrylate and 2-vinylpyridine formed mono and di-addition products. Figure 35 depicts concentration of (mono+2Di) products against time, in the case where only one product was formed, the mono is given.

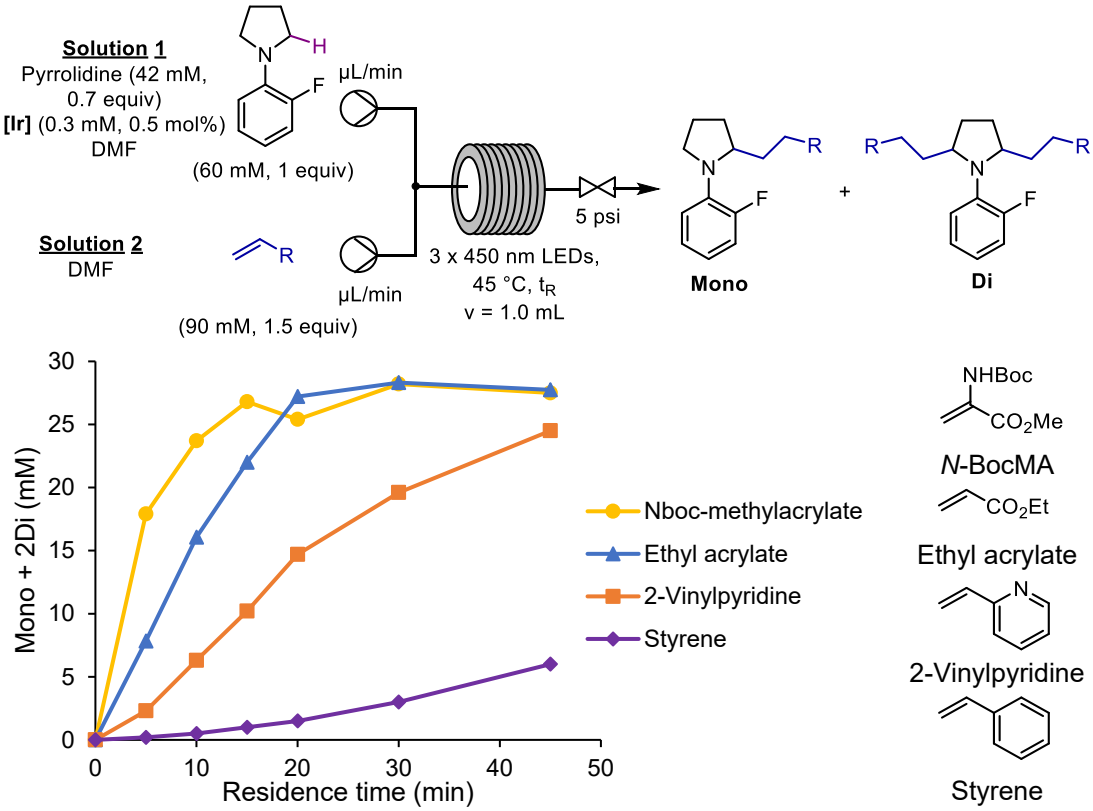


Figure 36: Profiles using different acceptors. Yields given as an average of three consecutive samples of flow output, calculated using ^{1}H NMR with a 10 s delay vs 1,4-dimethylterepthalate.

Different excess profiles were performed using variation in acceptor concentration, with styrene and ethyl acrylate as acceptors. The different excess profiles looked similar to the control profiles in both cases (Figure 37). However, it was not possible to provide reliable data or conduct full VTNA experiments due to difficulties in ^{1}H NMR analysis: the reaction with styrene proceeded very slowly and therefore would be prone to much larger error than the standard reaction. The reaction with ethyl acrylate, whilst being fast, had difficulties in finding a clear peak in the crude ^{1}H NMR spectra for di-addition analysis, therefore results were difficult to interpret. Computational studies were consequently used to investigate the effect of acceptor on the reaction and to help understand why different acceptors might lead to faster reactions when the acceptors themselves did not appear to feature in the observed rate equation (section 2.4.4.3).

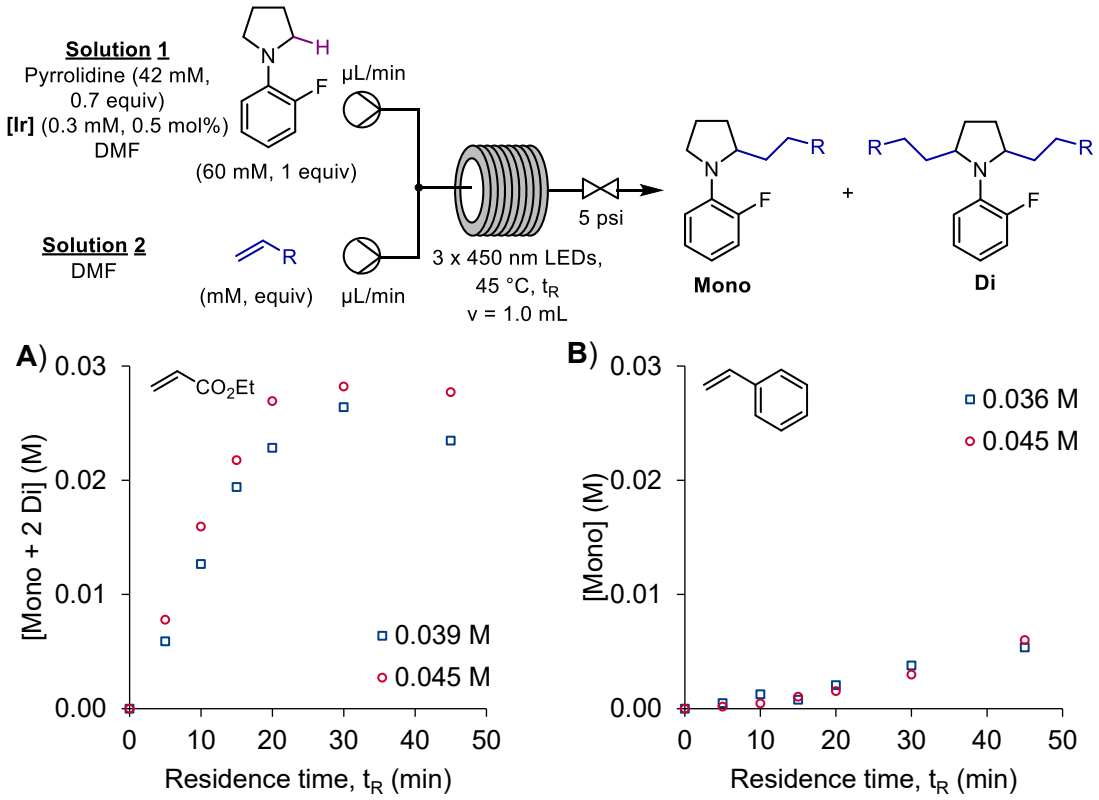


Figure 37: Profiles using standard and different excess concentrations of A) ethyl acrylate and B) styrene acceptor.

2.4.4.2. Kinetic isotope experiments

Kinetic isotope experiments (KIE) were undertaken with each of the acceptors to determine whether formation of the α-aminoalkyl radical with C–H bond breaking was turnover-limiting, and to investigate the reversibility of key steps in the reaction.

^{1}H NMR experiments identified there was no loss in deuteration at the α-NCD position in the starting material or the product, indicating that formation of the α-aminoalkyl radical is not reversible in this reaction, nor is the Giese addition. No deuterium incorporation was observed at the α-pyridine CH position, meaning that the proton (or in this case, deuterium) removed from the α-amine position is not the same proton that ends up at the α-pyridine position, instead perhaps from a different source other than the protonated (or in this case, deuterated) pyrrolidine base. Furthermore, the absence of any deuterium incorporation at this position precludes the presence of a chain-propagating 1,5-hydrogen atom transfer step to form either the mono- or di- products, further supporting SET from the excited photocatalyst as the substrate radical forming step in each case. It is likely that adventitious water present in the reaction may be responsible for some of the protonation of the product, as found in a similar Giese reaction by Woo and co-workers.[124]

The KIE analysis of rates of the standard reaction and deuterated reaction is depicted in Figure 38.

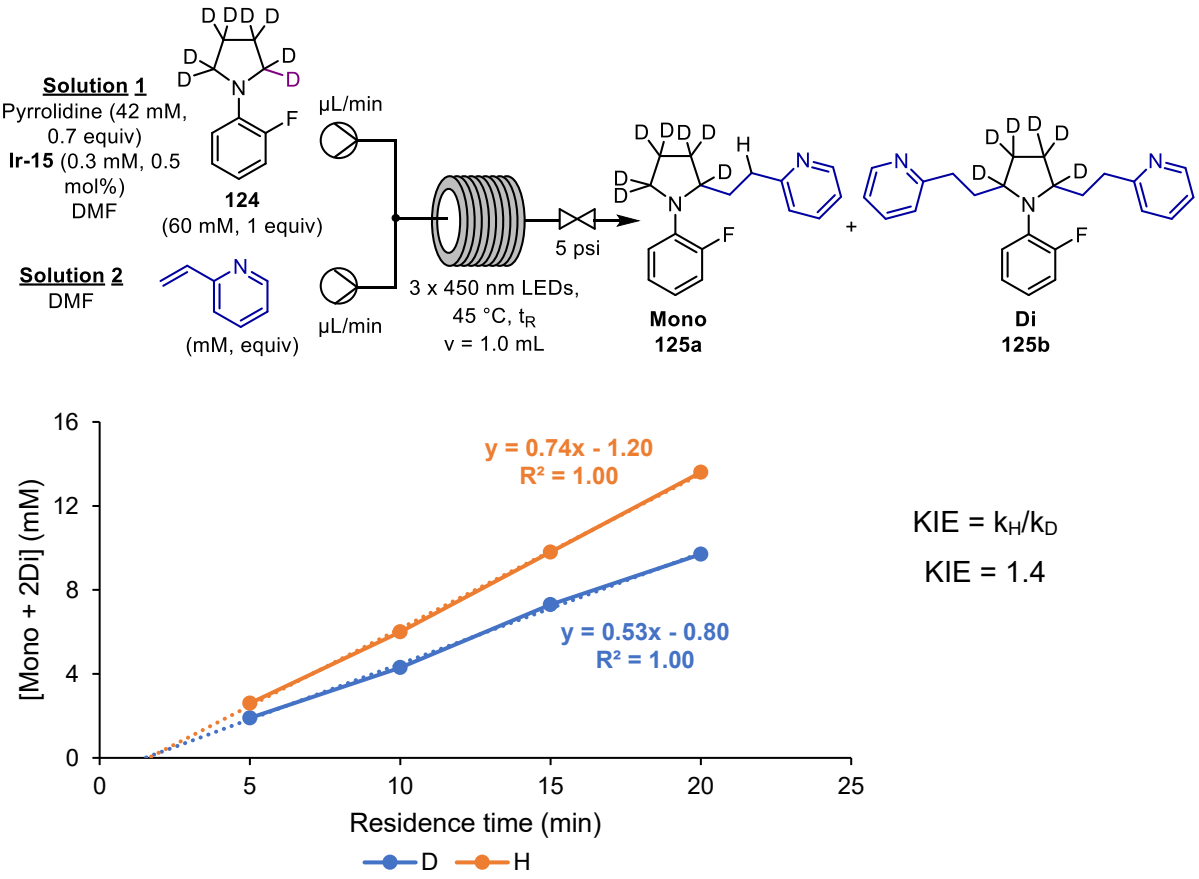


Figure 38: Kinetic isotope studies.

A KIE value of 1.4 is consistent with a secondary isotope effect, in which C–H bond cleavage is not turnover-limiting in the reaction. This matches the VTNA and substrate investigations indicating that deprotonation and rearrangement of the amine radical is not a turnover-limiting reaction step. Instead, a secondary isotope effect is consistent with turnover-limiting formation of the aminium radical cation. Hyperconjugation from the C–H or C–D bonds adjacent to nitrogen can stabilise the transition state and amine radical cation. In the reaction using deuterated substrate **124**, the C–D bonds alpha to nitrogen are stronger than the corresponding C–H bonds in protonated **91**, and therefore offer less stabilisation by hyperconjugation of the partially-filled nitrogen p-orbital.[125] This reduced stabilisation could account for a slower rate of reaction when using the deuterated substrate, and the observed KIE of 1.4 – giving a β-2° KIE. This is close to the KIE = 1.1 – 1.2 range typically observed for rate effects arising from hyperconjugation,

KIE analysis was also performed in the same manner using styrene and ethyl acrylate, respectively, as the acceptor, in place of 2-vinylpyridine. However, the same issues regarding

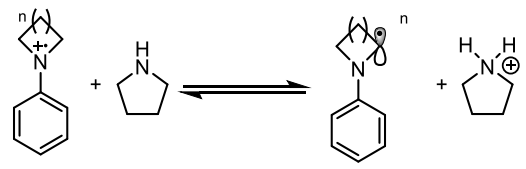
difficulties in quantifying the ^{1}H NMR data collected for styrene and ethyl acrylate was found here. Processing the control profiles and KIE profiles in the same way gave low KIE values similar to that when using 2-vinylpyridine (KIE = 0.5 for styrene, but likely to have a large error due to low concentrations over the measured timeframe, and 1.2 for ethyl acrylate).

2.4.4.3. Computational analysis

From here, we turned to the computational study performed by C. Romain to deepen understanding around this reaction. Density functional theory calculations were performed using Gaussian 15, at 298.15K and used the ωB97xD density functional, using the self-consistent reaction cavity continuum solvation model with DMF as the solvent. For reduction potentials, the M06-2X/def2-TVPD level of theory and SMD solvation model was used. For further detail on calculations see section 4.12.

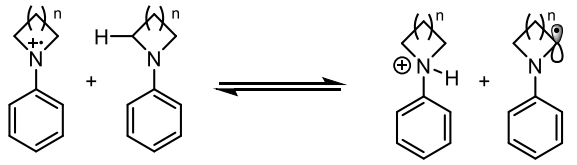
Subsequent steps to the initial SET were investigated, beginning with proton transfer and formation of the carbon-centred radical. There was no strong thermodynamic drive for proton transfer; which was consistent with the pK_a values of the different substrates (pyrrolidine pK_{aH} = 11.3 vs pK_a *N*,*N*-dimethylaniline radical cation ~ 9).[126] However, the equilibrium towards formation of the carbon-centred radical was less unfavoured as ring strain decreased: i.e. ΔG for formation of the carbon-centred radical from the amine radical cation ring size was in the order 4 > 5 > 6 (Scheme 26a). The transition state energy for each component was ≤ 9 kcal/mol, easily accessible at room temperature, and did not match the trend in reaction rates observed.

A)



n	Ring size	ΔG (kcal/mol)	ΔG‡ (kcal/mol)
1	4	+3.88	+9.13
2	5	+1.70	+9.33
3	6	+0.22	+7.70

B)

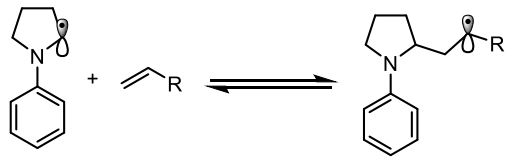


Scheme 26: A) Calculations for thermodynamic feasibility of radical deprotonation. B) Alternative proposed mechanism of α-aminoalkyl radical formation.

There is an alternative potential mechanism for aminium radical formation, which involves the aminium radical acting as a HAT agent with another molecule of substrate to form a second molecule of α-aminoalkyl radical and a protonated substrate molecule (which could be deprotonated back to the neutral molecule by the pyrrolidine base, Scheme 26B). The relative

pK_a of the species for *N*,*N*-dimethylaniline support the plausibility of this step, pK_{aH} for *N*,*N*-dimethylaniline = 5.2 and pK_a ~ 9 for the corresponding radical cation.[126] Whilst the observed secondary kinetic isotope effect suggests that if this mechanism were in play, it would not be turnover limiting (this step involves breaking of a C–H bond), it is a plausible method of carbon centred radical formation, and consistent with all the observed mechanistic data.

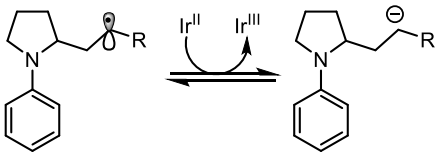
Investigations into the coupling step found that for each acceptor, addition of the carbon-centred radical into the acceptor was strongly thermodynamically favoured (ΔG > −10 kcal/mol) through a transition state accessible at ambient conditions ($\Delta G^{‡}$ < 13 kcal/mol, Scheme 27). VTNA data indicated the reaction was zero order in acceptor, and that this step would have a negligible effect on rate compared to the SET steps.



Entry	Acceptor	ΔG (kcal/mol)	$\Delta G^{‡}$ (kcal/mol)
1	Styrene	–12.82	+11.14
2	2-Vinylpyridine	–12.96	+9.37
3	Ethyl acrylate	–10.26	+7.82

Scheme 27: calculated ΔG and $\Delta G^{‡}$ values for addition into different radical acceptors.

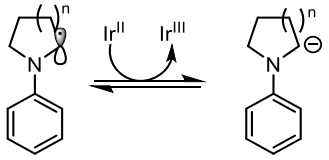
Redox potentials were calculated to investigate the energetics of the second single electron transfer event which forms the product anion (Scheme 28). Experimental values were not determined due to the difficulties with deprotonating at this position from the neutral molecule.



Entry	Acceptor	ΔG (kcal/mol)	E (V vs SCE)
1	Styrene	+4.7	−1.57
2	2-Vinylpyridine	−1.7	−1.30
3	Ethyl acrylate	−8.9	−0.98

Scheme 28: Calculated ΔG and calculated redox potentials for second single electron transfer. ΔG values use the experimental reduction redox potential for Ir^{III}/Ir^{II} −1.37 V.

Before coupling, reduction of the carbon centred radical to the anion was strongly thermodynamically disfavoured, with ΔG > +14 kcal/mol (Scheme 29) and redox potentials of ≥ 2.0 V. Coupling with the acceptor shifted the reduction potentials of the radicals to within the reduction window of the iridium catalyst (Scheme 28). The reduction potentials of the product radicals match trends in anion stability, predominantly determined by acceptor structure due to the position of the radical after coupling. This is less influenced by the chemistry of the nitrogen heterocycle and therefore ring size has little impact on this step.



Entry	Ring size	ΔG (kcal/mol)	E (V vs SCE)
1	4	+14.5	−2.00
2	5	+18.3	−2.16
3	6	+18.9	−2.19

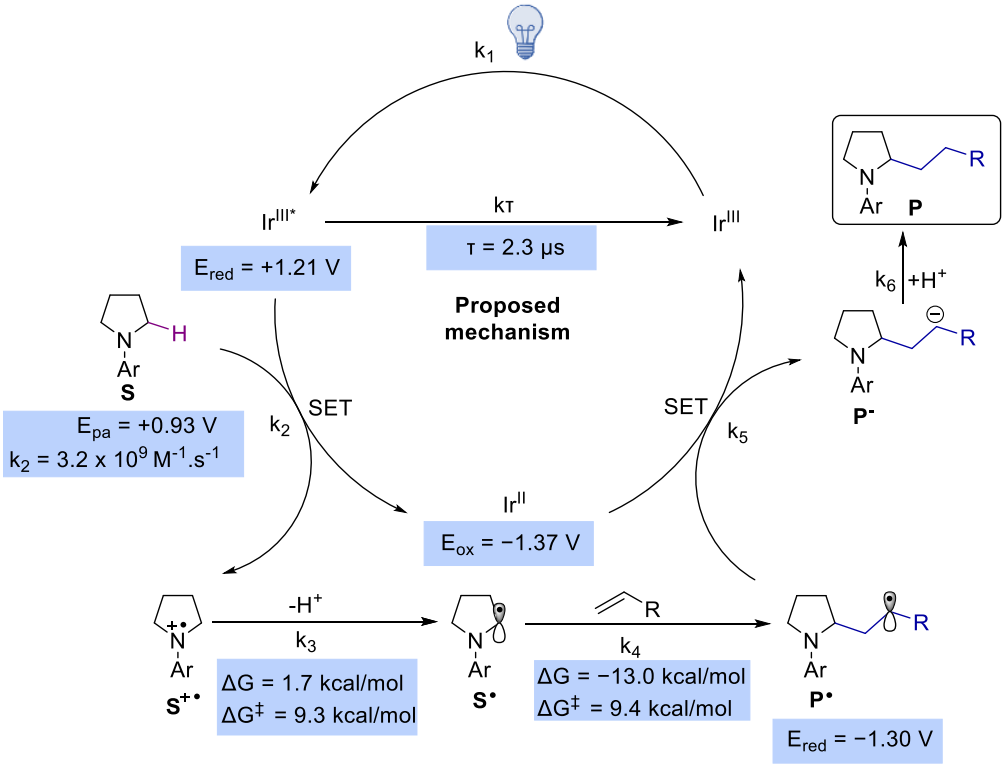
Scheme 29: Reduction potential of radical to anion before coupling.

A substrate coupled with ethyl acrylate as the acceptor has the most stable product anion compared with the other tested acceptors due to stabilisation as the enolate, and substrates with this acceptor have the least negative redox potentials. The enhanced stability of this enolate over 2-vinylpyridine or styrene anions may also be demonstrated in the product profiles of this reaction; when performing the reaction with ethyl acrylate in batch, a branched di-addition product formed, which could be due to addition of the product radical or anion into a second equivalent of ethyl acrylate. Conversely, 2-vinylpyridine only forms a symmetric di product formed from the mono product entering the catalytic cycle as a substrate, and no anion reactivity is observed. The trends in product reduction potentials matched the trends in reaction rates observed using different acceptors.

Previous work from our group on a related photoredox reaction of oxetane radicals adding into Giese acceptors showed that a branched di-addition product was formed by a polarity mismatched radical addition of a similar product radical into another equivalent of ethyl acrylate.[98] Further mechanistic investigation would be required to determine whether the formation of a telomer di-addition product in this reaction of N-phenylpyrrolidines with ethyl acrylate was through radical or anion addition into the second molecule of acceptor.

2.4.5. Deriving a reaction rate law

The data collected throughout this investigation have provided a several insights into the kinetics of this photoredox catalysed C–H functionalisation reaction. In this section the data is unified in a proposed kinetic model for this reaction. The mechanism and kinetic constants for each step in the reaction are described in Scheme 30, with appropriate redox potentials and rate data from previous sections provided as a summary.



Scheme 30: mechanistic model. Data in blue boxes is given for *N*-phenylpyrrolidine as substrate and 2-vinylpyridine as acceptor. All redox potentials are given in V vs SCE.

From the experimental and computational data available, a few simplifications can be made from the more complete proposed mechanism. Firstly, this reaction has been assumed to be a closed catalytic cycle reaction, with no contributions from radical chain propagation steps.

Quantum yield experiments are commonly used to identify radical chain vs closed cycle photocatalytic reactions, with actinometry used to determine the amount of light being received by the reaction.[127] Whilst there are methods for batch reactions under low light intensities, usually using ferroxialate actinometry, and there are increasing bespoke methods for flow systems,[128] there was insufficient time and readily available methods to determine the quantum yield for this reaction in this case. Quantum yield information would provide more conclusive evidence regarding the presence of a radical chain mechanism.

However, the results of the VTNA investigation showed a consistent increase in order in catalyst as the reaction concentration decreased, which points to a role of catalyst in the turnover limiting step throughout the reaction. This suggests that if there is a radical chain contribution, it is not the predominant mechanism in this reaction. Furthermore, the possibility of a radical chain step in which the product radical abstracts a hydrogen from the substrate to form carbon centred radical **S•** was deemed unlikely due to the absence of deuterium incorporation adjacent to the pyridine (Figure 38), although it is possible that the mechanism could change when using a deuterated substrate. No dimerised radical products, either **S-S**, **S-P** or **P-P** coupled products were present in the reaction (Figure 39).

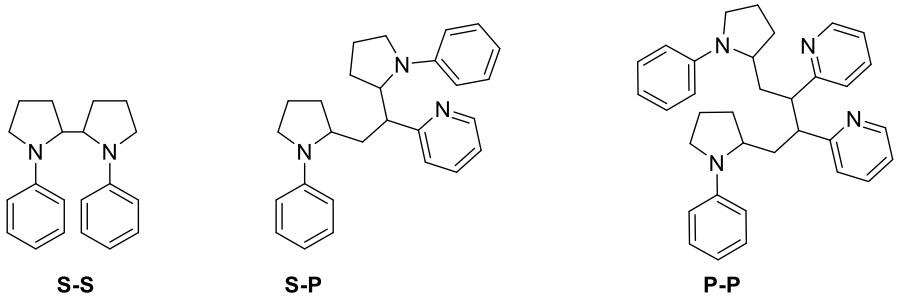


Figure 39: Possible radical-radical coupling products were not observed in the reaction.

Light intensity is assumed to be constant throughout the reaction, as the reactor geometry and light source used remain unchanged throughout the reaction, and at steady-state the catalyst concentration is unchanging; hence, the equilibrium between excited state catalyst Ir* and ground state Ir^{III} can be described using an equilibrium constant, K_{hv}. The proportion of ground state Ir^{III} molecules which form the excited state on irradiation is dependent on light intensity and light transmittance through the solution, and the processes by which the electron can decay back to the ground state are not the same pathway as that forming the photocatalyst excited state. As discussed in section 1.3.3, formation of the catalyst excited state requires formation of a singlet excited state following excitation to a triplet excited state and intersystem crossing. This triplet excited state can and does decay back to ground state through phosphorescence, and this is described by k_T, or the excited state lifetime. For simplicity, the equilibrium constant between Ir^{III} and Ir^{III}* will be described as K_{hv} and encompass all the possible formation and decay pathways which affect formation of Ir*.

The next simplification involves formation of carbon-centred radical **S•**. Firstly, whilst computational experiments determined that the radical deprotonation to form **S•** from $\mathbf{S^{+\bullet}}$ was slightly endergonic, the rate of this step will be influenced by the relative concentrations of either species. Even if all the photocatalyst present in the reaction was present in the excited state, which would be a gross overestimate of the true concentration, the pyrrolidine base is

present in 0.7 equiv, or 140 times the concentration the amine radical cation could be. This is not only a vast excess but an essentially unchanging excess throughout the reaction, and amounts to 'flooding conditions'. It is therefore reasonable to consider the rate of formation of $\mathbf{S}^{\bullet}$ from $\mathbf{S}^{+\bullet}$ to be much faster than the formation of $\mathbf{S}^{+\bullet}$ from **S**, and to have a negligible contribution to this rate law.

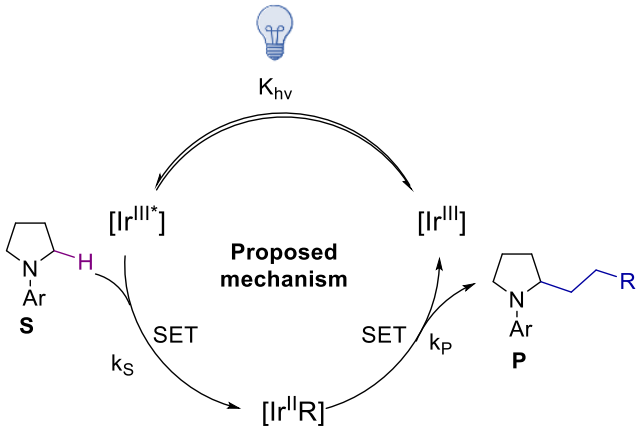
Computational experiments have shown that there is a strong thermodynamic driving force for formation of the product radical $\mathbf{P}^{\bullet}$, through a transition state accessible at room temperature. Furthermore, the acceptor was not found in the power law determined by VTNA (see section 2.3.1, equation 10), identifying that this step did not affect turnover rate within an acceptor series. Combining all these pieces of evidence, rate of formation of $\mathbf{P}^{\bullet}$ from $\mathbf{S}^{\bullet}$ is expected to be much faster than the rate of formation of $\mathbf{S}^{+\bullet}$ from **S**, and we can consider all radical species to be present as $\mathbf{P}^{\bullet}$. For clarity, radical species together will be referred to as **R**.

Additionally, as the reaction concentration is very low, the proportion of radical intermediates and Ir^{II} is therefore very low, and the concentration of **R** must be equal to Ir^{II} as they are formed and consumed in the same steps. The intermediate species Ir^{II} and **R** will therefore be considered together as a 'caged' species in the kinetic model, $\mathbf{Ir^{II}R}$.

We have assumed both single electron transfer steps are non-reversible. It is highly disfavoured to reform an excited state, which would be the reverse reaction of formation of $\mathbf{S}^{+\bullet}$, therefore this is assumed to be negligible. Similarly, it would be disfavoured to form a highly reactive organic radical intermediate species from a neutral or anionic molecule, therefore SET between $\mathbf{P}^{\bullet}$ and Ir^{II} is assumed to be essentially irreversible. As the protonation of the product anion is outside the catalytic cycle and base is not present in the observed power law, this off-cycle step is considered to be negligible to the rate and has been discounted from the model.

However, there is a possibility that there could be back electron transfer (BET) from the formed radical species to the Ir^{II} species to form the ground state Ir^{III}. BET has been found to limit the quantum efficiency of photoredox reactions.[129] The effects of BET have been excluded from this model; however, this is likely to be an oversimplification of the system. If BET is significant in this reaction, the Stern-Volmer derived k_2 value (3.2×10^9 M-1 s^{-1}) would be an overestimate of the effective rate constant for this step. Whilst not achieved in the timeframe of this project, transient absorption spectroscopy could be used to identify the contribution of BET to this reaction mechanism.

These considerations and assumptions together have led to a us proposing a simplified mechanism (Scheme 31), which can be described using a quasi-equilibrium approximation. This was solved using the product forming step (equation 16), solving for the concentration of Ir^{III} based on the description of formation of other catalytic species in equation 17, and the catalyst mass balance (equation 18), to obtain the reaction rate law (equation 19).



Scheme 31: Simplified kinetic model.

$$Rate = k_p[Ir^{II}R] \tag{16}$$

$$[Ir^*] = K_{hv}[Ir^{III}],\ [Ir^{II}R] = k_S[Ir^*][S] \tag{17}$$

$$[Ir]_T = [Ir^{III}] + [Ir^{II}R] + [Ir^*] \tag{18}$$

$$Rate = \frac{k_P k_S K_{hv}[S][Ir]_T}{1 + K_{hv} + k_S K_{hv}[S]} \tag{19}$$

The numerator of equation 19 describes the driving force for this reaction as a feature of the light properties of this reaction, K_{hv}, the rate of substrate oxidation, k_S, and the rate of radical reduction to obtain product P, k_P, and the concentration of the substrate, photocatalyst and light intensity. The denominator describes the states of the catalyst as either in the ground state as Ir^{III} (signified by 1), the excited state as Ir^{III*} ($Ir^{III*} = K_{hv}$) or the reduced state Ir^{II} ($Ir^{II} = k_s K_{hv}[S]$).

To determine how this system responds to light intensity, it becomes helpful to interrogate K_{hv} under the quasi-equillibrium approach. We defined this as the ratio between excitation of a molecule to form the excited, triplet state (k*) and the rate of excited state decay, termed k_τ. The rate of decay of the excited state, k_τ is proportional to the inverse of the excited state lifetime, a known quantity for most commercial photocatalysts, and 2.3 μs in this case,

therefore K_{hv} can be expressed in terms of excited state lifetime τ (equation (20). The rate constant for decay is therefore a feature of the photocatalyst and is unchanging throughout a reaction.

$$K_{hv} = \frac{k^*}{k_\tau} \propto k^* \tau \tag{20}$$

The kinetics of photocatalyst excitation have been studied in a very detailed report by Bernhard and co-workers in 2022. [130] The authors identified that the rate of excitation can be considered as the product of the incident irradiation k_0 (in Einsteins per second) and the fraction of light absorbed by the photocatalyst, Φ_{hv}, a feature of light transmittance through the solution. Therefore, the rate constant for the rate of excitation, k* is proportional to the light intensity and transmittance of light through the solution (equation 21). Combining equations 20 and 21, K_{hv} is consequently proportional to light intensity, light transmittance through the solution and photocatalyst excited state lifetime (22).

$$k^* \propto k_0 \Phi_{hv} \tag{21}$$

$$K_{hv} \propto k_0 \Phi_{hv} \tau \tag{22}$$

Furthermore, if we consider that every excited state molecule formed either decays back to ground state or reacts on in the mechanistic cycle, K_{hv} can also be expressed as quantum yield, i.e. the ratio of molecules of product formed to photons absorbed. Whilst not measured in this reaction due to constraints of time and limited applications of general actinometers to continuous flow, quantum yield is a useful quantity with which to optimise and model the kinetics of photoredox reactions.

At high light intensities, especially high light intensities relative to the catalyst concentration when transmittance is also high, K_{hv} will be large and the rate equation 19 can be simplified to equation 23.

$$K_{hv} \gg 1, \qquad Rate = k_P k_S [S][Ir]_T \tag{23}$$

Under these high light intensity conditions, the reaction is first order with respect to substrate [S] and with respect to the total catalyst concentration $[Ir]_T$, as observed in the power law for this reaction determined by VTNA. Whilst the acceptor is not included in the rate law, the identity of the acceptor influences the rate of reaction through changing the reduction potential of the product radical, and therefore k_P, providing this control over the reaction rate. As it has been observed experimentally that changing the substrate concentration and the identity of

the acceptor result in measurably different reaction rates, the magnitude of k_S and k_P are likely to be similar, with neither dominating the kinetics of this reaction.

Under low light intensity, K_{hv} becomes small and the rate equation 19 can be simplified to equation 24. Here, no rate dependency on the substrate concentration is observed.

$$K_{hv} \ll 1, \qquad Rate = k_P K_{hv} [Ir]_T \tag{24}$$

The rate in this instance becomes proportional to K_{hv} and catalyst concentration. As described in equation 12, K_{hv} is proportional to light intensity and transmittance of light through the solution. As discussed in the introduction section 1.4.1, transmittance is described by the Beer-Lambert law. K_{hv} is therefore by affected by light intensity and factors which affect transmittance: reactor geometry and catalyst concentration. This describes the two-fold effect of catalyst concentration on the rate of this photoredox reaction. Increasing catalyst concentration can increase the rate of reaction as observed in the $[Ir]_T$ term in equation 24. However, increasing catalyst concentration can also decrease transmittance of light through the solution, dependent on the reactor geometry and light intensity. This would decrease Φ_{hv}, decrease K_{hv} and lower the rate of reaction.

3. Conclusions and future work

Selective C–H functionalisation of nitrogen heterocycles is an increasingly desirable goal, in particular methods to generate new C(sp^3)–C(sp^3) centres. Photoredox methods have expanded the range of reactions possible, opening up new possibilities for nitrogen heterocycle synthesis. An explosion of photoredox methods for a variety of transformations has demonstrated the power of visible light-mediated chemistry often used on discovery scale. However, mechanistic understanding has lagged behind synthetic discovery. For photoredox methods to become a useful part of a synthetic chemist's toolkit at any scale, kinetic investigations are essential. This work has shown that understanding the kinetics of photoredox reactions is not facile, but crucial for gaining useful insights into the reaction mechanism.

This work has involved delving into the mechanism of the photoredox catalysed C(sp^3)–H functionalisation reaction of nitrogen heterocycles. The developed batch reaction compliments existing Giese literature using a readily commercially available iridium catalyst commonly used for such transformations. Care has been taken to identify sources of reaction variability; a sensitivity screen demonstrated that whilst reaction variability exists around ±10% yield, the reaction was tolerant of a range of different conditions that might be encountered when reproducing this reaction in another lab.

Flow chemistry was found to be a powerful tool for generating data from photoredox reactions, both as a way to control variables and increase reproducibility, as well as increasing light intensity and consequently reaction throughput. Specifically, using flow chemistry allowed the development of a non-light-limited reaction, and an analytical system which was consequently used to obtain rate data. Whilst *ex situ* analytical techniques such as cyclic voltammetry and Sten-Volmer analysis are very useful for understanding certain reaction parameters, these must be paired with an understanding of how these relate to the reaction itself. Electrochemical methods are complimentary to, but distinct from, photoredox methods and allow different processes such as two-electron oxidation of amines. Kinetic profiles and visual kinetic analysis have allowed direct probing of the reaction which is needed to contextualise the *ex situ* measurements.

This work has increased understanding of the kinetics of the photoredox catalysed C(sp^3)–H functionalisation of nitrogen heterocycles. Systematic investigations into changes in substrates and acceptors have led to insights into the selectivity of this C–H functionalisation reaction. Reaction rate was controlled by the two redox events in the catalytic cycle, in a way which was measurable, and to some extents predictable, based on the redox potentials and

quenching rates of substrates. Proposal of a kinetic model has combined the experimental findings into mathematical expressions, determining that the rate was set by a combination of redox potentials according to the equations below. The identity of both reactants, therefore, has rate implications, with k_S affected by properties of the nitrogen heterocycle, and k_P affected by the ease of reduction of the product radical after coupling with the acceptor, which depends on the nature of the acceptor. Thus, the identity of the acceptor affects reaction rate despite the concentration of acceptor not appearing in the derived rate equation. Additionally, at high light intensity, as in the system specifically developed in this project, the reaction rate is dependent on substrate concentration and the rate of redox events. At low light intensity, the reaction becomes mainly dependent on light intensity.

$$Rate = \frac{k_P k_S K_{hv}[S][Ir]_T}{1 + K_{hv} + k_S K_{hv}[S]}$$

$$K_{hv} \ll 1, \qquad Rate = k_P K_{hv}[Ir]_T$$

$$K_{hv} \gg 1, \qquad Rate = k_P k_S[S][Ir]_T$$

This investigation also demonstrated how specific an individual photoredox reaction is to the set-up being used, and therefore the importance of undertaking experiments to determine the light-dependence of the reaction, and to take this into consideration when interpreting mechanistic experiments.

Future work in this area would consist of expanding the data set of substrates and acceptors. There are numerous trends which unfortunately could not be investigated in the timeframe of this project, which would broaden understanding about the reaction rate and selectivity: these include, but are not limited to, selectivity when there are multiple sites of potential reactivity, either from multiple aryl-heterocycles or radical precursors known to be photoredox active, and different aryl or benzylic systems (Figure 40).

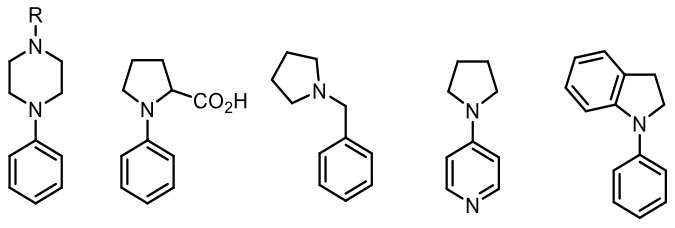


Figure 40: Proposed extended scope.

Furthermore, competition experiments would add an additional dimension to this work, with the aim towards not only predicting the most reactive site in a complex molecule, but also the

product distribution. Competition experiments would provide an indication of the extent to which the rate of functionalisation of a less reactive C–H bond is suppressed in the presence of a more active one. Transient absorption spectroscopy to investigate back electron transfer and quantum yield experiments would also be useful to further support mechanistic discussion.

More broadly, further kinetic investigations in the field of photoredox catalysis will allow the applicability of these techniques to be expanded from predominantly discovery and academic chemistry to larger scales. Reliable kinetic models are required to give confidence regarding the reproducibility of reaction rate and impurity profiles, and detailed work of this nature will therefore help extend the reach of photoredox catalysis.

4. Experimental details and Characterisation data

4.1. General experimental considerations

Non-photoredox batch reactions were conducted under an inert, argon atmosphere in oven- or flame-dried glassware using standard techniques. Photoredox catalysts were stored in an amber desiccator when not in use. Anhydrous solvents were obtained following filtration through drying columns (DMF, MeCN). Photoredox reactions were prepared in a fumehood with the light off, and orange plastic covering the front of the fumehood. Any solutions containing photocatalyst were stored wrapped in foil. Purification by flash column chromatography was performed over 230-400 mesh silica. Thin layer chromatography (TLC) was performed using pre-treated, glass backed silica plates and visualised using aqueous UV absorbance (254 nm) and phosphomolybdic acid stain.

NMR spectroscopy was conducted using Bruker 400 or 500 MHz spectrometers. The frequency used for each NMR spectrum is included in the compound assignment (^{1}H NMR recorded at 400 or 500 MHz, ^{13}C NMR recorded at 101 MHz or 126 MHz; ^{19}F NMR recorded at 377 MHz). For ^{1}H NMR spectra, proton shifts (δ) are recorded in parts per million (ppm) compared with tetramethylsilane with the protic solvent resonance as internal standard ($CDCl_3$: δ = 7.27 ppm). Data are reported as follows: chemical shift, multiplicity (s = singlet, d = doublet, t = triplet, q = quartet, m = multiplet), coupling constant (*J,* recorded in Hz), integration, assignment. For ^{13}C NMR spectra, proton decoupled chemical shifts are recorded in ppm compared with tetramethylsilane using solvent resonance as the internal standard ($CDCl_3$: δ = 77.16 ppm). Data are reported as follows: chemical shift, multiplicity, integration, assignment.

Assignments of ^{1}H and ^{13}C spectra were based on analysis of δ and *J* values along with COSY, HMQC and HMBC as required. ^{19}F NMR spectra were recorded with proton decoupling, and were referenced to $CFCl_3$ automatically by the spectrometer.

Infrared spectra (ν_{max}, FTIR ATR) were recorded using an Agilent Carey 630 FTIR spectrometer and recorded in wavenumber (cm^{-1}) (st = stretch). High resolution mass spectrometry (HRMS) analyses were obtained through the Imperial College mass spectrometry service. HRMS analyses were performed using electrospray ionisation (ESI) using a Waters LCT Premier (ES-ToF) equipped with an ESI source operated in positive or negative ion mode, electron ionisation (EI) performed using a Micromass Autospec Premier/Agilent HP6890 GC, or APCI performed using a Thermo Scientific Q-Extractive/Dionex Ultimate 3000 using an ASAP to insert samples into the APCI source operated in positive or negative mode. The software used was either MassLynx 4.1 or Bruker

Daltonics DataAnalysis 4.0. Please note, MassLynx 4.1 software does not account for loss of the electron and all the calibrations/references are calculated accordingly: $[M+H]^+$ was detected and the mass was calibrated to output [M+H]. In the cases where this software was used, the HRMS is reported as [M+H].

Melting points were obtained using an Optimelt MPA100 melting point apparatus with open glass capillaries and are uncorrected.

Data for VTNA, same excess and reaction profiles for substrate comparisons can be found at the Imperial College London Data Repository, DOI: 10.14469/hpc/13406, https://data.hpc.imperial.ac.uk/resolve/?doi=13406&access=z7gy-h4cq. Access code: z7gy-h4cq.

Reagents

Reagents were obtained from commercial suppliers if the synthesis is not otherwise stated. All volatile alkenes were distilled before use and stored at –18 °C prior to use.

- All volatile alkenes were distilled in the dark under vacuum, sealed with a septum and stored in the dark at –18 °C under argon. Alkenes were stored for a maximum of 1 month before being replaced.
- $Ir[dF(CF_3)ppy]_2(dtbbpy)PF_6$ (**Ir-15**) was purchased from Sigma-Aldrich (CAS: 870987-63-6, product code: 747793-100MG, purity not given) for some initial batch experiments, or Strem Chemicals (CAS: 870987-63-6, product code: 77-0425, purity: 99%) and used without further purification. No differences were seen between batches, the Strem Chemicals batch was used for all flow and kinetic experiments, and some batch experiments. Between uses the photocatalyst was stored in an amber, blue-light blocking desiccator.
- 1,2,3,5-Tetrakis(carbazol-9-yl)-4,6-dicyanobenzene (4CzIPN) was prepared by J. Rojas.
- 1,8-Diazabicyclo[5.4.0]undec-7-ene (DBU) was purchased from TCI (CAS: 6674-22-2, part number D1270), distilled under vacuum, sealed with a septum and stored at –18 °C under argon. DBU was stored for a maximum of one month before being replaced.
- Pyrrolidine was purchased from Sigma Aldrich (CAS: 123-71-1, part number P73803), distilled under vacuum, sealed with a septum and stored in the dark at –18 °C under argon. Pyrrolidine was stored for a maximum of one month before being replaced.
- 1,3,5-Trimethoxybenzene was purchased from Sigma Aldrich (CAS: 621-23-8, product number: 138827 and used without further purification.
- 1,4-Dimethylterepthalate was purchased from (CAS: 120-61-6, product number: T0015) and used without further purification.

4.2. Batch photoredox reactions

4.2.1. Batch photoredox reactor reaction set-up

Batch photoredox reactions were conducted in an EvoluChem PhotoRedOx Box TC™ (Temperature Controlled) photoredox reactor purchased from HepatoChem. Reactions were run in 4 mL vials (product code: 854190, SigmaAldrich) with a thickness of 1 mm which were sealed with screwcaps with PTFE/silicon septa (product code: SU860078, Sigma-Aldrich), placed in the sample holder of the photoredox reactor (see Figure 41). The reactions were illuminated by an EvoluChem P201-18-2 450 to 455 nm LED light source screwed into the holder at the back of the photoreactor, shining into a mirrored cavity. The vial holder suspends the vials in this same mirrored cavity. The temperature of all reactions was controlled using a heated bath circulator unit (Fisherbrand™ Isotemp™ model 5150 H7), connected to the photoredox reactor inlet on one side of the of the reactor and an outlet on the other, using tubing and secured with hose clips. This allowed the mirrored cavity to be filled with continuously replenishing water of a constant temperature. The reactor was sat on a stirrer hotplate, and reactions were stirred at 1000 rpm using this hotplate.

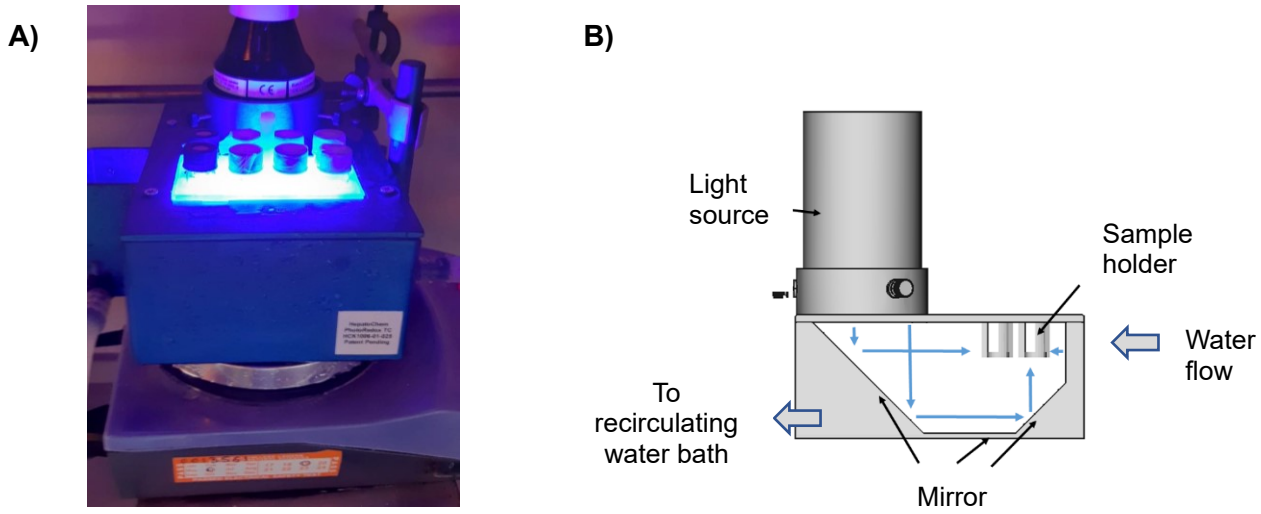


Figure 41: A) Photograph of temperature controlled photoredox reactor running 8 reactions. B) Schematic of the Hepatochem photoredox reactor showing mirror set up, figure adapted from Hepatochem.[99]

4.2.2. Batch experimental detail

General procedure A for batch reactions with solid bases

The recirculating water bath was set to 25 °C unless otherwise specified, and turned on to pre-heat the photoreactor to the desired temperature. This remained on for the duration of the reaction. *N*-(2-Fluorophenyl)pyrrolidine (33 mg, 0.2 mmol, 1.0 equiv) was added to an oven-dried 4 mL vial followed by $Ir[dF(CF_3)ppy]_2(dtbbpy)PF_6$ (2.2 mg, 0.002 mmol, 1 mol%) and base (either 0.2 mmol, 1 equiv or 0.14 mmol, 0.7 equiv) sequentially. The vial was sealed using HPLC lids containing septa, placed under argon and dry DMF (2 mL, 0.1 M) was added. The vial was sparged with Ar for 1 min and charged with 2-vinylpyridine (32, 0.3 mmol, 1.5 equiv). The vial was placed in the photoreactor, stirred at 1000 rpm, and the 450 nm LED light switched on. After 24 hours of irradiation, the light was switched off, the mixture was filtered over celite and concentrated *in vacuo*. 1,3,5–Trimethoxybenzene was added to the crude mixture (ca 0.04 mmol, 0.2 equiv, exact mass recorded) and yield determined by ^1H NMR spectroscopy with a 20 s delay.

In each instance, the change to these standard conditions was described in the reaction conditions reported in section 2.1. Occasionally, reactions were conducted in dichloromethane instead of DMF, as explained in section 2.1.4.1.

General procedure B for batch reactions with liquid bases

The recirculating water bath was set to 25 °C unless otherwise specified, and turned on to pre-heat the photoreactor to the desired temperature. This remained on for the duration of the reaction. *N*-(2-Fluorophenyl)pyrrolidine (33 mg, 0.2 mmol, 1.0 equiv) was added to an oven-dried 4 mL vial followed by $Ir[dF(CF_3)ppy]_2(dtbbpy)PF_6$ (2.2 mg, 0.002 mmol, 1 mol%). The vial was sealed using HPLC lids containing septa, placed under argon and dry DMF (2 mL, 0.1 M) was added. The vial was sparged with argon for 1 min and charged with base (either 0.2 mmol, 1 equiv or 0.14 mmol, 0.7 equiv) and 2-vinylpyridine (32, 0.3 mmol, 1.5 equiv). The vial was placed in the photoreactor, stirred at 1000 rpm, and the 450 nm LED light switched on. After 24 hours of irradiation, the light was switched off, the mixture was filtered over celite and concentrated *in vacuo*. 1,3,5–Trimethoxybenzene was added to the crude mixture (ca 0.04 mmol, 0.2 equiv) and yield determined by ^1H NMR spectroscopy with a 20 s delay.

In each instance, the change to these standard conditions was described in the reaction conditions reported in section 2.1. Occasionally, reactions were conducted in dichloromethane instead of DMF, as explained in section 2.1.4.1.

Testing reproducibility in the photoreactor

Using K_3PO_4 as base: The recirculating water bath was set to 40 °C and turned on to pre-heat the photoreactor to the desired temperature. A stock solution was made using *N*-(2-fluorophenyl)pyrrolidine (75 mg, 0.47 mmol), $Ir[dF(CF_3)ppy]_2(dtbbpy))PF_6$ (5.0 mg, 0.004 mmol, 1 mol%) and dry DMF (4.7 mL, 0.1 M w.r.t. amine). The solution was sparged with argon for 5 mins and charged with 2-vinylpyridine (70 µL, 0.65 mmol, 1.5 equiv), then mixed. Potassium phosphate tribasic (21 mg, 0.1 mmol) was added to 4 separate oven-dried vials, the vials were then sealed and placed under argon. The stock solution (1 mL, 0.1 mmol reaction mixture w.r.t. amine) was added to each vial. The vials were then placed in the photoreactor in the specified vial positions, stirred at 1000 rpm, and the 450 nm LED light switched on. After 24 hours of irradiation, the light was switched off and the mixtures were filtered over celite and concentrated *in vacuo*. 1,3,5–Trimethoxybenzene (ca 0.02 mmol, 0.2 equiv) was added to each of the crude mixtures and the yield determined by ^1H NMR spectroscopy with a 20 s delay. Results are reported in Table 2, section 2.1.2.

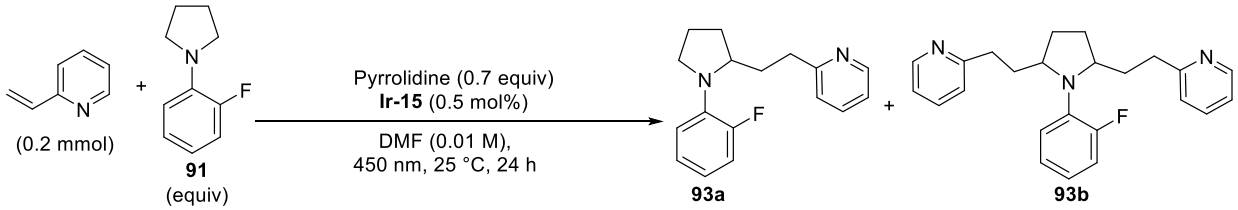
Using DBU as base: The recirculating water bath was set to 40 °C unless otherwise specified, and turned on to pre-heat the photoreactor to the desired temperature. A stock solution was made using *N*-(2-fluorophenyl)pyrrolidine (140.5 mg, 0.85 mmol, 1.0 equiv), $Ir[dF(CF_3)ppy]_2(dtbbpy)PF_6$ (9.6 mg, 0.0085 mmol, 1 mol%), DBU (140 µL, 0.94 mmol, 1.1 equiv) and dry DMF (8.5 mL, 0.1 M w.r.t. amine). The solution was sparged with argon for 5 mins and charged with 2-vinylpyridine (138 µL, 1.28 mmol, 1.5 equiv), then mixed. The stock solution (1 mL, 0.1 mmol reaction mixture w.r.t. amine) was added to 8 separate oven-dried vials, the vials were sealed and then placed under argon. The vials were then placed in the photoreactor in the specified vial positions, stirred at 1000 rpm, and the 450 nm LED light switched on. After 24 hours of irradiation, the light was switched off and the mixtures were filtered over celite and concentrated *in vacuo*. 1,3,5–Trimethoxybenzene (ca 0.02 mmol, 0.2 equiv) was added to each of the crude mixtures and the yield determined by ^1H NMR spectroscopy with a 20 s delay. Results are reported Results are reported in Table 2, section 2.1.2.

Wavelength screen: The reaction was conducted according to general procedure B. In each instance, the light source placed in the holder for the light (see Figure 41) was of the wavelength specified in Table 6, section 2.1.4.3, with details for the lights provided in Table 27. The emission spectrum for the 450 nm light source provided by the supplier is presented in Figure 42. Results of the wavelength screen are reported in Table 6, section 2.1.4.3.

Table 27: Details for light sources used in wavelength screen.

Entry	Light wavelength (nm)	Brand	Part number
1	450	EvoluChem	P201-18-2
2	440	Kessil	PR160 440 nm
3	427	Kessil	PR 160 427 nm
4	390	Kessil	PR160 390 nm

Testing different amine equivalents batch reaction



A stock solution of $Ir[dF(CF_3)ppy]_2(dtbbpy)PF_6$ (5.5 mg, in DMF (5.5 mg in 10 mL, 0.5 mM) was prepared. *N*-(2-Fluorophenyl)pyrrolidine **91** (variable, excess) was added to an oven dried vial followed by addition of the $Ir[dF(CF_3)ppy]_2(dtbbpy)PF_6$ stock solution in DMF (2 mL, 0.001 mmol, 0.5 mol%) and pyrrolidine (12 µL, 0.14 mmol, 0.7 equiv). The vials were sealed and purged with argon for 5 min. 2-Vinylpyridine (22 µL, 2.0 mmol, 1.0 equiv) was then added to the vial, which was placed in a Hepatochem photoreactor with the recirculating bath set to 25 °C and stirring set to 1000 rpm. The vials were illuminated with one 450 nm Evoluchem LED light for 24 h, after which the light was switched off and the solutions were filtered through a plug of celite and concentrated to a residue. Yields were determined by quantitative ^1H NMR analysis with a 20 s delay using 1,3,5-trimethoxybenzene as an internal standard. Results are reported in table 15, section 2.1.6.

Formation of di product 93b: The reaction was conducted according to general procedure B, using mono-alkylated **93a** (57.2 mg, 0.2 mmol, 1.0 equiv) instead of substrate **91**, and pyrrolidine base (11 µL, 0.14 mmol, 0.7 equiv). Results are reported in Table 14, section 2.1.6.

Sensitivity screen: Reactions were conducted according to general procedure B, using pyrrolidine as base (11 µL, 0.14 mmol 0.7 equiv) with adjustments as described in Table 28. Results are reported in Figure 12, section 2.1.7.

Table 28: Experimental detail for sensitivity screen.

Entry	Change from General procedure B	Experimental detail
1	None	N/A
2	High concentration (0.11 M)	DMF added: 1.8 mL, 0.11 M
3	Low concentration (0.09 M)	DMF added: 2.2 mL, 0.09 M
4	High O_2 (under air)	No argon sparge, vial sealed under air
5	Moderate O_2 (no sparge)	No argon sparge, vial sealed under argon
6	High H_2O (+ 20 µL water)	Water (20 µL) was added to the reaction mixture following 2-vinylpyridine addition
7	High temperature (35 ºC)	Recirculating bath set to 35 °C
8	Shorter wavelength (440 nm)	440 nm wavelength Kessil LED light used

Batch reaction profile

The recirculating water bath was set to 25 °C and turned on to pre-heat the photoreactor to the desired temperature. This remained on for the duration of the reaction. *N*-(2-Fluorophenyl)pyrrolidine (33 mg, 0.2 mmol, 1.0 equiv) and 1,4-dimethylterepthalate (ca 10 mg, 0.05 mmol, exact mass recorded) were added to 6 separate oven-dried vials. The vials were sparged with Argon for 1 min, then sealed under argon. A stock solution was prepared containing $Ir[dF(CF_3)ppy]_2(dtbbpy)PF_6$ (9.0 mg, 0.008 mmol, 0.33 mM), pyrrolidine (197 µL, 2.36 mmol, 0.10 M) and 2-vinylpyridine (345 µL, 3.20 mmol, 0.13 M) and DMF (24 mL). A portion of the stock solution (3.1 mL) was added to each vial, and the vials were sealed under argon. The vials were placed in the photoreactor, stirred at 1000 rpm, and the 450 nm LED light switched on.

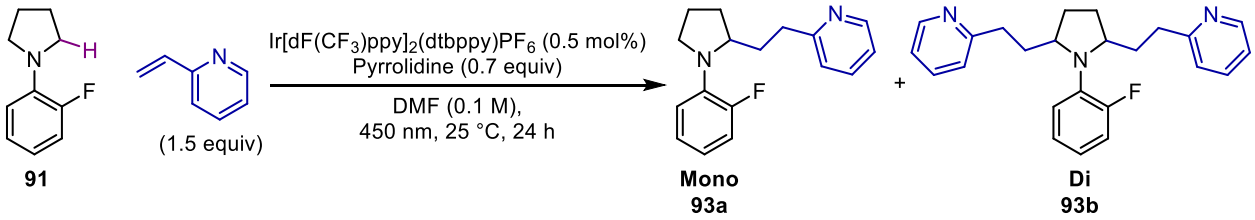
Individual reactions One of the reactions was worked up at each of the reaction times: 2, 4, 6, 21 and 24 h. Each reaction was filtered over celite and concentrated *in vacuo*. The yield was determined by ^{1}H NMR spectroscopy with a 20 s delay.

Sampled reactions: A sample (0.2 mL) of reaction solution was removed from the sixth vial at each of the timepoints: 2, 4, 6, 21 and 24 h. The sample was filtered over celite and concentrated *in vacuo*. The yield was determined by ^{1}H NMR spectroscopy with a 20 s delay.

Results of the profile experiments are reported in Figure 13, section 2.1.8.

Repeating standard conditions

General procedure B was followed using pyrrolidine (11 µL, 0.7 equiv) as base. Four separate reactions were run and the average presented in the table below.



Entry	Deviation from standard conditions	Yield (%)		
		Mono 93a	Di 93b	Total 93a+b
1	None	65	11	76
2	None	65	11	76
3	None	67	14	81
4	None	65 (58)	16 (12)	81 (70)
Average N = 4		65	13	79

4.3. Light Emission spectrum for Evoluchem 450 nm light source

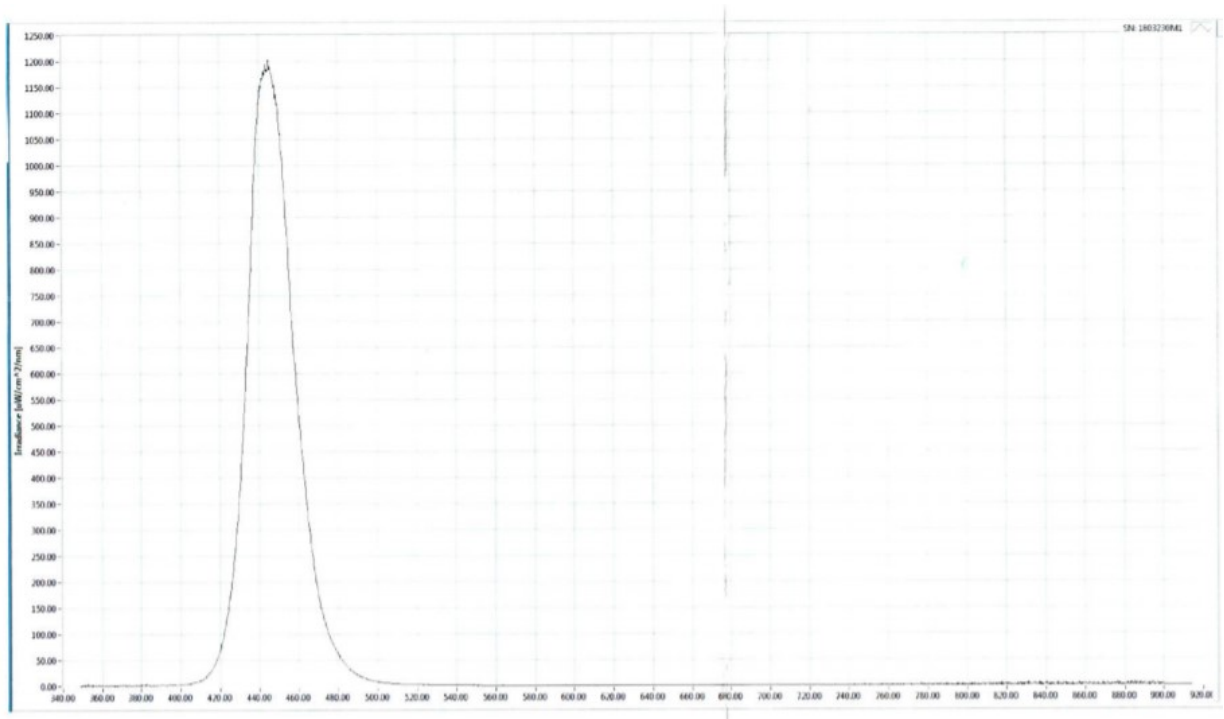


Figure 42: Emission spectrum of light source EvoluChem P201-18-2 450 to 455 nm LED, provided by supplier.

4.4. UV-Vis spectra

UV-Vis spectrum of Ir[dF(CF$_3$)ppy]$_2$(dtbbpy)PF$_6$ (Ir-15)

A solution of Ir[dF(CF$_3$)ppy]$_2$(dtbbpy)PF$_6$ in DMF (0.05 mM) was prepared under an argon atmosphere in a quartz cuvette with a pathlength of 10 mm. The ultraviolet-visible (UV-Vis) spectrum was measured using an Agilent Carey 60 UV-Vis Spectophotometer, recording wavelengths between 300 and 800 nm (Figure 43).

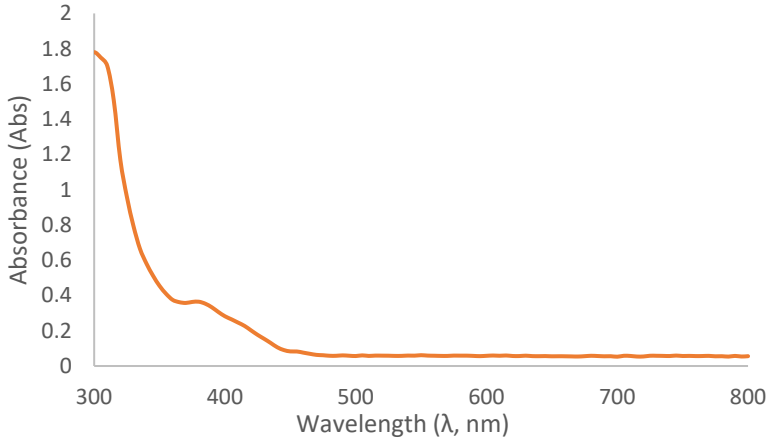


Figure 43: UV-Vis spectrum of photocatalyst **Ir-15**.

UV-Vis spectra of compounds

UV-Vis spectra were obtained by making 2 mL of a 10 mM solution of the desired substrate (2 mmol) in DMF using a volumetric flask. From this, sample was diluted to make the solutions in DMF to the desired concentration. A quartz cuvette with a pathlength of 10 mm was used to measure the UV-Vis spectra on an Agilent Carey 60 UV-Vis Spectophotometer, scan 800–200 nm. Spectra are given in Figure 44.

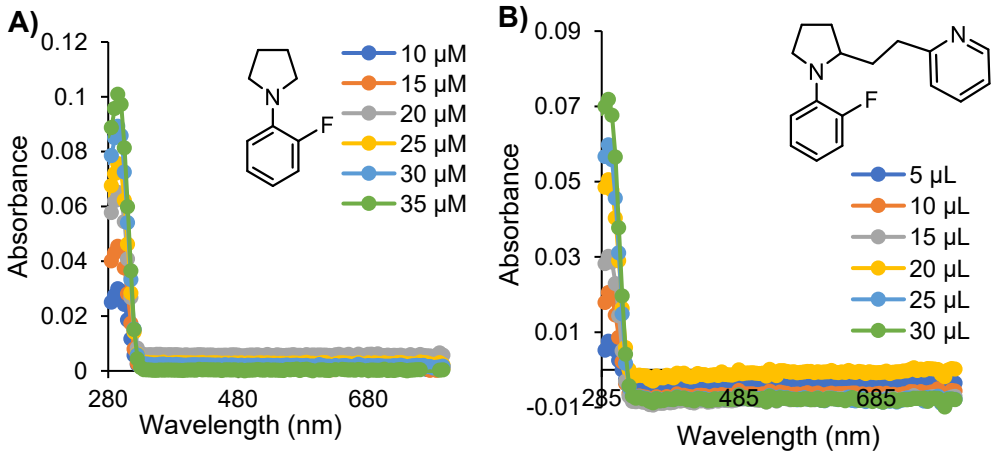


Figure 44: UV-Vis spectra of A) **91** and B) **93a** at different concentrations in DMF.

4.5. General continuous flow experimental considerations

The continuous flow reactor was constructed according to the general procedures as described in each section using the following equipment and settings, unless otherwise stated.

All yields presented correspond to those obtained at steady state, reported as the average of three consecutive samples of flow output, each filtered through a plug of celite, washed with EtOAc and concentrated *in vacuo.* The yield and/or concentration was determined with respect to 1,4-dimethylterephthalate as an internal standard added to the input stream containing photocatalyst by ^{1}H NMR with at least 20 s delay (D1).

Unless otherwise stated, the pump used was a syringe pump (a Harvard Apparatus Dual Syringe Infusion Pump Model 22) with SGE 10MDF-LL-GT syringes (10 mL, gas tight glass + plastic, fixed Luer lock, ID = 14.57 mm). All flow reactors were primed with DMF prior to the start of a reaction. Flangeless fittings (¼-28 thread, mixture of IDEX XP-202 Delrin red, and XP-218x ETFE natural) with flangeless ferrules (IDEX XP-200, ETFE blue) were used for all connections. All tubing was PFA (K63200068, OD = 1.60 mm, ID = 1.0 mm) of the given length. Luer lock adapters (IDEX P-628S ETFE natural, female Luer to 1/4-28 female) were used to connect syringes to tubing. Where a T-piece was used, it was an IDEX P-632 (1/4-28 thread ports, 0.5 mm thru-hole, 2.9 µL swept volume, ETFE natural).

The temperature of all flow reactions was controlled using a heated bath circulator unit (Fisherbrand™ Isotemp™ model 5150 H7), connected to the photoredox reactor (Temperature Controlled) photoredox reactor using tubing and secured using hose clips.

4.6. Flow reactor design details

1st generation flow reactor: 1 light, 1 input feed

The EvoluChem PhotoRedOx Box TC™ (Temperature Controlled) photoredox reactor (depicted in Figure 41) was adapted for a continuous flow setup (depicted in Figure 45). The vial holder was removed and in its place 1 mm diameter PFA tubing was wrapped to form a coil 1.3 mL in volume, ca 10 cm in diameter and secured in place with cable ties. This coil was submerged in the vial holder opening of the photoreactor. The tubing input was connected to a gas tight syringe containing the feed solution. The output tubing was fed out of the photoreactor and into a 5 psi back pressure regulator (IDEX P-790, 5 psi, 134 µL swept volume, PEEK black), and the output of this solution was collected in a vial.



Figure 45: 1st generation photoreactor showing A) reactor coil, B) the coil placed into the photoreactor and C) the reactor irradiated.

A solution of *N*-(2-fluorophenyl)pyrrolidine (91.5 mg, 0.55 mol, 1.00 equiv), $Ir[dF(CF_3)ppy]_2(dtbbpy)PF_6$ (6.3 mg, 0.006 mol, 1 mol%) and DBU (91 µL, 0.60 mmol, 1.1 equiv) in dry DMF (5.5 mL, 0.1 M) was prepared in the dark in flame-dried glassware. The solution was sparged with argon for 5 min, then charged with 2-vinylpyridine (90 µL, 0.83 mmol, 1.5 equiv). The resulting solution was added to a syringe, placed in the syringe pump (Aladdin AL-1000, injection only) and the photoreactor irradiated with 1 × 450 nm Evoluchem LEDs. Flow rates and therefore residence times were set at the syringe pumps and the reaction output collected in vials changed every 30 min. Results and changes from given conditions are described in Table 17, section 2.2.1.1.

2nd generation flow reactor: 1 light, 2 input feeds

The EvoluChem PhotoRedOx Box TC™ (Temperature Controlled) photoredox reactor (depicted in Figure 41) was adapted for a continuous flow setup. The vial holder was removed and in its place tubing was wrapped around a test tube to form a coil (length = 242 cm, OD 1.6 mm, ID 1.0 mm, coil 15 mm diameter, 1.9 mL reactor volume), secured in place with cable ties (Figure 46). This coil was submerged in the vial holder opening of the photoreactor.



Figure 46: 2nd generation flow reactor coil.

The input was connected to a T-piece with two short input lines each connected to gas tight syringes containing the desired solutions. The output was fed out of the photoreactor and into

a 5 psi back pressure regulator (IDEX P-790, 5 psi, 134 µL swept volume, PEEK black), and the output of this solution was collected in a vial.

N-(2-Fluorophenyl)pyrrolidine (**91**, 83 mg, 0.5 mol, 1.00 equiv), $Ir[dF(CF_3)ppy]_2(dtbbpy)PF_6$ (2.8 mg, 0.00025 mol, 0.5 mol%) and dry DMF (2.5 mL) were added to a flame-dried flask under argon. The solution was sparged with argon for 5 min, then pyrrolidine (29 µL, 0.35 mmol, 0.7 equiv) was added, forming a yellow solution. Dry DMF (2 mL) was then added to a separate flame-dried flask under argon, the 2-vinylpyridine (64 µL, 0.59 mmol, 1.18 equiv) was added. The resulting solutions were added to separate syringes, placed in a dual syringe pump and the photoreactor irradiated with 1 × 450 nm Evoluchem LEDs. Flow rates and therefore residence times were set at the syringe pumps and the reaction output collected in vials changed every 30 min. Results and changes from given conditions are described in Table 18, section 2.2.1.2.

3rd generation flow reactor: 3 lights, 3 solutions

The photoreactor was set up as for the 2nd generation flow reactor, with some modifications to the reactor coil, (tubing length = 127 cm, OD = 1.6 mm, ID 1.0 mm, coil 15 mm diameter, 60 mm length, reactor volume 1.0 mL). In addition to the light present in the vial holder, 2 more 450 nm LEDs were positioned over the vial holder opening as shown in Figure 47. During reactions, the coil was submerged in the water of the recirculating bath set to the specified temperature and irradiated with 3 x 450 nm Evoluchem LEDs arranged as shown in Figure 47.

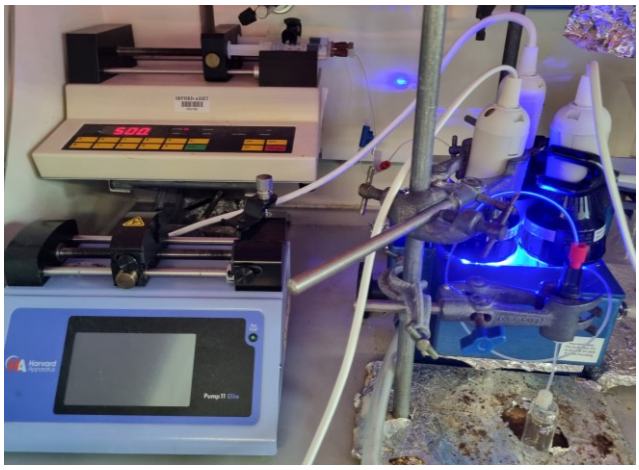


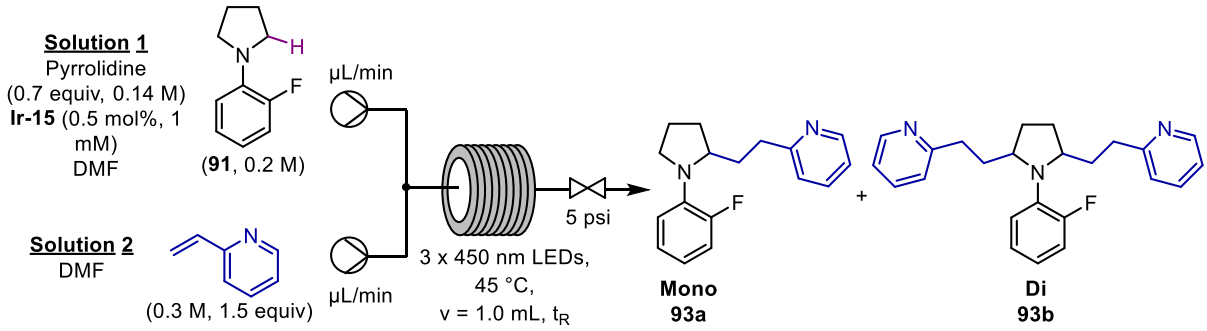
Figure 47: 3 light, 2 input stream flow photoreactor.

This setup was used for all further experiments, with any modifications detailed.

4.7. Kinetic profiles

Data for VTNA, same excess and reaction profiles for substrate comparisons can be found at the Imperial College London Data Repository, DOI: 10.14469/hpc/13406, https://data.hpc.imperial.ac.uk/resolve/?doi=13406&access=z7gy-h4cq. Access code: z7gy-h4cq.

General procedure C: photoredox kinetic profiles 0.1 M reaction, section 2.2



3rd generation flow reactor was used for this experiment. The recirculating water bath was set to 45 °C to pre-heat the photoreactor to the desired temperature. *N*-(2-fluorophenyl)pyrrolidine **91** (314 mg, 1.9 mmol), Ir[dF(CF_3)ppy]$_2$(dtbbpy)PF_6 (10.7 mg, 0.0096 mmol, 0.5 mol%) and dimethyl terephthalate (70 mg, ca 0.4 mmol, 0.2 equiv) were added to a flame dried flask and dissolved in DMF to give a 9.5 mL of 0.2 M solution w.r.t. the substrate, followed by addition of pyrrolidine (109 µL, 1.33 mmol, 0.7 equiv). 2-Vinylpyridine (307 µL, 2.85 mmol, 1.5 equiv) was dissolved in DMF to give 9 mL of 0.3 M solution. Both solutions were added to syringes and placed in the syringe pump. The flow rate was set depending on the residence time being tested. Once a flow rate was set and the system was at temperature, 3 x 450 nm lights were switched on and the pumps were started. The system was purged for 2 reactor volumes before sample collection at each residence time. Residence times and flow rates were set according to Table 29.

Table 29: Flow rates and purge lengths for each residence time.

Residence time (min)	Rate per syringe (µL/min)	Total Rate (µL/min)	Purge length (min)
5	100.0	200.0	10
10	50.0	100.0	20
15	33.3	66.7	30
20	25.0	50.0	40
30	16.6	33.3	60
45	11.1	22.2	90

Three samples were collected at each residence time, these were filtered through a plug of celite, washed with EtOAc and concentrated *in vacuo* before analysis by ^{1}H NMR spectroscopy using 1,4-dimethylterepthalate as an internal standard with a 20 s delay (D1). The reported yields were an average of the three samples.

4.7.1. Calculation of kinetic profiles

Concentrations and yields for reaction profiles were calculated using ^{1}H NMR spectroscopy with a 20 s delay or higher, using 1,4-dimethylterepthalate as an internal standard. The overlay in Figure 48 shows a typical crude spectrum stacked with starting material and both products.

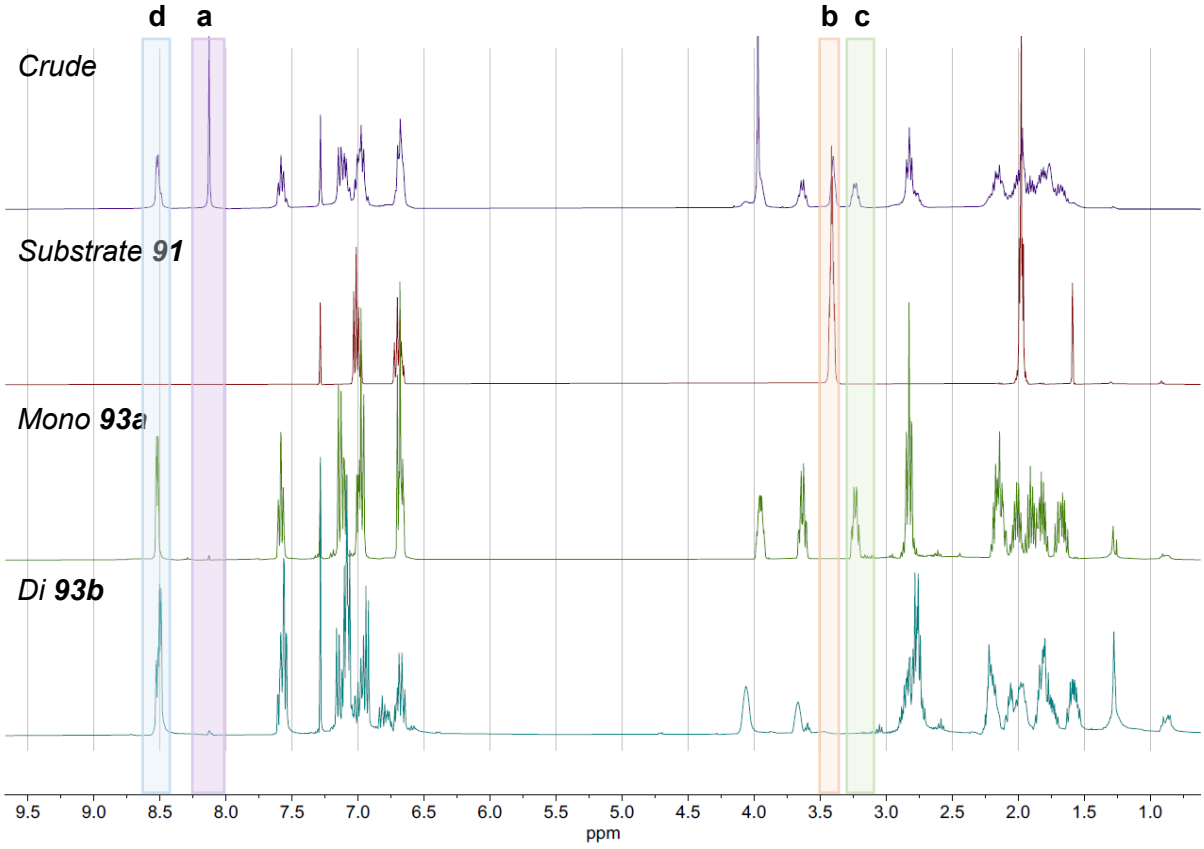


Figure 48: Overlay of a typical crude reaction mixture used for profile analysis, and the substrate, mono and di products (**93a** and **b** respectively).

Signals from the crude spectra were used to identify substrate, mono and di products in each case, as listed in Table 30.

Table 30: Peaks used for profile determination.

Peak	Species	Chemical shift (ppm)	No. of H's	Assignment
a	Dimethyl terephthalate internal standard	8.13 (s)	4	4 × Ar–CH
b	Substrate **91**	3.47–3.33 (m)	4	2 × NCH_2
c	Mono **93a**	3.29–3.18 (m)	1	NCH*H*
d	Mono + Di, **93a+b**	8.60–8.42 (m)	1 × Mono and 2 × Di	$Ar_{(pyridine)}$–CH mono 2 × $Ar_{(pyridine)}$–CH di

Note: ranges for integration varied slightly with substrate, analogous signals were used in each case.

Prior to analysis the samples were concentrated *in vacuo* extensively to remove DMF, this also removed 2-vinylpyridine, pyrrolidine and sometimes substrate from the spectra. Details of how all reaction components were calculated for VTNA analysis are provided in Table 31.

Table 31: How concentrations for all components were calculated.

Species	Measured or calculated	Details
Dimethyl terephthalate internal standard	Measured	Peak **a** Figure 48
Mono **93a**	Measured	Peak **c** Figure 48
Di **93b**	Calculated	Subtracting the integral of **mono** measured in peak **c** from **mono + di** peak **d** gives the integral for 2 protons of **di**.
Substrate **91**[a]	Calculated	[Substrate] = $[Substrate]_0$ − [**mono**] – [**di**]
Pyrrolidine	-	Assumed to be catalytic [Pyrrolidine] = $[Pyrrolidine]_0$
Photocatalyst	-	Assumed to be catalytic [Ir] = $[Ir]_0$
2-Vinylpyridine	Calculated	[2-Vinylpyridine] = $[2\text{-Vinylpyridine}]_0$ − [**mono**] – (2 × [**di**])

[a]The amine substrate was volatile in most cases, therefore the calculated rather than measured value was given. Square brackets denote concentration, $[x]_0$ denotes initial concentration of component x.

Comment on reproducibility: as discussed in section 2.2.2.1, there had been some changes in profile on running the same profile several months apart. As such, the control profile using general procedure C was run periodically, either monthly or before and after a run of profiles. Overlaying control profiles were used to confirm that the system was still reproducible, and that all profiles run between these control profiles were not affected by changes in equipment setup.

4.7.2. VTNA experiments

VTNA experiments, 0.1 M reaction concentration Figure 21, section 2.3.1

Experiments were conducted according to general procedure C with the following changes from standard conditions:

Table 32: Experimental detail for VTNA experiments in Figure 21, section 2.3.1.

Entry	Reaction component	Change from standard conditions	Order in component
1	Substrate **91**	Substrate **91** (377 mg, 2.28 mmol, 0.12 M)	0.5
2		None: Substrate **91** (314 mg, 1.90 mmol, 0.10 M)	
3		Substrate **91** (252 mg, 1.53 mmol, 0.08 M)	
4		Substrate **91** (190 mg, 1.15 mmol, 0.06 M)	
5	2-Vinylpyridine	2-Vinylpyridine (360 µL, 3.34 mmol, 0.19 M)	0
6		2-Vinylpyridine (330 µL, 3.08 mmol, 0.175 M)	
7		None: 2-Vinylpyridine (307 µL, 2.85 mmol, 0.15 M)	
8		2-Vinylpyridine (256 µL, 2.37 mmol, 0.125 M)	
9	$Ir[dF(CF_3)ppy]_2(dtbbpy)PF_6$ (**Ir-15**)	**Ir-15** (16.3 mg, 0.0145 mmol, 0.75 mM)	0.5
10		**Ir-15** (10.7 mg, 0.0095 mmol, 0.50 mM)	
11		**Ir-15** (6.4 mg, 0.0057 mmol, 0.25 mM)	
12	Pyrrolidine	Pyrrolidine (140 µL, 1.70 mmol, 0.09 M)	0
13		Pyrrolidine (109 µL, 1.33 mmol, 0.07 M)	
14		Pyrrolidine (80 µL, 0.97 mmol, 0.05 M)	

Graphs of concentration against a normalised time axis (this latter obtained by applying the time normalisation equation as described in equation 9) were then plotted for each reaction component as described in section 2.3.1.[3] The exponent α was varied and the value of best overlays determined for each reaction component. Graphs using three exponents of α (α = 0, 0.5 and 1.0) are presented for the order in substrate **91**, with the graphs considered to have the best overlay boxed in green (Figure 49). For all other reaction components, the graphs using the value of α which gave the best overlay has been provided (Figure 50). For each case, three outputs have been measured, **mono** formation, total product (**mono** + **di**) formation, and total catalytic cycles (**mono** + (2 × **di**)) have been presented.

The profile data for these experiments can be located at the Imperial College London Data Repository, DOI: 10.14469/hpc/13406, https://data.hpc.imperial.ac.uk/resolve/?doi=13406&access=z7gy-h4cq. Access code: z7gy-h4cq, in an Excel document titled 'VTNA all components 0.1 M'.

[3]Spreadsheet for VTNA analysis was adapted from the Excel file available in the supplementary information of Nielsen and Burés, *Chem. Sci.*, 2019, **10**, 348–353.

Order in substrate 91

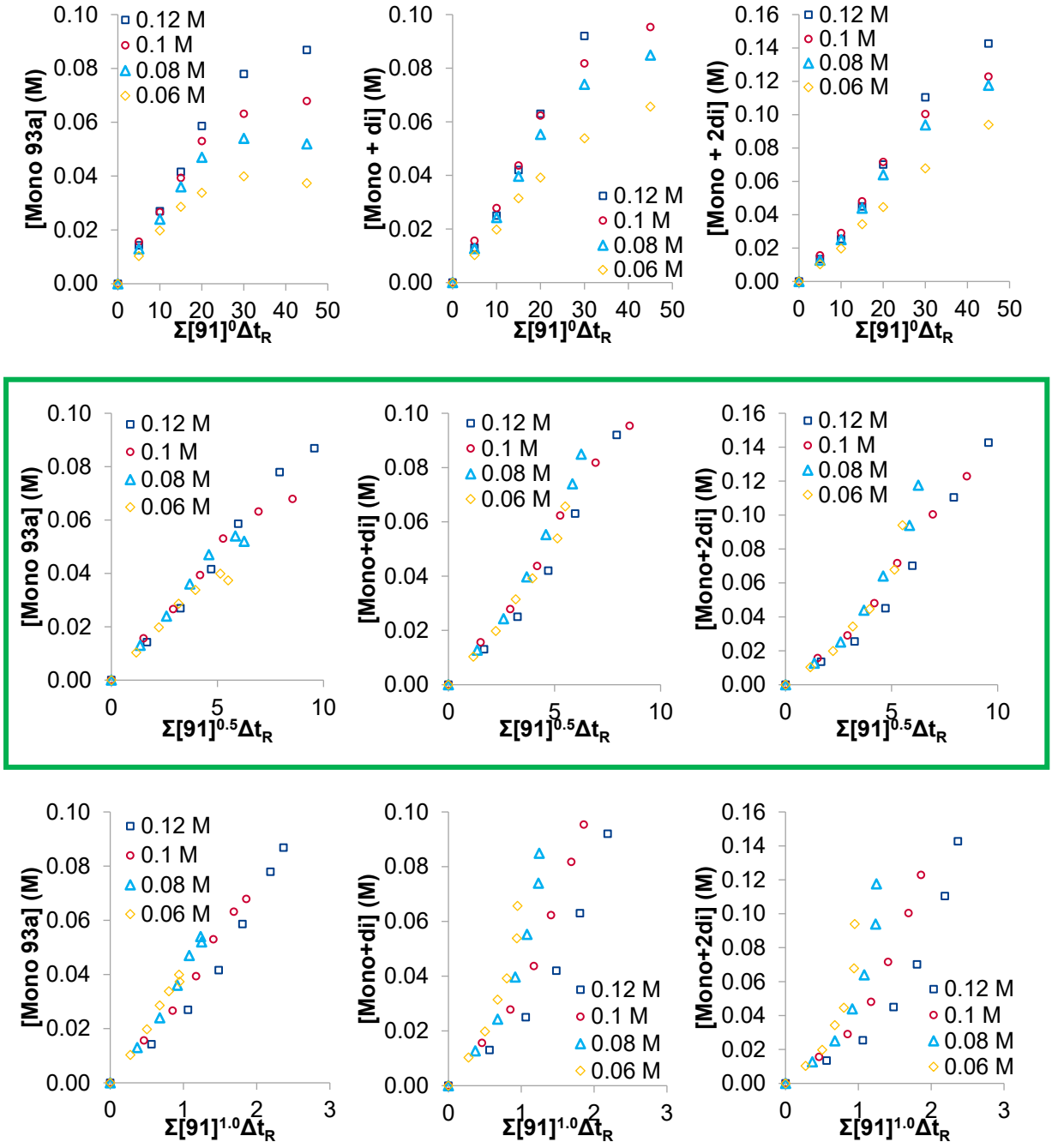
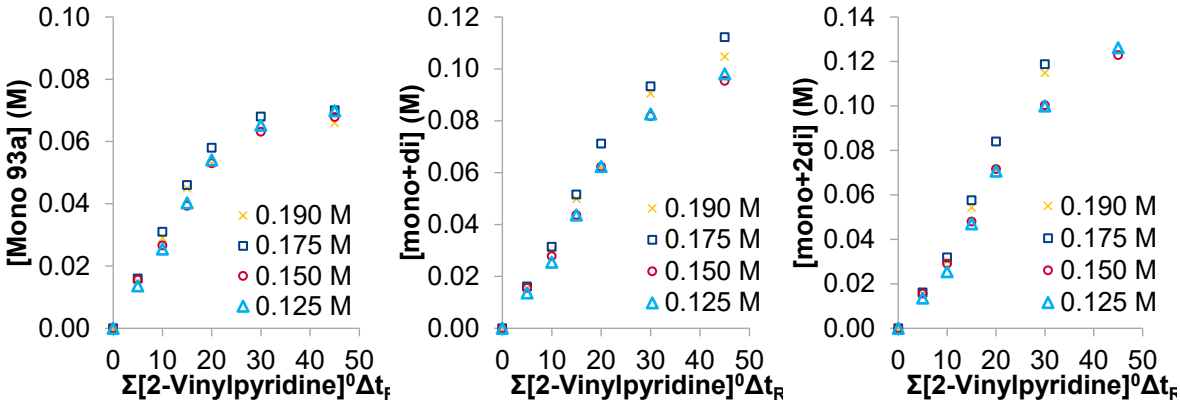
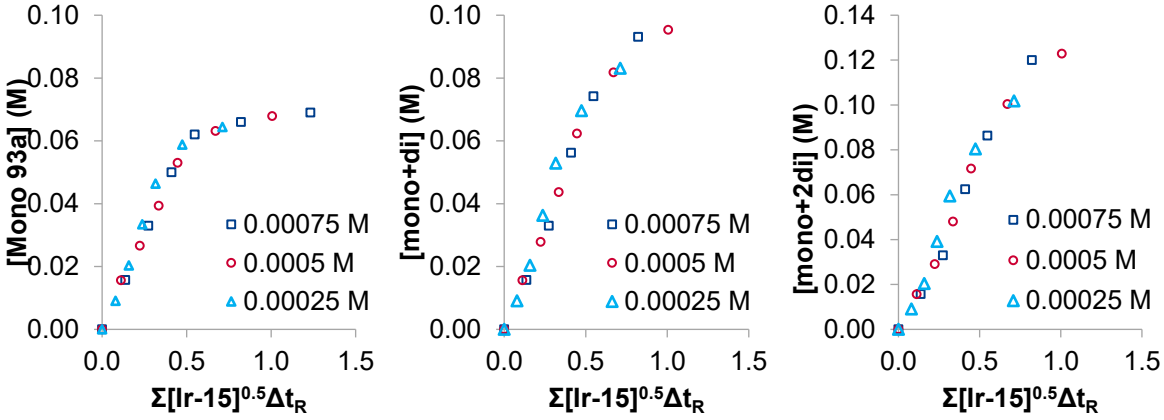


Figure 49: VTNA graphs depicting the overlay of profiles using different initial concentrations of **91** at different orders.

Order in 2-vinylpyridine



Order in Ir[dF(CF$_3$)ppy]$_2$(dtbbpy)PF$_6$



Order in pyrrolidine base

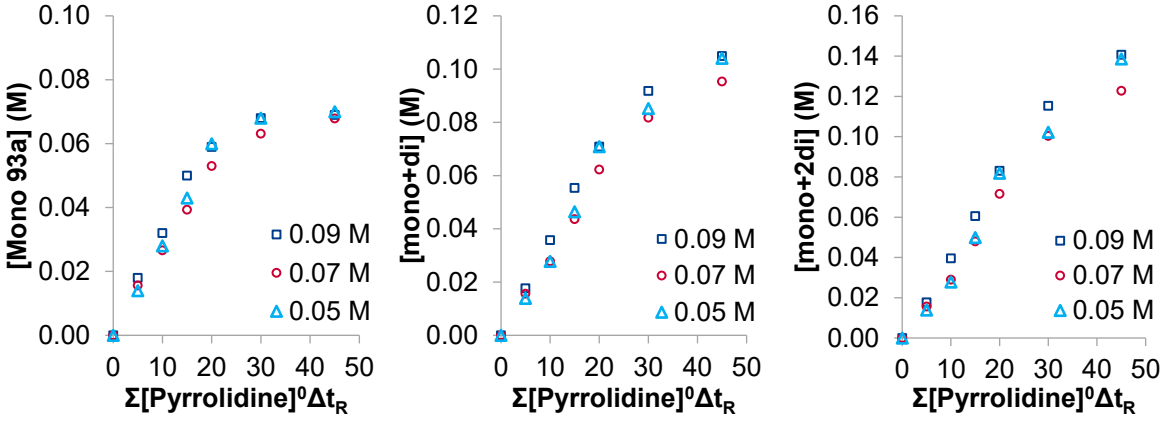
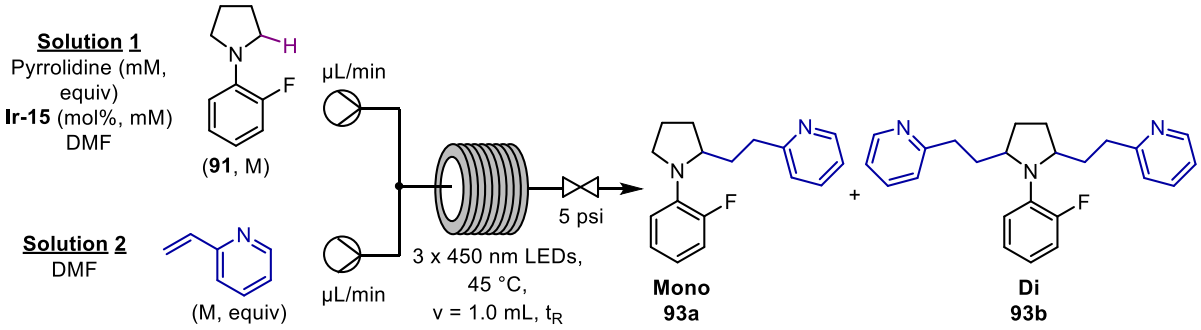


Figure 50: VTNA graphs at the order giving the best overlay for each reaction component.

VTNA investigation into changing catalyst and starting material orders



The 3rd generation photoreactor was used. The recirculating water bath was set to 45 °C to pre-heat the photoreactor to the desired temperature. *N*-(2-Fluorophenyl)pyrrolidine **91**, Ir[dF(CF_3)ppy]$_2$(dtbbpy)PF_6, dimethyl terephthalate (0.2 equiv) and pyrrolidine (0.7 equiv) were added to a flame-dried flask and dissolved in DMF (solution 1) to form a yellow solution. 2-Vinylpyridine (1.5 equiv) was dissolved in DMF (solution 2) to give a clear solution. Quantities for each reaction are detailed in Table 33. The solutions were added to separate 10 mL syringes and placed into a syringe pump. Residence times and flow rates were set according to Table 29. Once a flow rate was set and the system was at temperature, 3 x 450 nm lights were switched on and the pumps were started. The system was purged for 2 reactor volumes before sample collection at each residence time.

Quantities and concentrations of reaction components for each profile in this investigation looking at the order in photocatalyst are provided in Table 33, and those looking at the order in starting material are provided in Table 34.

Graphs of concentration against a normalised time axis (this latter obtained by applying the time normalisation equation as described in equation 9) were then plotted for each different concentration and catalyst loading. The exponent α was varied and the value of best overlays determined for each reaction concentration and catalyst loading, to the nearest 1 decimal point. These orders are reported in Table 20 and Figure 23 of section 2.3.1.

Concentrations for each profile and the overlays are available on the Imperial College London Data Repository, DOI: 10.14469/hpc/13406, https://data.hpc.imperial.ac.uk/resolve/?doi=13406&access=z7gy-h4cq. Access code: z7gy-h4cq titled 'Concentrations for VTNA investigation' with experiment codes provided to link to LabArchives data. The processed concentration data for each of the profiles used to obtain orders in catalyst presented in Table 20 and Figure 21 section 2.3.1 can be found in the

Excel document ‘VTNA investigation orders in Ir’, and the results for order in substrate **91** can be found in the Excel document ‘VTNA investigation orders in SM’.

Table 33: Quantities for VTNA investigation into orders in photocatalyst

Entry	Reaction Conc (M)	Catalyst loading (mol%)	Factor	91	Ir-15	DMT	DMF sol 1 (mL)	Pyrrolidine	2-Vinyl-pyridine	DMF sol 2 (mL)
1	0.1	1.0	Quantity (mg)	314	21.4	72.9	9	109 µL	307 µL	9.19
			Conc (M)	0.10	0.00100	0.020		0.070	0.150	
			Equiv	1	0.0100	0.20		0.70	1.50	
2	0.1	0.5	Quantity (mg)	314	10.7	73.5	9	109	307 µL	9.19
			Conc (M)	0.100	0.00050	0.020		0.070	0.150	
			Equivalents	1	0.0050	0.20		0.670	1.50	
3	0.1	0.3	Quantity (mg)	314	6.4	68.9	9.00	110 µL	307 µL	9.19
			Conc (M)	0.100	0.00030	0.019		0.071	0.150	
			Equivalents	1	0.0030	0.19		0.71	1.50	
4	0.05	1.0	Quantity (mg)	166	11.2	38.7	9.84	58 µL	162 µL	9.91
			Conc (M)	0.050	0.00049	0.010		0.035	0.074	
			Equivalents	1	0.0099	0.20		0.70	1.50	
5	0.05	0.5	Quantity (mg)	157	5.4	37.1	9.25	55 µL	155 µL	9.35
			Conc (M)	0.050	0.00025	0.010		0.035	0.076	
			Equivalents	1	0.0051	0.20		0.70	1.51	
6	0.05	0.3	Quantity (mg)	157	3.4	35.3	9.25	55 µL	155 µL	9.35
			Conc (M)	0.050	0.00016	0.010		0.035	0.076	
			Equivalents	1	0.0032	0.19		0.70	1.51	
7	0.03	1.0	Quantity (mg)	119	8.1	27.2	11.81	42 µL	117 µL	11.88
			Conc (M)	0.030	0.00030	0.006		0.021	0.045	
			Equivalents	1	0.0100	0.19		0.71	1.51	
8	0.03	0.5	Quantity (mg)	118.5	4	28.1	11.81	42 µL	117 µL	11.88
			Conc (M)	0.030	0.00015	0.006		0.021	0.045	
			Equivalents	1	0.0050	0.20		0.71	1.51	
9	0.03 M	0.3	Quantity (mg)	119.4	2.6	26.3	11.8	53 µL	117 µL	11.88
			Conc (M)	0.030	0.00010	0.006		0.027	0.045	
			Equivalents	1	0.0032	0.19		0.89	1.50	0

Table 34: Quantities for VTNA investigation into orders in amine starting material

Entry	Reaction conc (M)	Catalyst loading (mol%)	Factor	91	Ir-15	DMT	DMF sol 1 (mL)	Pyrrolidine	2-Vinylpyridine	DMF sol 2 (mL)
1	0.1 M	1.0 mol%	Quantity (mg)	314	21.4	72.9	9.00	109	307	9.19
			Conc (M)	0.100	0.00100	0.020		0.070	0.150	
			Equivalents	1	0.0100	0.20		0.70	1.50	
2	0.08 M	1.0 mol%	Quantity (mg)	376.9	21.4	73.3	9.00	109	307	9.19
			Conc (M)	0.120	0.00100	0.020		0.070	0.149	
			Equivalents	1.20	0.0100	0.20		0.70	1.49	
3	0.1 M	0.5 mol%	Quantity (mg)	314	10.7	73.5	9.00	109	307	9.19
			Conc (M)	0.100	0.00050	0.020		0.070	0.150	
			Equivalents	1	0.0050	0.20		0.70	1.50	
4	0.08	0.5 mol%	Quantity (mg)	252	10.7	73.5	9.06	110	307	9.19
			Conc (M)	0.080	0.00050	0.020		0.070	0.150	
			Equivalents	1	0.0050	0.20		0.704	1.50	
5	0.1 M	0.3 mol%	Quantity (mg)	313.8	6.4	68.9	9.00	110	307	9.19
			Conc (M)	0.100	0.00030	0.019		0.071	0.150	
			Equivalents	1	0.0030	0.19		0.71	1.50	
6	0.08	0.3 mol%	Quantity (mg)	251.1	6.4	70.8	9.06	110	307	9.19
			Conc (M)	0.080	0.00030	0.019		0.071	0.150	
			Equivalents	1	0.0030	0.19		0.71	1.50	
7	0.05 M	1.0 mol%	Quantity (mg)	165.9	11.2	38.7	9.84	58	162	9.91
			Conc (M)	0.050	0.00049	0.010		0.035	0.074	
			Equivalents	1	0.0099	0.20		0.70	1.50	
8	0.04 M	1.0 mol%	Quantity (mg)	125.6	10.7	36.4	9.27	55	155	9.35
			Conc (M)	0.040	0.00050	0.010		0.035	0.076	
			Equivalents	0.80	0.0101	0.20		0.71	1.52	
9	0.05 M	0.5 mol%	Quantity (mg)	157	5.4	37.1	9.25	55	155	9.35
			Conc (M)	0.050	0.00025	0.010		0.035	0.076	
			Equivalents	1	0.0051	0.20		0.70	1.51	

Entry	Reaction conc (M)	Catalyst loading (mol%)	Factor	91	Ir-15	DMT	DMF sol 1 (mL)	Pyrrolidine	2-Vinylpyridine	DMF sol 2 (mL)
10	0.04 M	0.5 mol%	Quantity (mg)	125.7	5.4	36.3	9.28	55	155	9.35
			Conc (M)	0.040	0.00025	0.010		0.035	0.076	
			Equivalents	0.80	0.0051	0.20		0.70	1.51	
11	0.05 M	0.3 mol%	Quantity (mg)	157	3.4	35.3	9.25	55	155	9.35
			Conc (M)	0.050	0.00016	0.010		0.035	0.076	
			Equivalents	1	0.0032	0.19		0.70	1.51	
12	0.04 M	0.3 mol%	Quantity (mg)	125.4	3.4	36.5	9.28	55	155	9.35
			Conc (M)	0.040	0.00016	0.010		0.035	0.076	
			Equivalents	0.80	0.0032	0.20		0.70	1.51	
13	0.03 M	1.0 mol%	Quantity (mg)	119	8.1	27.2	11.81	42	117	11.88
			Conc (M)	0.030	0.00030	0.006		0.021	0.045	
			Equivalents	1	0.0100	0.19		0.71	1.51	
14	0.03 M	1.0 mol%	Quantity (mg)	95.7	8.2	28.2	11.83	42	117	11.88
			Conc (M)	0.024	0.00030	0.006		0.021	0.045	
			Equivalents	0.80	0.0101	0.20		0.71	1.51	
15	0.03 M	1.0 mol%	Quantity (mg)	118.5	4	28.1	11.81	42	117	11.88
			Conc (M)	0.030	0.00015	0.006		0.021	0.045	
			Equivalents	1	0.0050	0.20		0.71	1.51	
16	0.03 M	1.0 mol%	Quantity (mg)	95.6	4	27.9	11.83	42	117	11.88
			Conc (M)	0.024	0.00015	0.006		0.021	0.045	
			Equivalents	0.80	0.0049	0.20		0.71	1.51	
17	0.03 M	1.0 mol%	Quantity (mg)	119.4	2.6	26.3	11.8	53	117	11.88
			Conc (M)	0.030	0.00010	0.006		0.027	0.045	
			Equivalents	1	0.0032	0.19		0.89	1.50	
18	0.03 M	1.0 mol%	Quantity (mg)	95.8	2.5	28.3	11.82	53	117	11.88
			Conc (M)	0.024	0.00009	0.006		0.027	0.045	
			Equivalents	0.80	0.0031	0.20		0.89	1.50	

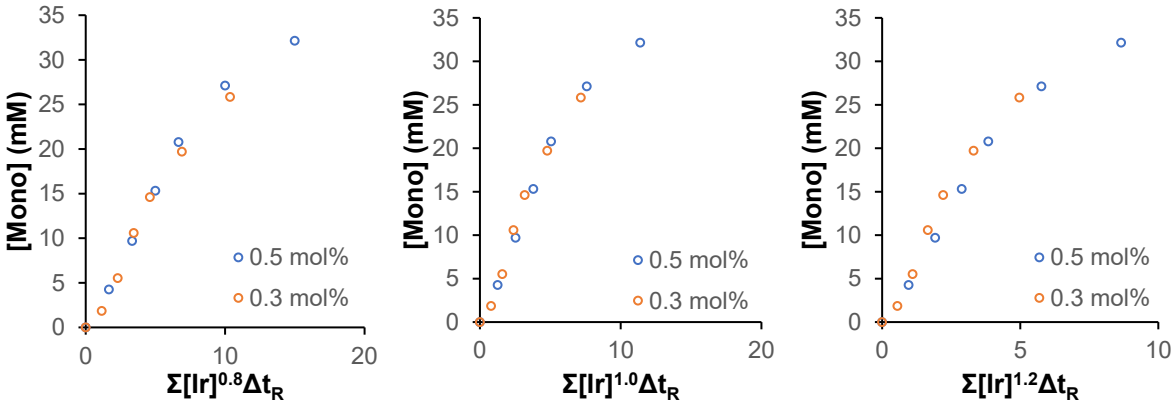
An example of obtaining one of the orders in starting material in this investigation is described here. This is to obtain the order in iridium catalyst using a reaction concentration of 0.05 M and a comparison between 0.5 and 0.3 mol% catalyst loading. Table 35 contains the data obtained from ^{1}H NMR analysis for the two relevant profiles.

Table 35: Concentration data used for two profiles used for VTNA analysis.

	Time (min)	Concentration (mM)[a]				
		[91]	[Mono]	[Di]	[Mono + Di]	[Mono + 2Di]
Reaction concentration: 0.05 M Catayst loading: 0.5 mol%	0[b]	50.0	0.0	0.0	0.0	0.0
	5	45.5	4.3	0.27	4.5	4.8
	10	39.6	9.7	0.7	10.4	11.1
	15	33.6	15.3	1.1	16.4	17.5
	20	26.9	20.8	2.3	23.1	25.5
	30	18.1	27.1	4.8	32	36.8
	45	8.8	32.1	9.1	41.2	50.3
Reaction concentration: 0.05 M Catayst loading: 0.3 mol%	0[b]	50.0	0.0	0.0	0.0	0.0
	5	47.9	1.9	0.3	2.1	2.4
	10	44.0	5.5	0.5	6.0	6.4
	15	38.7	10.6	0.7	11.3	12.0
	20	34.3	14.6	1.1	15.7	16.8
	30	28.0	19.7	2.3	22.1	24.4
	45	20.6	25.8	3.6	29.5	33.1

[a]Data obtained from integrations in ^{1}H NMR spectra against 1,4-dimethyl terephthalate as an internal standard. [b]Zero timepoint not measured, indicates starting concentrations in flask.

The time and change in concentration of **Ir-15** information was used to obtain the 'time normalised' profile using equation 9. Normalised time was plotted against concentration for each of the different excess profiles. As before, the exponent α was varied and the value which gave the best overlay described the order in starting material. The data in Table 35 had the best overlay when α was 1.0. The graphs obtained at α = 0.8, 1.0 and 1.2 are depicted in Figure 51 for both mono concentration and (mono + 2Di) concentration.



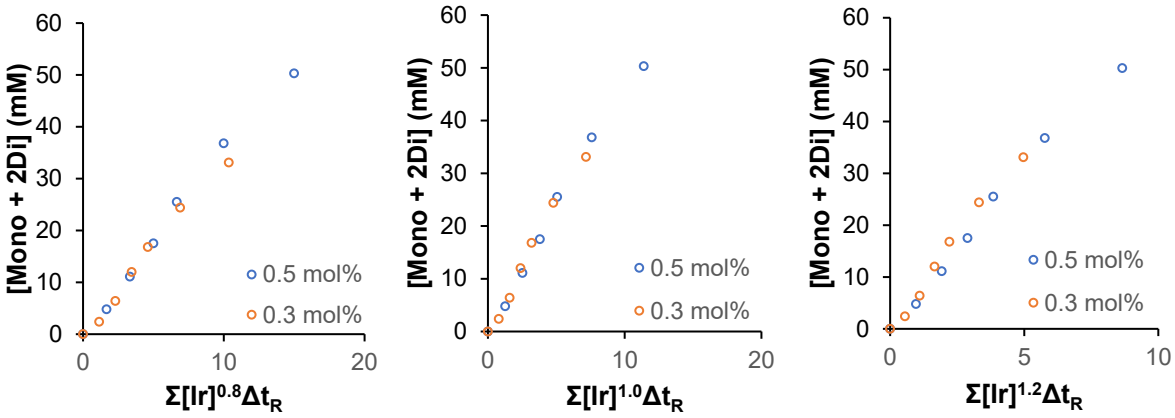
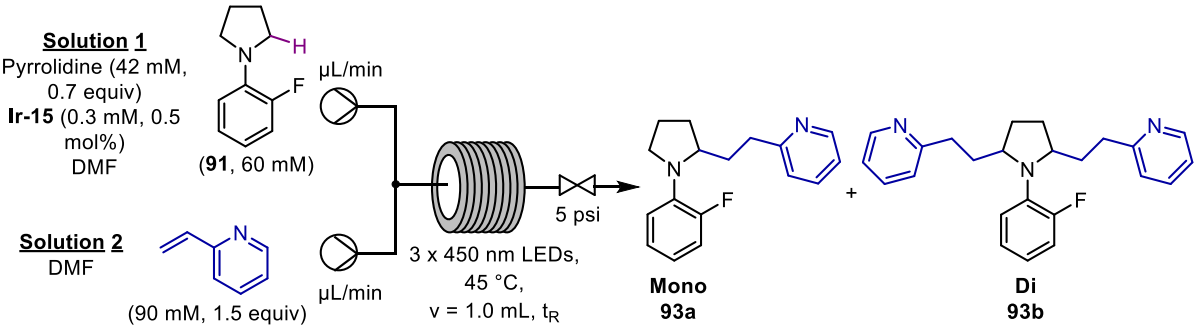


Figure 51: VTNA graphs depicting concentration against normalised time.

The different excess analysis was performed by overlaying two profiles in each case, with the concentration in either catalyst or starting material varied in order to determine the order in catalyst or starting material respectively.

General procedure D: photoredox kinetic profiles 0.03 M reaction



The recirculating water bath was set to 45 °C to pre-heat the photoreactor to the desired temperature. *N*-(2-Fluorophenyl)pyrrolidine **91** (118 mg, 0.71 mmol, 1 equiv), Ir[dF(CF$_3$)ppy]$_2$(dtbbpy)PF$_6$ (4.0 mg, 0.00036 mmol, 0.5 mol%), dimethyl terephthalate (28 mg, 0.14 mmol, 0.2 equiv) and pyrrolidine (42 µL, 0.51 mmol, 0.7 equiv) were added to a flame dried flask and dissolved in DMF to give 12 mL of 0.03 M solution w.r.t substrate **91**. 2-Vinylpyridine (117 µL, 1.08 mmol, 1.5 equiv) was dissolved in DMF to give 12 mL of 0.3 M solution. Both solutions were added to 10 mL syringe pumps and the flow rate set depending on the residence time being tested. Once a flow rate was set and the system was at temperature, 3 x 450 nm lights were switched on and the pumps were started. The system was purged for 2 reactor volumes before sample collection at each residence time. Residence times and flow rates were set according to Table 29.

Three consecutive samples were collected at each residence time, these were filtered through a plug of celite, washed with ethyl acetate and concentrated *in vacuo* before analysis by ^{1}H

NMR spectroscopy using 1,4-dimethylterepthalate as an internal standard with a 20 s relaxation time. Reported concentrations and yields are an average of the three samples.

VTNA analysis at 0.03 M reaction conditions: orders in 2-vinylpyridine and pyrrolidine

The reactions were conducted according to general procedure D, with changes from these standard conditions for each profile shown in Table 36.

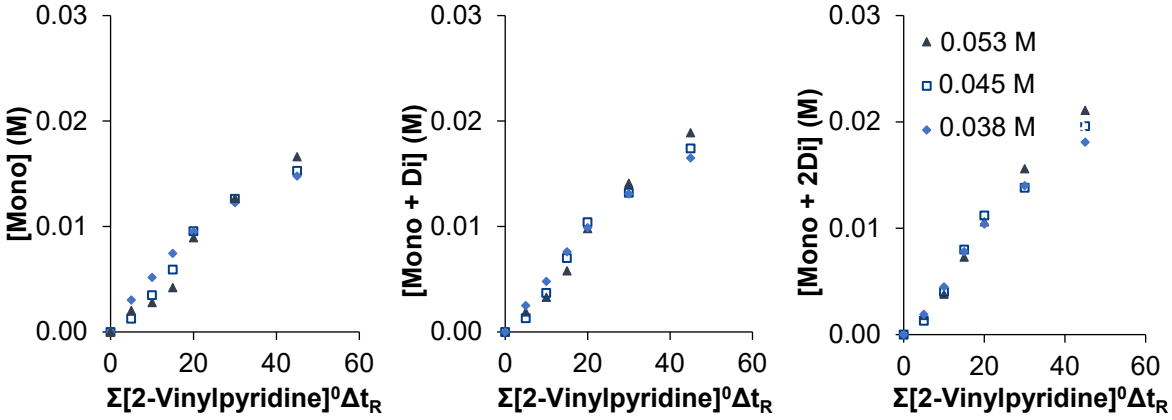
Table 36: Quantities of components used to generate profiles for VTNA analysis at 0.03 M reaction concentration.

Entry	Reaction component	Change from standard conditions	Order in reaction component
1	2-Vinylpyridine	2-Vinylpyridine (136 mg, 1.26 mmol, 0.053 M)	0
2		None: 2-Vinylpyridine (117 mg, 1.08 mmol, 0.45 M)	
3		2-Vinylpyridine (98 µL, 0.91 mmol, 0.038 M)	
4	Pyrrolidine	Pyrrolidine (54 mg, 0.66 mmol, 0.09 M)	0
5		Pyrrolidine (42 mg, 0.51 mmol, 0.0 M)	
6		Pyrrolidine (30 mg, 0.37 mmol, 0.05 M)	

In each instance concentrations were determined using ^{1}H NMR spectroscopy using 1,4-dimethylterepthalate as an internal standard with a 20 s delay (D1). Graphs of concentration against a normalised time axis (this latter obtained by applying the time normalisation equation as described in equation 9) were then plotted for each reaction component as described in Table 36. The exponent α was varied and the value of best overlays determined for each reaction component. Graphs depicting the best overlay for 2-vinylpyridine and pyrrolidine at 0.03 M reaction concentration and 0.5 mol% are presented in Figures 24 and 52.

The profile data for these experiments can be located at the Imperial College London Data Repository, DOI: 10.14469/hpc/13406, https://data.hpc.imperial.ac.uk/resolve/?doi=13406&access=z7gy-h4cq. Access code: z7gy-h4cq, in an Excel document titled ‘VTNA components 0.03 M’.

Order in 2-Vinylpyridine



Order in Pyrrolidine

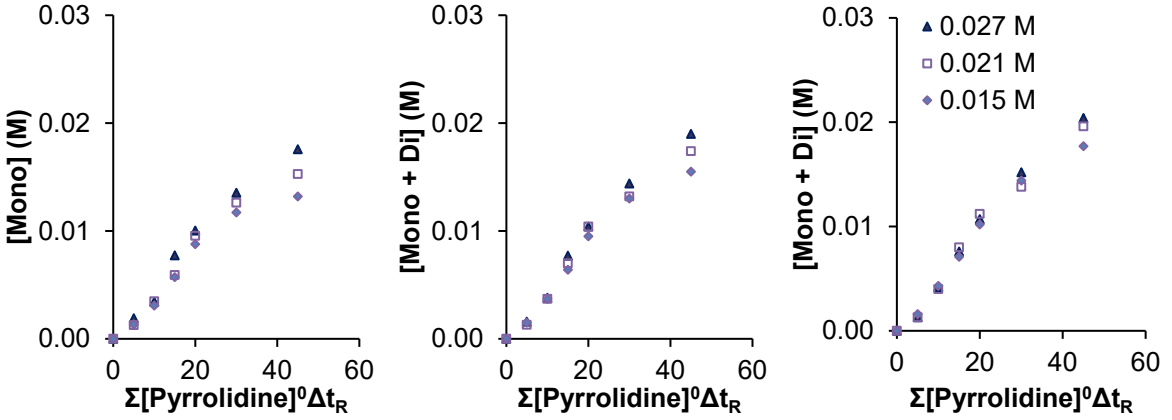


Figure 52: Graphs depicting concentration against a normalised time axis, using the value of α chosen to give the best profile overlay, to obtain orders in acceptor and base.

4.7.3. Same excess experiments

Substrate 91 control profile:

The control profile was conducted according to general procedure D.

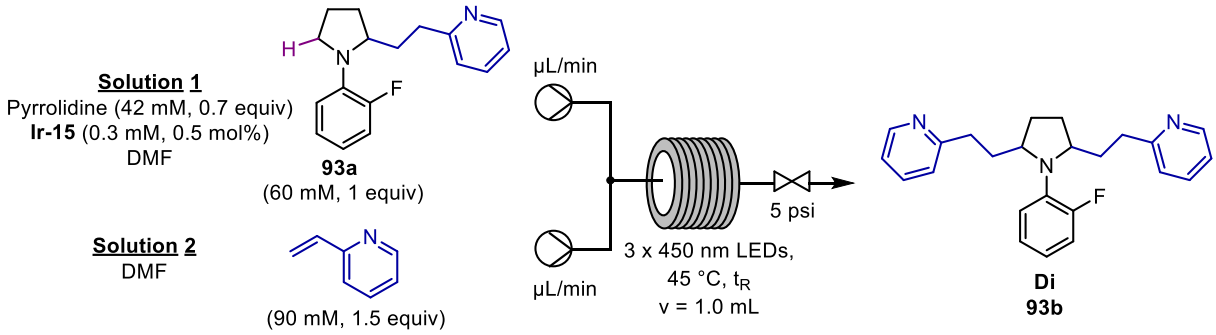
Substrate 91 same excess profile: A recirculating water bath was set to 45 °C to pre-heat the photoreactor to the desired temperature. *N*-(2-fluorophenyl)pyrrolidine **91** (161 mg, 0.97 mmol, 1 equiv), $Ir[dF(CF_3)ppy]_2(dtbbpy)PF_6$ (6.8 mg, 0.0061 mmol, 0.6 mol%) and dimethyl terephthalate (46 mg, 0.24 mmol, 0.24 equiv) were added to a volumetric flask under argon and dissolved in DMF (15 mL). Pyrrolidine (70 µL, 0.85 mmol, 0.87 equiv) was then added to the same volumetric flask and dry DMF added to form a 20 mL solution. In a separate 20 mL volumetric flask, dry DMF (15 mL) was added under argon followed by 2-vinylpyridine (168 µL,

1.56 mmol, 1.6 equiv) and the remainder of the DMF required to make a 20 mL solution. The solutions were added to 10 mL syringes and loaded onto a syringe pump. The flow rate was set depending on the residence time being tested. Once a flow rate was set and the system was at temperature, 3 x 450 nm lights were switched on and the pumps were started. The system was purged for 2 reactor volumes before sample collection at each residence time. Residence times and flow rates were set according to Table 29. The same excess graphs were plotted according to Table 37, with concentration against time plotted for each profile. Plots of these results are presented in Figure 27, section 2.3.3.

Table 37: Same excess analysis for standard reaction.

t_R	Control profile (mM)		Same excess profile (mM)			
	93a (Mono)	**91 (SM)**	**Time + 10 (min)**	**93a (Mono)**	**93a (Mono) + 5.05**	**93a (SM)**
0	0	30	10	0	5.05	24
5	2.17	27.6	15	2.15	7.20	22.2
10	5.05	24.5	20	4.77	9.82	19.5
15	8.31	20.9	25	7.99	13.04	15.9
20	11.48	17.4	30	10.39	15.44	13.1
30	14.74	13.4	40	12.70	17.75	9.7
45	17.6	8.9	55	20.35	25.40	-0.8

Mono to di control profile



The recirculating water bath was set to 45 °C to pre-heat the photoreactor to the desired temperature. Mono-alkylated **93a** (324 mg, 1.20 mmol, 1 equiv), $Ir[dF(CF_3)ppy]_2(dtbbpy)PF_6$ (6.7 mg, 0.0060 mmol, 0.5 mol%) and dimethyl terephthalate (46 mg, 0.24 mmol, 0.20 equiv) were added to a volumetric flask under argon and dissolved in DMF (15 mL). Pyrrolidine (70 µL, 0.85 mmol, 0.70 equiv) was then added to the same volumetric flask and dry DMF added to form a 20 mL solution. In a separate 20 mL volumetric flask, dry DMF (15 mL) was

added under argon followed by 2-vinylpyridine (195 µL, 1.81 mmol, 1.5 equiv) and the remainder of the DMF required to make a 20 mL solution. The solutions were added to 10 mL syringes and loaded onto a syringe pump. The flow rate was set depending on the residence time being tested. Once a flow rate was set and the system was at temperature, 3 x 450 nm lights were switched on and the pumps were started. The system was purged for 2 reactor volumes before sample collection at each residence time. Residence times and flow rates were set according to Table 29 up to 30 min residence time.

Mono to di same excess profile: The reaction conditions were chosen based on the concentrations in the control profile at 15 mins residence time. The recirculating water bath was set to 45 °C to pre-heat the photoreactor to the desired temperature. Mono-alkylated **93a** (285 mg, 1.05 mmol, 1 equiv), $Ir[dF(CF_3)ppy]_2(dtbbpy)PF_6$ (6.7 mg, 0.0060 mmol, 0.5 mol%) and dimethyl terephthalate (46 mg, 0.24 mmol, 0.22 equiv) were added to a volumetric flask under argon and dissolved in DMF (15 mL). Pyrrolidine (70 µL, 0.85 mmol, 0.81 equiv) was then added to the same volumetric flask and dry DMF added to form a 20 mL solution. In a separate 20 mL volumetric flask, dry DMF (15 mL) was added under argon followed by 2-vinylpyridine (172 µL, 1.60 mmol, 1.5 equiv) and the remainder of the DMF required to make a 20 mL solution. The solutions were added to 10 mL syringes and loaded onto a syringe pump. The flow rate was set depending on the residence time being tested. Once a flow rate was set and the system was at temperature, 3 x 450 nm lights were switched on and the pumps were started. The system was purged for 2 reactor volumes before sample collection at each residence time. Residence times and flow rates were set according to Table 29 up to 30 min residence time. The same excess graphs were plotted according to Table 38 of concentration against time for each profile.

Table 38: Same excess analysis for mono-alkylated to di-alkylated product formation.

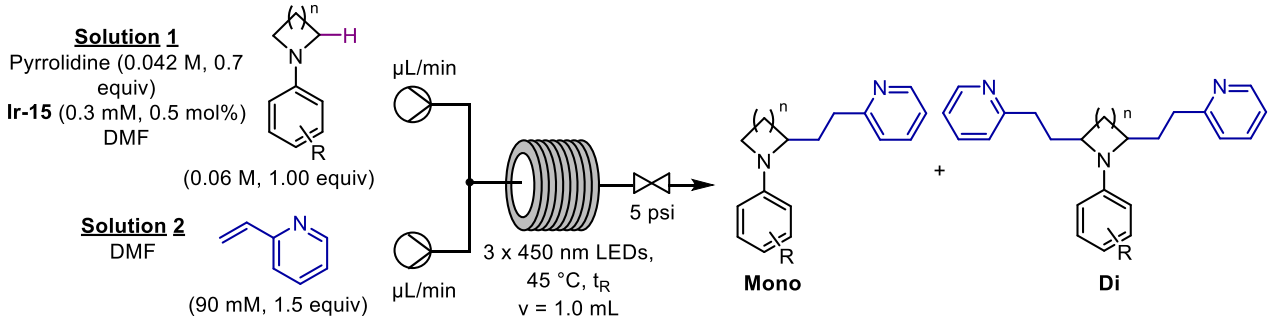
Residence time	Control profile (mM)		Same excess profile (mM)			
	Mono 93a	Substrate 91	Time + 15 (min)	Mono 93a	Mono + 5.05	Substrate 91
0	0.00	30.00	15	0.00	5.21	26.37
5	1.96	28.82	20	1.70	6.91	24.72
10	3.17	28.31	25	3.24	8.45	23.31
15	5.21	26.33	30	4.85	10.06	21.78
20	7.21	24.49	35	5.83	11.04	21.05
30	9.87	22.55	45	8.28	13.49	18.52
45	14.37	19.41	-	-	-	-

Data in Table 38 is presented graphically in Figure 28, section 2.3.3. The profile data for these experiments can be located at the Imperial College London Data Repository, DOI:

10.14469/hpc/13406, https://data.hpc.imperial.ac.uk/resolve/?doi=13406&access=z7gy-h4cq. Access code: z7gy-h4cq, in an Excel document titled 'Same excess 0.03 M'.

4.7.4. Comparing different substrates

General procedure E: Profiles to obtain reaction rate with different substrates



The amine substrate (1.2 mmol, 1.00 equiv) was added to a 20 mL volumetric flask followed by photocatalyst $Ir[dF(CF_3)ppy]_2(dtbbpy)PF_6$ (6.7 mg, 0.006 mmol, 0.5 mol%), and dimethyl terepthalate (46 or 47 mg, 0.24 mmol, 0.2 equiv). The flask was put under argon, then the contents were dissolved in dry DMF (~18 mL), followed by addition of pyrrolidine (70 µL, 0.84 mmol, 0.7 equiv) and the remainder of the DMF required to make a 20 mL solution (0.06 M w.r.t. amine substrate).

In a second volumetric flask, dry DMF (~ 18 mL) was added to a 20 mL volumetric flask under argon, followed by addition of 2-vinylpyridine (195 µL, 1.80 mmol) and the remainder of the DMF required to make a 20 mL solution (0.09 M w.r.t. 2-vinylpyridine, 1.5 equiv). The resulting solutions were added to separate syringes, placed in a dual syringe pump and the photoreactor irradiated with 3 × 450 nm Evoluchem LEDs. Once a flow rate was set and the system was at temperature, the pumps were started. The system was purged for 2 reactor volumes before sample collection at each residence time. Residence times and flow rates were set according to Table 29.

Rate data was obtained from the concentrations obtained from ^{1}H NMR analysis using the data for concentration of (mono + 2 x di) products for each substrate against time for timepoints 5, 10, 15 and 20 minutes of reaction, as this was typically the linear part of the reaction progression. Linear regression in Excel was used to calculate the rate of reaction from this data. Data for all substrates is presented in Figure 53, as well as in section 2.4.

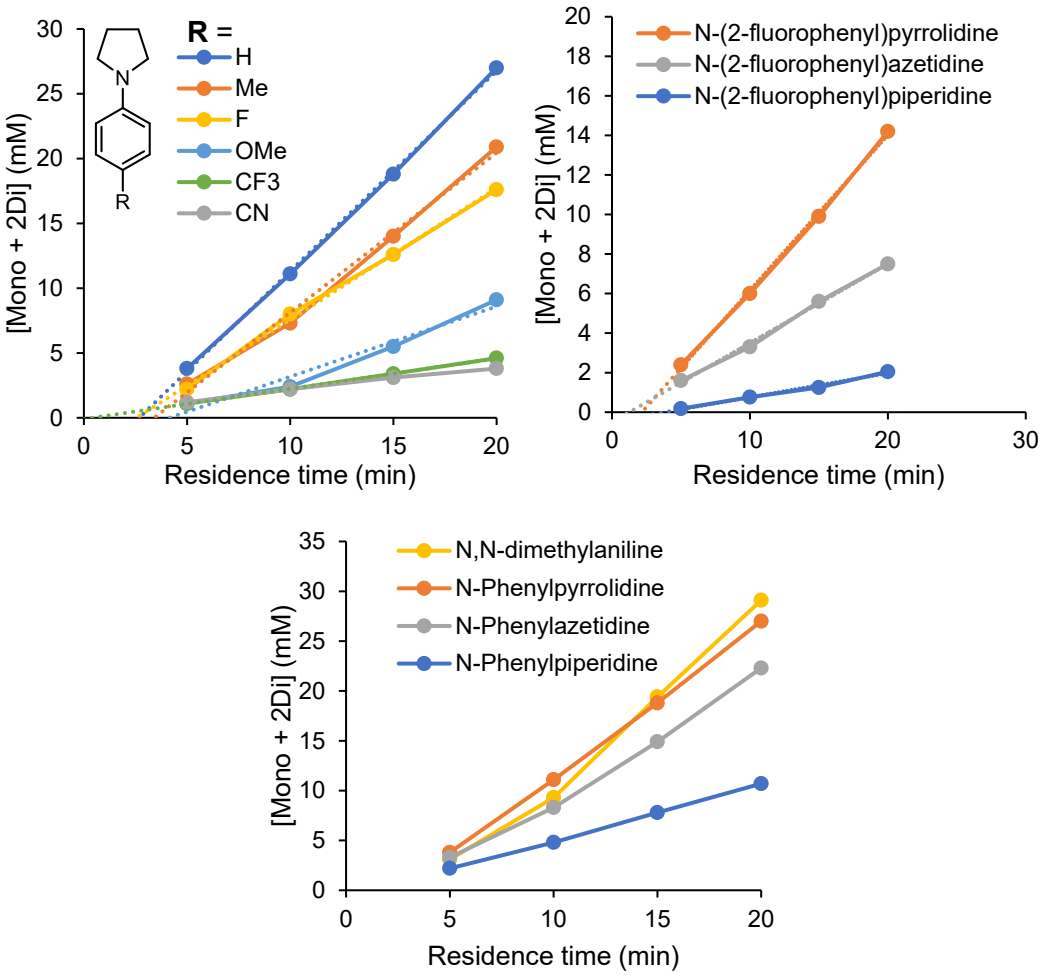
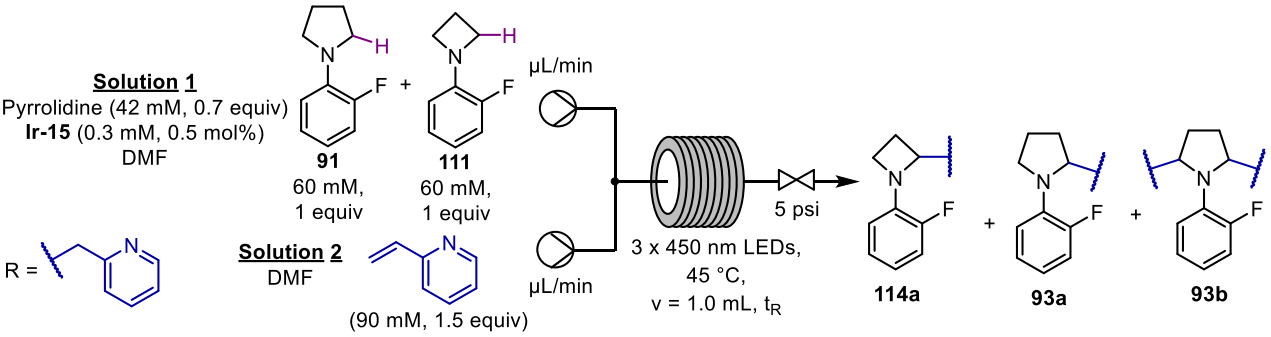


Figure 53: Concentration vs time data used to calculate reaction rates for each substrate.

The profile data for these experiments can be located at the Imperial College London Data Repository, DOI: 10.14469/hpc/13406, https://data.hpc.imperial.ac.uk/resolve/?doi=13406&access=z7gy-h4cq. Access code: z7gy-h4cq.

4.7.5. Competition experiment



Reaction was conducted according to general procedure E to obtain reaction rate, using *N*-(2-fluorophenyl)pyrrolidine (199 mg, 1.2 mmol, 1 equiv) and *N*-(2-fluorophenyl)azetidine (181 mg, 1.2 mmol, 1 equiv) as substrates. Results are shown in section 2.4.2.1 and replicated here in Figure 54.

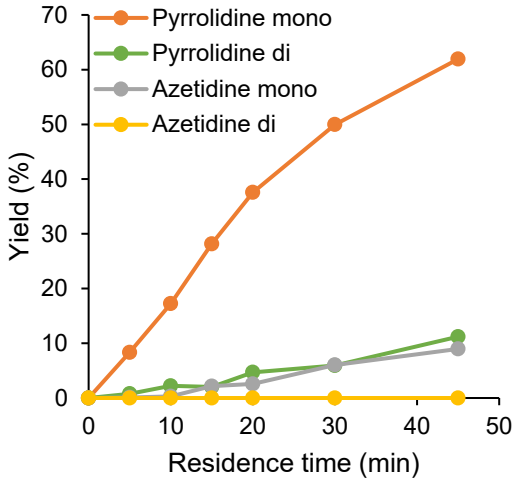
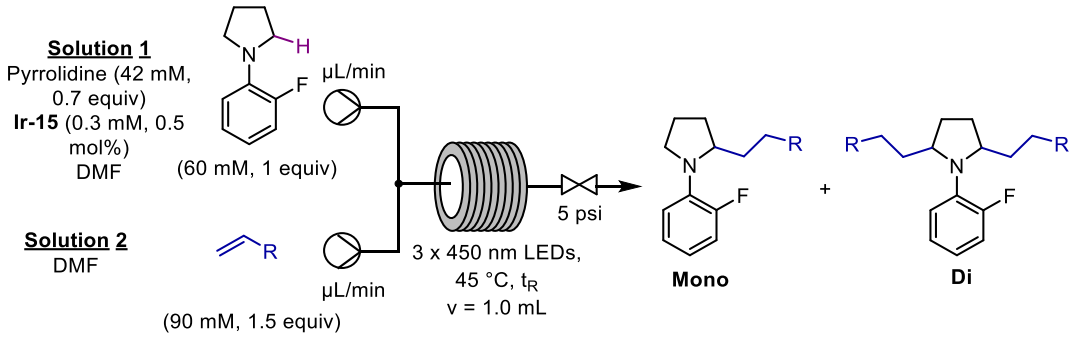


Figure 54: Competition experiment product profile.

4.7.6. Profiles to obtain reaction rate with different acceptors



N-(2-Fluorophenyl)pyrrolidine (1.2 mmol, 1.00 equiv) was added to a 20 mL volumetric flask followed by photocatalyst Ir[dF(CF_3)ppy]$_2$(dtbbpy)PF_6 (6.7 mg, 0.006 mmol, 0.5 mol%), and dimethyl terepthalate (46 or 47 mg, 0.24 mmol, 0.2 equiv). The flask was put under argon, then the contents were dissolved in dry DMF (~18 mL), followed by addition of pyrrolidine (70 µL, 0.84 mmol, 0.7 equiv) and the remainder of the DMF required to make a 20 mL solution (60 mM w.r.t. amine substrate). In a second volumetric flask, dry DMF (~ 18 mL) was added to a 20 mL volumetric flask under argon, followed by addition of acceptor (1.80 mmol) and the remainder of the DMF required to make a 20 mL solution (90 mM w.r.t. acceptor, 1.5 equiv). The resulting solutions were added to separate syringes, placed in a dual syringe pump and the photoreactor irradiated with 3 × 450 nm Evoluchem LEDs. Once a flow rate was set and

the system was at temperature, the pumps were started. The system was purged for 2 reactor volumes before sample collection at each residence time. Residence times and flow rates were set according to Table 29.

Profiles were compared for all products accounting for how many times the catalytic cycle had been completed. N-boc methacrylate and styrene had no di-addition products, so only formation of the one product was used. 2-Vinylpyridine and ethyl acrylate formed a di-alkylation product, therefore the sum of (**mono** and (2 × **di)**) product concentrations was used. Data for all acceptors is presented in Fig 36, section 2.4.4.1 and replicated below (Figure 55).

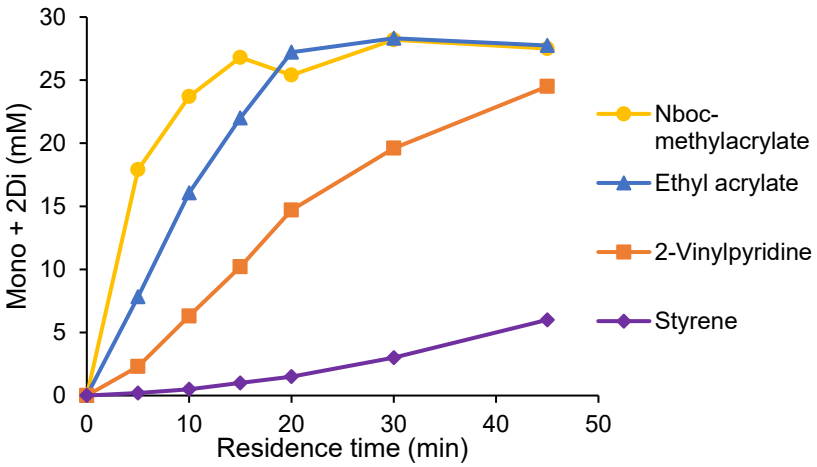
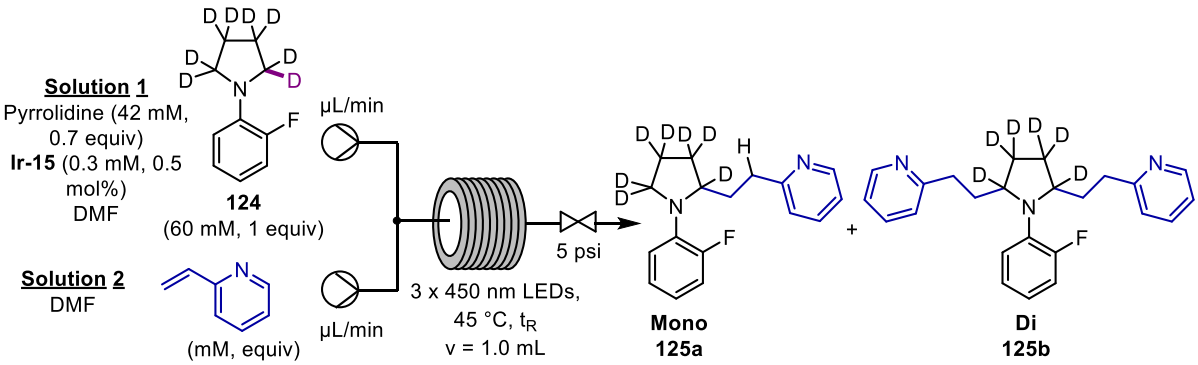


Figure 55: Rates of reaction when using different acceptors.

4.7.7. Kinetic isotope experiments



N-(2-fluorophenyl)pyrrolidine-d_8 **124** (208 mg, 1.2 mmol, 1.00 equiv) was added to a 20 mL volumetric flask followed by photocatalyst Ir[dF(CF_3)ppy]$_2$(dtbbpy)PF_6 (6.7 mg, 0.006 mmol, 0.5 mol%) and dimethyl terepthalate (46 or 47 mg, 0.24 mmol, 0.2 equiv). The flask was put under argon, then the contents were dissolved in dry DMF (~18 mL), followed by addition of

pyrrolidine (70 µL, 0.84 mmol, 0.7 equiv) and the remainder of the DMF required to make a 20 mL solution (0.06 M w.r.t. amine substrate). In a second volumetric flask, dry DMF (~ 18 mL) was added to a 20 mL volumetric flask under argon, followed by addition of acceptor (1.80 mmol) and the remainder of the DMF required to make a 20 mL solution (0.09 M w.r.t. acceptor, 1.5 equiv). The resulting solutions were added to separate syringes, placed in a dual syringe pump and the photoreactor irradiated with 3 × 450 nm Evoluchem LEDs. Once a flow rate was set and the system was at temperature, the pumps were started. The reactor was purged for 2 reactor volumes before sample collection at each residence time. Residence times and flow rates were set according to Table 29.

Three consecutive samples were collected at each residence time, each diluted with deuterated chloroform and analysed by ^{1}H NMR spectroscopy. This was to prevent evaporation of the starting material during concentration, to identify whether there was any loss of deuteration at the α-nitrogen protons (overlay in Figure 56 peak **d** shows α-NCH protons looked for in the spectra. The samples were then filtered, concentrated *in vacuo,* and analysed by ^{1}H NMR spectroscopy using 1,4-dimethylterepthalate as an internal standard with a 20 s delay. Signals used for quantitative analysis are described in Tables 39–41 and depicted in Figures 56–58 for each acceptor as a ^{1}H NMR overlay.

KIE profile with 2-vinylpyridine

Experiment was conducted according to the procedure for kinetic isotope experiments using 2-vinylpyridine (195 µL, 1.8 mmol, 1.5 equiv, 90 mM). Peaks used for calculation of the 2-vinylpyridine profile are detailed in Table 39 and shown in Figure 56. No protonation of the σ-C–H protons was observed, and no deuteration at the CH_2–$Ar_{(pyridine)}$ position was observed.

Table 39: Peaks used for KIE profile determination reaction with 2-vinylpyridine.

Peak	Species	Chemical shift (ppm)	No. of H's	Assignment
a	1,4-Dimethyl terephthalate internal standard	8.13 (s)	4	4 × Ar–CH
b	Mono + Di **125a+b**	8.56–8.45	1 × Mono and 2 × Di	$Ar_{(pyridine)}$–CH mono 2 × $Ar_{(pyridine)}$–CH di
c	Di **125a**	8.49–8.47	1H	Half of peak for 2 × $Ar_{(pyridine)}$–CH
d	Any protonated mono or di	Peaks in range 4.1–3.0	1 × Mono per signal and 2 × Di per	NCH

Note: ranges for integration varied slightly over the course of the reaction, but analogous signals were used in each case.

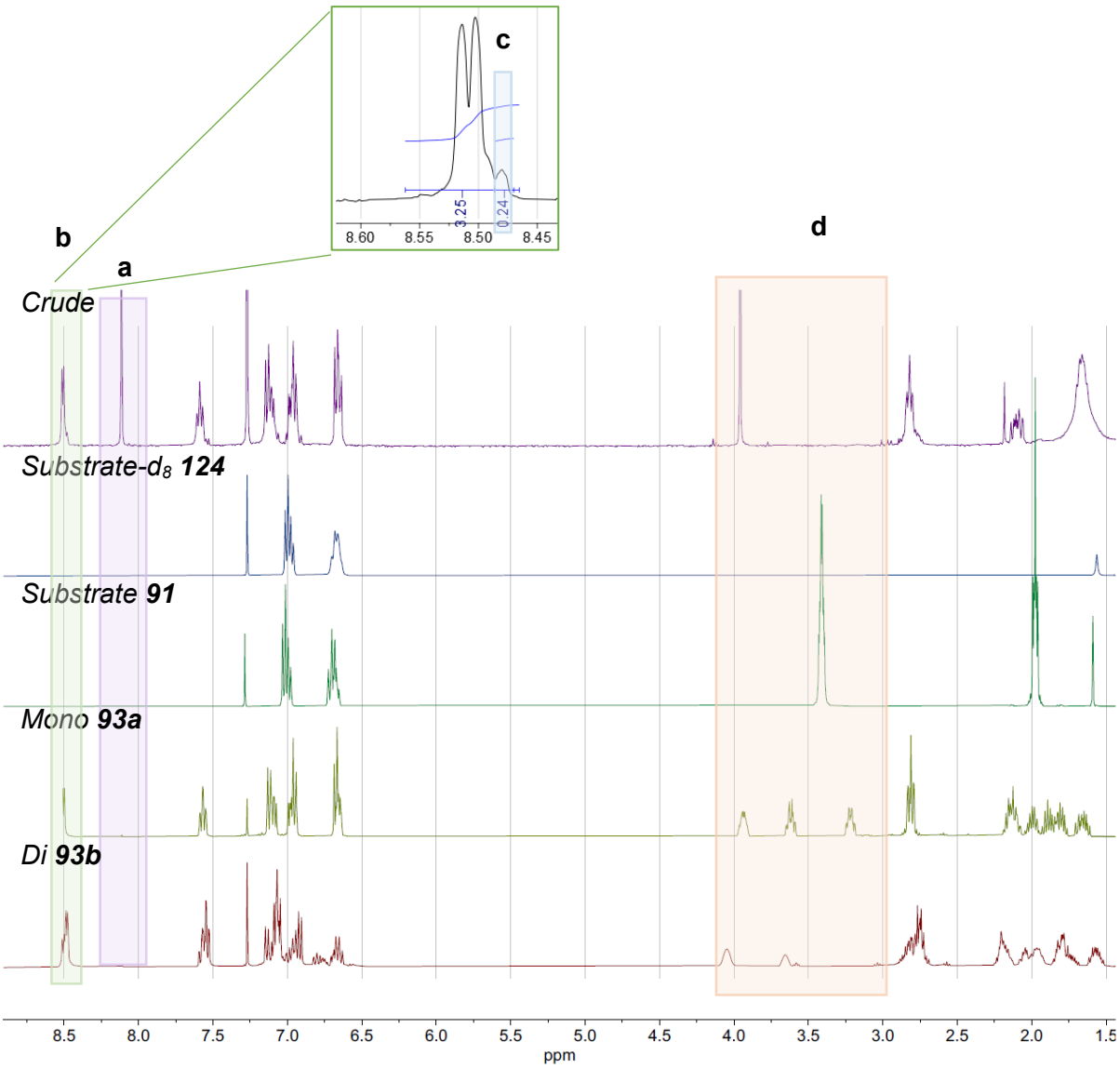


Figure 56: Overlay of a crude reaction mixture ^{1}H NMR for the reaction between deuterated *N*-(2-fluorophenyl)pyrrolidine-d_8 **124** and 2-vinylpyridine used for profile analysis, and deuterated substrate **124**, protonated substrate **91**, and mono and di products **93a** and **93b**.

KIE profile with styrene

Experiment was conducted according to the procedure for kinetic isotope experiments using styrene (207 µL, 1.8 mmol, 1.5 equiv, 90 mM). Peaks used for calculation of the styrene profile are detailed in Table 40 and shown in Figure 57. No protonation of the σ-C–H protons was observed, and no deuteration at the CH_2–$Ar_{(styrene)}$ position was observed.

Table 40: Peaks used for KIE profile determination.

Peak	Species	Chemical shift (ppm)	No. of H's	Assignment
a	1,4-Dimethyl terephthalate internal standard	8.13 (s)	4	4 × Ar–CH
b	Mono **126a**	2.73–2.53	2	$CH_2Ar_{(styrene)}$
c	Any protonated mono or di	Peaks in range 4.1–3.0	1 × Mono per signal	NCH

Note: ranges for integration varied slightly over the course of the reaction, but analogous signals were used in each case.

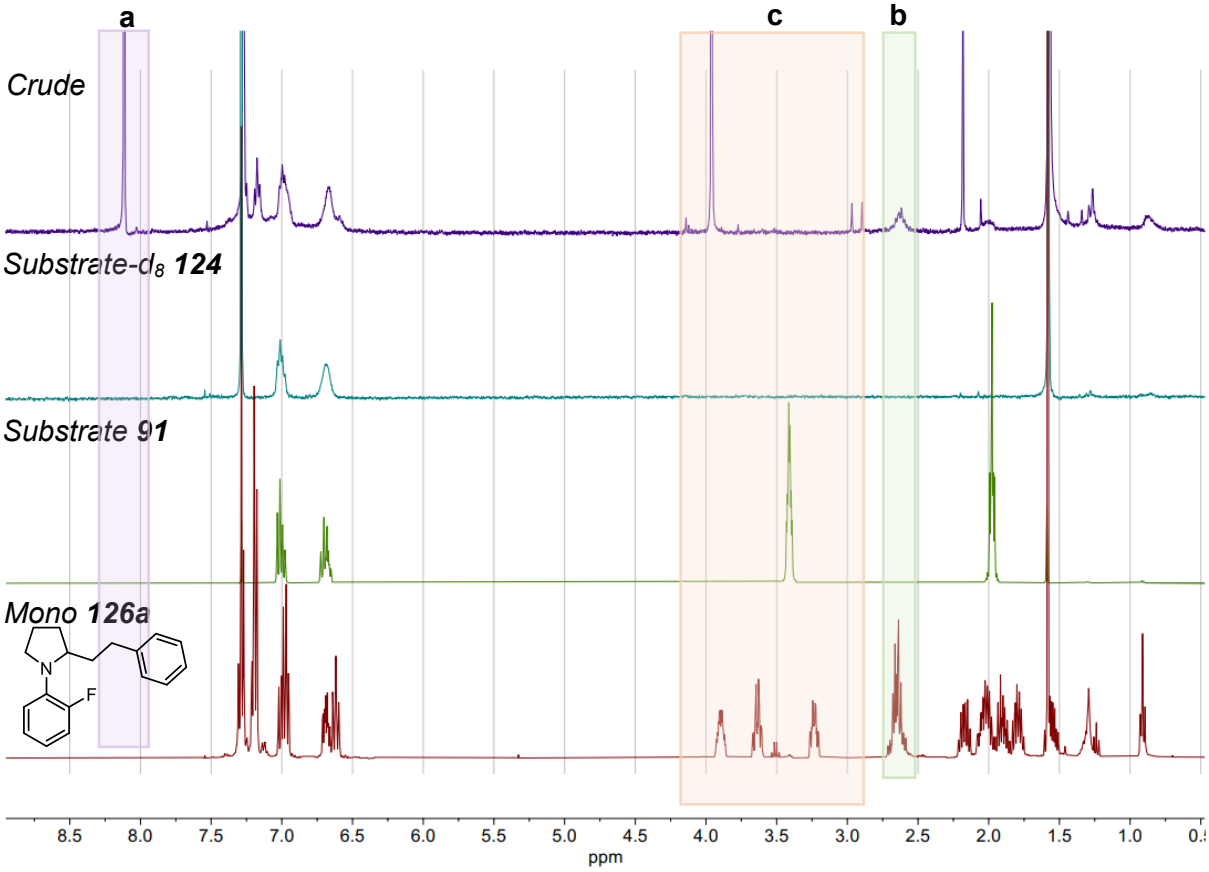


Figure 57: Overlay of a crude reaction mixture ^{1}H NMR for the reaction between deuterated *N*-(2-fluorophenyl)pyrrolidine-d_8 and styrene used for profile analysis, and the deuterated substrate **124**, protonated substrate **91** and mono-alkylated product **126a**. No di-alkylation products were observed in this reaction.

KIE profile with ethyl acrylate

Experiment was conducted according to the procedure for Kinetic isotope experiments using ethyl acrylate (196 µL, 1.8 mmol, 1.5 equiv, 90 mM). Peaks used for calculation of the styrene profile are shown in Figure 58 and detailed in Table 41. No protonation of the σ-C–H protons was observed, and no deuteration at the CH_2–C=O position was observed.

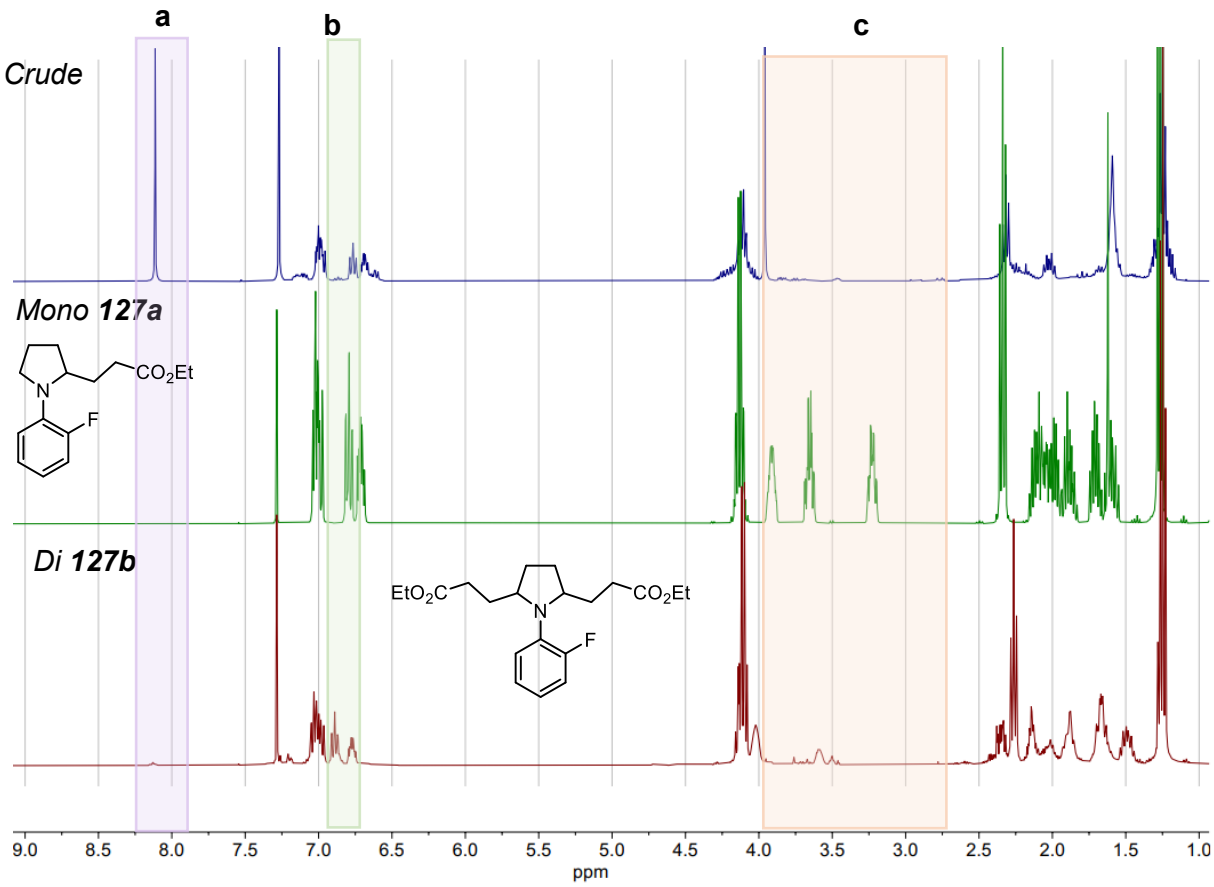


Figure 58: Overlay of a crude reaction mixture ^{1}H NMR for the reaction between deuterated *N*-(2-fluorophenyl)pyrrolidine-d_8 and ethyl acrylate used for profile analysis, and the protonated mono product **127a**, and di product **127b**.

Table 41: Peaks used for profile determination when acceptor was ethyl acrylate.

Peak	Species	Chemical shift (ppm)	No. of H's	Assignment
a	Dimethyl terephthalate internal standard	8.13 (s)	4	4 × Ar–CH
b	Mono + Di **127a+b**	8.56–8.45	1 × Mono and 1 × Di	Ar–CH mono + Ar–CH di

Mono and di products were not individually quantifiable. Therefore, KIE analysis was performed on the combined mono + di signal. This is no expected to be accurate in terms of

the amount of product formed, but having analysed the profiles the same way it was hoped any drastic change in KIE would be observed.

In all cases, due to the absence of NCH peaks usually used for analysis in the deuterated material, the control profile it was compared to was re-processed using the same peaks and integration. Rate data was determined from the concentrations obtained from ^{1}H NMR analysis using the data for concentration of (mono + (2 x di)) products for the reaction with 2-vinylpyridine and ethyl acrylate and mono for the reaction with styrene (only one product). Data at timepoints 5, 10, 15 and 20 minutes of reaction was used, as this was typically the linear part of the reaction progression, and compared to the rate of reaction of the same acceptor with *N*-(2-fluorophenyl)pyrrolidine. Linear regression in Excel was used to calculate the rate of reaction from this data. Data for all acceptors is presented in Figure 59.

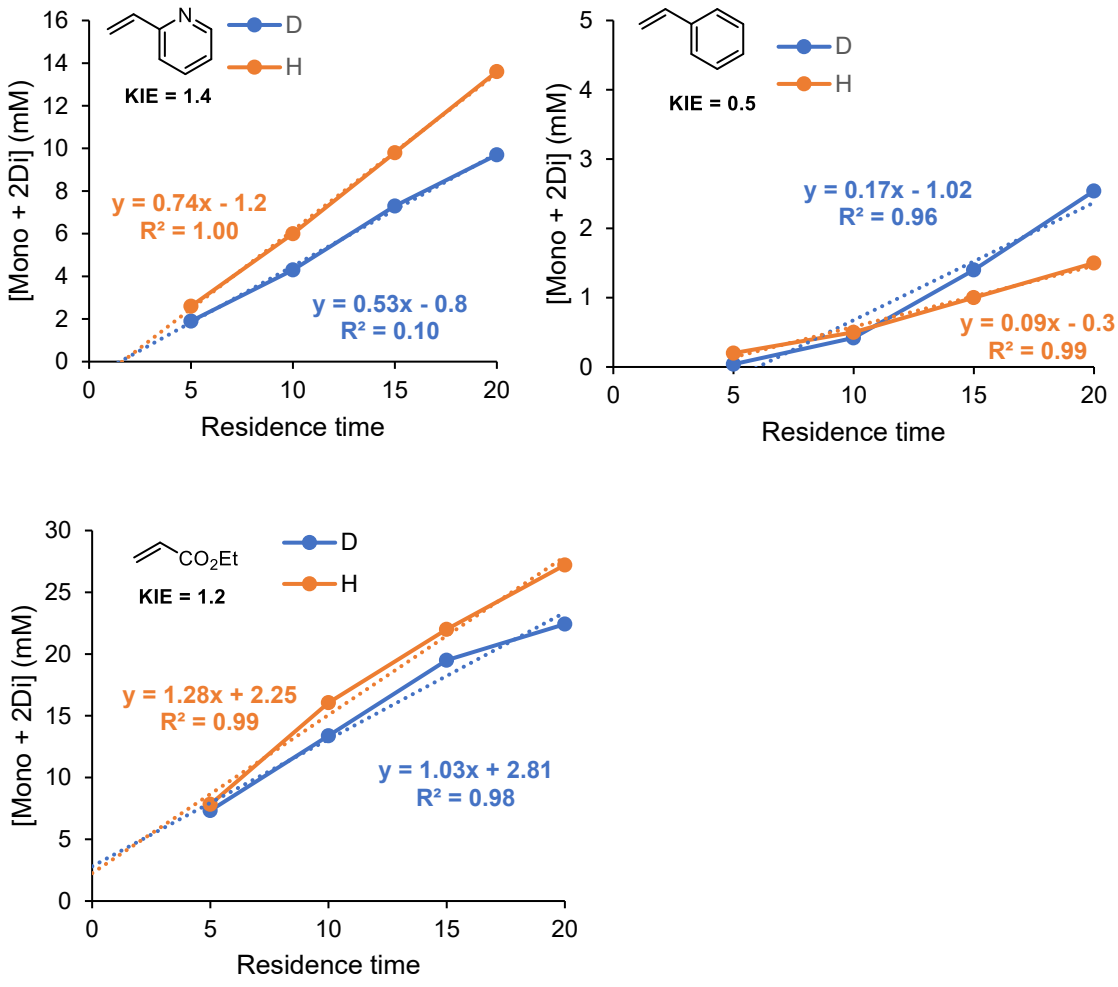


Figure 59: KIE experiment data for different acceptors.

Note there was no loss of deuteration at any α-C–D positions in the starting material or products. No new deuterium incorporation was observed in any products.

4.8. Hammett analysis

Rates for different substrates were obtained according to General procedure E, and data for the Hammett analysis obtained according to Table 42. A plot of this data is shown in Figure 31, section 2.4.1.1.

Table 42: Data for Hammett analysis.

Substituent (R =)	Rate (mM/Min)	σ_p	Log (K_X/K_H)
H	1.55	0.00	0.00
Me	1.23	−0.17	−0.10
F	1.02	0.06	−0.18
OMe	0.54	−0.27	−0.46
CF_3	0.23	0.54	−0.82
CN	0.17	0.66	−0.95

4.9. Swain-Lupton analysis

Rates for different substrates were obtained according to General procedure E, oxidation potential data was determined by cyclic voltammetry according to section 4.9 and quenching constants k_q were determined according to Stern-Volmer luminescence quenching experiments as described in section 4.10. Modified Swain-Lupton field F and resonance R constants were obtained from Taft and co-workers.[118] Regression analysis in Excel was used to find α in each instance using the measured parameter (oxidation potential, k_q, or rate data respectively) and the F and R constants. In each instance the value of α was found without including data for the substrate with an OMe substituent. This data is summarised in Table 43, and presented graphically in Figure 32, section 2.4.1.2.

Table 43: Swain-Lupton analysis.

Substituent	Oxidation potential (E_{pa}, V vs SCE)	k_q (10^9, $M^{-1}.s^{-1}$)	Rate [M+2Di] (mM)	F	R	σ = αF + R		
						Redox α = 0.89	kq α = 1.40	[M+2Di] α = 1.49
H	0.93	3.2	1.55	0.03	0	0.03	0.04	0.04
Me	0.75	4	1.23	0.01	-0.18	-0.17	-0.17	-0.17
F	0.93	2.8	1.02	0.45	-0.39	0.01	0.24	0.28
CF_3	1.53	1.7	0.23	0.38	0.16	0.50	0.69	0.73
CN	2	1.4	0.17	0.51	0.15	0.60	0.86	0.91
OMe	1.1	2.6	0.54	0.29	-0.56	-0.30	-0.15	-0.13

4.10. Cyclic Voltammetry

Cyclic voltammetry (CV) measurements were performed on an Autolab PGSTAT204 potentiostat from Metrohm and processed using Nova 2.1 software. All electrodes used were obtained from Metrohm: a glassy carbon electrode (3 mm surface area circular disk) was used as the working electrode, a platinum electrode was used as a counter electrode and an Ag/AgCl electrode used as a reference electrode.

Cyclic voltammograms were measured at room temperature, using a voltage range of −1.0 to +2.0 V, unless otherwise specified, at 100 mV s^{-1} rate starting at 0 V in the positive scan direction, in 10 mV steps and with 1 mA current range. The glassy carbon electrode was polished before measurements and between measurement of each analyte using an aqueous suspension of nanometric alumina. Cyclic voltammograms were obtained using a 0.1 M solution of $LiClO_4$ in DMF as supporting electrolyte, sparged with argon before each measurement. For each measurement, a blank CV measurement was taken first, the analyte being tested was then added to the cell to form a 5 mM solution and a second CV was recorded. Ferrocene (Fc) was then added to the analyte solution as an internal standard[131] to form a 5 mM solution and the CV recorded again. For each of the measurements, 3 scans were recorded and results for the 3rd scan was used. The analyte and ferrocene CV was used, blank corrected, to obtain redox potentials.

Anodic peak potentials (E_{pa}) were referenced to the E1/2 of ferrocene (Fc^+/Fc), then were reported vs the standard calomel electrode following conversion from V vs Fc^+/Fc to V vs SCE by addition of 0.38 V.[132] As the compounds tested had irreversible oxidation waves, peak anodic potentials were reported in each case.[56] Values were exported from the Nova software as Excel files. E_{pa} data for all compounds is presented in Table 44. See appendix section 6.1 for cyclic voltammogram data.

Table 44: Cyclic voltammogram data for all tested compounds.

Entry	Substrate	E / V			
		E_{pa} (Obs)	$E_{1/2}$ (Fc^+/Fc)	E_{pa} (vs Fc^+/Fc)	E_{pa} (vs SCE)
1[b]	*N*-(2-Fluorophenyl)pyrrolidine	+1.34	+0.59	+0.75	+1.13
2[a b]	Mono **93a**	+1.32	+0.63	0.69	+1.07
3[a,b]	Di **93b**	+1.26	+0.63	0.63	+0.97
4[b]	2-Vinylpyridine	>+1.50	+0.56	>+0.94	>+1.32
5[a]	Pyrrolidine	>+1.50	+0.63	>+0.87	>+1.25
6	*N*-(2-Fluorophenyl)azetidine	+1.48	+0.59	+0.89	+1.27
7	*N*-(2-Fluorophenyl)piperidine	+1.58	+0.57	+1.01	+1.39
8	*N*-(2-Fluorophenyl)morpholine	+1.51	+0.62	+0.89	+1.27
9[b]	*N*-(4-Fluorophenyl)pyrrolidine	+1.17	+0.62	+0.55	+0.93
10	*N*-(4-Methylphenyl)pyrrolidine	+0.95	+0.58	+0.37	+0.75
11[b]	*N*-(4-Methoxyphenyl)pyrrolidine (E_{pa1})	+0.80	+0.62	+0.18	+0.56
	N-(4-Methoxyphenyl)pyrrolidine (E_{pa2})	1.34	+0.62	+0.72	+1.10
12	*N*-Phenylpyrrolidine	+1.11	+0.56	+0.55	+0.93
13	*N*-(4-Trifluoromethylphenyl)pyrrolidine	+1.77	+0.62	+1.15	+1.53
14	*N*-(4-Cyanophenyl)pyrrolidine	>+2.00	+0.66	>+1.34	>+1.72
15	*N*,*N*-Dimethylaniline	+1.38	+0.59	+0.79	+1.17
16	*N*-Phenylazetidine	+1.36	+0.52	+0.84	+1.22
17	*N*-Phenylpiperidine (E_{pa1})	+1.43	+0.66	+0.77	+1.15
	N-Phenylpiperidine (E_{pa2})	+1.83	+0.66	+1.17	+1.55
18	N-(2-Fluorophenyl)pyrrolidine-d_8	+1.19	+0.50	+0.69	+1.07

[a]In these measurements, ferrocene was run as a separate cyclic voltammagram following the analyte rather than in solution with the analyte. [b]Scan performed between −0.5 and +1.5 V.

4.11. Stern-Volmer luminescence quenching experiments

Luminescence emission spectra were recorded on a Carey Eclipse Fluorescence Spectrophotometer. A solution of $Ir[dF(CF_3)ppy]_2(dtbbpy)PF_6$ in DMF (0.05 mM) was prepared in a 10 mL volumetric using dry DMF under an argon atmosphere (solution 1). In a separate 5 mL volumetric flask, a quencher was added (0.1 mmol) followed by addition of solution 1 to form 5 mL of a 20 mM solution w.r.t. quencher and 0.05 mM w.r.t. photocatalyst (solution 2). All solutions were kept in the dark by being wrapped in foil and prepared in a fumehood with the light off unless when not in the fluorescence spectrometer.

A portion of solution 1 (2 mL) was transferred to a quartz cuvette under argon with a pathlength of 10 mm. The luminescence emission spectrum was measured at 450 nm wavelength, with data collected between 450–600 nm. Consecutive 10 µL portions of quencher solution 2 were added to the quartz cuvette to increase the concentration of quencher in the vial by 0.1 mM on each addition. Between each addition the cuvette was sparged with argon for 30 s and the luminescence emission spectrum of the solution then recorded three times using a Carey Eclipse Fluorescence Spectrophotometer irradiated at 450 nm, with spectra collected between 450 and 600 nm. The experiment was conducted three times for each sample unless otherwise specified.

The emission intensity at the wavelength of maximum luminescence emission (λ_{max}) was recorded at each concentration of quencher (example given in Figure 60A). These values were used to calculate I_0/I_q at each concentration. A graph of the average I_0/I_q values for all three repeats was plotted against averaged concentration (example given in Figure 60B) to find the Stern Volmer constant, K_{SV}, according to equation 11, section 2.3.2.2. K_{SV} was calculated using linear regression in Excel. Any repeats were averaged to obtain the K_{SV}. K_{SV} was then converted to k_q using equation 12 and the excited-state lifetime of the photocatalyst, 2.3 µs.[24]

This experiment was repeated for each of the tested compounds, with data provided in Table 45 and averaged graphs of I_0/I_q against concentration for each compound available in appendix section 6.2.

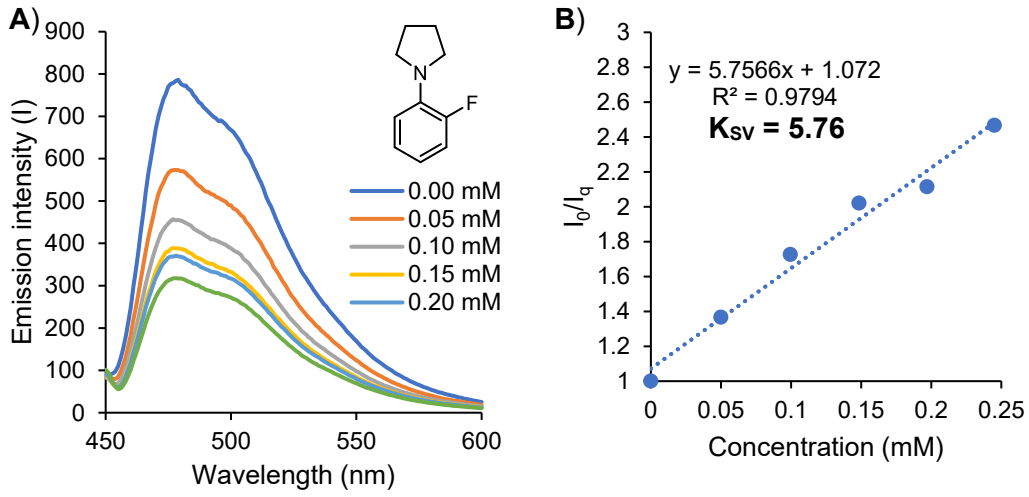


Figure 60: A) Luminescence emission spectrum of *N*-(2-fluorophenyl)pyrrolidine at different concentrations of **91**. B) Graph of I_0/I_q against concentration obtained at the maximum emission wavelength of graph A.

Table 45: Stern-Volmer data for all tested compounds.

Entry	Reaction component	K_{SV} (mM^{-1})	R^2	k_q (10^9, $M^{-1}.s^{-1}$)
1	*N*-(2-fluorophenyl)pyrrolidine	5.3	1.00	2.3
2[a]	Mono **93a**	3.6	0.99	1.6
3[a]	Di **93b**	4.1	1.00	1.8
4[a]	2-Vinylpyridine	0.6	0.65	0.3
5[a]	Pyrrolidine	1.3	0.88	0.6
6[a]	*N*-(2-fluorophenyl)pyrrolidine + Pyrrolidine	6.8	0.98	3.0
7	*N*-(4-methylphenyl)pyrrolidine	9.3	1.00	4.0
8[b]	*N*-phenylpyrrolidine	7.3	1.00	3.2
9[b]	*N*-(4-fluorophenyl)pyrrolidine	6.5	1.00	2.8
10	*N*-(4-trifluoromethylphenyl)pyrrolidine	4.0	1.00	1.7
11[a]	*N*-(4-methoxyphenyl)pyrrolidine	6.0	0.98	2.6
12	*N*-(4-cyanophenyl)pyrrolidine	3.2	0.99	1.4
13	*N*-(2-fluorophenyl)azetidine	4.7	1.00	2.0
14[b]	*N*-(2-fluorophenyl)piperidine	2.6	0.99	1.1
15[b]	*N*-(2-fluorophenyl)morpholine	1.5	1.00	0.7
16	*N*,*N*-dimethylaniline	7.5	1.00	3.3
17	*N*-phenylazetidine	5.9	1.00	2.6
18	*N*-phenylpiperidine	5.3	0.99	2.3
19	*N*-(2-fluorophenyl)pyrrolidine-d8	5.9	1.00	2.6
20	Styrene	0.6	0.29	0.2
21	Ethyl acrylate	0.8	0.99	0.4

[a]Experiment was run once. [b]Results given as an average of 2 agreeing profiles, with the third discarded as an outlier.

4.12. General computation considerations

DFT calculations were performed following previously reported methods used to investigate photoredox catalysed reactions involving benzylic oxetane and azetidine radicals.[98]

DFT calculations were performed using Gaussian 16 (revision C01).[133] Unless stated otherwise, calculations were performed at 298.15K (default) and used the ωB97xD density functional (which includes a second-generation dispersion and long-range corrections) with Def2-TZVP basis set (from the Basis Set Exchange).[134] Unless stated otherwise, self-consistent reaction cavity continuum solvation model was used with dimethylformamide as the solvent [scrf=(cpcm, solvent= *N*,*N*-dimethylformamide)]. All geometry optimisations were carried out without any symmetry restrictions (nosymmm). All open-shell systems were calculated using an unrestricted formalism. All transition states were characterised by normal

coordinate analysis revealing precisely one imaginary mode corresponding to the intended reaction.

GoodVibes 3.0.2 was used to calculate all Gibbs free energies (ΔG_{298}) and to perform concentration corrections (c = 1 M) as well as to take into consideration the deviation that could be due to low frequencies.[135] An entropic quasi-harmonic treatment has been applied with frequency cut-off value of 100.0 wavenumber.

Natural Bond Orbital (NBO) analyses were carried out using the NBO 6 program.[136] Natural orbitals and molecular orbitals were plotted using Gaussview 6.1.1. Atomic charges and spin densities were calculated using Natural Population analysis (NPA) implemented in NBO 6 program.

Molecular structures: X-Ray diffraction data of related *N*-arylheterocycles with different aryl substituents were used as a starting point to build the molecular structure of the *N*-arylheterocycle compounds studied here. Thus, molecular structure TUZDEW, EHERAM and AGETUD from the Cambridge Crystallographic Database were used to build *N*-phenylazetidine, *N*-phenylpyrrolidine and *N*-phenylpiperidine respectively.

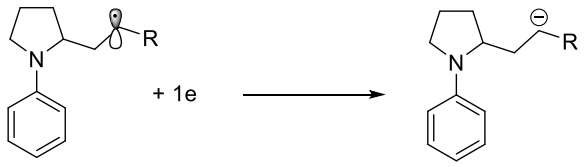
Reduction potentials

Calculations were carried out using M06-2X/def2-TVPD level of theory, and the SMD solvation model was used.[81] The standard free energy $\Delta G°_{298}$ for the reduction reactions in solution (i.e. c = 1 M) were estimated following a simple approach as reported by others, [54,98] based directly on the standard free energies of the reduced ($G°_{red,298}$) and oxidised ($G°_{ox,298}$) species in solution (SMD = DMF, c = 1 M) and taking the free energy of the electron as −0.04 eV (based on the 'ion convention' formalism).[137] The standard reduction potential $E°_{1/2}$ was then calculated using the Nernst equation as expressed in equation 25, with n being the number of electron transferred (i.e. n = 1 for the reduction of the radical species investigated here) and *F* being the Faraday constant (96485 C.mol^{-1}). The calculated value was then corrected to be referenced versus the conventional standard calomel electrode (SCE). More advanced approaches based on thermodynamic cycles considering solvation energies have also been reported.[137]

$$E°_{1/2} = \frac{-\Delta G°}{nF} \qquad (25)$$

Thus, the value of ΔG_{298} and the corresponding $E°_{1/2}$ for the reduction of the different *N*-phenylpyrrolidine (PP) radical derivatives after reaction with the different acceptor (Scheme 32) are provided in Table 46. Considering the experimental reduction potential of −1.37 V for

Ir(III)/Ir(II),[24] the cell potential E_{cell} for the reduction of the radical species by Ir(II) was estimated, along with the corresponding free energy associated with the transformation (ΔG_{cell}).

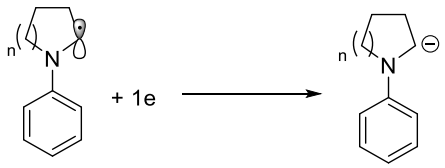


Scheme 32: Reduction of the radical species derivatives (after reaction with the acceptor).

Table 46: Standard Gibbs free energy (ΔG_{298}) and standard reduction potential ($E^{0}_{1/2}$) for the reduction of *N*-phenylpyrrolidine radical derivatives along with cell potential (E_{cell}) and free energies (ΔG_{cell}) corresponding to the their reduction by Ir(II).

Entry	Acceptor	ΔG_{298} (kcal/mol)	$E^{\circ}_{1/2}$ (V)	E_{cell} (V)	ΔG_{cell} (kcal/mol)
1	Styrene	−68.07	−1.57	-0.20	4.66
2	2-vinylpyridine	−74.40	−1.30	0.07	-1.67
3	Ethyl acrylate	--81.61	−0.98	0.39	-8.88

The same analysis was conducted for the reduction of the different *N*-arylheterocycles without reaction with an acceptor (Scheme 33). The value of ΔG_{298} and the corresponding $E^{\circ}_{1/2}$ for the reduction are provided in Table 47, and discussed within the thesis in section 2.4.4.3.



Scheme 33: Reduction of the radical species without reaction with the acceptor.

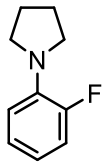
Table 47*:* Standard Gibbs free energy (ΔG_{298}) and standard reduction potential ($E_{1/2}$) for the reduction of *N*-phenylpyrrolidine radical derivatives along with cell potential (E_{cell}) and free energies (ΔG_{cell}) corresponding to the their reduction by Ir(II).

Entry	n	Ring size	ΔG_{298} (kcal/mol)	$E^{\circ}_{1/2}$ (V)	E_{cell} (V)	ΔG_{cell} (kcal/mol)
1	0	4	−58.26	-2.53	-0.63	14.47
2	1	5	−54.42	-2.36	-0.79	18.31
3	2	6	−53.81	-2.33	-0.82	18.92

4.13. Experimental details and compound characterisation

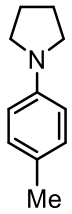
4.13.1. Substrate synthesis

1-(2-Fluorophenyl)pyrrolidine (91)



Potassium carbonate (4.56 g, 33 mmol, 2.2 equiv) and potassium iodide (5.48 g, 33 mmol, 2.2 equiv) were added to a flame-dried flask. The flask was put under argon and acetonitrile (25 mL, 0.6 M) was added, followed by 1,4-dibromobutane (1.79 mL, 15 mmol, 1.0 equiv) and 2-fluoroaniline (1.88 mL, 19.5 mmol, 1.3 equiv). The stirred mixture was heated at 90 °C for 24 h, before being cooled to ambient temperature and filtered. The filtrate was concentrated *in vacuo*, dissolved in dichloromethane (ca 20 mL), filtered over celite and concentrated *in vacuo*. The concentrate was purified by flash column chromatography (0–2% diethyl ether/hexane). The obtained material was further purified by distillation under reduced pressure (1.2 mbar, 70–84 °C) to afford **91** as a colourless oil (1.93 g, 81%). R_f 0.47 (2% diethyl ether/pentane). IR (film)/cm^{-1} 2966, 1612, 1503, 1454, 1358, 1203, 1161, 962, 737. ^{1}H NMR (400 MHz, $CDCl_3$) δ 7.04–6.95 (m, 2H, 2 × Ar–CH), 6.72–6.63 (m, 2H, 2 × Ar–CH), 3.44–3.35 (m, 4H, 2 × NCH_2), 2.01–1.91 (m, 4H, 2 × NCH_2CH_2). ^{13}C NMR (101 MHz, $CDCl_3$) δ 152.3 (d, J_{CF} = 241.2 Hz, Ar–C_qF), 137.6 (d, J_{CF} = 9.3 Hz, Ar–C_qN), 124.5 (d, J_{CF} = 3.1 Hz, Ar–CH), 117.3 (d, J_{CF} = 7.2 Hz, Ar–CH), 116.2 (d, J_{CF} = 21.1 Hz, Ar–CH), 115.4 (d, J_{CF} = 5.1 Hz, Ar–CH), 49.9 (d, J_{CF} = 5.1 Hz, 2 × NCH), 25.3 (d, J_{CF} = 1.9 Hz, 2 × $NCHCH_2$). ^{19}F NMR (377 MHz, $CDCl_3$) δ –127.0. The observed characterisation data (^{1}H, ^{13}C and ^{19}F NMR) were consistent with that previously reported in the literature.[138]

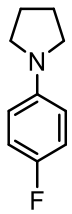
1-(4-Methylphenyl)pyrrolidine (105)



4-Iodotoluene (4.36 g, 20 mmol, 1.0 equiv), copper iodide (381 mg, 2 mmol, 10 mol%), potassium carbonate (5.53 g, 40 mmol, 2.0 equiv) and L-proline (461 mg, 4 mmol, 20 mol%) were added consecutively to a flame dried flask and the contents placed under argon. DMSO (13 mL, 1.5 M) and pyrrolidine (2.48 mL, 30 mmol, 1.5 equiv) were added consecutively to the flask. The reaction was heated to 70°C and stirred for 24 h, then cooled to ambient temperature and quenched with sat. aq. NH_4Cl (50 mL). The aqueous phase was extracted with diethyl ether (4 × 50 mL). The combined organic layers were dried over Na_2SO_4, filtered, and concentrated *in vacuo*. The brown residue was distilled under reduced pressure (ca 0.7 mbar, 90–100°C) to afford **105** as a yellow solid (1.87 g, 57%). mp = 42–43 °C (lit. 41–43 °C).[125] IR (film)/cm^{-1} 2965, 2826, 1621, 1520, 1487, 136, 1341, 1183, 800, 510. ^{1}H NMR (400 MHz, $CDCl_3$) δ 7.05 (d, J = 8.1 Hz, 2H, 2 × Ar–CH), 6.52 (d, J = 8.1 Hz, 2H, 2 × Ar–CH), 3.29–3.23 (m, 4H, 2 × NCH_2), 2.27 (s, 3H, CH_3), 2.04–1.96 (m, 4H, 2 × NCH_2CH_2). ^{13}C NMR

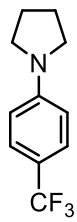
(101 MHz, $CDCl_3$) δ 146.1 (Ar–C_qN), 129.6 (2 × Ar–CH), 124.5 (Ar–$C_q$$CH_3$), 111.8 (2 × Ar–CH), 47.9 (2 × NCH_2), 25.4 (2 × NCH_2CH_2), 20.3 (CH_3). The observed characterisation data (mp, ^{1}H and ^{13}C NMR) was consistent with that previously reported in the literature.[125,139]

1-(4-Fluorophenyl)pyrrolidine (107)



Potassium carbonate (6.08 g, 44 mmol, 2.2 equiv) and potassium iodide (7.30 g, 44 mmol, 2.2 equiv) were added to a flame-dried flask. The flask was put under argon and acetonitrile (40 mL, 0.5 M) was added, followed by 1,4-dibromobutane (2.39 mL, 20 mmol, 1.0 equiv) and 4-fluoroaniline (2.50 mL, 26 mmol, 1.3 equiv). The stirred mixture was heated under reflux for 24 h, before being cooled to ambient temperature, filtered over celite and concentrated *in vacuo*. The residue was dissolved in diethyl ether (20 mL) and extracted with 1 M aq. HCl (2 × 20 mL then 10 mL). The aqueous phases were combined and basified with 1 M aq. NaOH (60 mL). The product was extracted with diethyl ether (3 x 50 mL) and the organic phases were combined, dried over Na_2SO_4 and concentrated *in vacuo*. Purification by flash column chromatography (1–2% diethyl ether/hexane) followed by distillation under reduced pressure (1.2 mbar, 140–150°C) afforded **107** as an off-white solid (2.54 g, 70%). R_f 0.32 (2% diethyl ether/hexane). mp = 29–31 °C. IR (film)/cm^{-1} 2966, 2874, 2828, 1608, 1511, 1486, 1460, 1219, 1182, 1157, 1101, 962, 807, 716, 471, 580, 509. ^{1}H NMR (400 MHz, $CDCl_3$) δ 7.01–6.90 (m, 2H, 2 × Ar–CH), 6.54–6.44 (m, 2H, 2 × Ar–CH), 3.30–3.22 (m, 4H, 2 × NCH_2), 2.12–1.91 (m, 4H, 2 × NCH_2CH_2). ^{13}C NMR (101 MHz, $CDCl_3$) δ 155.8 (d, J_{CF} = 233.0 Hz, Ar–CF), 144.8 (Ar–C_qN), 115.3 (d, J_{CF} = 22.0 Hz, 2 × Ar–CH), 112.0 (d, J_{CF} = 7.3 Hz, 2 × Ar–CH), 48.0 (2 × NCH_2), 25.4 (2 × NCH_2CH_2). ^{19}F NMR (377 MHz, $CDCl_3$) δ −130.9. The observed characterisation data (^{1}H, ^{13}C and ^{19}F NMR) was consistent with that previously reported in the literature.[140]

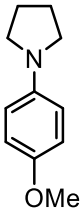
1-(4-Trifluoromethylphenyl)pyrrolidine (108)



Potassium carbonate (6.08 g, 44 mmol, 2.2 equiv) and potassium iodide (7.30 g, 44 mmol, 2.2 equiv) were added to a flame-dried flask. The flask was put under argon and acetonitrile (35 mL, 0.6 M) was added, followed by 1,4-dibromobutane (2.39 mL, 20 mmol, 1 equiv), and 4-(trifluoromethyl)aniline (3.27 mL, 26 mmol, 1.3 equiv). The stirred mixture was heated under reflux for 24 h. The mixture was then cooled to ambient temperature, filtered over celite, and concentrated *in vacuo*. The residue was dissolved in diethyl ether (20 mL), washed with 1 M aq. HCl (2 × 20 mL then 10 mL), dried over Na_2SO_4 and concentrated *in vacuo* to afford a brown oil. Purification by flash column chromatography (hexane) afforded **108** as a white solid (1.49 g, 35%). mp = 95–96 °C (lit.

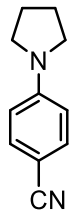
93–94 °C).[141] R_f 0.18 (hexane). IR (film)/cm^{-1} 2972, 2851, 1619, 1536, 1391, 1342, 1152, 1069, 816. ^{1}H NMR (400 MHz, $CDCl_3$) δ 7.44 (d, *J* = 8.6 Hz, 2H, 2 × Ar–CH), 6.55 (d, *J* = 8.6 Hz, 2H, 2 × Ar–CH), 3.36–3.29 (m, 4H, 2 × NCH_2), 2.08–2.00 (m, 4H, 2 × NCH_2CH_2). ^{13}C NMR (101 MHz, $CDCl_3$) δ 149.8 (Ar–C_qN), 126.4 (q, J_{CF} = 3.9 Hz, 2 × Ar–CH), 125.4 (q, J_{CF} = 270 Hz, CF_3), 116.7 (q, J_{CF} = 33 Hz, Ar–C_qCF_3), 110.8 (2 × Ar–CH), 47.5 (2 × NCH_2), 25.5 (2 × NCH_2CH_2). ^{19}F NMR (377 MHz, $CDCl_3$) δ −60.6. The observed characterisation data (mp, ^{1}H, ^{13}C and ^{19}F NMR) were consistent with that previously reported in the literature.[142,142]

1-(4-Methoxyphenyl)pyrrolidine (109)



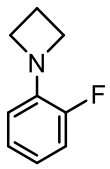
4-Iodoanisole (2.34 g, 10 mmol, 1 equiv), copper iodide (191 mg, 1 mmol, 10 mol%), potassium carbonate (2.76 g, 20 mmol, 2.0 equiv) and L-proline (230.5 mg, 2 mmol, 20 mol%) were added consecutively to a flame-dried microwave vial. The vial was capped under argon and charged with DMSO (6 mL, 1.7 M) and pyrrolidine (1.23 mL, 15 mmol, 1.5 equiv), heated to 70 °C and stirred for 4 days. The reaction mixture was then cooled and quenched with sat. aq. NH_4Cl (20 mL). The mixture was extracted with EtOAc (3 × 50 mL), the organic extracts were combined and washed with water (2 × 50 mL) and brine (50 mL) before being concentrated *in vacuo*. The residue was dissolved in EtOAc (30 mL) and extracted with 1 M aq. HCl (3 × 30 mL). The aqueous extracts were combined, basified with 1 M aq. NaOH (100 mL) and extracted with EtOAc (3 × 50 mL) and ether (50 mL). The organic extracts were combined and washed with purified water (2 × 30 mL) which removed observed solids at the phase boundary, and the organic phase wa s dried over Na_2SO_4 and concentrated *in vacuo* to afford **109** as an impure brown solid (1.52 g). Purity by ^{1}H NMR using 1,3,5-trimethoxybenzene as an internal standard was 94% w/w. A portion of this material (510 mg, 2.9 mmol) was purified by flash column chromatography on silica (2–4% EtOAc/pentane), affording impure **109** as a brown solid (479 mg, 80%). R_f 0.28 (5% EtOAc/pentane). mp = 44–45 °C (lit. 43–45 °C).[143] ^{1}H NMR (400 MHz, $CDCl_3$) δ 6.88 (d, *J* = 8.9 Hz, 2H, 2 × Ar–CH), 6.57 (d, *J* = 8.9 Hz, 2H, 2 × Ar–CH), 3.79 (s, 3H, OCH_3), 3.29–3.24 (m, 4H, 2 × NCH_2), 2.07–1.96 (m, 4H, 2 × NCH_2CH_2). ^{13}C NMR (101 MHz, $CDCl_3$) δ 150.9 (Ar–C_qOMe), 143.3 (Ar–C_qN), 115.1 (2 × Ar–CH), 112.7 (2 × Ar–CH), 56.2 (OCH_3), 48.4 (2 × NCH_2), 25.5 (2 × NCH_2CH_2). Purity by ^{1}H NMR with a 30 s delay using 1,3,5-trimethoxybenzene as an internal standard was 99% w/w. The observed characterisation data (mp, ^{1}H and ^{13}C NMR) was consistent with that previously reported in the literature.[139,144] Purified material was used in further experiments.

1-(4-Cyanophenyl)pyrrolidine (110)



Copper iodide (381 mg, 2 mmol, 10 mol%), potassium carbonate (5.53 mg, 40 mmol, 2.0 equiv) and L-proline (461 mg, 4 mmol, 20 mol%) were added to a flame dried microwave vial and the tube sealed under argon. DMSO (12 mL, 1.7 M), 4-iodobenzenonitrile (4.58 g, 20 mmol, 1.0 equiv) and pyrrolidine (2.5 mL, 30 mmol, 1.5 equiv) were added consecutively to the flask. The stirred reaction was heated to 70°C for 24 h, then cooled to ambient temperature and quenched with sat. aq. NH_4Cl (50 mL). The aqueous phase was extracted with diethyl ether (4 × 50 mL). The combined organic layers were dried over Na_2SO_4, filtered, and concentrated *in vacuo*. Purification by flash column chromatography (5–10% EtOAc/pentane) afforded **110** as a yellow solid (2.46 g, 72%). mp = 86–87 °C (lit. 85–86°C).[142] R_f 0.18 (5% EtOAc/pentane). IR (film)/cm^{-1} 2978, 2854, 2209, 1604, 1520, 1487, 1462, 1390, 1347, 1158, 957, 814, 541. ^{1}H NMR (400 MHz, $CDCl_3$) δ 7.45 (d, *J* = 8.4 Hz, 2H, 2 × Ar–CH), 6.50 (d, *J* = 8.4 Hz, 2H, 2 × Ar–CH), 3.37–3.28 (m, 4H, 2 × NCH_2), 2.10–1.99 (m, 4H, 2 × NCH_2CH_2). ^{13}C NMR (101 MHz, $CDCl_3$) δ 150.1 (Ar–C_qN), 133.6 (2 × Ar–CH), 121.2 (CN), 111.6 (2 × Ar–CH), 96.7 (Ar–C_qCN), 47.6 (2 × NCH_2), 25.6 (2 × NCH_2CH_2). The observed characterisation data (mp, ^{1}H and ^{13}C NMR) were consistent with that previously reported in the literature.[142, 142]

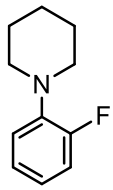
1-(2-Fluorophenyl)azetidine (111)



Copper iodide (209 mg, 1.1 mmol, 10 mol%), potassium carbonate (3.04 mg, 22 mmol, 2.0 equiv) and L-proline (253 mg, 2.2 mmol, 20 mol%) were added to a flame-dried microwave vial and the tube sealed under argon. DMSO (6.5 mL, 1.7 M), 2-fluoroiodobenzene (1.28 mL, 11 mmol, 1.0 equiv) and azetidine (1.12 mL, 16 mmol, 1.5 equiv) were added consecutively to the flask. The stirred reaction was heated to 70°C for 24 h, then cooled to ambient temperature and quenched with sat. aq. NH_4Cl (50 mL). The aqueous phase was extracted with diethyl ether (4 × 50 mL). The combined organic layers were dried over Na_2SO_4, filtered, and concentrated *in vacuo*. Purification by flash column chromatography (1–2% diethyl ether/pentane) followed by distillation under reduced pressure (1 mbar, 90–102°C) afforded **111** as a colourless oil (1.02 g, 61%). R_f 0.42 (2% diethyl ether/pentane). IR (film)/cm^{-1} 2964, 2920, 2852, 1612, 1500, 1454, 1333, 1306, 1238, 1204, 1155, 1118, 944, 917, 807, 740, 653, 520. ^{1}H NMR (400 MHz, $CDCl_3$) δ 7.04–6.91 (m, 2H, 2 × Ar–CH), 6.75–6.66 (m, 1H, Ar–CH), 6.49 (dd, *J* = 8.6, 8.6 Hz, 1H, Ar–CH), 3.99 (t, *J* = 7.2 Hz, 4H, 2 × NCH_2), 2.36 (p, *J* = 7.2 Hz, 2H, CH_2). ^{13}C NMR (101 MHz, $CDCl_3$) δ 152.4 (d, J_{CF} = 241.3 Hz, Ar–C_qF), 140.1 (d, J_{CF} = 10.8 Hz, Ar–C_qN), 124.1 (d, J_{CF} = 3.4 Hz, Ar–CH), 118.4

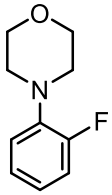
(d, J_{CF} = 6.8 Hz, Ar–CH) 115.5 (d, J_{CF} = 18.6 Hz, Ar–CH), 114.2 (d, J_{CF} = 4.5 Hz, Ar–CH) 53.9 (d, J_{CF} = 1.9 Hz, 2 × NCH_2), 18.0 (d, J_{CF} = 2.4 Hz, CH_2). ^{19}F NMR (377 MHz, $CDCl_3$) δ –132.2. HRMS (TOF ES$^+$) *m/z* Calcd for $C_9H_{11}NF$ [M+H]: 152.0876; Found 152.0876.

1-(2-Fluorophenyl)piperidine (112)



Potassium carbonate (2.74 mg, 19.8 mmol, 2.2 equiv) and potassium iodide (3.29 g, 19.8 mmol, 2.2 equiv) were added to a flame-dried round bottom flask. The flask was put under argon, and acetonitrile (15 mL, 1.7 M), 1,5-dibromopentane (1.23 mL, 9 mmol, 1 equiv) and 2-fluoroaniline (1.13 mL, 11.7 mmol, 1.3 equiv) were added. The mixture was heated under reflux for 24 h. The mixture was then cooled to ambient temperature, filtered over celite, and concentrated *in vacuo*. The residue was dissolved in 50 mL diethyl ether and extracted with 1 M aq. HCl (3 × 30 mL). The aqueous phases were combined and basified with 1 M aq. NaOH (100 mL) and the product was extracted with diethyl ether (3 x 50 mL). The organic phases were combined, dried over Na_2SO_4 and concentrated *in vacuo*. Purification by flash column chromatography (0 to 3% diethyl ether/hexane) followed by distillation under reduced pressure (1.2 mbar, ca 100–120 °C) afforded **112** as a colourless oil (2.97 g, 55%). R_f 0.36 (2% diethyl ether/hexane). IR (film)/cm^{-1} 2933, 2852, 2807, 1608, 1498, 1450, 1384, 1338, 1239, 1217, 1122, 1099, 1042, 1027, 924, 806, 748, 722. ^1H NMR (400 MHz, $CDCl_3$) δ 7.10–6.87 (m, 4H, 4 × Ar–CH), 3.03 (t, *J* = 5.5 Hz, 4H, 2 × NCH_2), 1.81–1.72 (m, 4H, 2 × NCH_2CH_2), 1.64–1.54 (m, 2H, CH_2). ^{13}C NMR (101 MHz, $CDCl_3$) δ 156.0 (d, J_{CF} = 245.7 Hz, Ar–C_qF), 141.5 (d, J_{CF} = 8.0 Hz, Ar–C_qN), 124.5 (d, J_{CF} = 3.6 Hz, Ar–CH), 122.1 (d, J_{CF} = 7.9 Hz, Ar–CH), 119.3 (Ar–CH), 116.1 (d, J_{CF} = 21.0 Hz, Ar–CH), 52.3 (d, *J* = 3.4 Hz, 2 × NCH_2), 26.3 (2 × NCH_2CH_2), 24.4 (CH_2). ^{19}F NMR (377 MHz, $CDCl_3$) −122.8. HRMS (TOF ES$^+$) *m/z* Calcd for $C_{11}H_{15}NF$ [M+H]: 180.1189; Found 180.1183.

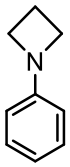
4-(2-Fluorophenyl)morpholine (113)



Potassium carbonate (5.53 g, 40 mmol, 2.0 equiv), copper iodide (381 mg, 2 mmol, 10 mol%) and L- proline (461 mg, 4 mmol, 20 mol%) were added to a flame dried flask. DMSO (13 mL, 1.5 M), 2-fluoroiodobenzene (2.33 mL, 20 mmol, 1 equiv) and morpholine (2.62 mL, 30 mmol, 1.5 eqiuv) were then added to form a slurry. The stirred reaction was heated to 70°C for 24 h, then cooled to ambient temperature, sat. aq. NH_4Cl (50 mL) was added, and the aqueous mixture was extracted with diethyl ether (4 × 50 mL). The combined organic phase was concentrated *in vacuo*, dissolved in 50 mL ether, extracted with 1 M aq. HCl (3 x 25 mL). The combined aqueous extracts were basified with 1M aq. NaOH (90 mL) and extracted with diethyl ether (4 x 50 mL). The organic extracts were

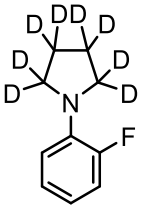
combined, dried over Na_2SO_4 and concentrated *in vacuo* to afford a brown oil. Distillation under reduced pressure (1 mbar, 115–125°C) afforded **113** as an amorphous white glassy solid (596 mg, 16%). IR (film)/cm^{-1} 2822, 2854, 1610, 1498, 1449, 1234, 1207, 1116, 1036, 929, 809, 748, 725, 490. ^{1}H NMR (400 MHz, $CDCl_3$) δ 7.10–6.87 (m, 4H, 4 × Ar–CH), 3.03 (t, J = 5.5 Hz, 4H, 2 × NCH_2), 1.81–1.72 (m, 4H, 2 × NCH_2CH_2), 1.64–1.54 (m, 2H, CH_2). ^{13}C NMR (101 MHz, $CDCl_3$) δ 155.8 (d, J_{CF} = 245.7 Hz, Ar–CF), 141.4 (d, J_{CF} = 8.08 Hz, Ar–CN), 124.3 (d, J_{CF} = 3.6 Hz, Ar–CH), 122.0 (d, J_{CF} = 7.9 Hz, Ar–CH), 119.2 (Ar–CH) 116.0 (d, J_{CF} = 21.0 Hz, Ar–CH), 52.1 (J_{CF} = 3.4 Hz, 2 × NCH_2) 26.2 (2 × NCH_2CH_2), 24.2 (CH_2). ^{19}F NMR (377 MHz, $CDCl_3$) −122.79. HRMS (APCI) *m/z* Calcd for $C_{10}H_{12}NOF$ [M+H]: 182.0976; Found: 182.0974.

1-Phenylazetidine (115)



Copper iodide (209 mg, 1.1 mmol, 10 mol%), potassium carbonate (3.04 mg, 22 mmol, 2.0 equiv) and L-proline (253 mg, 2.2 mmol, 20 mol%) were added to a flame dried microwave vial and the tube sealed under argon. DMSO (6.5 mL, 1.7 M), iodobenzene (1.23 mL, 11 mmol, 1 equiv) and azetidine (1.12 mL, 16 mmol, 1.5 equiv) were added consecutively to the vial. The stirred reaction was heated to 70°C for 24 h, then cooled to ambient temperature and quenched with sat. aq. NH_4Cl (50 mL). The aqueous mixture was extracted with diethyl ether (4 × 50 mL). The combined organic layers were dried over Na_2SO_4, filtered, and concentrated *in vacuo*. Purification by flash column chromatography (2–4% diethyl ether/pentane) followed by distillation under reduced pressure (1 mbar, 90–100 °C) afforded **115** as a colourless oil (0.82 g, 56%). R_f 0.15 (4% diethyl ether/pentane). IR (film)/cm^{-1} 2962, 2911, 2842, 1597, 1499, 1479, 1341, 1305, 1173, 1117, 746, 690. ^{1}H NMR (400 MHz, $CDCl_3$) δ 7.22 (dd, J = 8.5, 7.4 Hz, 2H, 2 × Ar–CH), 6.74 (dd, J = 7.4, 7.4 Hz, 1H, Ar–CH), 6.47 (d, J = 8.5 Hz, 2H, 2 × Ar–CH), 3.88 (t, J = 7.2 Hz, 4H, 2 × NCH_2), 2.37 (p, J = 7.2 Hz, 2H, NCH_2CH_2). ^{13}C NMR (101 MHz, $CDCl_3$) δ 152.4 (Ar–C_q–N), 129.0 (2 × Ar–CH), 117.4 (Ar–CH), 111.5 (2 × Ar–CH), 52.6 (NCH_2), 17.1 (NCH_2CH_2). The observed characterisation data (^{1}H and ^{13}C NMR) were consistent with that previously reported in the literature. [144]

1-(2-Fluorophenyl)pyrrolidine-2,2,3,3,4,4,5,5-d_8 (124)

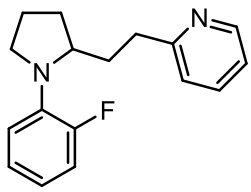


Potassium iodide (4.38 g, 26.4 mmol, 2.2 equiv) and potassium carbonate (3.65 g, 26.4 mmol, 2.2 equiv) were added to a flame dried flask. The flask was put under argon, then acetonitrile (20 mL, 0.6 M), 2-fluoroaniline (1.5 mL, 15.6 mmol, 1.3 equiv) and 1,4-dibromobutane-d_8 (1.38 mL, 12 mmol, 1 equiv) were added sequentially. The stirred mixture was heated to 90 °C for 18 h. The mixture was then cooled to ambient temperature and concentrated *in vacuo*. EtOAc (30 mL) was

added to the residue to form a slurry which was filtered over filter paper and the filter cake washed with EtOAc (2 × 10 mL). The filtrate was added to a separating funnel and the organic phase extracted with 1 M aq. HCl (3 x 30 mL). The combined aqueous phases were basified with 1 M a.q. NaOH (120 mL), and extracted with EtOAc (3 x 50 mL) and diethyl ether (2 x 50 mL). The organic phases were combined, dried over Na_2SO_4, filtered, and concentrated *in vacuo*. Purification by column chromatography (5% EtOAc/hexane) followed by distillation under reduced pressure (0.1 mbar, 90–100°C) afforded **124** as a colourless oil (909 mg, 44%). R_f 0.19 (5% EtOAc/hexane). IR (film)/cm^{-1} (2231, 2075, 1612, 1504, 1346, 1206, 1181, 1156, 1117, 740. ^{1}H NMR (400 MHz, $CDCl_3$) δ 7.04–6.93 (m, 2H, 2 × Ar–CH), 6.73–6.61 (m, 2H, 2 × Ar–CH). ^{13}C NMR (101 MHz, $CDCl_3$) δ 153.2 (d, J_{CF} = 241.0 Hz, Ar–C_qF), 137.6 (d, J_{CF} = 9.0 Hz, Ar–C_qN), 124.4 (d, J_{CF} = 2.9 Hz, Ar–CH), 117.2 (d, J_{CF} = 7.1 Hz, Ar–CH), 116.1 (d, J_{CF} = 20.9 Hz, Ar–CH), 115.3 (d, J_{CF} = 5.0 Hz, Ar–CH), 58.5 (2 × NCH_2), 18.4 (2 × NCH_2CH_2). ^{2}H NMR (61 MHz, $CHCl_3$) δ 3.50–3.22 (m, 4D, 2 × NCD_2), 2.00–1.79 (m, 4D, 2 × NCD_2CD_2). ^{19}F NMR (377 MHz, $CDCl_3$) δ –127.1. HRMS (ES$^+$) *m/z* Calcd for $C_{10}H_5ND_8$ [M+H]$^+$: 174.1534; Found: 174.1535.

4.13.2. C–H functionalisation product formation

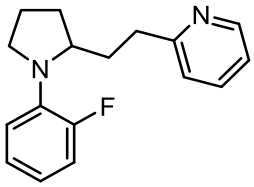
2-(2-(1-(2-Fluorophenyl)pyrrolidin-2-yl)ethyl)pyridine (93a)



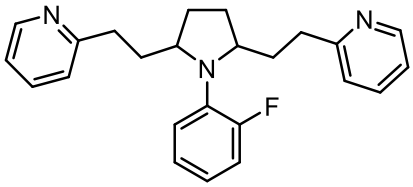
N-(2-Fluorophenyl)pyrrolidine **91** (33 mg, 0.2 mmol, 1.0 equiv) and Ir[dF(CF_3)ppy]$_2$(dtbbpy))PF_6 (2.2 mg, 0.002 mmol, 1 mol%) were added to a flame-dried vial followed by DMF (2.0 mL, 0.1 M). The mixture was sparged with argon for 5 minutes and sealed. DBU (33 µL, 0.2 mmol, 1.0 equiv), and 2-vinylpyridine (0.3 mmol, 1.5 equiv) were added to a vial via a syringe under argon to form a yellow solution. The vial was placed in the batch photoreactor, irradiated with one 450 to 455 nm Evoluchem LED for 24 h with the temperature maintained at 40 °C with a recirculating bath. The mixture was then filtered over celite, washed with EtOAc then concentrated *in vacuo*. Purification by flash column chromatography (20% EtOAc/pentane) afforded **93a** as a colourless oil (25 mg, 52%). R_f 0.17 (20% EtOAc/pentane). IR (film)/cm^{-1} 2958, 1609, 1502, 1474, 1356, 1204, 744. ^{1}H NMR (400 MHz, $CDCl_3$) δ 8.51 (d, *J* = 4.5, 1H, $Ar_{(pyridine)}$–CH), 7.63–7.57 (m, 1H, $Ar_{(pyridine)}$–CH), 7.17–7.10 (m, 2H, 2 × $Ar_{(pyridine)}$–CH), 7.0–6.93 (m, 2H, 2 × Ar–CH), 6.70–6.63 (m, 2H, 2 × Ar–CH), 3.99–3.91 (m, 1H, NC*H*), 3.66–3.58 (m, 1H, NC*H*H), 3.26–3.18 (m, 1H, NCH*H*), 2.88–2.81 (m, 2H, C$H_2Ar_{(pyridine)}$), 2.19–2.08 (m, 2H, C*H*HC$H_2Ar_{(pyridine)}$ and N$(CH_2)_2$C*H*H), 2.05–1.96 (m, 1H, NCH_2C*H*H), 1.92–1.77 (m, 2H, NCH_2CH*H* and N$(CH_2)_2$CH*H),* 1.74–1.62 (m, 1H, CH*H*C$H_2Ar_{(pyridine)}$).^{13}C NMR (101 MHz, $CDCl_3$) δ 161.6 ($Ar_{(pyridine)}$–C_q), 152.7 (d, J_{CF} = 242.5 Hz, Ar–C_qF), 148.6 ($Ar_{(pyridine)}$–CH), 136.7

($Ar_{(pyridine)}$–CH), 136.3 (d, J_{CF} = 8.6 Hz, Ar–C_qN), 124.3 (d, J_{CF} = 3.0 Hz, Ar–CH), 122.9 ($Ar_{(pyridine)}$–CH), 121.1 ($Ar_{(pyridine)}$–CH), 117.7, (d, J_{CF} = 7.3 Hz, Ar–CH), 116.5 (d, J_{CF} = 4.8 Hz, Ar–CH), 116.2 (d, J_{CF} = 21.4 Hz, Ar–CH), 58.8 (d, J_{CF} = 4.3 Hz, N*C*H), 50.9 (d, J_{CF} = 4.7 Hz, NCH_2), 34.9 ($CH_2Ar_{(pyridine)}$), 33.7 ($CH_2CH_2Ar_{(pyridine)}$), 30.8 ($N(CH_2)_2CH_2$), 23.7 (NCH_2CH_2). ^{19}F NMR (377 Hz, $CDCl_3$) δ –125.8. HRMS (ESI) *m/z* Calcd for $C_{17}H_{20}N_2F$ [M+H]: 271.1611; Found: 271.1604.

2-(2-(1-(2-Fluorophenyl)pyrrolidin-2-yl)ethyl)pyridine (93a) and 2,2'-((1-phenylpyrrolidine-2,5-diyl)bis(ethane-2,1-diyl))dipyridine (93b)



93a



93b

N-(2-fluorophenyl)pyrrolidine **91** (33 mg, 0.2 mmol, 1.0 equiv) and Ir[dF(CF_3)ppy]$_2$(dtbbpy))PF_6 (2.2 mg, 0.002 mmol, 1 mol%) were added to a flame-dried vial followed by DMF (2.0 mL, 0.1 M). The mixture was sparged with argon for 5 minutes and sealed. Pyrrolidine (11 µL, 0.2 mmol, 1.0 equiv), and 2-vinylpyridine (0.3 mmol, 1.5 equiv) were added to a vial via a syringe under argon to form a yellow solution. The vial was placed in the batch photoreactor, irradiated with one 450 to 455 nm Evoluchem LED for 24 h with the temperature maintained at 40 °C with a recirculating bath. The mixture was then filtered over celite, washed with EtOAc then concentrated *in vacuo*. Purification by flash column chromatography (20% EtOAc/pentane) afforded **93a** as a colourless oil (30 mg, 55%). Increasing the column eluent gradient (100% EtOAc) afforded **93b** as a mixture of diastereomers, d.r. 69.31.

Mono 93a: R_f 0.17 (20% EtOAc/pentane). ^{1}H NMR (400 MHz, $CDCl_3$) δ 8.51 (ddd, *J* = 4.9, 1.9, 0.9 Hz, 1H, $Ar_{(pyridine)}$–CH), 7.57 (td, *J* = 7.7, 1.9 Hz, 1H, $Ar_{(pyridine)}$–CH), 7.16–7.06 (m, 2H, 2 × $Ar_{(pyridine)}$–CH), 7.01–6.93 (m, 2H 2 × Ar–CH), 6.70–6.63 (m, 2H, 2 × Ar–CH), 3.99–3.89 (m, 1H, NCH) 3.62 (dddd, *J* = 9.5, 6.9, 6.9, 2.5 Hz, 1H, NC*H*H), 3.22 (dddd, *J* = 9.6, 7.6, 5.3, 2.1 Hz, 1H, NCH*H*), 2.88–2.78 (m, 2H, $CH_2Ar_{(pyridine)}$), 2.20–2.08 (m, 2H, C*H*H$CH_2Ar_{(pyridine)}$ and $N(CH_2)_2CHH$), 2.06–1.95 (m, 1H, NCH_2CHH), 1.94–1.76 (m, 2H, NCH_2CH*H* and $N(CH_2)_2CHH$), 1.72–1.60 (m, 1H, *CHH*$CH_2Ar_{(pyridine)}$). ^{19}F NMR (377 Hz, $CDCl_3$) δ –125.8. The observed characterisation data (R_f, ^{1}H and ^{19}F NMR) were consistent with that previously obtained in this project, see page 46.

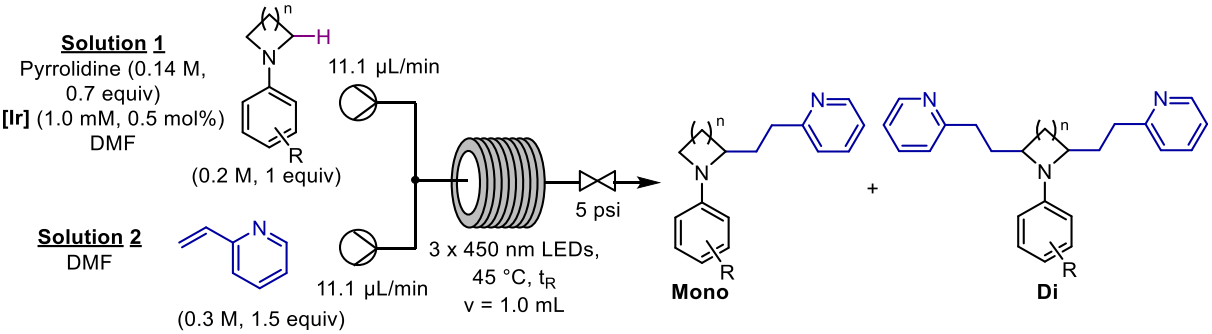
Di 93b: R_f 0.17 (50% EtOAc/pent). IR (film)/cm^{-1} 2956, 1593, 1506, 1431, 1342, 1260, 746. ^{1}H NMR (400 MHz, $CDCl_3$, major diastereomer **93b**) δ 8.56–8.43 (m, 2H, 2 × $Ar_{(pyridine)}$–CH),

7.60–7.50 (m, 2H, 2 × $Ar_{(pyridine)}$–CH), 7.16–7.03 (m, 4H, 4 × $Ar_{(pyridine)}$–CH), 7.02–6.90 (m, 2H, 2 × Ar–CH), 6.72–6.62 (m, 2H, 2 × Ar–CH), 4.12–3.98 (m, 1H, 2 × NCH), 3.73–3.61 (m, 2H, 2 × $CH_2Ar_{(pyridine)}$), 2.26–2.11 (m, 2H, 2 × NCHRC*H*H), 2.11–1.88 (m, 2H, 2 × C*H*HCH_2–$Ar_{(pyridine)}$), 1.89–1.66 (m, 1H, 2 × NCHRCH*H*), 1.62–1.50 (m, 2H, 2 × C*H*HCH_2–$Ar_{(pyridine)}$). ^{13}C NMR (101 MHz, $CDCl_3$, major diastereomer **93b**) δ 162.0 (2 × $Ar_{(pyridine)}$–C_q), 154.1 (d, J_{CF} = 243.3 Hz, Ar–C_qF), 149.2 (2 × $Ar_{(pyridine)}$–CH), 136.4 (2 × $Ar_{(pyridine)}$–CH), 134.1 (d, J_{CF} = 9.6 Hz, Ar–C_qN), 124.4 (d, *J* = 3.0 Hz, Ar–CH), 122.8 (2 × $Ar_{(pyridine)}$–CH), 121.1 (2 × $Ar_{(pyridine)}$–CH), 119.6 (d, *J* = 5.1 Hz, Ar–CH), 118.7 (d, *J* = 7.6 Hz, Ar–CH), 116.3 (d, J_{CF} = 21.4 Hz, Ar–CH). 58.9 (d, *J* = 2.7 Hz, 2 × NCH), 35.2 (2 × $CH_2Ar_{(pyridine)}$), 33.3 (2 × *C*$H_2CH_2Ar_{(pyridine)}$), 28.7 (2 × NCHR*C*H_2). ^{19}F NMR (377 MHz, $CDCl_3$, major diastereomer **93b**) δ −124.0. HRMS (TOF ES$^+$) *m/z* Calcd for $C_{24}H_{27}N_3F$ [M+H]: 376.2189; Found: 376.2192.

Note: The major/minor diastereomers of **128b** could not be conclusively characterised as *cis*/*trans* by the NMR data obtained. However, through analogy to the work of Savoia and co-workers and Melumad and co-workers, the major diastereomer has been tentatively assigned through the relative ^{1}H NMR shifts of the NCHR protons in each diastereomer. The more shifted peak at 4.12–3.98 of the major diastereomer (compared to 3.70–3.57 in the minor diastereomer) is therefore believed to be from ***trans*-93b,** indicating that the major diastereomer is ***trans*-93b**.[96,97]

General procedure F: Experiments to obtain yield information for different substrates

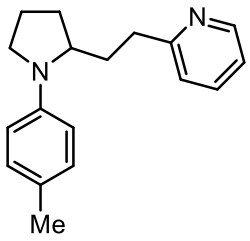
Procedure to obtain yields under 0.1 M reaction conditions. Yield data is presented in section 2.4, Tables 22 and 23.



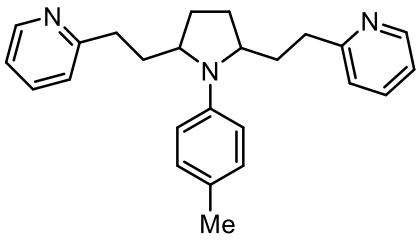
The third-generation flow reactor was used for these reactions. The amine substrate (1.00 mmol, 1.0 equiv) was added to a 5 mL volumetric flask followed by photocatalyst Ir[dF(CF_3)ppy]$_2$(dtbbpy)PF_6 (5.6 mg, 0.005 mmol, 0.5 mol%), and dimethyl terepthalate (38–39 mg, 0.20 mmol, 0.2 equiv). The flask was put under argon, then the contents were dissolved in DMF (~4 mL), followed by addition of pyrrolidine (58 µL, 0.70 mmol, 0.7 equiv) and the remainder of the DMF required to make a 5 mL solution (0.20 M w.r.t. amine substrate). In a

second volumetric flask, DMF (~ 8 mL) was added to a 10 mL volumetric flask under argon, followed by addition of 2-vinylpyridine (325 µL, 1.50 mmol) and the remainder of the DMF required to make a 10 mL solution (0.3 M w.r.t. 2-vinylpyridine, 1.5 equiv). The resulting solutions were added to separate syringes, placed in a dual syringe pump and the photoreactor irradiated with 3 × 450 nm Evoluchem LEDs. The flow rate was set to 11.1 µL for each syringe. The reactor was purged for 90 mins (2 reactor volumes), then the output collected for 90 mins (2 ml, 0.2 mmol reaction scale). The output was filtered over celite, concentrated *in vacuo* and purified by column chromatography.

2-(2-(1-(p-Tolyl)pyrrolidin-2-yl)ethyl)pyridine (128a) and
2,2'-((1-(p-tolyl)pyrrolidine-2,5-diyl)bis(ethane-2,1-diyl))dipyridine (128b)



128a



128b

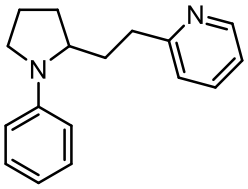
Reaction was conducted according to general procedure F using *N*-(4-methylphenyl)pyrrolidine **105** (161 mg). Purification by column chromatography (20% EtOAc/hexane) afforded **128a** (16 mg, 30%) as a brown oil. Increasing the column eluent polarity (80% to 100% EtOAc/hexane) afforded **128b** as a brown oil. This was collected as mixtures of diastereomers (37 mg, 47% total yield) in two portions for the purpose of characterisation, P1 (8 mg, 11%, d.r. 32:68) and P2 (29 mg, 36%, d.r. 77:23). P1 was used for analysis to characterise the overall minor diastereomer.

Mono 128a: R_f 0.13 (20% EtOAc/hexane). IR (film)/cm^{-1} 2921, 1618, 1591, 1518, 1363, 802. ^{1}H NMR (400 MHz, $CDCl_3$) δ 8.54 (d, *J* = 4.7, 1H, $Ar_{(pyridine)}$–CH), 7.60 (ddd, *J* = 7.8, 7.6, 1.6 Hz, 1H, $Ar_{(pyridine)}$–CH), 7.18 (d, *J* = 7.8 Hz, 1H, $Ar_{(pyridine)}$–CH), 7.12 (dd, *J* = 7.5, 4.7, Hz, 1H, $Ar_{(pyridine)}$–CH), 7.01 (d, *J* = 8.4 Hz, 2H, 2 × Ar–CH), 6.45 (d, *J* = 8.4 Hz, 2H, 2 × Ar–CH), 3.76–3.67 (m, 1H, NCH), 3.48–3.39 (m, 1H, NC*H*H), 3.18–3.08 (m, 1H, NCH*H*), 2.94–2.78 (m, 2H, $CH_2Ar_{(pyridine)}$), 2.24 (s, 3H, CH_3), 2.21–2.13 (m, 1H, C*H*H$CH_2Ar_{(pyridine)}$), 2.11–1.94 (m, 3H, NCH_2CH_2, and $N(CH_2)_2CHH$), 1.94–1.88 (m, 1H, $N(CH_2)_2CHH$), 1.71 (dddd, J = 13.5, 9.6, 9.6, 5.7 Hz, 1H, CH*H*$CH_2Ar_{(pyridine)}$). ^{13}C NMR (101 MHz, $CDCl_3$) δ 161.9 ($Ar_{(pyridine)}$–C_q), 149.3 ($Ar_{(pyridine)}$–CH), 145.4 (Ar–C_qN), 136.5 ($Ar_{(pyridine)}$–CH), 129.8 (2 × Ar–CH), 124.5 (Ar–C_qMe), 122.9 ($Ar_{(pyridine)}$–CH), 121.2 ($Ar_{(pyridine)}$–CH), 112.1 (2 × Ar–CH), 58.3 (NCH), 48.7 (NCH_2), 35.6 ($CH_2Ar_{(pyridine)}$), 33.5 ($CH_2CH_2Ar_{(pyridine)}$), 30.4 ($N(CH_2)_2CH_2$), 23.7 (NCH_2CH_2), 20.3 (CH_3). HRMS (TOF ES$^+$) *m/z* Calcd for $C_{18}H_{23}N_2$ [M+H]: 267.1861; Found: 267.1865.

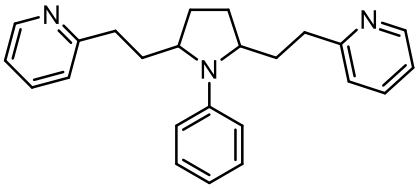
Di 128b P1: R_f 0.12 (100% EtOAc). IR (film)/cm^{-1} 2923, 1616, 1591, 1515, 1473, 1434, 1361, 804, 751. ^{1}H NMR (400 MHz, $CDCl_3$) δ 8.57–8.49 (m, 2H, 2 x $Ar_{(pyridine)}$–CH), 7.63–7.54 (m, 2H, 2 x $Ar_{(pyridine)}$–CH), 7.19–7.07 (m, 4H, 4 x $Ar_{(pyridine)}$–CH), 6.98 (d, *J* = 8.5 Hz, 2H, 2 × Ar–CH), 6.48 (d, *J* = 8.5 Hz, 2H, 2 × Ar–CH), 3.71–3.61 (m, 2H, 2 × NCH), 2.95–2.67 (m, 2H, 2 × $CH_2Ar_{(pyridine)}$), 2.29 (dddd, *J* = 13.4, 10.1, 6.8, 3.2 Hz, 2H, 2 ×C*H*HCH$_2$–$Ar_{(pyridine)}$), 2.23 (s, 3H, CH_3), 2.08–2.00 (m, 2H, NCHC*H*HC*H*HCH), 1.94–1.83 (m, 2H, NCHC*H*HC*H*HCH), 1.81–1.70 (m, 4H, 2 × NCHRCH*H* and 2 × NCH*H*$CH_2Ar_{(pyridine)}$). ^{13}C NMR (101 MHz, $CDCl_3$) δ 161.9 (2 × $Ar_{(pyridine)}$–C_q), 149.3 (2 × $Ar_{(pyridine)}$–CH), 145.6 (Ar–C_q–N), 136.5 (2 × $Ar_{(pyridine)}$–CH), 129.7 (2 × Ar–CH), 124.9 (Ar–C_qMe), 122.9 (2 × $Ar_{(pyridine)}$–CH), 121.2 (2 × $Ar_{(pyridine)}$–CH), 112.3 (2 × Ar–CH), 60.6 (2 × NCH), 35.6 (2 × $CH_2Ar_{(pyridine)}$ or 2 × *C*H_2CH_2–$Ar_{(pyridine)}$), 35.5 (2 × $CH_2Ar_{(pyridine)}$ or 2 × *C*$H_2CH_2Ar_{(pyridine)}$), 29.9 (2 × NCHRCH_2), 20.3 (CH_3). HRMS (TOF ES^+) ***m/z*** Calcd for $C_{25}H_{30}N_3$ $[M+H]^+$: 372.2440; Found: 372.2441.

Note: The major/minor diastereomers of **128b** could not be conclusively characterised as *cis*/*trans* by the NMR data obtained. However, through analogy to the work of Savoia and co-workers and Melumad and co-workers, the major diastereomer has been tentatively assigned through the relative ^{1}H NMR shifts of the NCHR protons in each diastereomer. The less shifted peak at 3.71–3.61 of the minor diastereomer (compared to 3.89–3.81 in the major diastereomer) is therefore believed to be from ***cis*-128b,** indicating that the major diastereomer is ***trans*-93b**.[96,97]

2-(2-(1-Phenylpyrrolidin-2-yl)ethyl)pyridine (129a) and
2,2'-((1-phenylpyrrolidine-2,5-diyl)bis(ethane-2,1-diyl))dipyridine (129b)



129a



129b

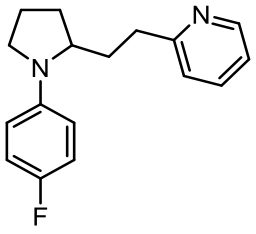
Reaction was conducted according to general procedure F using *N*-phenylpyrrolidine **106** (147.9 mg). Purification by column chromatography (20% EtOAc/hexane) afforded **129a** (18 mg, 36%) as a yellow oil, then increasing the column eluent polarity (100% EtOAc) afforded **129b** as a brown oil. This was collected as mixtures of diastereomers (31 mg, 43% total yield) in two portions for the purpose of characterisation, P1 (23 mg, 32%, d.r. 64:36) and P2 (8 mg, 11%, d.r. 87:13). P1 was used for analysis to characterise the overall major diastereomer.

Mono 129a: R_f 0.13 (20% EtOAc/hexane). IR (film)/cm^{-1} 2955, 1595, 1568, 1504, 1476, 1434, 1365, 1343, 1187, 992, 746, 693. ^{1}H NMR (400 MHz, $CDCl_3$) δ 8.55 (d, *J* = 4.9 Hz, 1H, $Ar_{(pyridine)}$–CH), 7.60 (ddd, *J* = 7.7, 7.6, 1.9 Hz, 1H, $Ar_{(pyridine)}$–CH), 7.23–7.17 (m, 3H, $Ar_{(pyridine)}$–CH and 2 × Ar–CH), 7.12 (dd, *J* = 7.6, 4.9, 1H, $Ar_{(pyridine)}$–CH), 6.64 (t, *J* = 7.3 Hz, 1H, Ar–CH), 6.53 (d, *J* = 8.2 Hz, 2H, 2 × Ar–CH), 3.79–3.72 (m, 1H, NCH), 3.48–3.41 (m, 1H, NC*H*H), 3.21–3.12 (m, 1H, NCH*H*), 2.95–2.80 (m, 2H, $CH_2Ar_{(pyridine)}$), 2.23–2.13 (m, 1H, C*H*H$CH_2Ar_{(pyridine)}$), 2.12–1.88 (m, 4H, NCH_2CH_2 and $N(CH_2)_2CH_2$) 1.73 (dddd, *J* = 13.5, 9.6, 9.6, 9.6, 5.7 Hz, 1H, CH*H*$CH_2Ar_{(pyridine)}$). ^{13}C NMR (101 MHz, $CDCl_3$) δ 161.8 ($Ar_{(pyridine)}$–C_q), 149.3 ($Ar_{(pyridine)}$–CH), 147.4 (Ar–C_qN), 136.5 ($Ar_{(pyridine)}$–CH), 129.3 (2 × Ar–CH), 122.9 ($Ar_{(pyridine)}$–CH), 121.2 ($Ar_{(pyridine)}$–CH), 115.4 (Ar–CH), 112.0 (2 × Ar–CH), 58.2 (NCH), 48.4 (NCH_2), 35.6 ($CH_2Ar_{(pyridine)}$), 33.2 ($CH_2CH_2Ar_{(pyridine)}$), 30.3 ($N(CH_2)_2CH_2$, 23.6 NCH_2CH_2. HRMS (TOF ES^+) *m/z* Calcd for $C_{17}H_{21}N_2$ [M+H]: 253.1705; Found: 253.1700.

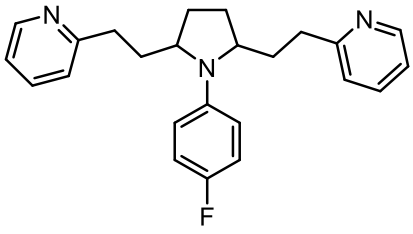
Di 129b P1: R_f 0.17 (80% EtOAc/hexane). IR (film)/cm^{-1} 2949, 1592, 1499, 1473, 1433, 1361, 1150, 772, 747, 695. ^{1}H NMR (400 MHz, $CDCl_3$, major diastereomer **129b**) δ 8.57–8.49 (m, 2H, 2 × $Ar_{(pyridine)}$–CH), 7.63–7.54 (m, 2H, 2 × $Ar_{(pyridine)}$–CH), 7.21–7.08 (m, 6H, 4 × $Ar_{(pyridine)}$–CH, 2 × Ar–CH), 6.60–6.52 (m, 1H, Ar–CH), 6.38 (d, *J* = 8.2 Hz, 2H, 2 × Ar–CH), 3.90–3.81 (m, 2H, 2 × NCH), 2.95–2.74 (m, 4H, 2 × $CH_2Ar_{(pyridine)}$), 2.22–2.12 (m, 4H, 2 × NCHRC*H*H and 2 × C*H*H$CH_2Ar_{(pyridine)}$), 1.95–1.86 (m, 2H, 2 × NCHCH*H*), 1.54 (ddd, *J* = 13.6, 9.8, 9.8, 5.5 Hz, 2H, 2 × CH*H*$CH_2Ar_{(pyridine)}$). ^{13}C NMR (101 MHz, $CDCl_3$, major diastereomer **129b**) δ 161.7 ($Ar_{(pyridine)}$–C_q × 2 minor), 161.6 ($Ar_{(pyridine)}$–C_q × 2), 149.1 (2 × $Ar_{(pyridine)}$–CH), 144.7 (Ar–C_qN), 136.4 (2 × $Ar_{(pyridine)}$–CH), 129.1 (2 × Ar–CH), 122.7 ($Ar_{(pyridine)}$–CH), 121.1 (2 × $Ar_{(pyridine)}$–CH), 114.9 (Ar–CH), 113.6 (2 × Ar–CH), 57.2 (2 × NCH), 35.6 (2 × $CH_2Ar_{(pyridine)}$), 31.3 (2 × $CH_2CH_2Ar_{(pyridine)}$), 27.6 (2 × NCHRCH_2). HRMS (TOF ES^+) *m/z* Calcd for $C_{24}H_{28}N_3$ $[M+H]^+$: 358.2283; Found: 358.2271.

Note: The major/minor diastereomers of **129b** could not be conclusively determined by the NMR data obtained. However, through analogy to the work of Savoia and co-workers and Melumad and co-workers, the major diastereomer has been tentatively assigned through the relative ^{1}H NMR shifts of the NCHR protons in each diastereomer. The more shifted peak at 3.90–3.81 of the major diastereomer (compared to 3.77–3.64 in the minor diastereomer) is therefore believed to be from ***trans*-129b,** indicating that the major diastereomer is ***trans*-129b.**[96,97]

2-(2-(1-(4-Fluorophenyl)pyrrolidin-2-yl)ethyl)pyridine (130a) and
2,2'-((1-(4-fluorophenyl)pyrrolidine-2,5-diyl)bis(ethane-2,1-diyl))dipyridine (130b)



130a



130b

Reaction was conducted according to general procedure F using *N*-(4-fluorophenyl)pyrrolidine **107** (165.1 mg). Purification by column chromatography (30% EtOAc/pentane) afforded **130a** (33 mg, 61%) as a yellow oil. Increasing the column eluent polarity (90% EtOAc/pentane) afforded by **130b** as a brown oil, this was collected as mixtures of diastereomers (13 mg, 17% total yield) in three portions for the purpose of characterisation, P1 (1 mg, 1%, d.r. 5:95), P2 (10 mg, 13% d.r. 61:39), P3 (2 mg, 3%, d.r. 91:9).

Mono 130a: R_f 0.19 (30% EtOAc/pentane). IR (film)/cm^{-1} 2954, 1591, 1511, 1477, 1434, 1366, 1224, 813, 789. ^{1}H NMR (400 MHz, $CDCl_3$) δ 8.55 (d, *J* = 4.8 Hz, 1H, $Ar_{(pyridine)}$–CH), 7.60 (ddd, *J* = 7.7, 7.6, 1.9 Hz, 1H, $Ar_{(pyridine)}$–CH), 7.17 (d, *J* = 7.7 Hz, 1H, $Ar_{(pyridine)}$–CH), 7.12 (ddd, *J* = 7.6, 4.9, 1.2 Hz, 1H, $Ar_{(pyridine)}$–CH), 6.94–6.86 (m, 2H, 2 × Ar–CH), 6.46–6.40 (m, 2H, 2 × Ar–CH), 3.71–3.63 (m, 1H, NCH), 3.44–3.38 (m, 1H, NC*H*H), 3.15–3.06 (m, 1H, NCH*H*), 2.93–2.77 (m, 2H, $CH_2Ar_{(pyridine)}$), 2.22–2.09 (m, 1H, C*H*H$CH_2Ar_{(pyridine)}$), 2.09–1.95 (m, 3H, NCH_2CH_2, $N(CH_2)_2CHH$), 1.95–1.88 (m, 1H, $N(CH_2)_2CHH$), 1.71 (dddd, *J* = 13.6, 9.6, 9.6, 5.5 Hz, 1H, CH*H*$CH_2Ar_{(pyridine)}$). ^{13}C NMR (101 MHz, $CDCl_3$) δ 161.7 ($Ar_{(pyridine)}$–C_q), 154.8 (d, J_{CF} = 233.2 Hz, Ar–C_qF), 149.3 ($Ar_{(pyridine)}$–CH), 144.1 (Ar–C_qN), 136.6 ($Ar_{(pyridine)}$–CH), 122.9 ($Ar_{(pyridine)}$–CH), 121.3 ($Ar_{(pyridine)}$–CH), 115.6 (d, J_{CF} = 21.9 Hz, 2 × Ar–CH), 112.4 (d, J_{CF} = 7.1 Hz, 2 × Ar–CH) , 58.5 (NCH), 49.0 (NCH_2), 35.4 ($CH_2Ar_{(pyridine)}$), 33.2 ($CH_2CH_2Ar_{(pyridine)}$), 30.4 ($N(CH_2)_2CH_2$), 23.7 (NCH_2CH_2). ^{19}F NMR (377 MHz, $CDCl_3$) δ −131.1. HRMS (TOF ES$^+$) *m/z* Calcd for $C_{17}H_{20}N_2F$ [M+H]: 271.1611; Found: 271.1621.

Di 130b P1: R_f 0.13 (90% EtOAc/pentane). IR (film)/cm^{-1} 2926, 1591, 1510, 1474, 1434, 1225, 814. ^{1}H NMR (400 MHz, $CDCl_3$, minor diastereomer **130b**) δ 8.55 (ddd, *J* = 4.9, 1.3 1.3 Hz, 2H, 2 × $Ar_{(pyridine)}$–CH), 7.61 (dd, *J* = 7.6, 7.6, 1.9 Hz, 2H, 2 × $Ar_{(pyridine)}$–CH), 7.17 (d, *J* = 7.8 Hz, 2H, 2 × $Ar_{(pyridine)}$–CH), 7.15–7.10 (m, 2H, 2 × $Ar_{(pyridine)}$–CH), 6.92–6.81 (m, 2H, 2 × Ar–CH), 6.50–6.43 (m, 2H, 2 × Ar–CH), 3.65–3.55 (m, 2H, 2 × NCH), 2.96–2.77 (m, 4H, 2 × $CH_2Ar_{(pyridine)}$), 2.27 (dddd, *J* = 13.4, 10.0, 6.7, 3.1 Hz, 2H, 2 × C*H*H$CH_2Ar_{(pyridine)}$), 2.12–2.01 (m, 2H, NCHRC*H*HC*H*H), 1.94–1.83 (m, 2H, NCHRCH*H*CH*H*), 1.76 (dddd, *J* = 13.8, 9.6, 4.9, 4.9 Hz, 2H, 2 × CH*H*$CH_2Ar_{(pyridine)}$). ^{13}C NMR (101 MHz, $CDCl_3$, minor diastereomer **130b**) δ

161.6 (2 × $Ar_{(pyridine)}$–C_q), 149.2 (2 × $Ar_{(pyridine)}$–CH), 144.2 (Ar –C_qN) 136.4 (2 × $Ar_{(pyridine)}$–CH), 122.8 (2 × $Ar_{(pyridine)}$–CH), 121.1 (2 × $Ar_{(pyridine)}$–CH), 115.3 (d, J_{CF} = 21.7 Hz, 2 × Ar–CH), 112.8 (d, J_{CF} = 6.9 Hz, 2 × Ar–CH), 60.8 (2 × NCH), 35.2 ($CH_2Ar_{(pyridine)}$ and $CH_2CH_2Ar_{(pyridine)}$), 29.7 (NCHR*C*HH*C*HH). ^{19}F NMR (377 MHz, $CDCl_3$) δ −130.4. HRMS (TOF ES$^+$) ***m/z*** calcd for $C_{24}H_{27}N_3F$ $[M+H]^+$ 376.2189, found 376.2194.

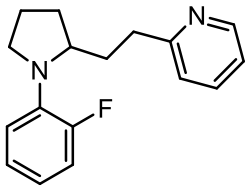
Note: The quaternary Ar–C_qF signal in the ^{13}C NMR was not observed due to low intensity spectrum.

Di 130b P3: R_f 0.13 (90% EtOAc/pentane). IR (film)/cm^{-1} 2920, 1590, 1515, 1474, 1433, 1359, 1150, 803, 749. ^{1}H NMR (400 MHz, $CDCl_3$, major diastereomer **130b**) δ 8.52 (ddd, *J* = 5.0, 1.3, 1.3 Hz, 2H, 2 × $Ar_{(pyridine)}$–CH), 7.59 (ddd, *J* = 7.7, 7.7, 1.9 Hz, 2H, 2 × $Ar_{(pyridine)}$–CH), 7.15–7.08 (m, 4H, 4 × $Ar_{(pyridine)}$–CH), 6.86–6.80 (m, 2H, 2 × Ar–CH), 6.31–6.25 (m, 2H, 2 × Ar–CH), 3.79 (ddd, *J* = 7.4, 6.9, 3.6 Hz, 2H, 2 × NCH), 2.92–2.69 (m, 4H, 2 × $CH_2Ar_{(pyridine)}$), 2.23–2.16 (m, 2H, 2 × C*H*HC$H_2Ar_{(pyridine)}$), 2.14–2.03 (m, 2H, NCHRC*H*HC*H*H), 1.96–1.83 (m, 2H, NCHRCH*H*CH*H*), 1.54 (dddd, *J* = 13.7, 9.7, 9.7, 5.4 Hz, 2H, 2 × CH*H*C$H_2Ar_{(pyridine)}$).^{13}C NMR (101 MHz, $CDCl_3$, major diastereomer **130b**) δ 161.7 (2 × $Ar_{(pyridine)}$–C_q), 154.3 (d, J_{CF} = 233.3 Hz, Ar–C_qF), 149.3 (2 × $Ar_{(pyridine)}$–CH), 141.4 (Ar–C_qN), 136.5 (2 × $Ar_{(pyridine)}$–CH), 122.9 (2 × $Ar_{(pyridine)}$–CH), 121.2 (2 × $Ar_{(pyridine)}$–CH), 115.6 (d, J_{CF} = 21.9 Hz, 2 × Ar–CH), 114.3 (d, J_{CF} = 7.1 Hz, 2 × Ar–CH), 57.6 (2 × NCH), 35.6 (2 × $CH_2Ar_{(pyridine)}$), 31.3 (2 × $CH_2CH_2Ar_{(pyridine)}$) 27.9 (2 × NCHRCH_2). ^{19}F NMR (377 MHz, $CDCl_3$) δ −131.2.

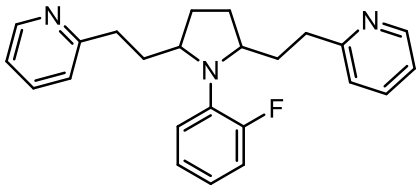
Mass spec not obtained for P3: due to contamination with minor diastereomer obtaining the desired mass ion would not necessarily be determining.

Note: The major/minor diastereomers of **130b** could not be conclusively characterised as *cis*/*trans* by the NMR data obtained However, through analogy to the work of Savoia and co-workers and Melumad and co-workers, the major diastereomer has been tentatively assigned through the relative ^{1}H NMR shifts of the NCHR protons in each diastereomer. The more shifted peak at 3.79 of the major diastereomer (compared to 3.65–3.55 in the minor diastereomer) is therefore believed to be from ***trans*-130b**, indicating that the major diastereomer (P3) is ***trans*-130b.**[96,97]

2-(2-(1-Phenylpyrrolidin-2-yl)ethyl)pyridine (93a) and
2,2'-((1-phenylpyrrolidine-2,5-diyl)bis(ethane-2,1-diyl))dipyridine (93b)



93a



93b

Reaction was conducted according to general procedure F using *N*-(2-fluorophenyl)pyrrolidine **91** (165.8 mg). Purification by column chromatography (20% EtOAc/hexane) afforded **93a** (30 mg, 56%) as a yellow oil, then increasing the column eluent polarity (90% EtOAc/hexane) afforded **93b** as a brown oil (12 mg, 16%) as an inseparable mixture of diastereomers, d.r. 67:33.

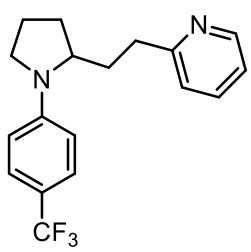
Mono 93a: R_f 0.12 (20% EtOAc/hexane). IR (film)/cm^{-1} 2958, 1611, 1503, 1476, 1355, 1205, 736. ^{1}H NMR (400 MHz, $CDCl_3$) δ 8.50 (d, *J* = 4.9 Hz, 1H, $Ar_{(pyridine)}$–CH), 7.57 (ddd, *J* = 7.7, 7.7, 1.8 Hz, 1H, $Ar_{(pyridine)}$–CH), 7.15–7.05 (m, 2H, 2 × $Ar_{(pyridine)}$–CH), 7.02–6.91 (m, 2H, 2 × Ar–CH), 6.72–6.61 (m, 2H, 2 × Ar–CH), 3.98–3.89 (m, 1H, NCH), 3.68–3.56 (m, 1H, NC*H*H), 3.26–3.17 (m, 1H, NCH*H*), 2.85–2.78 (m, 2H, $CH_2Ar_{(pyridine)}$), 2.22–2.07 (m, 2H, C*H*H$CH_2Ar_{(pyridine)}$ and $N(CH_2)_2CHH$), 2.05–1.94 (m, 1H, NCH_2CHH), 1.94–1.75 (m, 2H, NCH_2CHH and NCH_2CH_2CHH), 1.66 (dddd, *J* = 13.3, 9.3, 9.3, 6.7 Hz, 1H, CH*H*$CH_2Ar_{(pyridine)}$). ^{13}C NMR (101 MHz, $CDCl_3$) δ 161.9 ($Ar_{(pyridine)}$–C_q), 152.9 (d, J_{CF} = 241.8 Hz, Ar–C_qF), 149.2 ($Ar_{(pyridine)}$–CH), 136.6–136.4 (m, Ar–C_qN and $Ar_{(pyridine)}$–CH), 124.4 (d, J_{CF} = 3.0 Hz, Ar–CH), 122.8 ($Ar_{(pyridine)}$–CH), 121.1 ($Ar_{(pyridine)}$–CH), 117.7 (d, J_{CF} = 7.4 Hz, Ar–CH) , 116.6 (d, J_{CF} = 5.0 Hz, Ar–CH), 116.3 (d, J_{CF} = 21.3 Hz, Ar–CH), 58.9 (d, J_{CF} = 4.2 Hz, NCH), 51.0 (d, J_{CF} = 4.8 Hz, NCH_2), 35.2 ($CH_2Ar_{(pyridine)}$), 33.8 ($CH_2CH_2Ar_{(pyridine)}$), 30.9, ($N(CH_2)_2CH_2$), 23.7 (NCH_2CH_2). ^{19}F NMR (377 MHz, $CDCl_3$) δ −125.8. The data obtained for this molecule (IR, ^{1}H, ^{13}C and ^{19}F NMR) match those previously obtained for this molecule.

Di 93b: R_f 0.09 (80% EtOAc/hexane). IR (film)/cm^{-1} 2928, 1608, 1590, 1568, 1474, 1453, 1208, 747. ^{1}H NMR (400 MHz, $CDCl_3$) δ 8.55–8.44 (m, 2H, 2 × $Ar_{(pyridine)}$–CH), 7.61–7.51 (m, 2H, 2 × $Ar_{(pyridine)}$–CH), 7.16–7.02 (m, 4H, 4 × $Ar_{(pyridine)}$–CH) 7.02–6.89 (m, 2H, 2 × Ar–CH), 6.72–6.62 (m, 2H, 2 × Ar–CH), 4.10–3.97 (br s, 2H, 2 × NCH), 2.92–2.69 (m, 4H, 2 × $CH_2Ar_{(pyridine)}$), 2.26–2.12 (m, 2H, 2 × NCHRC*H*H), 2.10–1.91 (m, 2H, 2 × C*H*HCH_2–$Ar_{(pyridine)}$), 1.88–1.68 (m, 2H, 2 × NCHRCH*H*), 1.58 (dddd, *J* = 13.3, 9.7, 9.6, 5.9 Hz, 2H, 2 × C*H*HCH_2–$Ar_{(pyridine)}$). ^{13}C NMR (101 MHz, $CDCl_3$) δ 162.0 (2 × $Ar_{(pyridine)}$–C_q), 154.1 (d, J_{CF} = 243.1 Hz, Ar–C_qF), 149.2 (2 × $Ar_{(pyridine)}$–CH), 136.5 (2 × $Ar_{(pyridine)}$–CH), 134.1 (d, J_{CF} = 9.6 Hz,

Ar–C_qN), 124.4 (d, J_{CF} = 3.0 Hz, Ar–CH), 122.8–122.8 (m, 2 × $Ar_{(pyridine)}$–CH), 121.1 (2 × $Ar_{(pyridine)}$–CH), 119.6 (d, J_{CF} = 5.1 Hz, Ar–CH), 118.7 (d, J_{CF} = 7.6 Hz, Ar–CH), 116.3 (d, J_{CF} = 21.2 Hz, Ar–CH), 59.2 (2 × NCH), 35.2 (2 × $CH_2Ar_{(pyridine)}$), 33.3 (2 × *C*$H_2CH_2Ar_{(pyridine)}$), 28.7 (2 × NCHR*C*H_2). ^{19}F NMR (377 MHz, $CDCl_3$) δ −124.0. The data obtained for this molecule (IR, ^{1}H, ^{13}C and ^{19}F NMR) match those previously obtained for this molecule.

Note: The major/minor diastereomers of **128b** could not be conclusively characterised as *cis*/*trans* by the NMR data obtained. However, through analogy to the work of Savoia and co-workers and Melumad and co-workers, the major diastereomer has been tentatively assigned through the relative ^{1}H NMR shifts of the NCHR protons in each diastereomer. The more shifted peak at 4.12–3.98 of the major diastereomer (compared to 3.70–3.57 in the minor diastereomer) is therefore believed to be from ***trans*-93b,** indicating that the major diastereomer is ***trans*-93b**.[96,97]

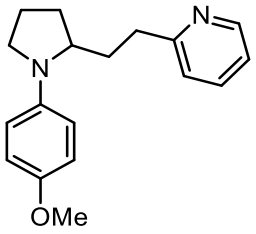
2-(2-(1-(4-(Trifluoromethyl)phenyl)pyrrolidin-2-yl)ethyl)pyridine (131a)



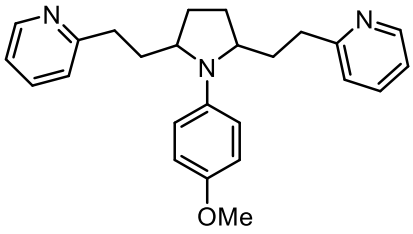
Reaction was conducted according to general procedure F using *N*-(4-trifluorophenyl)pyrrolidine **108** (215.0 mg). Purification by column chromatography (40–50% EtOAc/hexane) afforded **131a** (14 mg, 22%) as a yellow oil. R_f 0.27 (40% EtOAc/hexane). IR (film)/cm^{-1} 2951, 1614, 1591, 1531, 1380, 1324, 1195, 1150, 1103, 1068, 817. ^{1}H NMR (400 MHz, $CDCl_3$) δ 8.56 (ddd, J = 5.0, 1.9, 0.9 Hz, 1H, $Ar_{(pyridine)}$–CH), 7.62 (ddd, J = 7.7, 7.7, 1.9 Hz, 1H, $Ar_{(pyridine)}$–CH), 7.39 (d, *J* = 8.7 Hz, 2H, 2 × Ar–CH), 7.18 (dt, *J* = 7.8, 1.1 Hz, 1H, $Ar_{(pyridine)}$–CH), 7.14 (ddd, J = 7.5, 4.9, 1.1 Hz, 1H, $Ar_{(pyridine)}$–CH), 6.50 (d, *J* = 8. Hz, 2H, 2 × Ar–CH), 3.85–3.75 (m, 1H, NCH), 3.50–3.40 (m, 1H, NC*H*H), 3.25–3.14 (m, 1H, NCH*H*), 2.96–2.77 (m, 2H, $CH_2Ar_{(pyridine)}$), 2.21–1.93 (m, 5H, NCH_2CH_2, C*H*HC$H_2Ar_{(pyridine)}$, $N(CH_2)_2CH_2$), 1.81–1.66 (m, 1H, CH*H*C$H_2Ar_{(pyridine)}$). ^{13}C NMR (126 MHz, $CDCl_3$) δ 161.4 ($Ar_{(pyridine)}$–C_q), 149.4 ($Ar_{(pyridine)}$–CH), 149.2 (Ar–C_qN), 136.6 ($Ar_{(pyridine)}$–CH), 126.5 (q, J_{CF} = 3.7 Hz, 2 × Ar–CH), 125.6 (q, J_{CF} = 270.0 Hz, CF_3)*, 123.0 ($Ar_{(pyridine)}$–CH), 121.4 ($Ar_{(pyridine)}$–CH), 116.8 (q, J_{CF} = 32.6 Hz, Ar–*C*$_q$$CF_3$), 111.3 (2 × Ar–CH), 58.1 (NCH), 48.2 (NCH_2), 35.4 (*C*$H_2Ar_{(pyridine)}$), 32.5 (*C*$H_2CH_2Ar_{(pyridine)}$), 30.2 $N(CH_2)_2CH_2$, 23.5 (NCH_2CH_2). ^{19}F NMR (377 MHz, $CDCl_3$) δ −60.6. HRMS (TOF ES$^+$) *m/z* Calcd for $C_{18}H_{20}N_2F_3$ [M+H]: 321.1579; Found: 321.1583.

*The second peak of the quartet was obscured, J values given as the distance between peaks 3 and 4.

2-(2-(1-(4-Methoxyphenyl)pyrrolidin-2-yl)ethyl)pyridine (132a) and 2,2'-((1-(4-methoxyphenyl)pyrrolidine-2,5-diyl)bis(ethane-2,1-diyl))dipyridine (132b)



132a



132b

Reaction was conducted according to general procedure F using *N*-(4-methoxyphenyl)pyrrolidine **109** (177.2 mg). Purification by column chromatography (30% EtOAc/pentane) afforded **132a** (22 mg, 39%) as a yellow oil. Increasing the column eluent polarity to (90% EtOAc/pentane) afforded **132b** as a brown oil. This was collected as mixtures of diastereomers (7 mg, 9% total yield) in three portions for the purpose of characterisation, P1 (2 mg, 3%, d.r. 45:55) P2 (4 mg, 5%, d.r. 74:26) and P3 (1 mg, 1%, 87:13). P3 was used for analysis characterising for the overall major diastereomer.

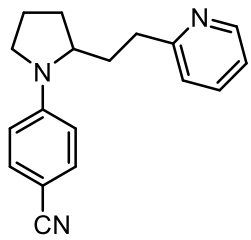
Mono 132a: R_f 0.15 (30% EtOAc/hexane). IR (film)/cm^{-1} 2948, 2829, 1590, 1511, 1471, 1435, 1364, 1275, 1239, 1179, 1041, 813, 772. ^{1}H NMR (400 MHz, $CDCl_3$) δ 8.54 (dd, *J* = 5.0, 0.9 Hz, 1H, $Ar_{(pyridine)}$–CH), 7.60 (ddd, *J* = 7.6, 7.6, 1.9 Hz, 1H, $Ar_{(pyridine)}$–CH), 7.17 (d, *J* = 7.8 Hz, 1H, $Ar_{(pyridine)}$–CH), 7.12 (ddd, *J* = 7.5, 4.9, 1.2 Hz, 1H, $Ar_{(pyridine)}$–CH), 6.85–6.79 (m, 2H, 2 × Ar–CH), 6.55–6.44 (m, 2H, 2 × Ar–CH), 3.75 (s, 3H, OCH_3), 3.70–3.63 (m, 1H, NCH), 3.46–3.39 (m, 1H, NC*H*H), 3.14–3.06 (m, 1H, NCH*H*), 2.94–2.78 (m, 2H, $CH_2Ar_{(pyridine)}$), 2.16 (dddd, J = 13.1, 9.8, 6.9, 2.7 Hz, 1H, C*H*H$CH_2Ar_{(pyridine)}$), 2.11–1.93 (m, 3H, NCH_2CHH, NCH_2CHH and NCH_2CH_2CHH), 1.93–1.87 (m, 1H, NCH_2CH_2CHH), 1.72 (dtd, J = 13.5, 9.8, 5.6 Hz, 1H, CH*H*$CH_2Ar_{(pyridine)}$). ^{13}C NMR (101 MHz, CDCl3) δ 161.9 ($Ar_{(pyridine)}$–C_q), 150.9 (Ar–C_qOMe), 149.3 ($Ar_{(pyridine)}$–CH), 142.4 (Ar–C_qN), 136.5 ($Ar_{(pyridine)}$–CH), 122.9 ($Ar_{(pyridine)}$–CH), 121.2 ($Ar_{(pyridine)}$–CH), 115.2 (2 × Ar–CH), 113.0 (2 × Ar–CH), 58.8 (NCH), 56.1 (OCH_3), 49.4 (NCH_2), 35.5 ($CH_2Ar_{(pyridine)}$), 33.5 ($CH_2CH_2Ar_{(pyridine)}$), 30.5 ($N(CH_2)_2CH_2$), 23.8 (NCH_2CH_2). HRMS (ESI) *m/z* Calcd for $C_{18}H_{23}N_2O$ [M+H]: 283.1810; Found: 283.1799.

Di 132b P3: R_f 0.09 (90% EtOAc/hexane); IR (film)/cm^{-1} 2926, 1725, 1591, 1511, 1471, 1436, 1242, 1040. ^{1}H NMR (400 MHz, $CDCl_3$, major diastereomer **132b**) δ 8.56–8.50 (m, 2H, 2 × $Ar_{(pyridine)}$–CH), 7.59 (ddd, *J* = 7.6, 7.6, 1.8 Hz, 2H, 2 × $Ar_{(pyridine)}$–CH), 7.16–7.09 (m, 4H, 4 × $Ar_{(pyridine)}$–CH), 6.76 (d, *J* = 9.0 Hz, 2H, 2 × Ar–CH), 6.37 (d, *J* = 9.0 Hz, 2H, 2 × Ar–CH), 3.86–3.79 (m, 2H, 2 × NCH), 3.75 (s, 3H, OCH_3), 2.90–2.71 (m, 4H, 2 × $CH_2Ar_{(pyridine)}$), 2.25–2.06 (m, 4H, 2 × NCHRC*H*H and 2 × C*H*H$CH_2Ar_{(pyridine)}$), 1.92–1.86 (m, 1H, 2 × NCHRCH*H*), 1.58–1.49 (m, 2H, 2 × CH*H*$CH_2Ar_{(pyridine)}$). ^{13}C NMR (101 MHz, $CDCl_3$, major

diastereomer **132b**) δ 161.9 (2 × $Ar_{(pyridine)}$–C_q), 150.3 (Ar–$C_q$$OCH_3$), 149.3 (2 × $Ar_{(pyridine)}$–CH), 139.6 (Ar–C_qN), 136.5 (2 × $Ar_{(pyridine)}$–CH), 122.9 (2 × $Ar_{(pyridine)}$–CH), 121.2 (2 × $Ar_{(pyridine)}$–CH), 115.1 (2 × Ar–CH), 114.9 (2 × Ar–CH), 57.7 (2 × NCH), 56.0 (OCH_3), 35.7 (2 × $CH_2Ar_{(pyridine)}$), 31.6 (2 × $CH_2CH_2Ar_{(pyridine)}$), 28.0 (2 × NCHRCH_2). HRMS (TOF ES$^+$) *m/z* Calcd for $C_{25}H_{30}N_3O$ $[M+H]^+$: 388.2389; Found: 388.2377.

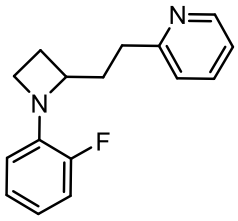
Note: The major/minor diastereomers of **132b** could not be conclusively characterised as *cis*/*trans* by the NMR data obtained. However, through analogy to the work of Savoia and co-workers and Melumad and co-workers, the major diastereomer has been tentatively assigned through the relative ^{1}H NMR shifts of the NCHR protons in each diastereomer. The more shifted peak at 3.86–3.79 of the major diastereomer (compared to 3.65–3.58 in the minor diastereomer) is therefore believed to be from ***trans*-132b**, indicating that the major diastereomer is ***trans*-132b.**[96,97]

4-(2-(2-(Pyridin-2-yl)ethyl)pyrrolidin-1-yl)benzonitrile (133a)

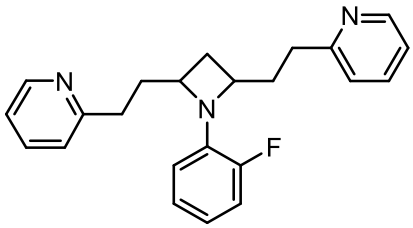


Reaction was conducted according to general procedure F using *N*-(4-cyanophenyl)pyrrolidine **110** (172.0 mg). Purification by column chromatography (20–40% EtOAc/pentane) afforded **133a** (6 mg, 12%) as a colourless oil. R_f 0.10 (30% EtOAc/hexane). IR (film)/cm^{-1} 2955, 2863, 2208, 1604, 1520, 1385, 1176, 817. ^{1}H NMR (400 MHz, $CDCl_3$) δ 8.56 (d, *J* = 4.8 Hz, 1H, $Ar_{(pyridine)}$–CH), 7.62 (dd, *J* = 7.7, 7.7, 1.9 Hz, 1H, $Ar_{(pyridine)}$–CH), 7.41 (d, *J* = 8.8 Hz, 2H, 2 × Ar–CH), 7.21–7.11 (m, 2H, 2 × $Ar_{(pyridine)}$–CH), 6.46 (d, *J* = 8.8 Hz, 2H, 2 × Ar–CH), 3.85–3.77 (m, 1H, NCH), 3.49–3.39 (m, 1H, NC*H*H), 3.27–3.16 (m, 1H, NCH*H*), 2.96–2.76 (m, 2H, $CH_2Ar_{(pyridine)}$), 2.21–1.95 (m, 5H, CH*H*$CH_2Ar_{(pyridine)}$, NCH_2CH_2 and $N(CH_2)_2CH_2$), 1.73 (dddd, *J* = 14.4, 9.5, 9.5, 5.4 Hz, 1H, CH*H*$CH_2Ar_{(pyridine)}$). ^{13}C NMR (101 MHz, $CDCl_3$) δ 161.1 ($Ar_{(pyridine)}$–C_q), 149.5 (Ar–C_qN), 149.5 ($Ar_{(pyridine)}$–CH), 136.6 ($Ar_{(pyridine)}$–CH), 133.6 (2 × Ar–CH), 123.0 ($Ar_{(pyridine)}$–CH), 121.5 ($Ar_{(pyridine)}$–CH), 121.1 (CN), 111.9 (2 × Ar–CH), 96.8 (Ar–C_qCN), 58.1 (NCH), 48.1 (NCH_2), 35.3 ($CH_2Ar_{(pyridine)}$), 32.1 ($CH_2CH_2Ar_{(pyridine)}$), 30.0 ($(NCH_2)_2CH_2$), 23.3 (NCH_2CH_2). HRMS (TOF ES$^+$) *m/z* Calcd for $C_{18}H_{20}N_3$ [M+H]: 278.1657; Found: 278.1658.

2-(2-(1-(2-Fluorophenyl)azetidin-2-yl)ethyl)pyridine (134a) and
2,2'-((1-(2-fluorophenyl)azetidine-2,4-diyl)bis(ethane-2,1-diyl))dipyridine (134b)



134a



134b

Reaction was conducted according to general procedure F using *N*-(2-fluorophenyl)azetidine **111** (151.7 mg). Purification by column chromatography (20% EtOAc/pentane) afforded **134a** (25 mg, 49%) as a yellow oil, then increasing the column eluent gradient (100% EtOAc) afforded **134b** as a brown oil (6 mg, 8%) with 10% unknown impurity, as an inseparable 2.7:1 mixture of *cis* and *trans* diastereomers.

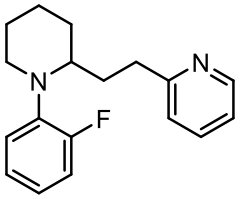
Mono 134a: R_f 0.24 (20% EtOAc/pentane). IR (film)/cm^{-1} 2925, 2862, 1612, 1590, 1501, 1475, 1435, 1454, 1330, 1204, 1113, 745. ^{1}H NMR (400 MHz, $CDCl_3$) δ 8.54 (d, J = 4.8 Hz, 1H, $Ar_{(pyridine)}$–CH), 7.60 (dd, J = 7.7, 7.7 Hz, 1H, $Ar_{(pyridine)}$–CH), 7.19 (d, J = 7.8 Hz, 1H, $Ar_{(pyridine)}$–CH), 7.12 (dd, J = 6.3, 6.3 Hz, 1H, $Ar_{(pyridine)}$–CH), 7.00–6.89 (m, 2H, 2 × Ar–CH), 6.72–6.66 (m, 1H, Ar–CH), 6.58 (dd, J = 8.7, 8.5 Hz, 1H, Ar–CH), 4.22–4.15 (m, 1H, NCH), 4.15–4.06 (m, 1H, NC*H*H), 3.76–3.64 (ddd, 1H, J = 8.0, 8.0, 8.0 Hz, NCH*H*), 2.96–2.77 (m, 2H $CH_2Ar_{(pyridine)}$), 2.44–2.29 (m, 2H, NCH_2CHH and $CHHCH_2Ar_{(pyridine)}$), 2.21–2.03 (m, 2H, NCH_2CHH and $CHHCH_2Ar_{(pyridine)}$). ^{13}C NMR (101 MHz, $CDCl_3$) δ 161.6 ($Ar_{(pyridine)}$–C_q), 152.5, (d, J_{CF} = 241.6 Hz, Ar–C_qF), 149.4 ($Ar_{(pyridine)}$–CH), 139.8 (d, J_{CF} = 10.9 Hz, Ar–C_qN), 136.5 ($Ar_{(pyridine)}$–CH), 124.3 (d, J_{CF} = 3.2 Hz, Ar–CH), 122.8 ($Ar_{(pyridine)}$–CH), 121.2 ($Ar_{(pyridine)}$–CH), 118.7 (d, J_{CF} = 7.0 Hz, Ar–CH), 115.8 (d, J_{CF} = 19.0 Hz, Ar–CH), 114.4 (d, J_{CF} = 4.6 Hz, Ar–CH), 64.4 (NCH), 51.9 (d, J_{CF} = 4.2 Hz, NCH_2), 35.8 ($CH_2CH_2Ar_{(pyridine)}$), 33.8 ($CH_2Ar_{(pyridine)}$), 24.1 (NCH_2CH_2). ^{19}F NMR (377 MHz, $CDCl_3$) –130.6. HRMS (ES+) *m/z* calcd for $C_{16}H_{18}N_2F$ $[M+H]^+$: 257.1454; Found: 257.1456.

Di 134b: R_f 0.13 (80% EtOAc/pentane). IR (film)/cm^{-1} 2926, 1612, 1434, 1591, 1501, 1474, 1332, 1202, 743. ^{1}H NMR (400 MHz, $CDCl_3$, major diastereomer ***trans*-134b**) δ 8.58–8.46 (m, 2H, 2 × $Ar_{(pyridine)}$–CH), 7.65–7.52 (m, 2H, 2 × $Ar_{(pyridine)}$–CH), 7.23–7.06 (m, 4H, 4 × $Ar_{(pyridine)}$–CH), 6.99–6.86 (m, 2H, 2 × Ar–CH), 6.73–6.60 (m, 1H, Ar–CH), 6.60–6.51 (m, 1H, Ar–CH), 4.35–4.26 (m, 2H, 2 × NCH), 2.99–2.69 (m, 4H, 2 × $CH_2Ar_{(pyridine)}$), 2.30–2.09 (m, 3H, 2 × $CHHCH_2Ar_{(pyridine)}$ and $NCHRCH_2$) 1.97–1.85 (m, 2H, 2 × $CHHCH_2Ar_{(pyridine)}$). ^{13}C NMR (101 MHz, $CDCl_3$, major diastereomer ***trans*-134b**) δ 161.6 (2 × $Ar_{(pyridine)}$–C_q), 149.4 (2 × $Ar_{(pyridine)}$–CH), 136.5 (2 × $Ar_{(pyridine)}$–CH), 124.5 (d, J_{CF} = 3.0 Hz, Ar–CH), 122.8 (2 ×

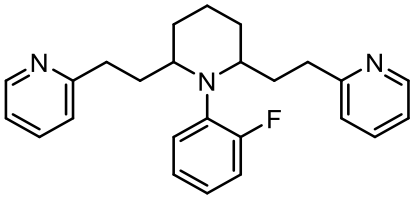
$Ar_{(pyridine)}$–CH), 121.2 (2 × $Ar_{(pyridine)}$–CH), 118.8 (d, J_{CF} = 6.7 Hz, Ar–CH), 115.6 (d, J_{CF} = 18.7 Hz, Ar–CH), 115.1 (d, J_{CF} = 4.6 Hz, Ar–CH), 61.1 (2 × NCH), 33.9 ($CH_2Ar_{(pyridine)}$), 33.7 ($CH_2CH_2Ar_{(pyridine)}$), 29.6 (NCHRCH_2). ^{19}F NMR (377 MHz, $CDCl_3$, major diastereomer ***trans*-134b**) δ −128.1. HRMS (TOF ES$^+$) *m/z* Calcd for $C_{23}H_{25}N_3F$ $[M+H]^+$: 362.2033; Found: 362.2022.

Note: due to the low intensity of the ^{13}C NMR, quaternary signals Ar–C_qF and Ar–C_qN were not observed. Sample contained an unknown impurity at ca 10%. Major diastereomer has been assigned as *trans* due to the NCHRCH_2 protons being in the same environment, in the minor diastereomer these protons are split into two distinct signals.

2-(2-(1-(2-Fluorophenyl)piperidin-2-yl)ethyl)pyridine (135a) and 2,2'-((1-(2-fluorophenyl)piperidine-2,6-diyl)bis(ethane-2,1-diyl))dipyridine (135b)



135a



135b

Reaction was conducted according to general procedure F using *N*-(2-fluorophenyl)piperidine **112** (179.9 mg). Purification by column chromatography (20% EtOAc/pentane) afforded **135a** (10 mg, 18%) as a yellow oil, increasing the column eluent polarity (90% EtOAc/pentane) afforded **135b** as a brown oil (3 mg, 4%), as an inseparable 2.6:1 mixture of *cis* and *trans* diastereomers.

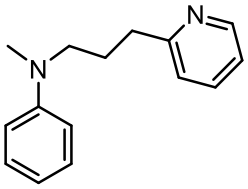
Mono 135a: R_f 0.30 (20% EtOAc/pentane). IR (film)/cm^{-1} 2933, 2856, 1608, 1473, 1499, 1450, 1436, 1249, 1218, 1123, 750. ^{1}H NMR (400 MHz, $CDCl_3$) δ 8.46 (d, *J* = 4.9 Hz, 1H, $Ar_{(pyridine)}$–CH), 7.51 (dd, *J* = 7.8, 7.6 Hz, 1H, $Ar_{(pyridine)}$–CH), 7.05 (dd, *J* = 6.4 Hz, 1H, $Ar_{(pyridine)}$–CH), 7.02–6.87 (m, 5H, $Ar_{(pyridine)}$–CH and 4 × Ar–CH), 3.56–3.46 (m, 1H, NCH), 3.25–3.15 (m, 1H, NC*H*H), 3.00–2.90 (m, 1H, NCH*H*), 2.80–2.69 (m, 1H, C*H*H$Ar_{(pyridine)}$), 2.69–2.57 (m, 1H, CH*H*$Ar_{(pyridine)}$) 2.00–1.81 (m, 3H, C*H*H$CH_2Ar_{(pyridine)}$ and $N(CH_2)_3CH_2$), 1.81–1.61 (m, 4H, $N(CH_2)_2CHH$, CH*H*$CH_2Ar_{(pyridine)}$, and NCH_2CH_2), 1.61–1.51 (m, 1H, $N(CH_2)_2CHH$). ^{13}C NMR (101 MHz, $CDCl_3$) δ 162.2 ($Ar_{(pyridine)}$–C_q), 156.8 (d, J_{CF} = 246.0 Hz, Ar–C_qF), 149.2 ($Ar_{(pyridine)}$–CH), 140.1 (d, J_{CF} = 8.4 Hz, Ar–C_qN), 136.4 ($Ar_{(pyridine)}$–CH), 124.3 (d, J_{CF} = 3.5 Hz, Ar–CH), 122.8 ($Ar_{(pyridine)}$–CH), 122.9–122.7 (m, 2C, $Ar_{(pyridine)}$–CH and Ar–CH), 122.6 (d, J_{CF} = 8.0 Hz, Ar–CH), 121.0 ($Ar_{(pyridine)}$–CH), 116.3 (d, J_{CF} = 21.3 Hz, Ar–CH), 57.1 (d, J_{CF} = 4.8 Hz, N*C*H), 48.4 (NCH_2), 35.3 ($CH_2Ar_{(pyridine)}$), 29.5 ($N(CH_2)_3CH_2$), 29.2

($CH_2CH_2Ar_{(pyridine)}$), 26.2 (NCH_2CH_2), 20.8 ($N(CH_2)_2CH_2$). ^{19}F NMR (377 MHz, $CDCl_3$) δ –122.0. HRMS (ES+) *m/z* calcd for $C_{18}H_{22}N_2F$ $[M+H]^+$ 285.1767; Found: 285.1761.

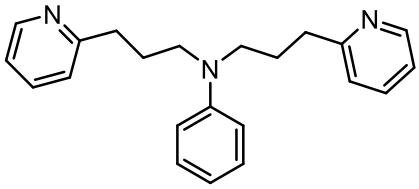
Di 135b: R_f 0.16 (80% EtOAc/pentane). IR (film)/cm^{-1} 2926, 2855, 1722, 1591, 1497, 1472, 1435, 1257, 1100, 800, 753. ^1H NMR (400 MHz, $CDCl_3$) δ 8.51–8.39 (m, 2H, 2 × $Ar_{(pyridine)}$–CH), 7.49 (dd, *J* = 8.0, 8.0 Hz, 1H, 2 × $Ar_{(pyridine)}$–CH), 7.10–6.94 (m, 6H, 4 × $Ar_{(pyridine)}$–CH and 2 × Ar–CH), 6.88 (d, *J* = 7.5 Hz, 1H, 2 × Ar–CH), 3.39 (s, 2H, 2 × NCH), 2.85–2.65 (m, 2H, 2 × C*H*H$Ar_{(pyridine)}$), 2.64–2.52 (m, 2H, 2 × CH*H*$Ar_{(pyridine)}$), 2.00–1.80 (m, 6H, 2 × $CH_2CH_2Ar_{(pyridine)}$ and 2 × NCHRC*H*H), 1.76–1.46 (m, 4H, 2 × NCHRCH*H* and CH2CH_2CH_2). ^{19}F NMR (377 MHz, $CDCl_3$) δ −121.2. HRMS (TOF ES^+) *m/z* Calcd for $C_{25}H_{29}N_3F$ $[M+H]^+$: 390.2346; Found 390.2350.

Insufficient material was obtained for ^{13}C NMR. *Cis* and *trans* diastereomers were not assigned.

N-Methyl-N-(3-(pyridin-2-yl)propyl)aniline (136a) and
N,N-bis(3-(pyridin-2-yl)propyl)aniline (136b)



136a



136b

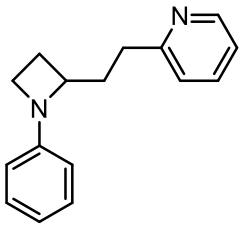
Reaction was conducted according to general procedure F using *N,N*-dimethylaniline (121.5 mg). Purification by column chromatography (20–40% EtOAc/pentane) afforded **136a** as a colourless oil (11 mg, 25% containing 15% unknown impurity) and **136b** as a brown oil (35 mg, 52%).

Mono 136a: R_f 0.4 (20% EtOAc/pentane). IR (film)/cm^{-1} 2931, 1598, 1589, 1505, 1474, 1368, 1195, 748, 692. ^1H NMR (400 MHz, $CDCl_3$) δ 8.57–8.51 (m, 1H, $Ar_{(pyridine)}$–CH), 7.60 (ddd, *J* = 7.6, 7.6, 1.9 Hz, 1H, $Ar_{(pyridine)}$–CH), 7.25–7.19 (m, 2H, 2 × Ar–CH), 7.18–7.10 (m, 2H, 2 × $Ar_{(pyridine)}$–CH) 6.71–6.65 (m, 3H, 3 × Ar–CH), 3.43–3.37 (m, 2H, NCH_2), 2.94 (s, 3H, CH_3), 2.87–2.80 (m, 2H, $CH_2Ar_{(pyridine)}$), 2.04 (tt, *J* = 7.9, 7.9 Hz, 2H, $CH_2CH_2CH_2$). ^{13}C NMR (101 MHz, $CDCl_3$) δ 161.7 ($Ar_{(pyridine)}$–C_q), 149.4 (m, Ar–C_qN and $Ar_{(pyridine)}$–CH), 136.5 ($Ar_{(pyridine)}$–CH), 129.3 (2 × Ar–CH), 122.9 ($Ar_{(pyridine)}$–CH), 121.2 ($Ar_{(pyridine)}$–CH), 116.1 (Ar–CH), 112.3 (2 × Ar–CH), 52.4 (NCH_2), 38.4 (CH_3), 35.9 (CH_2–$Ar_{(pyridine)}$), 26.9 ($CH_2CH_2CH_2$). HRMS (TOF ES^+) *m/z* calcd for $C_{15}H_{19}N_2$ $[M+H]^+$: 227.1548; Found: 227.1550.

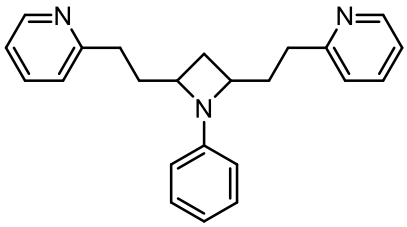
Note: Characterised with 15% unknown impurity due to difficult purification.

136b: R_f 0.13 (80% EtOAc/pentane). IR (film)/cm^{-1} 2947, 1593, 1567, 1504, 1474, 1434, 1367, 1194, 748, 694. ^{1}H NMR (400 MHz, $CDCl_3$) δ 8.53 (dd, *J* = 5.0, 1.8 Hz, 2H, 2 × $Ar_{(pyridine)}$–CH), 7.59 (ddd, *J* = 7.7, 7.7, 1.9 Hz, 2H, 2 × $Ar_{(pyridine)}$–CH), 7.21–7.09 (m, 3H, 4 × $Ar_{(pyridine)}$–CH and 2 × Ar–CH), 6.66–6.60 (m, 3H, 3 × Ar–CH), 3.36 (t, *J* = 7.6, Hz, 4H, 2 × NCH_2) 2.82, (t, *J* = 7.7 Hz, 4H, 2 x CH_2–$Ar_{(pyridine)}$), 2.03 (tt, 4H J = 7.7, 7.7 Hz, 2 × $CH_2C\mathit{H}_2CH_2$). ^{13}C NMR (101 MHz, $CDCl_3$) δ 161.6 (2 × $Ar_{(pyridine)}$–C_q), 149.4 (2 × $Ar_{(pyridine)}$–CH), 148.1 (Ar–C_q–N), 136.5 (2 × $Ar_{(pyridine)}$–CH), 129.3 (2 × Ar–CH) , 122.8 (2 × $Ar_{(pyridine)}$–CH), 121.2 (2 × $Ar_{(pyridine)}$–CH), 115.7 (Ar–CH), 112.2 (2 × Ar–CH), 50.6 (2 × NCH), 35.9 (2 × CH_2–$Ar_{(pyridine)}$), 27.3 (2 × NCH$\mathit{C}H_2$). HRMS (TOF MS ES+) *m/z* calcd for $C_{22}H_{26}N_3$ $[M+H]^+$: 332.2127; Found: 332.2131.

2-(2-(1-Phenylazetidin-2-yl)ethyl)pyridine (137a) and
2,2'-((1-phenylazetidine-2,4-diyl)bis(ethane-2,1-diyl))dipyridine (137b)



137a



137b

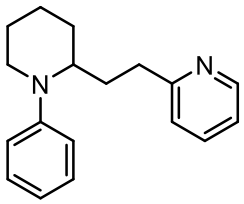
Reaction was conducted according to general procedure F using *N*-phenylazetidine **115** (133.6 mg). Purification by column chromatography (30% EtOAc/hexane) afforded **137a** (21 mg, 44%) as a yellow oil, then increasing the column eluent gradient (100% EtOAc to 5% MeOH/EtOAc) afforded **137b** as a yellow oil (21 mg, 31%). This was collected in two portions for the purpose of characterisation: P1 (1 mg, 1%, single diastereomer, major) and P2 (18 mg, 24%, d.r. 71:29).

Mono product 137a: R_f 0.08 (30% EtOAc/hexane). IR (film)/cm^{-1} 2951, 2923, 2854, 1597, 1499, 1475, 1434, 1333,750, 693. ^{1}H NMR (400 MHz, $CDCl_3$) δ 8.56 (dd, *J* = 5.1, 1.8 Hz, 1H, $Ar_{(pyridine)}$–CH), 7.61 (dd, *J* = 7.7, 7.7, 1.9 Hz, 1H, $Ar_{(pyridine)}$–CH), 7.23–7.17 (m, 3H, $Ar_{(pyridine)}$–CH and 2 × Ar–CH), 7.13 (dd, *J* = 7.5, 4.9 Hz, 1H, $Ar_{(pyridine)}$–CH), 6.74 (t, *J* = 7.3 Hz, 1H, Ar–CH), 6.53 (d, *J* = 8.0 Hz, 2H, 2 × Ar–CH), 4.08 (dddd, *J* = 7.7, 7.7, 7.7, 3.6 Hz, 1H, NCH), 3.96 (ddd, *J* = 8.6, 7.1, 3.7 Hz, 1H, NCH*H*), 3.59 (ddd, *J* = 8.0, 8.0, 7.9 Hz, 1H, NCH*H*), 2.96–2.80 (m, 2H, $CH_2Ar_{(pyridine)}$), 2.49–2.29 (m, 2H, $NCH_2C\mathit{H}H$ and $C\mathit{H}HCH_2Ar_{(pyridine)}$), 2.23–2.10 (m, 2H, $NCH_2CH\mathit{H}$ and $C\mathit{H}HCH_2Ar_{(pyridine)}$). ^{13}C NMR (101 MHz, $CDCl_3$) δ 161.7 ($Ar_{(pyridine)}$–C_q), 152.4 (Ar–C_qN), 149.4 ($Ar_{(pyridine)}$–CH) 136.5 ($Ar_{(pyridine)}$–CH), 129.0 (2 × Ar–CH), 122.8 ($Ar_{(pyridine)}$–CH), 121.2 ($Ar_{(pyridine)}$–CH), 117.7 (Ar–CH), 112.0 (2 × Ar–CH), 64.5 (NCH), 49.9 (NCH_2), 36.7

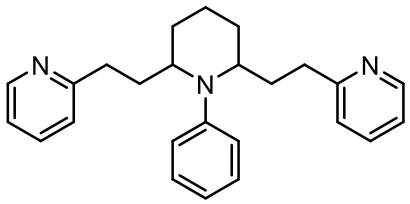
(CH$_2$CH$_2$Ar$_{(pyridine)}$), 33.7 (CH$_2$Ar$_{(pyridine)}$), 23.5 (NCH$_2$$CH_2$). HRMS (TOF ES$^+$) *m/z* calcd for $C_{16}H_{19}N_2$ [M+H]$^+$: 239.1548; Found 239.1546.

Di product 137b P1, major diastereomer: R_f 0.16 (100% EtOAc). IR (film)/cm^{-1} 2926, 1723, 1595, 1498, 1474, 1434, 1320, 843, 752, 695. ^{1}H NMR (400 MHz, $CDCl_3$) δ 8.55 (d, *J* = 4.7 Hz, 2H, 2 × Ar$_{(pyridine)}$–CH), 7.62 (dd, *J* = 7.8 7.8 Hz, 2H, 2 × Ar$_{(pyridine)}$–CH), 7.22–7.11 (m, 6H, 2 × Ar–CH, 4 × Ar$_{(pyridine)}$–CH), 6.74 (dd, *J* = 7.3, 7.3 Hz, 1H , Ar–CH), 6.61 (d, *J* = 8.1 Hz, 2H, 2 × Ar–CH), 3.91–3.82 (m, 2H, 2 × NCH), 2.98–2.78 (m, 4H, 2 × CH$_2$Ar$_{(pyridine)}$), 2.60–2.50 (m, 1H, NCHRCHH), 2.49–2.38 (m, 2H, 2 × CHHCH$_2$Ar$_{(pyridine)}$), 2.23–2.09 (m, 2H, 2 × CHHCH$_2$Ar$_{(pyridine)}$), 1.89–1.79 (m, 1H, NCHRCHH). ^{13}C NMR (126 MHz, $CDCl_3$) δ 161.7 (2 × Ar$_{(pyridine)}$–C$_q$), 152.9 (Ar–C$_q$N), 149.5 (2 × Ar$_{(pyridine)}$–CH), 136.6 (2 × Ar$_{(pyridine)}$–CH), 129.1 (2 × Ar–CH), 122.9 (2 × Ar$_{(pyridine)}$–CH), 121.3 (2 × Ar$_{(pyridine)}$–CH), 118.2 (Ar–CH), 112.2, (2 × Ar–CH), 61.9 (2 × NCH), 37.7 (2 × CH$_2$CH$_2$Ar$_{(pyridine)}$), 33.9 (2 × CH$_2$Ar$_{(pyridine)}$), 29.9 (NCHRCH$_2$). HRMS (TOF ES$^+$) *m/z* Calcd for $C_{23}H_{26}N_3$ [M+H]$^+$: 344.2127; Found: 344.2124.

2-(2-(1-Phenylpiperidin-2-yl)ethyl)pyridine (138a) and
2,2'-((1-phenylpiperidine-2,6-diyl)bis(ethane-2,1-diyl))dipyridine (138b)



138a



138b

Reaction was conducted according to general procedure F using *N*-phenylpiperidine **116** (161.3 mg). Purification by column chromatography (30% EtOAc/pentane) afforded **138a** (18 mg, 35%) as a brown oil. Increasing the column eluent gradient (100% EtOAc) afforded **138b** as a brown oil. This was collected in two portions for the purpose of characterisation, P1 (6 mg, 8%, d.r. 91:9), P2 (4 mg, 5%, d.r. 55:45) and P3 (1 mg, 1%, >95 : 5), all diastereomeric ratios given as major:minor for overall reaction.

Mono 138a: R_f 0.26 (30% EtOAc/pentane). IR (film)/cm^{-1} 2930, 2855, 1593, 1498, 1434, 1248, 750, 692. ^{1}H NMR (400 MHz, $CDCl_3$) δ 8.51 (d, *J* = 5.0 Hz, 1H, Ar$_{(pyridine)}$–CH) 7.54 (ddd, *J* = 7.7, 7.6, 1.8 Hz, 1H, Ar$_{(pyridine)}$–CH), 7.20 (dd, *J* = 7.7, 7.7 Hz, 2H, 2 × Ar–CH), 7.08 (dd, *J* = 7.5, 4.9 Hz, 1H, Ar$_{(pyridine)}$–CH), 7.04 (d, *J* = 7.8 Hz, 1H, Ar$_{(pyridine)}$–CH), 6.83 (d, *J* = 8.2 Hz, 2H, 2 × Ar–CH), 6.74 (t, *J* = 7.2 Hz, 1H, Ar–CH), 3.93–3.85 (m, 1H, NCH), 3.43–3.33 (m, 1H, NCHH), 3.10–2.99 (m, 1H, NCHH), 2.83–2.66 (m, 2H, CH$_2$Ar$_{(pyridine)}$), 1.99 (dt, *J* = 7.5, 7.5 Hz, 2H, CH_2CH$_2$Ar$_{(pyridine)}$), 1.88–1.56 (m, 6H, NCH$_2$CH_2, N(CH$_2$)$_2$CH_2 N(CH$_2$)$_3$CH_2). ^{13}C NMR

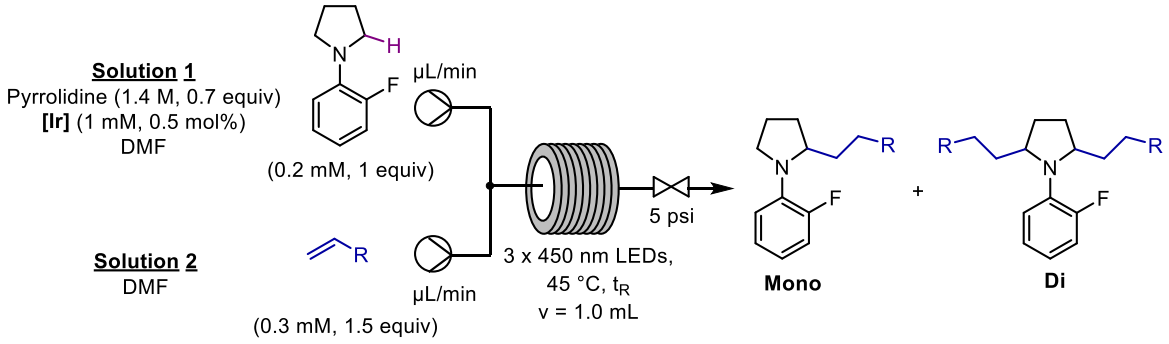
(101 MHz, $CDCl_3$) δ 162.1 ($Ar_{(pyridine)}$–C_q), 151.1 (Ar–C_qN), 149.3 ($Ar_{(pyridine)}$–CH), 136.4 ($Ar_{(pyridine)}$–CH), 129.2 (2 × Ar–CH), 122.9 ($Ar_{(pyridine)}$–CH), 121.1 ($Ar_{(pyridine)}$–CH), 118.2 (Ar–CH), 116.4 (2 × Ar–CH), 55.4 (NCH), 43.7 (NCH_2), 35.8 ($CH_2Ar_{(pyridine)}$), 28.0 ($N(CH_2)_3CH_2$), 27.9 ($CH_2CH_2Ar_{(pyridine)}$), 25.4 (NCH_2CH_2), 19.5 ($N(CH_2)_2CH_2$). HRMS (TOF ES$^+$) *m/z* Calcd for $C_{18}H_{23}N_2$ [M+H]: 267.1861; Found 267.1862.

Di 138b P1 major, *trans*-138b: R_f 0.10 (100% EtOAc). IR (film)/cm^{-1} 2934, 1592, 1567, 1499, 1474, 1434, 749. ^{1}H NMR (400 MHz, $CDCl_3$, major diastereomer **trans-138b**) δ 8.48 (dd, *J* = 4.9, 1.7 Hz, 2H, 2 × $Ar_{(pyridine)}$–CH), 7.54 (ddd, *J* = 7.7, 7.7, 1.9 Hz, 2H, 2 × $Ar_{(pyridine)}$–CH), 7.20 (dd, *J* = 7.7, 7.7 Hz, 2H, 2 × Ar–CH), 7.08 (dd, *J* = 7.5, 4.9 Hz, 2H, 2 × $Ar_{(pyridine)}$–CH), 7.00 (d, *J* = 7.8 Hz, 2H, 2 × $Ar_{(pyridine)}$–CH), 6.87 (dd, *J* = 7.3, 7.3 Hz, 1H, Ar–CH), 6.83 (d, *J* = 8.1 Hz, 2H, 2 × Ar–CH), 3.46–3.35 (m, 2H, 2 × NCH), 2.85 (ddd, *J* = 13.5, 8.2, 8.2 Hz, 2H, 2 × C*H*H$Ar_{(pyridine)}$), 2.68 (dd, *J* = 13.7, 8.1, 8.1 Hz, 2H, 2 × CH*H*$Ar_{(pyridine)}$), 1.94–1.68 (m, 9H, NCH_2CH_2CHH, 4 × $NCHRCH_2$), 1.59–1.49 (m, 1H, $NCHRCH_2CHH$). ^{13}C NMR (126 MHz, $CDCl_3$, major diastereomer ***trans*-138b**) δ 162.2 (2 × $Ar_{(pyridine)}$–C_q), 149.5 (Ar–C_qN), 149.2 (2 × $Ar_{(pyridine)}$–CH), 136.4 (2 × $Ar_{(pyridine)}$–CH), 129.2 (2 × Ar–CH), 122.8 (2 × $Ar_{(pyridine)}$–CH), 121.0 (2 × $Ar_{(pyridine)}$–CH), 120.6 (Ar–CH), 119.9 (2 × Ar–CH), 56.5 (2 × NCH), 35.6 (2 × $CH_2Ar_{(pyridine)}$), 33.5 (2 × $CH_2CH_2Ar_{(pyridine)}$) 29.4 (2 × $NCHRCH_2$), 19.3 ($NCHRCH_2CH_2$). HRMS (TOF ES$^+$) *m/z* Calcd for $C_{25}H_{30}N_3$ [M+H]$^+$: 372.2440; Found: 372.2443.

Di 138b P3 minor, *cis*-138b: R_f 0.10 (100% EtOAc). IR (film)/cm^{-1} 2933, 1592, 1567, 1494, 1473, 1434, 750, 702. ^{1}H NMR (400 MHz, $CDCl_3$) δ 8.47 (d, *J* = 4.3 Hz, 2H, 2 × $Ar_{(pyridine)}$–CH), 7.50 (dd, *J* = 7.9, 7.9 Hz, 2H, 2 × $Ar_{(pyridine)}$–CH), 7.20 (dd, *J* = 7.7, 7.7 Hz, 2H, 2 × Ar–CH), 7.05 (dd, *J* = 7.4, 5.0 Hz, 2H, 2 × $Ar_{(pyridine)}$–CH), 6.96–6.89 (m, 5H, 2 × $Ar_{(pyridine)}$–CH, 3 × Ar–CH), 3.48–3.38 (m, 2H, 2 × NCH), 2.79–2.68 (m, 2H, 2 × C*H*H–$Ar_{(pyridine)}$), 2.68 – 2.57 (m, 2H, 2 × CH*H*–$Ar_{(pyridine)}$), 2.03–1.77 (m, 6H, 2 × $CH_2CH_2Ar_{(pyridine)}$ and NCHRC*H*HCH$_2$C*H*H*), 1.76–1.65 (m, 4H, NCHRCH*HCH*$_2$CH*H*). ^{13}C NMR (126 MHz, $CDCl_3$) δ 162.3 (2 × $Ar_{(pyridine)}$–C_q), 149.2 (2 × $Ar_{(pyridine)}$–CH), 136.4 (2 × $Ar_{(pyridine)}$–CH), 128.6 (2 × Ar–CH), 124.2 (2 × Ar–CH), 122.7 (2 × $Ar_{(pyridine)}$–CH), 121.5 (Ar–CH), 121.0 (2 × $Ar_{(pyridine)}$–CH), 56.2 (2 × NCH), 35.3 (2 × $CH_2Ar_{(pyridine)}$), 30.4 (2 × $CH_2CH_2Ar_{(pyridine)}$), 28.9 (2 × $NCHRCH_2$), 18.5 (CH_2). HRMS (TOF ES$^+$) *m/z* Calcd for $C_{25}H_{30}N_3$ [M+H]$^+$: 372.2440; Found: 372.2440.

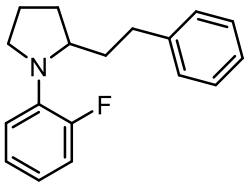
Note: Quaternary Ar–C_qN signal was not identifiable in ^{13}C NMR due to low intensity spectrum. *Major diastereomer tentatively assigned as ***trans*-138b** due to the NCHRC*H*H and NCHRCH*H* signals appearing together in the major product, and being split and appearing as separate signals in the minor product.

General procedure G: yield experiments different acceptors



The third-generation flow reactor was used for these reactions. *N*-(2-Fluorophenyl)pyrrolidine **91** (165.3 mg, 1.00 mmol, 1.00 equiv) was added to a 5 mL volumetric flask followed by photocatalyst $Ir[dF(CF_3)ppy]_2(dtbbpy)PF_6$ (5.6 mg, 0.005 mmol, 0.5 mol%), and dimethyl terepthalate (38 or 39 mg, 0.20 mmol, 0.2 equiv). The flask was put under argon, then the contents were dissolved in DMF (~4 mL), followed by addition of pyrrolidine (58 µL, 0.70 mmol, 0.7 equiv) and the remainder of the DMF required to make a 5 mL solution (0.20 M w.r.t. amine substrate). In a second volumetric flask, DMF (~ 3 mL) was added to a 5 mL volumetric flask under argon, followed by addition of acceptor (1.50 mmol) and the remainder of the DMF required to make a 10 mL solution (0.3 M w.r.t. acceptor, 1.5 equiv). The two solutions were added to separate syringes, placed in a dual syringe pump and the photoreactor irradiated with 3 × 450 nm Evoluchem LEDs. The flow rate was set to 11.1 µL for each syringe. The reactor was purged for 90 mins (2 reactor volumes), then the output collected for 90 minutes (2 mL, 0.2 mmol reaction scale). The output was filtered over celite, concentrated *in vacuo* and purified by column chromatography.

1-(2-Fluorophenyl)-2-phenethylpyrrolidine (126a)

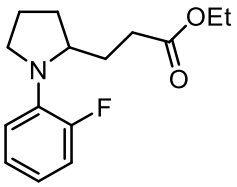


Reaction was conducted according to general procedure G using styrene (172 µL). Purification by column chromatography (5–20% EtOAc/hexane) afforded **126a** as a clear, colourless oil (4 mg, 7%). R_f 0.33 (10% EtOAc/hexane). IR (film)/cm^{-1} 2961, 2941, 1610, 1502, 1454, 1358, 1335, 1206, 742, 699. ^{1}H NMR (400 MHz, $CDCl_3$) δ 7.30–7.24 (m, 2H, 2 × $Ar_{(styrene)}$–CH), 7.21–7.15 (m, 3H, 3 × $Ar_{(styrene)}$–CH), 7.02–6.92 (m, 2H, 2 × Ar–CH), 6.71–6.64 (m, 1H, Ar–CH), 6.60 (ddd, *J* = 10.0, 8.4, 1.7 Hz, 1H, Ar–CH), 3.88 (dddd, *J* = 9.8, 7.5, 5.1, 2.4 Hz, 1H, NCH), 3.62 (ddd, *J* = 9.5, 7.0, 2.6 Hz, 1H, NC*H*H), 3.22 (dddd, *J* = 9.7, 7.6, 5.3, 2.1 Hz, 1H, NCH*H*), 2.71–2.55 (m, 2H, $CH_2Ar_{(styrene)}$), 2.16 (dddd, *J* = 11.8, 7.0, 7.0, 7.0 Hz, 1H, $N(CH_2)_2CHH$), 2.09–1.95 (m, 2H, NCH_2CHH and $CHHCH_2Ar_{(styrene)}$), 1.94–1.84 (m, 1H, NCH_2CHH), 1.78 (dddd, *J* = 12.4, 7.2, 7.2, 5.2 Hz, 1H, $N(CH_2)_2CHH$), 1.60–1.48 (m, 1H, $CHHCH_2Ar_{(styrene)}$). ^{13}C NMR (101 MHz, $CDCl_3$) δ 142.2 ($Ar_{(styrene)}$–C_q), 136.5 (d, J_{CF} = 9.4 Hz, Ar–C_qN), 128.5 (2 ×

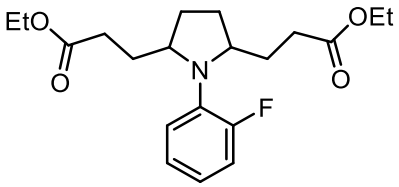
$Ar_{(styrene)}$–CH), 128.5 (2 × $Ar_{(styrene)}$–CH), 125.9 ($Ar_{(styrene)}$–CH), 124.4 (d, J_{CF} = 2.9 Hz, Ar–CH), 117.8 (d, J_{CF} = 7.3 Hz, Ar–CH), 116.6 (d, J_{CF} = 5.1 Hz, Ar–CH), 116.3 (d, J_{CF} = 21.3 Hz, Ar–CH), 58.9 (d, J_{CF} = 4.2 Hz, NCH), 51.0 (d, J_{CF} = 4.9 Hz, NCH_2), 35.5 ($CH_2CH_2Ar_{(styrene)}$), 32.8 ($CH_2Ar_{(styrene)}$), 31.1 ($N(CH_2)_2CH_2$), 23.9 (NCH_2CH_2). ^{19}F NMR (377 MHz, $CDCl_3$) δ −125.8. HRMS (TOF ES^+) *m/z* calcd for $C_{18}H_{21}NF$ $[M+H]^+$: 270.1658; Found: 270.1655.

Note: ^{13}C NMR was not sufficiently intense to observe Ar–C_qF signal.

Ethyl 3-(1-(2-fluorophenyl)pyrrolidin-2-yl)propanoate (127a) and diethyl 3,3'-(1-(2-fluorophenyl)pyrrolidine-2,5-diyl)dipropionate (127b)



127a



127b

Reaction was conducted according to general procedure G using ethyl acrylate (167 μL). Purification by column chromatography (5–7% EtOAc/hexane) afforded **127a** as a colourless oil (36 mg, 69%) and **127b** as a yellow oil (11 mg, 15%), as an inseparable mixture of diastereomers.

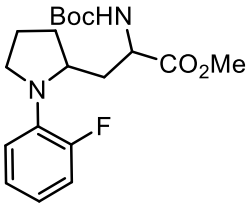
Mono product 127a: R_f 0.13 (5% diethyl ether/pentane). IR (film)/cm^{-1} 2967, 1731 (C=O), 1611, 1503, 1337, 1359, 1205, 1181, 1164, 744. ^1H NMR (400 MHz, $CDCl_3$) δ 7.05–6.94 (m, 2H, 2 × Ar–CH), 6.78 (ddd, *J* = 8.6, 8.6, 1.6 Hz, 1H, Ar–CH), 6.73–6.66 (m, 1H, 2 × Ar–CH), 4.17–4.08 (m, 2H, CH_2CH_3), 3.95–3.85 (m, 1H, NCH), 3.64 (dddd, *J* = 9.6, 7.0, 7.0, 2.7 Hz, 1H, NC*H*H), 3.21 (dddd, *J* = 9.7, 7.7, 5.3, 2.2 Hz, 1H, NCH*H*), 2.32 (dd, *J* = 8.3, 7.1 Hz, 2H, CH_2C=O), 2.16–1.93 (m, 3H, NCH_2CHH, $N(CH_2)_2CHH$ and $CHHCH_2C$=O), 1.93–1.81 (m, 1H, NCH_2CHH), 1.69 (dddd, *J* = 12.3, 7.2, 7.1, 5.3 Hz, 1H, $N(CH_2)_2CHH$), 1.64–1.52 (m, 1H, $CHHCH_2C$=O), 1.25 (t, *J* = 7.1 Hz, 3H, CH_3). ^{13}C NMR (101 MHz, $CDCl_3$) δ 173.6 (C=O), 153.0 (d, *J* = 241.8 Hz, Ar–C_qF), 136.5 (d, *J* = 9.1 Hz, Ar–C_qN), 124.5 (d, J_{CF} = 3.0 Hz, Ar–CH), 118.1 (d, J_{CF} = 7.4 Hz, Ar–CH), 116.7 (d, J_{CF} = 4.8 Hz, Ar–CH), 116.4 (d, J_{CF} = 21.3 Hz, Ar–CH), 60.5 (CH_2CH_3), 58.3 (d, J_{CF} = 3.9 Hz, NCH), 51.3 (d, J_{CF} = 5.2 Hz, NCH_2), 31.3 (CH_2C=O), 30.7 ($N(CH_2)_2CH_2$), 28.8 (CH_2CH_2C=O), 23.8 (NCH_2CH_2), 14.3 (CH_3). ^{19}F NMR (377 MHz, $CDCl_3$) δ −125.5. The observed characterisation data (^1H, ^{13}C and ^{19}F NMR) was consistent with that previously reported in the group.[17]

Di product 127b: R_f 0.24 (20% diethyl ether/pentane). IR (film)/cm^{-1} 2975, 1732 (C=O), 1501, 1453, 1257, 1206, 1181, 749. ^1H NMR (400 MHz, $CDCl_3$, major diastereomer **127b**) δ 7.05–6.94 (m, 2H, 2 × Ar–CH), 6.88 (ddd, *J* = 8.6, 8.6, 1.7 Hz, 1H, Ar–CH), 6.80–6.72 (m, 1H,

Ar–CH), 4.17–4.06 (m, 4H, 2 × OCH_2), 4.06–3.96 (m, 2H, 2 × NCH), 2.25 (t, *J* = 7.8 Hz, 2H, CH_2C=O), 2.18–2.08 (m, 2H, 2 × NCHRC*H*H), 1.94–1.82 (m, 2H, 2 × C*H*HCH_2C=O), 1.71–1.58 (m, 2H, 2 × NCHRCH*H*), 1.48 (ddd, *J* = 16.5, 14.1, 7.8 Hz, 2H, 2 × CH*H*CH_2C=O), 1.23 (t, *J* = 7.1 Hz, 6H, 2 × CH_3). ^{13}C NMR (101 MHz, $CDCl_3$, major diastereomer **127b**) δ 173.5 (2 × C=O), 154.3 (d, J_{CF} = 243.9 Hz, Ar–C_qF), 133.8 (d, J_{CF} = 9.5 Hz, Ar–C_qN), 124.5 (d, J_{CF} = 2.8 Hz, Ar–CH) 119.9 (d, J_{CF} = 4.6 Hz, Ar–CH), 119.4 (d, J_{CF} = 7.8 Hz, Ar–CH), 116.4 (d, J_{CF} = 21.4 Hz, Ar–CH), 60.5 (2 × OCH_2), 58.4 (2 × NCH), 31.2 (2 × *C*H_2C=O), 28.4 (2 × NCHR*C*H_2), 28.1 (2 × *C*H_2CH_2C=O), 14.3 (2 × CH_3). ^{19}F NMR (377 MHz, $CDCl_3$ major diastereomer **127a**) δ −123.6. HRMS (TOF ES$^+$) *m/z* Calcd for $C_{20}H_{29}O_4NF$ $[M+H]^+$: 366.2081; Found: 366.2065.

Note: The major/minor diastereomers of **127b** could not be conclusively characterised as *cis*/*trans* by the NMR data obtained However, through analogy to the work of Savoia and co-workers and Melumad and co-workers, the major diastereomer has been tentatively assigned through the relative ^{1}H NMR shifts of the NCHR protons in each diastereomer. The more shifted peak at 4.06–3.96 of the major diastereomer (compared to 3.61–3.53 in the minor diastereomer) is therefore believed to be from ***trans*-127b**, indicating that the major diastereomer is ***trans*-127b.**[96,97]

Methyl 2-((*tert*-butoxycarbonyl)amino)-3-(1-(2-fluorophenyl)pyrrolidin-2-yl)propanoate (139)



Reaction was conducted according to general procedure G using methyl 2-*tert*-butyloxycarbonylaminoacrylate (140 µL, 0.9 mmol). Purification by flash column chromatography (10% EtOAc/hexane) afforded **139** as a yellow oil (45 mg, 65%), as an inseparable mixture of diastereomers, d.r. 0.55:0.45. R_f 0.23 (10% EtOAc/hexane). IR (film)/cm^{-1} 3440, 2973, 1744 (C=O), 1715 (C=O), 1612, 1504, 1454, 1365, 1165, 1049, 1022, 746. ^{1}H NMR (400 MHz, $CDCl_3$ major diastereomer **139**) δ 7.04–6.92 (m, 2H, 2 × Ar–CH), 6.76–6.62 (m, 2H, 2 × Ar–CH), 5.14 (d, *J* = 8.0 Hz, 1H, NH, major diastereomer), 5.08 (d, *J* =8.0 Hz, NM, minor diastereomer), 4.38–4.24 (m, CH), 4.11–3.95 (m, NCH), 3.76 (s, 1H, CO_2CH_3), 3.62–3.48 (m, 1H, NC*H*H), 3.26–3.12 (m, 1H, NCH*H*), 2.28–2.07 (m, 2H, N$(CH_2)_2$C*H*H and C*H*HCHCO_2Me), 2.04–1.76 (m, 3H, CH*H*CHCO_2Me and NCH_2C*H*$_2$), 1.74–1.54 (m, 1H, N$(CH_2)_2$CH*H*), 1.47 (s, 9H, C$(CH_3)_3$). ^{13}C NMR (101 MHz, $CDCl_3$, major diastereomer **139**) δ 173.3 (C=O), 155.5 (d, J_{CF} = 61.1 Hz, Ar–C_qF), 136.2 (Ar–C_qN), 124.6 (d, J_{CF} = 10.6 Hz, Ar–CH), 118.4 (Ar–CH), 116.6 (Ar–CH), 116.4 (Ar–CH), 80.1 (OCH_3), 56.5 (NCH), 52.4 *C*$(CH_3)_3$), 51.8 (CH), 51.0 (NCH_2), 36.7 (*C*H_2CHCO_2Me), 31.2 (N$(CH_2)_2$*C*H_2), 28.4 ($(CH_3)_3$), 23.4 (NCH_2*C*H_2). ^{19}F NMR (377 MHz,

$CDCl_3$, major diastereomer **139**) δ –125.7. HRMS (TOF ES$^+$) *m/z* Calcd for $C_{19}H_{28}N_2O_4F$ [M+H]: 367.2033; Found: 367.2039.

5. References

1 K. Godula and D. Sames, *Science*, 2006, **312**, 67–72.
2 E. Vitaku, D. T. Smith and J. T. Njardarson, *J.Med.Chem.*, 2014, **57**, 10257−1027.
3 D. Antermite and J. A. Bull, *Synthesis,* 2019, **51**, 3171–3204.
4 G. Chessari, R. Grainger, R. S. Holvey, R. F. Ludlow, P. N. Mortenson and D. C. Rees, *Chem. Sci.*, 2021, **12**, 11976–11985.
5 L. Guillemard, N. Kaplaneris, L. Ackermann and M. L. Johansson, *Nat. Rev. Chem.*, 2021, **5**, 522–545.
6 F. Zhang and D. R. Spring, *Chem. Soc. Rev.*, 2014, **43**, 6906–6919.
7 For reviews on C–H functionalisation, see a) L. McMurray, F. O'Hara and M. J. Gaunt, *Chem. Soc. Rev.*, 2011, **40**, 1885–1898. b) S. St John-Campbell and J. A. Bull, *Org. Biomol. Chem.*, 2018, **16**, 4582–4595.
8 N. Holmberg-Douglas and D. A. Nicewicz, *Chem. Rev.*, 2022, **122**, 1925−2016.
9 M. D. Kärkäs, *Chem. Soc. Rev.*, 2018, **47**, 5786–5865.
10 G. Barker, P. O'Brien, and K. R. Campos, *Org. Lett.*, 2014, **12**, 4176–4179
11 G. E. M. Crisenza and P. Melchiorre, *Nat. Commun*., 2020, **11**, 803.
12 H. E. Bonfield, T. Knauber, F. Lévesquie, E G. Moschetta, F. Susanne and L. J. Edwards, *Nat. Commun***.,** 2020, **11**, 804.
13 T. Noël, and E. Zysman-Colman, *Chem Catalysis,* 2022, **2**, 468–476.
14 C. K. Prier, D. A. Rankic and D. W. C. MacMillan, *Chem. Rev.*, 2013, **113**, 5322−5363.
15 A. G. Condie, J. C. Gonzalez-Gomez and C. R. J. Stephenson, *J. Am. Chem. Soc*., 2010, **132**, 1464–1465.
16 Shi and W. Xia, *Chem. Soc. Rev.*, 2012, **41**, 7687–7697.
17 H. C. Broderick, MRes Thesis, Imperial College London, 2020.
18 A. McNally, C. K. Prier and D. W. C. MacMillan, *Science*, 2011, **334**, 1114–1117.
19 M. Ohashi, K. Miyake and K. Tsujimoto, *Bull. Chem. Soc. Jpn.*, 1980, **53**, 1683–1688.
20 Y. Mori, W. Sakaguchi, H. Hayashi, *J. Phys. Chem. A*, 2000, **104**, 4896–4905
21 L. Wei, M. Yuan, Y. Yingwu and Z. Yufen, *Bull. Chem. Soc. Jpn.*, 2006, **79**, 577–579.
22 H. Fischer, *Chem. Rev.*, 2001, 101, 3581–3610.
23 K.-S. Focsaneanu and J. C. Scaiano, *Helv. Chim. Acta*., 2006, **89**, 2473–2482.
24 A. A. Alsam, S. M. Aly, A. Usman, M. R. Parida, S. Del Gobbo, E. Alarousu, and O. F. Mohammed, *J. Phys. Chem. C*, 2015, **119**, 21896−21903
25 B. G. Stevenson, C. Gironda, E. Talbott, A. Prascsak, N. L. Burnett, V. Kompanijec, R. Nakhamiyayev, L. A. Fredin, and J. R. Swierk, J. Org. Chem., 2023, 10.1021/acs.joc.3c00490
26 L. Buzzetti, G. E. M. Crisenza and P. Melchiorre, *Angew. Chem. Int. Ed.*, 2019, **58**, 3730–3747.
27 V. D. Parker and M. Tilset, *J. Am. Chem. Soc.*, 1991, **113**, 8778–8781
28 P. J. Sarver, N. B. Bissonnette and D. W. C. MacMillan, *J. Am. Chem. Soc.,* 2021, **143**, 9737−9743.
29 W. Luo, J.-D. Yang and J.P. Chang, *iScience*, 2020, **23**, 100851.
30 T. Toshili and N. Atsushi, *Chem. Lett.*, 2009, **38**, 160–161.
31 K. Kalyanasundaram, *Coord. Chem. Rev.*, 1982, **46**, 159–244.
32 M. S. Lowry, J. I. Goldsmith, J. D. Slinker, R. Rohl, R. A. Pascal, G. G. Malliaras and S. Bernhard, *Chem. Mater.*, 2005, **17**, 5712–5719.
33 H. Uoyama, K. Goushi, K. Shizu, H. Nomura and C. Adachi, *Nature*, 2012, **492**, 234–2338.
34 A. Joshi-Pangu, F. Lévesque, H. G. Roth, S. F. Oliver, L.-C. Campeau, D. Nicewicz and D. A. DiRocco, *J. Org. Chem.*, 2016, **81**, 7244−7249.
35 P. Kohls, D. Jadhav, G. Pandey and O. Reiser, *Org. Lett.*, 2012, **14,** 672–675.
36 L. Ruiz Espelt, E. M. Wiensch and T. P. Yoon, *J. Org.Chem.*, 2013, **78**, 4107–4114.

37 J. B. McManus, N. P. R. Onuska and D. A. Nicewicz*, J. Am. Chem. Soc.*, 2018, **140**, 9056−9060.
38 J. B. McManus, N. P. R. Onuska, M. S. Jeffreys, N. C. Goodwin and D. A. Nicewicz, *Org. Lett.*, 2020, **22**, 679−683.
[39] K. Ohkubo, K. Mizushima, R. Iwata, S. Fukuzumi, *Chem. Sci.*, 2011, **2**, 715–722.
[40] K. A. Margrey, J. B. McManus, S. Bonazzi, F. Zecri and D. A. Nicewicz, *J. Am. Chem. Soc.*, 2017, **139**, 11288–11299.
41 E. Speckmeier, T. G. Fischer and K. Zeitler, *J. Am. Chem. Soc.*, 2018, **140**, 15353–15365.
[42] M. V. Bobo, J. J. Kuchta and A. K. Vannucci, *Org. Biomol. Chem.*, 2021, **19**, 4816–4834
43 G. J. Choi, Q. Zhu, D. C. Miller, C. J. Gu and R. R. Knowles, *Nature*, 2016, **539**, 268-271.
44 R. Grainger, T. D. Heightman, S. V. Ley, F. Lima and C. N. Johnson, *Chem. Sci*., 2019, **10**, 2264–2271.
[45] Z. Zuo, D. T. Ahneman, L. Chu, L., J. A. Terrett, A. G. Doyle, D. W. C. MacMillan, *Science,* 2014, **345**, 437−440.
46 D. T. Ahneman and and A. G. Doyle, *Chem. Sci.*, 2016, **7**, 7002-7006.
47 M. H. Shaw, V. W. Shurtleff., J. A. Terrett, J. D. Cuthbertson and D. W. C. MacMillan, *Science*, 2016, **352**, 1304–1308.
48 Reviews on metallophotoredox: a) A. Y. Chan, I. B. Perry, N. B. Bissonnette, B. F. Buksh, G. A. Edwards, L. I. Frye, O. L. Garry, M. N. Lavagnino, B. X. Li, Y. Liang, E. Mao, A. Millet, J. V. Oakley, N. L. Reed, H. A. Sakai, C. P. Seath and D. W. C. MacMillan, *Chem. Rev.*, 2022, **122**, 1485–1542. b) J. Zhang and M. Rueping, *Chem. Soc. Rev.*, 2023, **52**, 4099–4120.
49 C. Le, Y. Liang, R. W. Evans, X. Li and D. W. C. MacMillan, *Nature*, 2017, **547**, 79–83.
[50] B. Maity, C. Zhu, H. Yue, L. Huang, M. Harb, Y. Minenkov, M. Rueping and L. Cavallo, *J. Am. Chem. Soc.*, 2020, 142, 16942–16952.
[51] B. G. Stevenson, E. H. Spielvogel, E. A. Loiaconi, V. M. Wambua, R. V. Nakhamiyayev and J. R. Swierk*, J. Am. Chem. Soc.*, 2021, **143**, 8878–8885.
[52] G. E. M. Crisenza, D. Mazzarella and P. Melchiorre, *J. Am. Chem. Soc.*, 2020, **142**, 5461-5476.
53 D. Rehm, A. Weller, *Isr. J. Chem.*, 1970, **8**, 259–271.
54 H. G. Roth, N. A. Romero, D. A. Nicewicz, *Synlett.*, 2016, **27**, 714–723.
55 N. Elgrishi, K. J. Rountree, B. D. McCarthy, E. S. Rountree, T. T. Eisenhart, J. L. Dempsey, *J. Chem. Educ.*, 2018, **95**, 197−206.
56 M. C. Leech and K. Lam, *Nat. Rev. Chem.*, 2022, **6**, 275–286.
57 G. A. Mabbott, *J. Chem. Educ.*, 1983, **60**, 697–701.
58 P. P. Fehér, Á. Madarász and A. Stirling, *J. Chem. Theory Comput*., 2023,**19**, 4125−4135.
59 O. Stern and M. Volmer, *Z. Phys.*, 1919, **20**, 183–188.
60 J. C. Scaiano, *Chem. Soc. Rev.*, 2023, **52**, 6330–6343.
[61] M. Sneha, G. L. Thornton, L. Lewis-Borrell, A. S. H. Ryder, S. G. Espley, I. P. Clark, A. J. Cresswell, M. N. Grayson and A. J. Orr-Ewing, *ACS Catal.*, 2023, **13**, 8004–8013.
62 D. A. Nicewicz and D. W. C. MacMillan, *Science*, 2008, **322**, 77–80.
63 C. Zhu, H. Yue, B. Maity, I. Atodiresei, L. Cavallo and M. Rueping, *Nat. Catal.*, 2019, **2**, 678–687.
64 M. N. Hopkinson, A. Gómez-Suµrez, M. Teders, B. Sahoo and F. Glorius, *Angew. Chem. Int. Ed.*, 2016, **55**, 4361–4366.
65 K. P. L. Kuijpers, C. Bottecchia, D. Cambié, K. Drummen, N. J. König and T. Noël, *Angew. Chem. Int. Ed.*, 2018, **57**, 11278–11282.
66 X.-J.Wei, W. Boon, V. Hessel, T. Noël, *ACS Catal.*, 2017, **7**, 7136 –7140.
67 A. Juneau, T. O. Hope, J. Malenfant, M. Mesko, J. McNeill and M. Frenette, *ACS Catal.*, 2022, **12**, 2348−2356.
68 A. S. Gentleman, T. Lawson, M. G. Ellis, M. Davis, J. Turner-Dore, A. S. H. Ryder, M. H. Frosz, M. Ciaccia, E. Reisner, A. J. Cresswell and T. G. Euser, *Chem. Commun.*, 2022, **58**, 10548–10551.

69 E. Stadler, A. Eibel, D. Fast, H. Freißmuth, C. Holly, M. Wiech, N. Mosznerb and G. Gescheid, *Photochem. Photobiol. Sci.*, 2018, **17**, 660–669.
70 Y. Ji, D. A. DiRocco, C. M. Hon M. K. Weisner and M. Reibarkh, *Org. Lett*., 2018, **20**, 2156−2159.
71 J. Z. Bloh, *Front. Chem.*, 2019, **7**, 1–13.
72 H. E. Bonfield, K. Mercer, A. Diaz-Rodriguez, G. C. Cook, B. S. J. McKay, P. Slade, G. M. Taylor, W. X. Ooi, J. D. Williams, J. P. M. Roberts, J. A. Murphy, L. Schmermund, W. Kroutil, T. Mielke, J. Cartwright, G. Grogan and L. J. Edwards, *ChemPhotoChem*, 2020, **4**, 45–51.
73 S. Govaerts, A. Nyuchev and T. Noël, *J. Flow Chem*., 2020, **10,** 13–71.
74 M. Neumann and K. Zeitler, *Org. Lett*., 2012, **14**, 2658–2661.
75 J. W. Tucker, Y. Zhang, T. F. Jamison and C. R. J. Stephenson, *Angew. Chem. Int. Ed*., 2012, **51**, 4144–4147.
76 E. G. Moschetta, S. M.Richter and S. J. Wittenberger, *ChemPhotoChem*, 2017, **1**, 539–543.
77 S. Andrews, J. J. Becker and M. R. Gagné, *Angew. Chem. Int. Ed.*, 2012, **51**, 4140–4143.
78 K. C. Harper, E. G. Moschetta, S. V. Bordawekar and S. J. Wittenberger, *ACS Cent. Sci.*, 2019, **5**, 109–115.
79 E. B. Corcoran, M. T. Pirnot, S. Lin, S. D. Dreher, D.A. DiRocco, I. W. Davies, S. L. Buchwald and D. W. C. MacMillan, *Science*, 2016, **353**, 279–283.
80 K. C. Harper, E.-X. Zhang, Z.-Q. Liu, T. Grieme, T. B. Towne, D. J. Mack, J. Griffin, S. -Y. Zheng, N.-N. Zhang, S. Gangula, J.-L. Yuan, R. Miller, P.-Z. Huang, J. Gage, M. Diwan, and Y.-Y. Ku, *Org. Process Res. Dev.*, 2022, **26**, 404−412.
81 E. B. Corcoran, J. P. McMullen, F. Lévesque, M. K. Wismer and J. R. Naber, *Angew. Chem. Int. Ed.*, 2020, **59**, 11964–11968.
82 D. G. Blackmond, *Angew. Chem. Int. Ed.*, 2005, **44**, 4302–4320.
83 D. G. Blackmond, *J. Am. Chem. Soc.*, 2015, **137**, 10852–10866.
84 J. Burés*, Angew. Chem. Int. Ed.*, 2016, **55**, 16084–16087.
85 C. D.-T. Nielsen and J. Burés, *Chem. Sci*., 2019, **10**, 348–353.
86 H. E. Askey, J. D. Grayson, J. D. Tibbetts, J. C. Turner-Dore, J. M. Holmes, G. Kociok-Kohn, G. L. Wrigley and A. J. Cresswell, *J. Am. Chem. Soc.*, 2021, **143**, 15936–15945.
87 J. Zheng, W. B. Swords, H. Jung, K. L. Skubi, J. B. Kidd, G. J. Meyer, M.-H. Baik and T. P. Yoon, *J. Am. Chem. Soc.*, 2019, **141**, 13625–1363.
88 W. B. Swords, S. J. Chapman, H. Hofstetter, A. L. Dunn and T. P. Yoon, *J. Org. Chem.* 2022, **87**, 11776–11782.
89 C. Feldmeier, H. Bartling, E. Riedle and R. M. Gschwind, *J. Magn. Reson.* 2013, **232**, 39–44.
90 For a review on in situ reaction monitoring for organic photoredox reactions, see A. Madani, B. Pieber, *ChemCatChem*, 2023, **15**, e2022015.
91 Y. Ben-Tal and G. C. Lloyd-Jones, *J. Am. Chem. Soc.*, 2022, **144**, 15372–15382.
92 J. A. Malik, A. Madani, B. Pieber and P.H. Seeberger, *J. Am. Chem. Soc.*, 2020, **142**, 11042–11049.
93 E. R. Welin, C. Le, D. M. Arias-Rotondo, J. K. McCusker and D. W. C. MacMillan, *Science*, 2017, **355**, 380–385.
[94] D. M. Kitcatt, S. Nicolleb and A.-L. Lee, *Chem. Soc. Rev.*, 2022, **51**, 1415–1453.
[95] A. L. Gant Kanegusuku and J. L. Roizen, *Angew. Chem. Int. Ed.*, 2021, 60, 21116–21149.
96 E. Breuer and D. Melumad, *J. Org. Chem.*, 1973, **38**, 1601–1602.
97 C. Boga, F. Manescalchi and D. Savoia, *Tetrahedron*, 1994, **50**, 4709–4722.
98 M. A. J. Dubois, J. J. Rojas, A. J. Sterling, H. C. Broderick, M. A. Smith, A. J. P. White, P. W. Miller, C. Choi, J. J. Mousseau, F. Duarte and J. A. Bull, *J. Org. Chem*., 2023, **88**, 6476–6488.

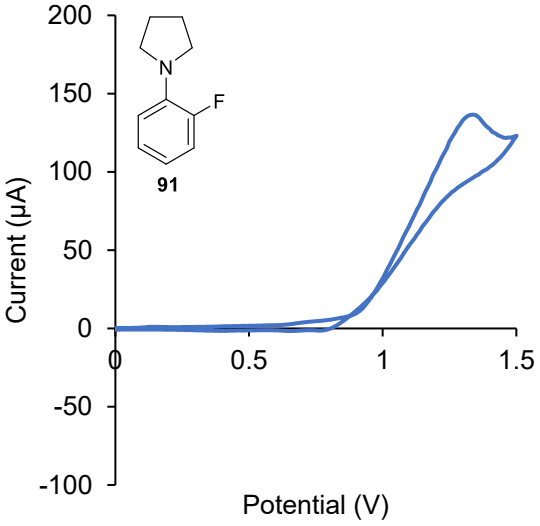
99 Hepatochem, https://www.hepatochem.com/photoreactors-leds-accessories-old/photoredox-temperature-controlled, (accessed June 2021).
100 C. K. Prier, D. A. Rankic and D. W. C. MacMillan, *Chem. Rev.*, 2013, **113**, 5322–5363.
101 Electrochemical Series of Photocatalysts and Common Organic Compounds, Merck https://macmillan1.wpengine.com/wp-content/uploads/Merck-Photocatalysis-Chart.pdf (accessed September 2019).
102 J. Luo and J. Zhang, *ACS Catal.,* 2016, **6**, 873–877.
103 Y. Liu, X.-L. Chen, X.-Y. Li, S.-S. Zhu, S.-J. Li, Y. Song, L.-B. Qu and B. Yu., *J. Am. Chem. Soc*., 2021, **143**, 964−972.
104 S. Ladouceur, D. Fortin, E. Zysman-Colman, *Inorganic Chemistry.,* 2011, **50**, 11514–11526.
For review: M. A. Brydena, E. Zysman-Colman, *Chem. Soc. Rev.*, 2021, **50**, 7587–7680.
105 For review on 4CzIPN reactions, see: T.-Y. Shang, L.-H. Lu, Z. Cao, Y. Liu, W.-M. He and B. Yu, *Chem. Commun.*, 2019, **55**, 5408–5419.
106 A. Quintavalla, D. Carboni and M. Lombardo, *ChemCatChem*, 2024, e202301225
107 LED irradiance vs wavelength data obtained from HepatoChem, plotted using WebPlotDigitizer, https://automeris.io/WebPlotDigitizer/index.html (accessed September 2023).
108 I. M. Irshadeen, V. X. Truong, H. Frisch and C. Barner-Kowollik, *Chem. Commun.*, 2023, **59**, 11959–11962.
109 S. Tshepelevitsh, A. Kütt, M. Lõkov, I. Kaljurand, J. Saame, A. Heering, P. G. Plieger, R. Vianello and I. Leito, *Eur. J. Org. Chem.*, 2019, 6735–6748.
110A. Streitwieser and Y.-J. Kim, *J. Am. Chem. Soc.*, 2000, **122**, 11783–11786.
111 L. Pitzer, F. Schäfers and F. Glorius, *Angew. Chem. Int. Ed*. 2019, **58**, 8572–8576.
112 Reviews on Shono oxidation: a) A. M. Jones and C. E. Banks, *Beilstein J. Org. Chem*. 2014, **10**, 3056–3072. b) M. D. Kärkäs, *Chem. Soc. Rev.*, 2018, **47**, 5786–5865. c) K. Yamamoto, M. Kuriyama and O. Onomura, *Chem.Rec.*, 2021, **21**, 2239–2253.
113 D. Gunasekera, J. P. Mahajan, Y. Wanzi, S. Rodrigo, W. Liu, T. Tan and L. Luo, *J. Am. Chem. Soc.*, 2022, **144**, 22, 9874–9882.
114 M. Jonsson, D. D. M. Wayner and J. Lusztyk, *J. Phys. Chem. 1996*, **100**, 17539–17543.
115 J.B. Geri, J. V. Oakley, T. Reyes-Robles, T. Wang, S. J. McCarver, C. H. White, F. P. Rodriguez-Rivera, D. L. Parker, E. C. Hett, O. O. Fadeyi, R. C. Oslund and D. W. C MacMillan, *Science*, 2020, **367**, 1091–1097.
116 F. Strieth-Kalthoff and F. Glorius, *Cell*, 2020, **6**, 1888–1903.
117 J. M. M. Verkade, L. J. C. van Hemert, P. J. L. M. Quaedflieg, P. L. Alsters, F. L. van Delft and F. P. J. T. Rutjes, *Tetrahedron Lett.*, 2006, **47**, 8109–8113.
118 C. Hansch, A. Leo and R. W. Taft, *Chem. Rev.* 1991, **91**, 165–195.
119 H. C. Brown and Y. Okamato, *J. Am. Chem. Soc.*, 1958, **80**, 4979–4987.
120 J. O. Schreck, *J. Chem. Educ.*, 1971, **48**, 103–107.
121 C. G. Swain, and E. C. Lupton, *J. Am. Chem. Soc.*, 1968, **90**, 4328–4337.
122 J. N. McPherson, R. W. Hogue, F. S. Akogun, L. Bondi, E. T. Luis, J. R. Price, A. L. Garden, S. Brooker and S. B. Colbran, *Inorg. Chem*., 2019, **58**, 2218–2228.
123 A. T. Bottini and C. P. Nash, *J. Am. Chem. Soc.* 1962, **84**, 734–739.
124 Y. W. Kang, R. H. Kim, S. R. Atriardi, and S. K. Woo, *J. Org. Chem.,* 2023, **88**, 3555−3566.
125 D. Dougherty and E. Anslyn, Modern Physical Organic Chemistry, University Science Books, Sausalito, CA, 2005.
126 J.P. Dinnocenzo and T.E. Banach, *J. Am. Chem. Soc.*, 1989, 111, 8646–8653.
127 M. A. Cismesia and T. P. Yoon, *Chem. Sci.*, 2015, **6**, 5426 – 5434.
128 B. Vandekerckhove, N. Piens, B. Metten, C. V. Stevens and T. S. A. Heugebaert, *Org. Process Res. Dev.*, 2022, **26**, 2392–2402.
129 S. Ruccolo, Y. Qin, C. Schnedermann and D. G. Nocera, *J. Am. Chem. Soc.*, 2018, **140**, 14926−14937.

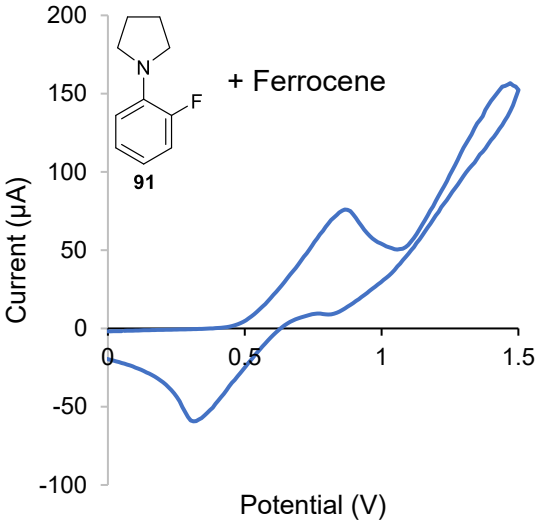
130 S. DiLuzio, T. U. Connell, V. Mdluli, J. F. Kowalewski and S. Bernhard, *J. Am. Chem. Soc.*, 2022, **144**, 1431−1444.
131 R. R. Gagne, C. A. Koval and G. C. Lisensky, *Inorg. Chem.*, 1980, **19**, 2854–2855.
132 V. V. Pavlishchuk and A. W. Addison, *Inorganica Chim. Acta,* 2000, **298**, 97–102.
133 M. J. Frisch, G. W. Trucks, H. B. Schlegel, G. E. Scuseria, M. A. Robb, J. R. Cheeseman, G. Scalmani, V. Barone, G. A. Petersson, H. Nakatsuji, X. Li, M. Caricato, A. V. Marenich, J. Bloino, B. G. Janesko, R. Gomperts, B. Mennucci, H. P Hratchian, J. V. Ortiz, A. F Izmaylov, J. L. Sonnenberg Williams, F. Ding, F. Lipparini, F. Egidi, J. Goings, B. Peng, A. Petrone, T. Henderson, D. Ranasinghe, V. G. Zakrzewski, J. Gao, N. Rega, G. Zheng, W. Liang, M. Hada, M. Ehara, K. Toyota, R. Fukuda, J. Hasegawa, M. Ishida, T. Nakajima, Y. Honda, O. Kitao, H. Nakai, T. Vreven, K. Throssell, J. A. Montgomery, J. E. Peralta, F. Ogliaro, M. J. Bearpark, J. J. Heyd, E. N. Brothers, K. N Kudin, V. N. Staroverov, T. A. Keith, R. Kobayashi, J. Normand, K. Raghavachari, A. P. Rendell, J. C. Burant, S. S. Iyengar, J. Tomasi, M. Cossi, J. M. Millam, M. Klene, C. Adamo, R. Cammi, J. W. Ochterski, R. L. Martin, K. Morokuma, O. Farkas, J. B. Foresman and D. J. Fox, *Gaussian 16 Rev. C.01*, Wallingford, CT, 2016.
134 B. P. Pritchard, D. Altarawy, B. Didier, T. D. Gibson and T. L. Windus, *J. Chem. Inf. Model.*, 2019**, 59**, 4814-4820.
135 G. Luchini, J. Alegre-Requena, I. Funes-Ardoiz and R. Paton, *F1000Research*, 2020**, 9**, 291.
136 E. D. Glendening, J. K. Badenhoop, A. E. Reed, J. E. Carpenter, J. A. Bohmann, C. M. Morales, C. R. Landis and F. Weinhold, NBO 6.0, Theoretical Chemistry Institute, University of Wisconsin, Madison, WI*,* 2013.
137 J. Ho, M. L. Coote, C. J. Cramer, and D. G. Truhlar, in *Organic Electrochemistry*, ed. O. Hammerich and B. Speiser, CRC Press, Boca Raton, FL, 5th edn, 2016, ch. 4, pp. 229–259.
138 J. J. Gair, R. L. Grey, S. Giroux and M. A. Brodney, *Org. Lett.*, 2019, **21,** 2482–2487.
139 H. Jo, A. H. E. Hassan, S. Y. Jung, J. K. Lee, Y. S. Cho and S.-J. Min, *Org. Lett.* 2018, **20**, 1175−1178.
140 G. Xu and Y.-G Wang, *Angew. Chem. Int. Ed.*, 2020, **59**, 7921–7927.
[141] C. Pezzetta, A. Folli,O. Matuszewska, D. Murphy, R. W. M. Davidson and D. Bonifazi, *Adv. Synth.Catal.*, 2021,**363**, 4740–4753.
142 M. Traxler, S. Gisbertz, P. Pachfule, J. Schmidt, J. Roeser, S. Reischauer, J. Rabeah, B. Pieber and A. Thomas, *Angew. Chem. Int. Ed.*, 2022, **61**, e202117738.
[143] C. Mudithanapelli and M.-H. Kim*, Org. Biomol. Chem.*, 2020, **18**, 450–464.
144 D. Hori, J. H. Yum, H. Sugiyama, S. Park, *Bull. Chem. Soc. Jpn.*, 2021, **94**, 1948–1953.

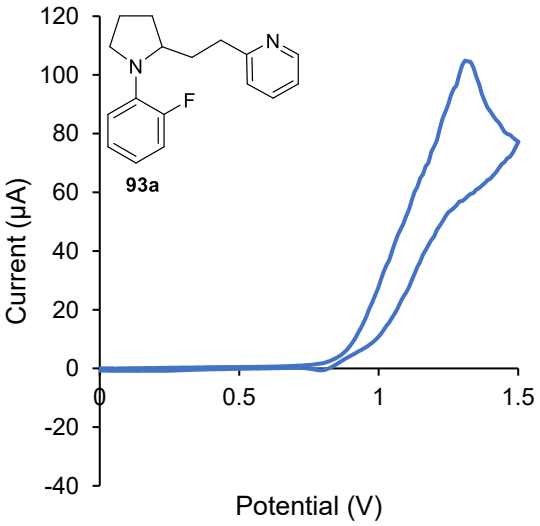
6. Appendix

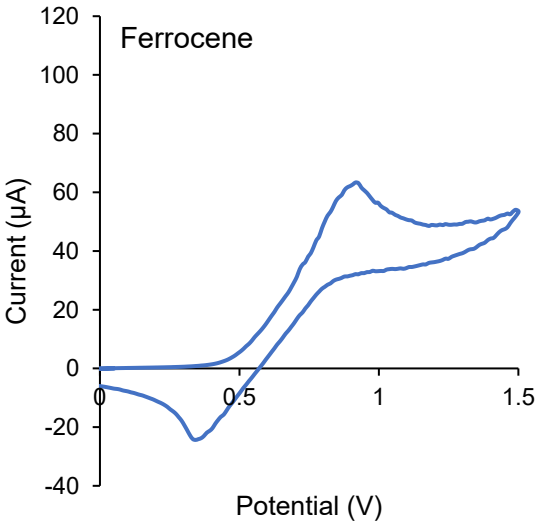
6.1. Cyclic voltammograms

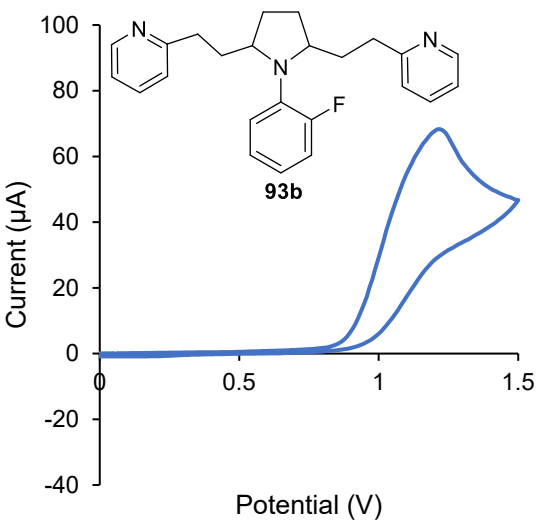
All cyclic voltammograms were performed according to the procedure in section 4.9. The third of three scans for each compound is provided between 0 and the upper voltage limit of the experiment, either +1.5 V or +2.0 V, below. The left graphs in each instance contain the compound tested, and the right graphs contain the ferrocene scan used as an internal reference. Where ferrocene is given alone, this was run without the analyte preset. Potentials are given as the measured working potential determined by the Metrohm potentiostat setup Nova software (see section 4.9). Correction to the ferrocene reference and consequently SCE was performed after determination of E_{pa}.

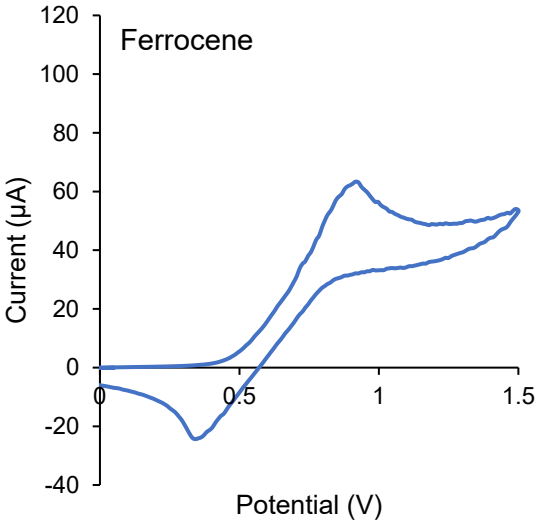


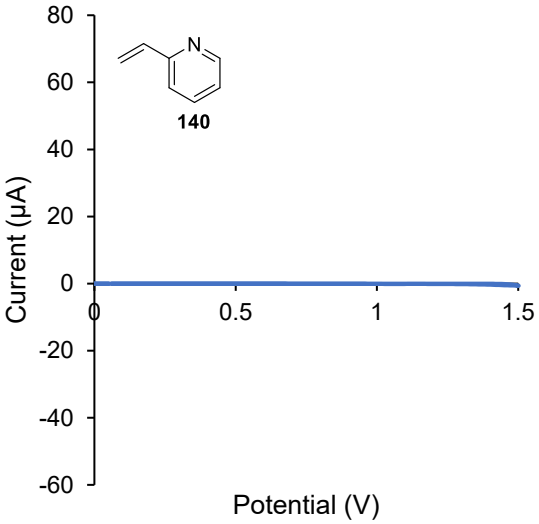


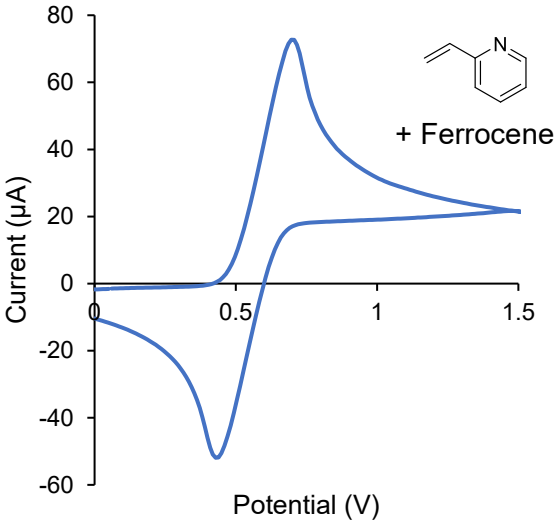


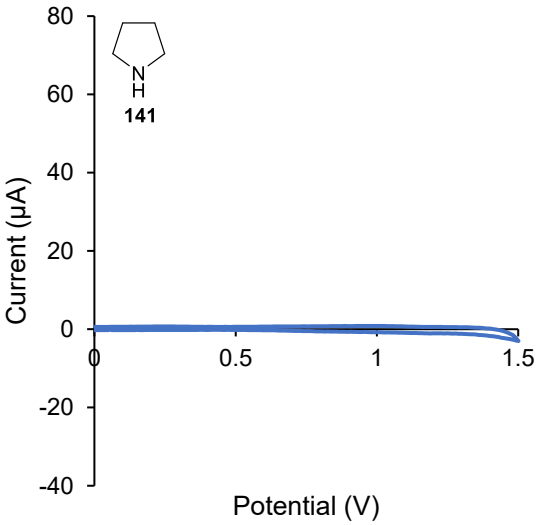


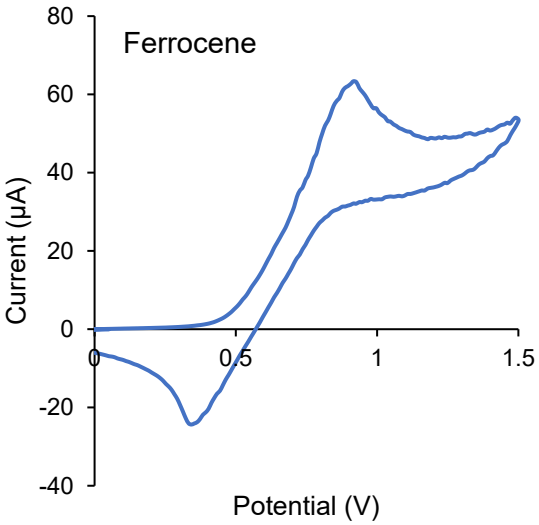

N
N
N
F
93b
Current (μA)
Potential (V)

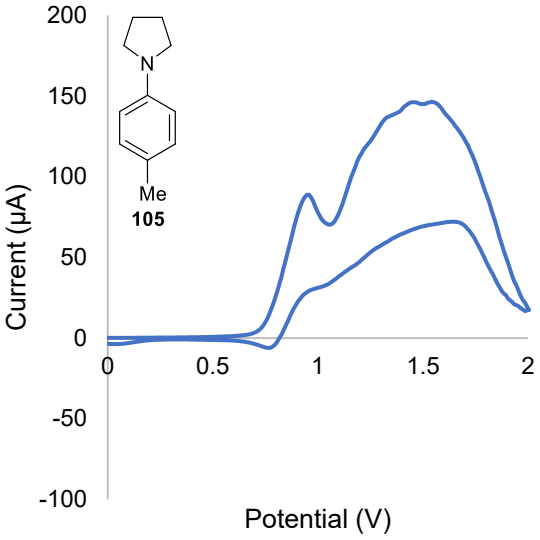

Ferrocene
Current (μA)
Potential (V)

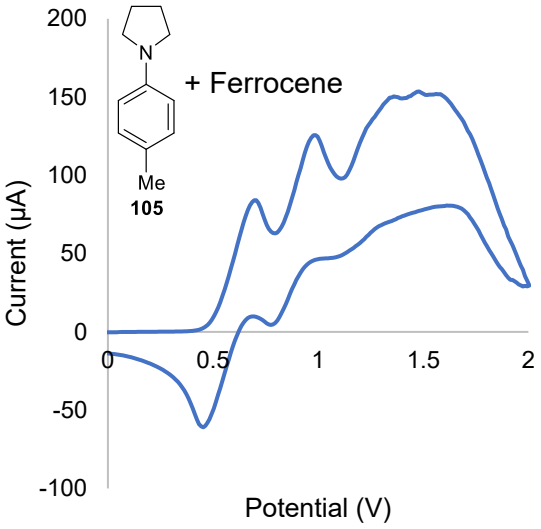

N
140
Current (μA)
Potential (V)

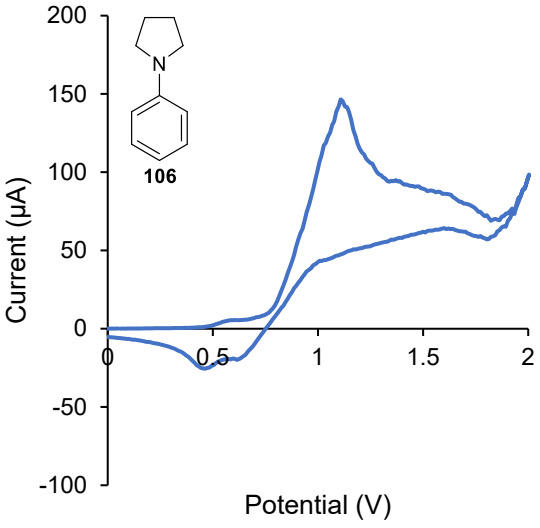

N
+ Ferrocene
Current (μA)
Potential (V)

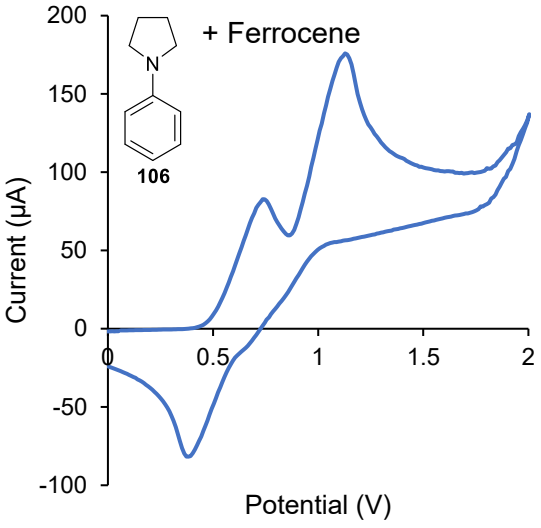

N
H
141
Current (μA)
Potential (V)

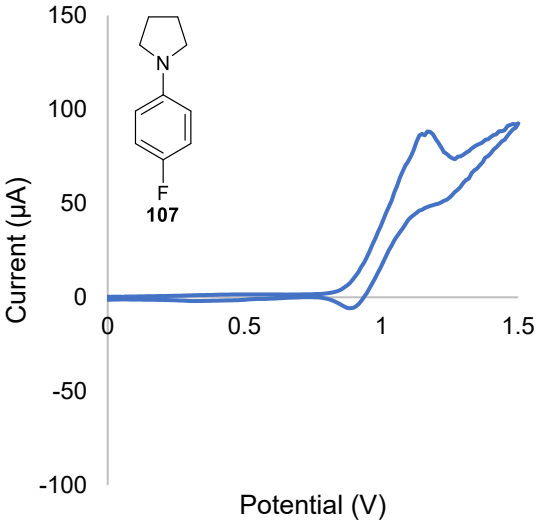

Ferrocene
Current (μA)
Potential (V)

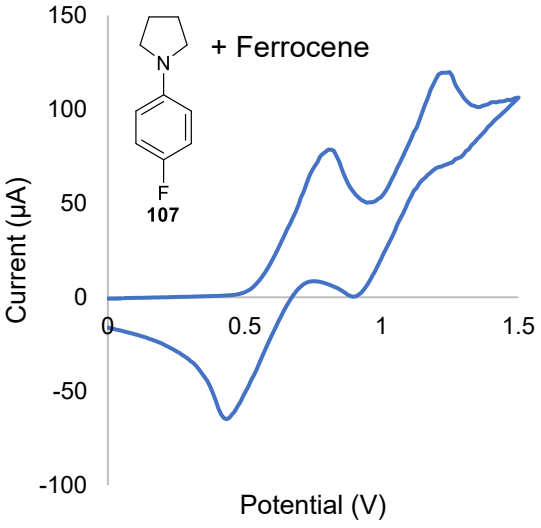

Current (μA)
Potential (V)
Me
105

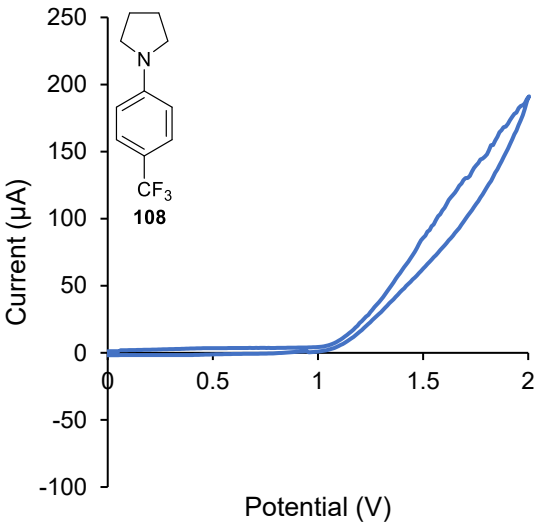

+ Ferrocene
Current (μA)
Potential (V)
Me
105

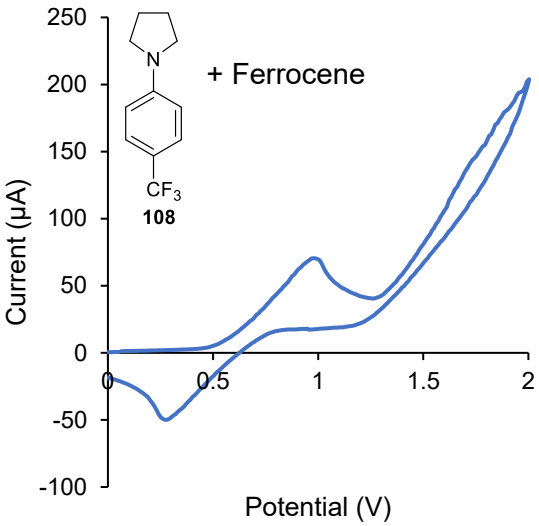

Current (μA)
Potential (V)
106

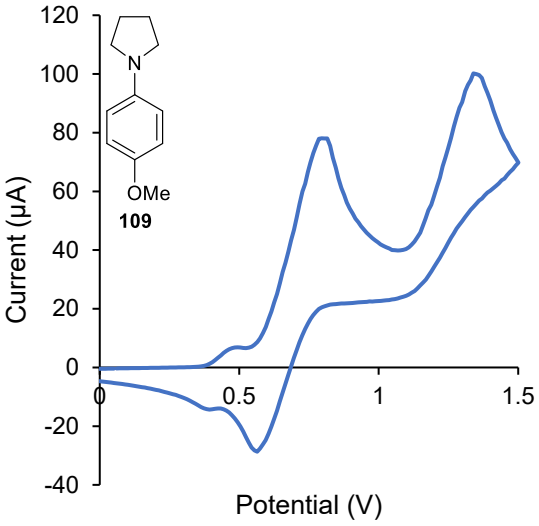

+ Ferrocene
Current (μA)
Potential (V)
106

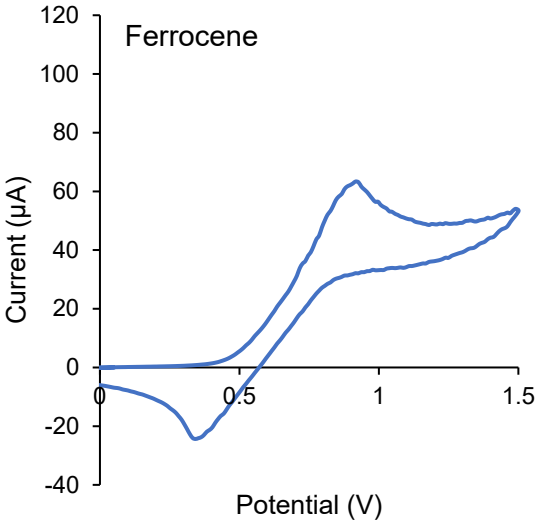

Current (μA)
Potential (V)
F
107

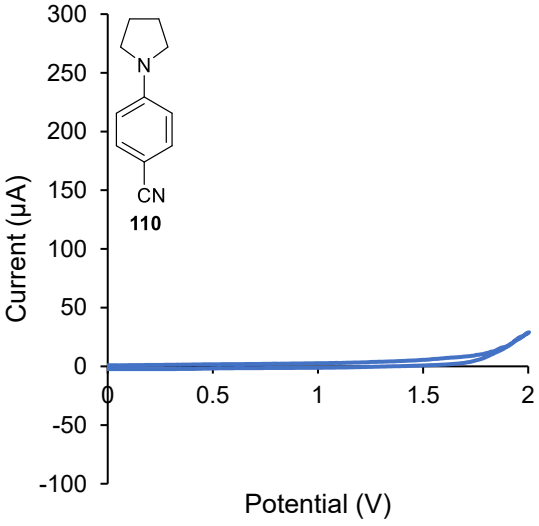

+ Ferrocene
Current (μA)
Potential (V)
F
107

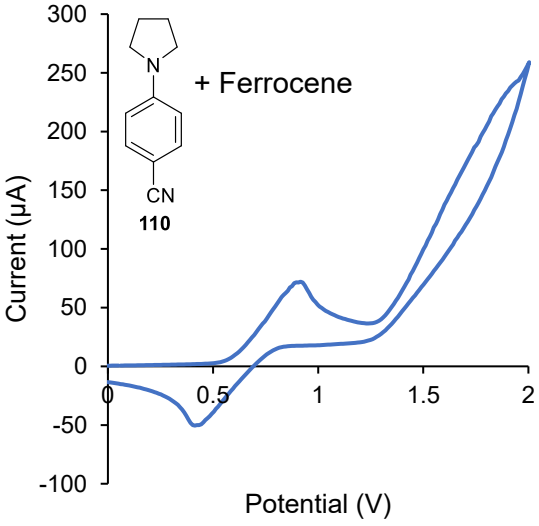

250
200
150
100
50
0
-50
-100
0
0.5
1
1.5
2
Current (μA)
Potential (V)
N
CF3
108

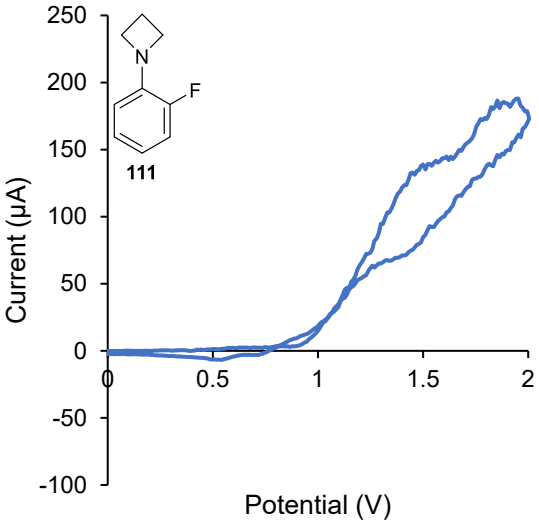

250
200
150
100
50
0
-50
-100
0
0.5
1
1.5
2
Current (μA)
Potential (V)
N
CF3
108
+ Ferrocene

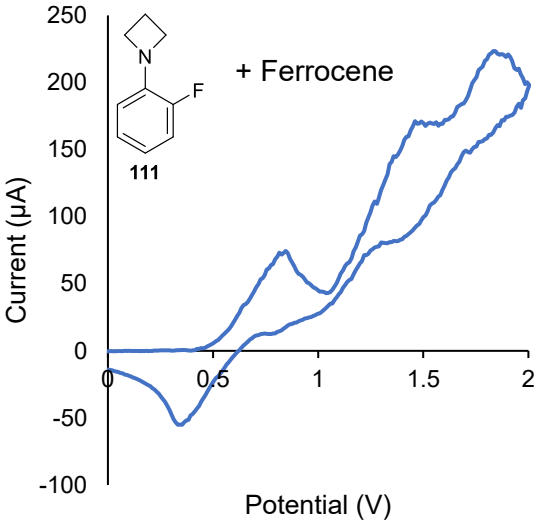

120
100
80
60
40
20
0
-20
-40
0
0.5
1
1.5
Current (μA)
Potential (V)
N
OMe
109

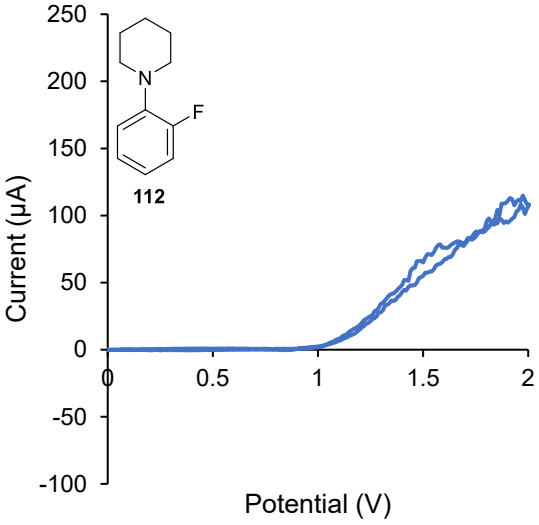

120
100
80
60
40
20
0
-20
-40
0
0.5
1
1.5
Current (μA)
Potential (V)
Ferrocene

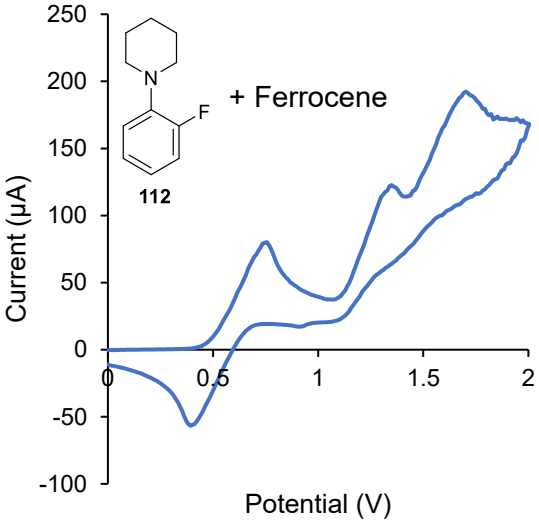

300
250
200
150
100
50
0
-50
-100
0
0.5
1
1.5
2
Current (μA)
Potential (V)
N
CN
110

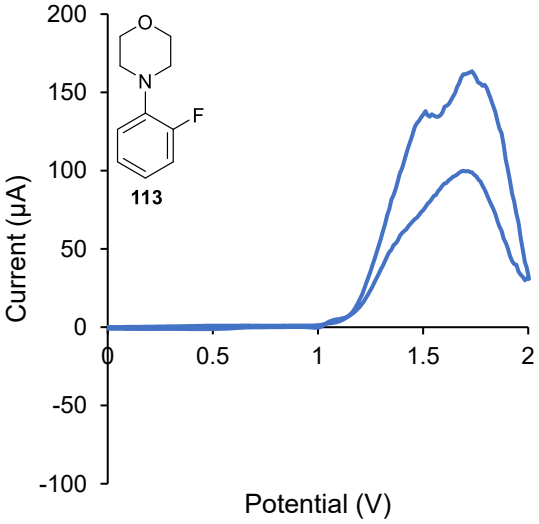

300
250
200
150
100
50
0
-50
-100
0
0.5
1
1.5
2
Current (μA)
Potential (V)
N
CN
110
+ Ferrocene

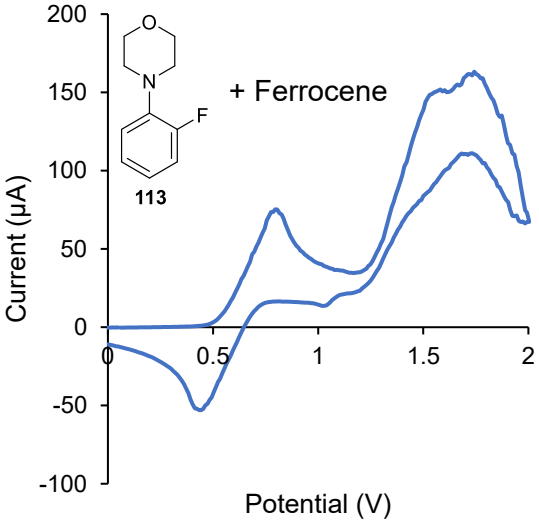

111
Current (μA)
Potential (V)

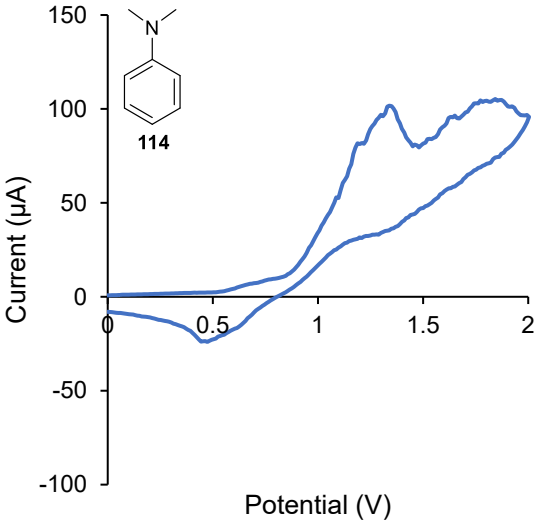

+ Ferrocene
111
Current (μA)
Potential (V)

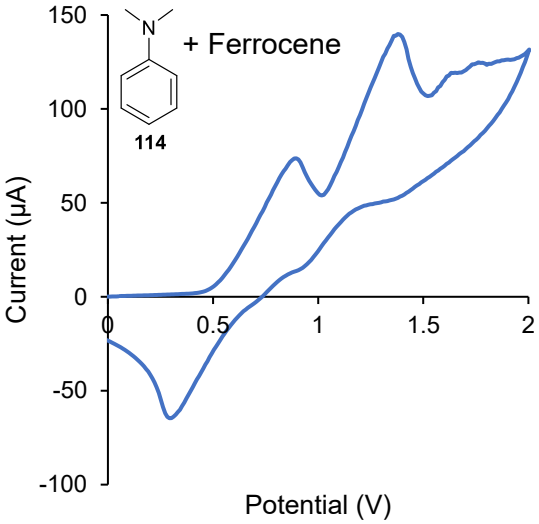

112
Current (μA)
Potential (V)

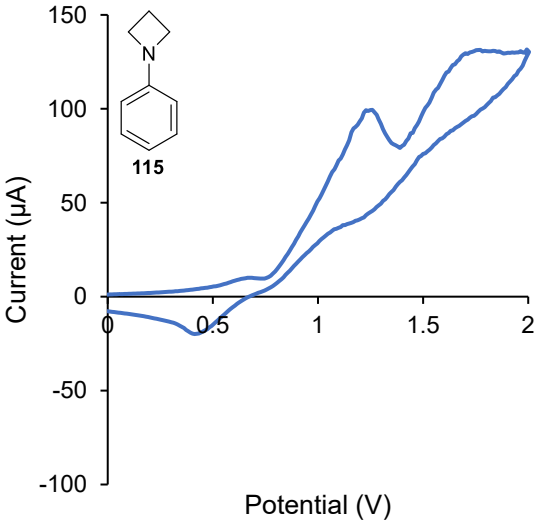

+ Ferrocene
112
Current (μA)
Potential (V)

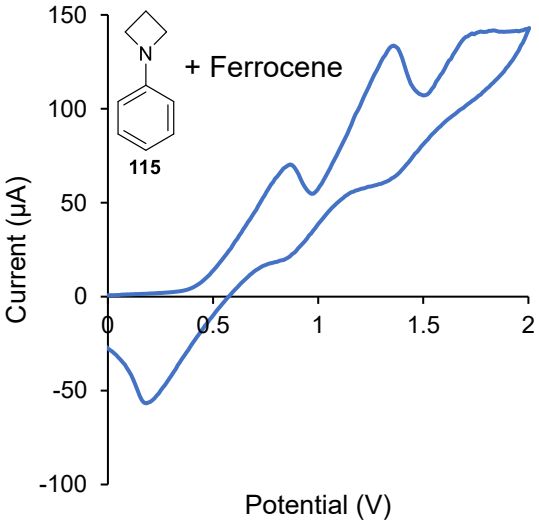

113
Current (μA)
Potential (V)

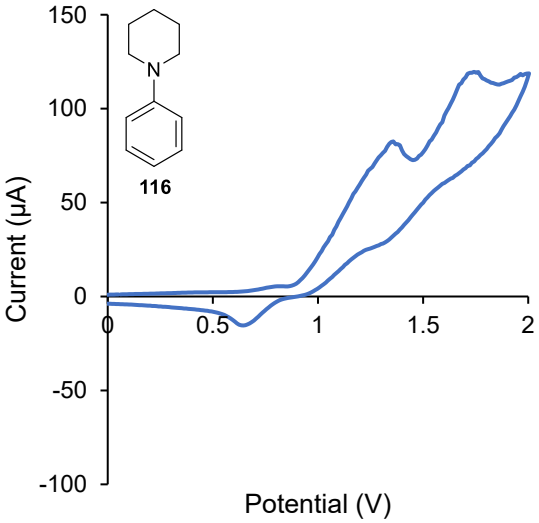

+ Ferrocene
113
Current (μA)
Potential (V)

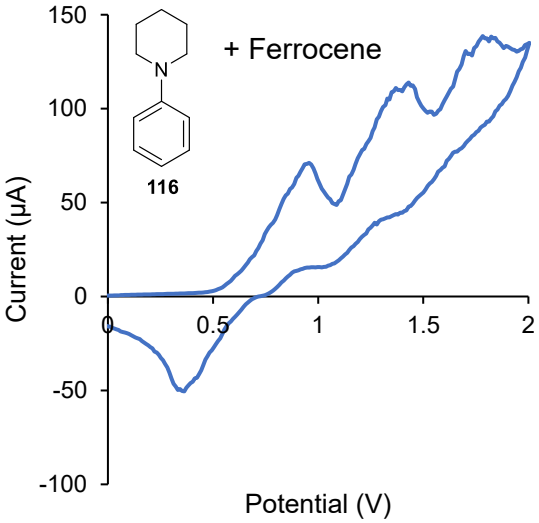

150
100
50
0
-50
-100
0
0.5
1
1.5
2
Current (μA)
Potential (V)
114

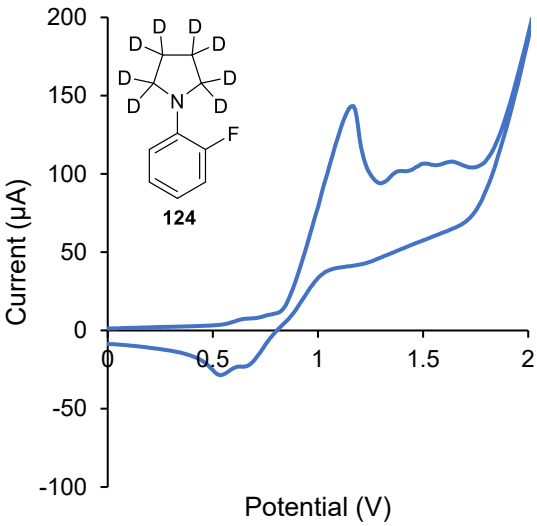

150
100
50
0
-50
-100
0
0.5
1
1.5
2
Current (μA)
Potential (V)
+ Ferrocene
114

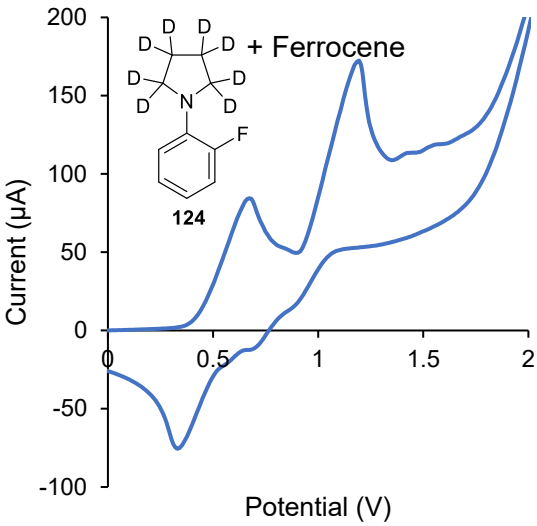

150
100
50
0
-50
-100
0
0.5
1
1.5
2
Current (μA)
Potential (V)
115


150
100
50
0
-50
-100
0
0.5
1
1.5
2
Current (μA)
Potential (V)
+ Ferrocene
115


150
100
50
0
-50
-100
0
0.5
1
1.5
2
Current (μA)
Potential (V)
116

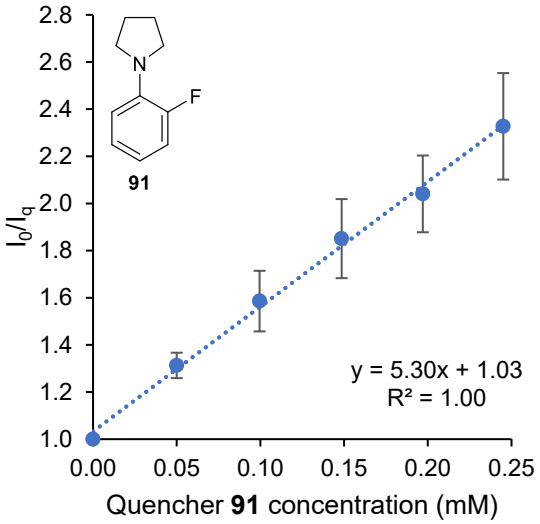

150
100
50
0
-50
-100
0
0.5
1
1.5
2
Current (μA)
Potential (V)
+ Ferrocene
116

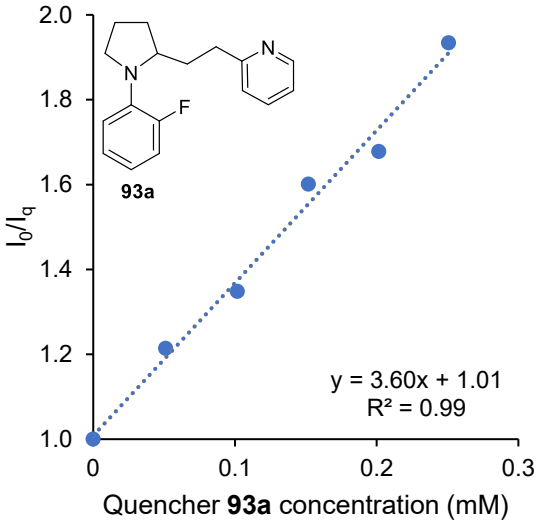

200
150
100
50
0
-50
-100
Current (µA)
0
0.5
1
1.5
2
Potential (V)
D
N
F
124

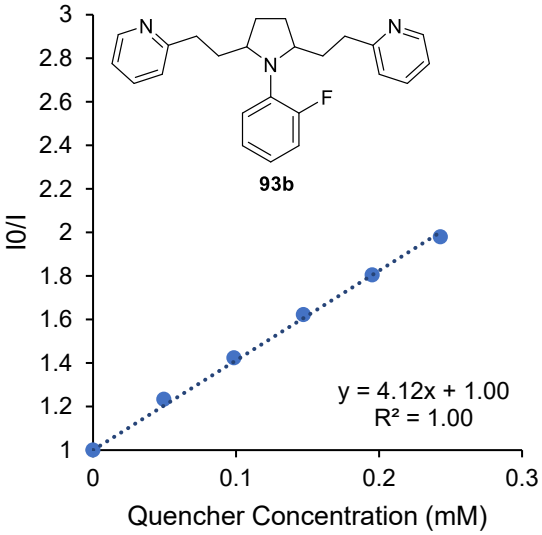

200
150
100
50
0
-50
-100
Current (µA)
0
0.5
1
1.5
2
Potential (V)
+ Ferrocene
D
N
F
124

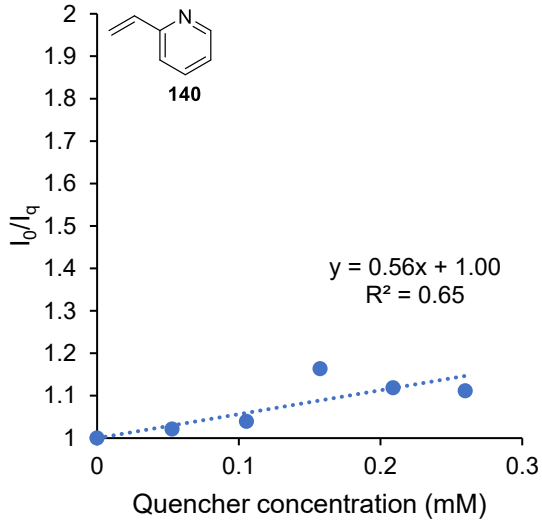
6.2. Stern-Volmer graphs

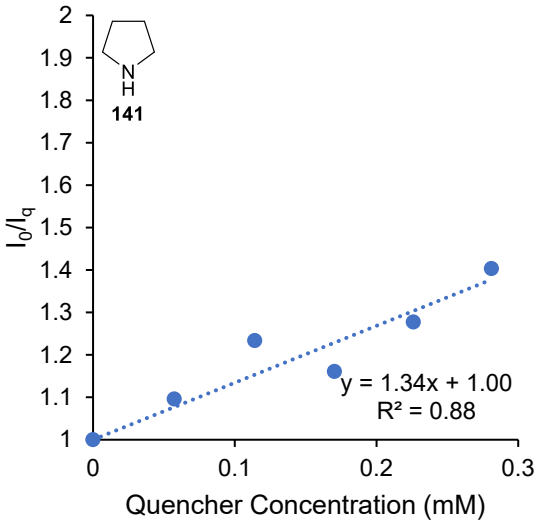
Graphs of I_0/I_q vs quencher concentration for each substrate has been obtained using the method described in section 4.10 and presented below. Error bars are given as standard deviation between repeats.

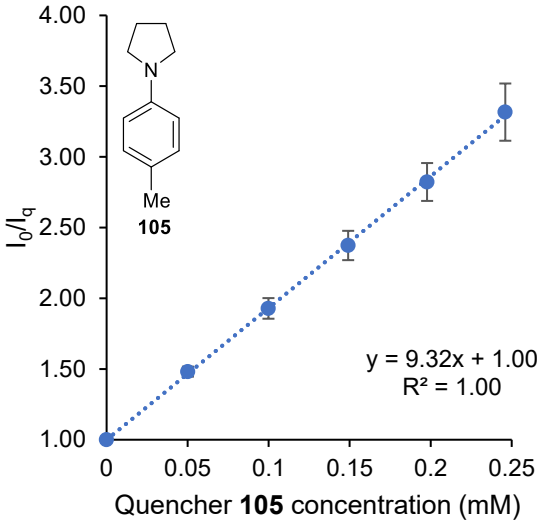


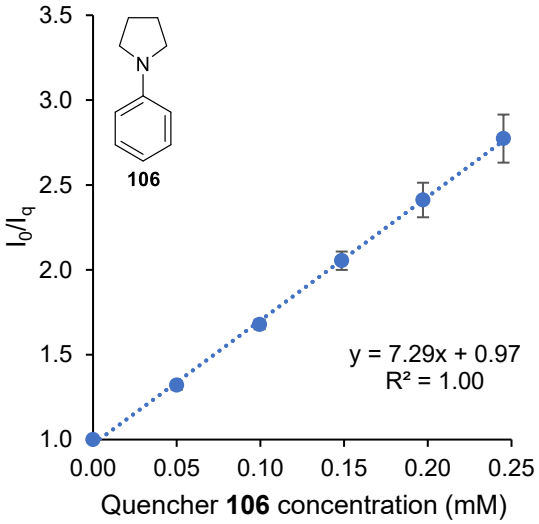


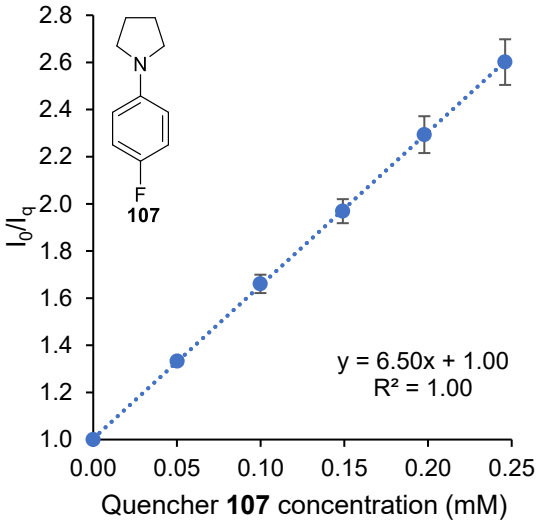


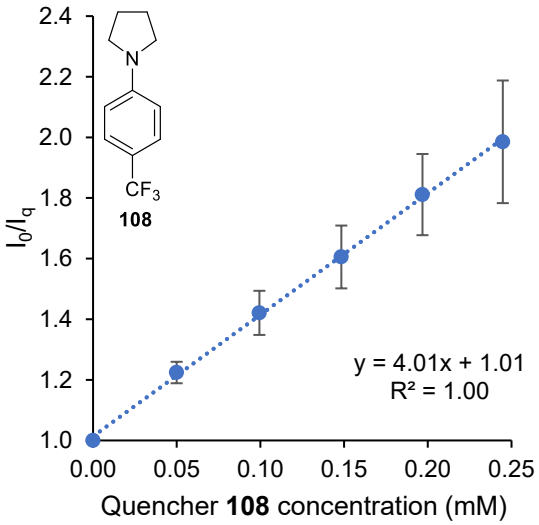


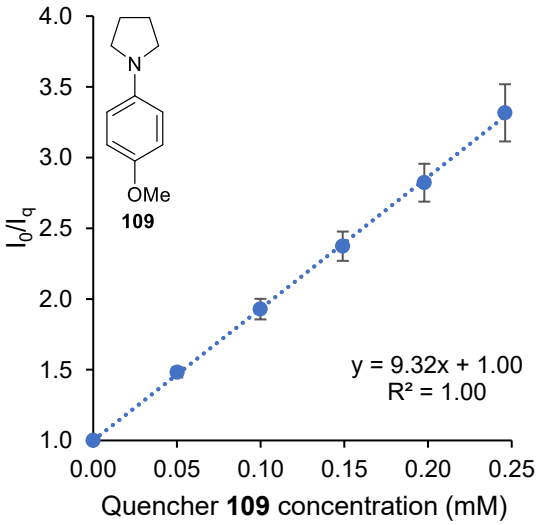

N
H
141
I_0/I_q
y = 1.34x + 1.00
R² = 0.88
Quencher Concentration (mM)

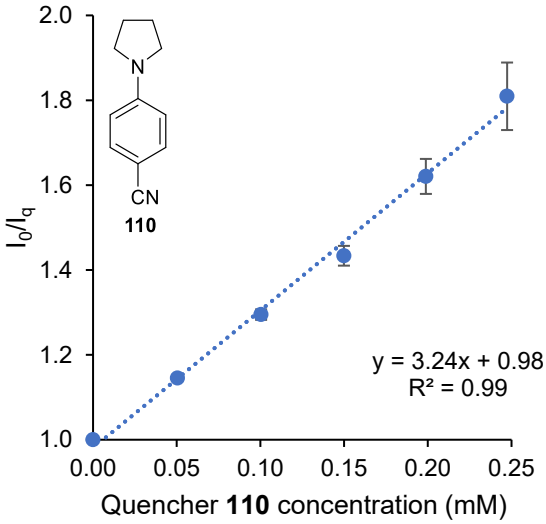

N
Me
105
I_0/I_q
y = 9.32x + 1.00
R² = 1.00
Quencher **105** concentration (mM)

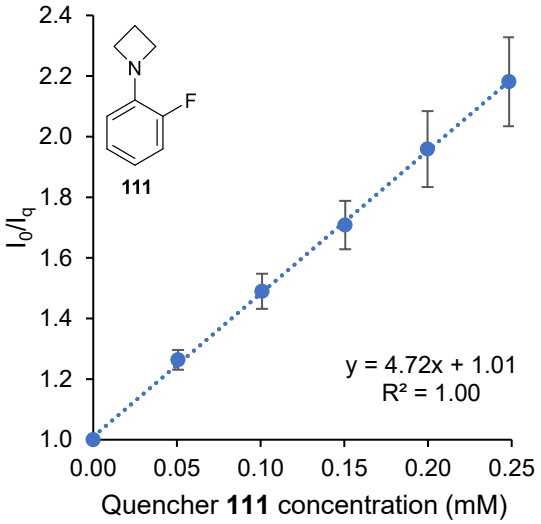

N
106
I_0/I_q
y = 7.29x + 0.97
R² = 1.00
Quencher **106** concentration (mM)

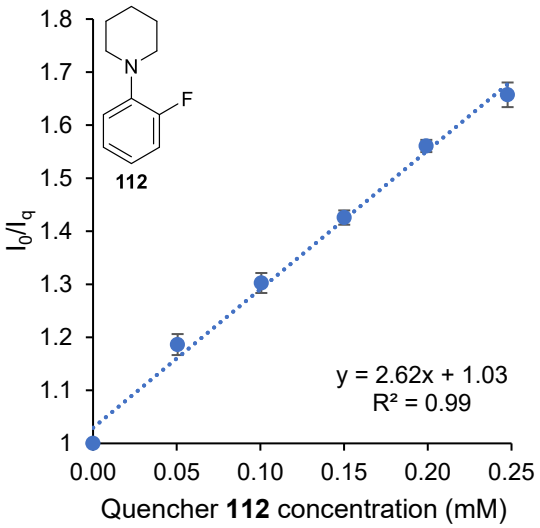

N
F
107
I_0/I_q
y = 6.50x + 1.00
R² = 1.00
Quencher **107** concentration (mM)

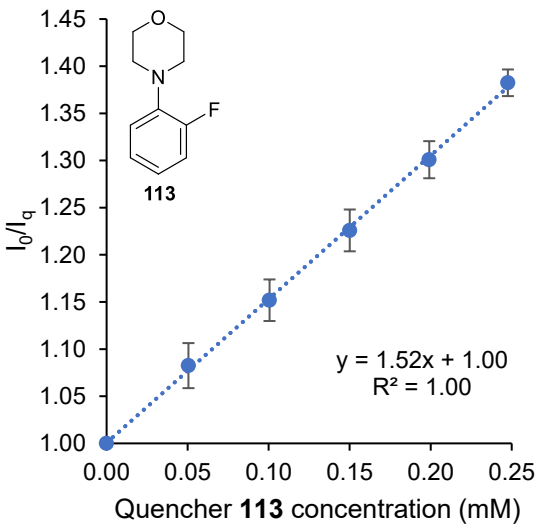

N
CF_3
108
I_0/I_q
y = 4.01x + 1.01
R² = 1.00
Quencher **108** concentration (mM)

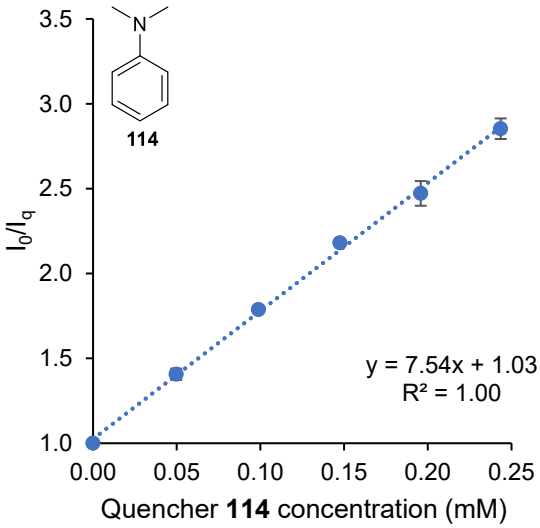

N
OMe
109
I_0/I_q
y = 9.32x + 1.00
R² = 1.00
Quencher **109** concentration (mM)

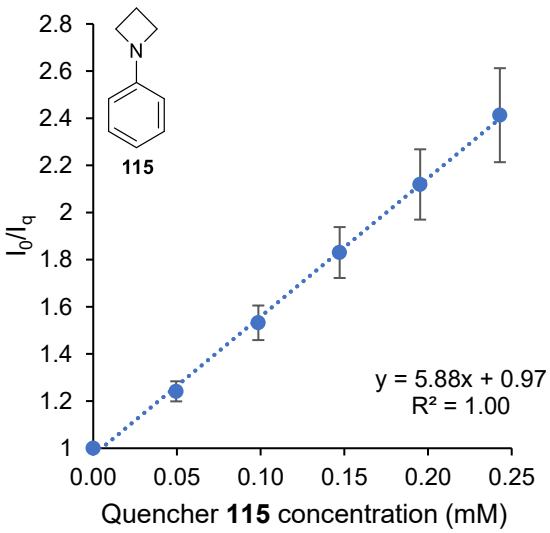

N
CN
110
y = 3.24x + 0.98
R² = 0.99
I0/Iq
Quencher 110 concentration (mM)

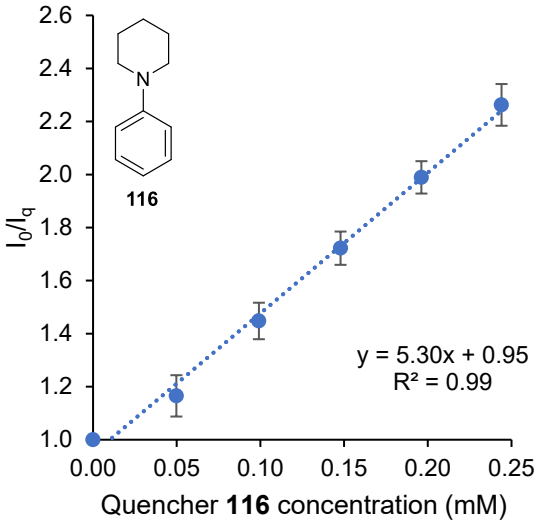

N
F
111
y = 4.72x + 1.01
R² = 1.00
I0/Iq
Quencher 111 concentration (mM)

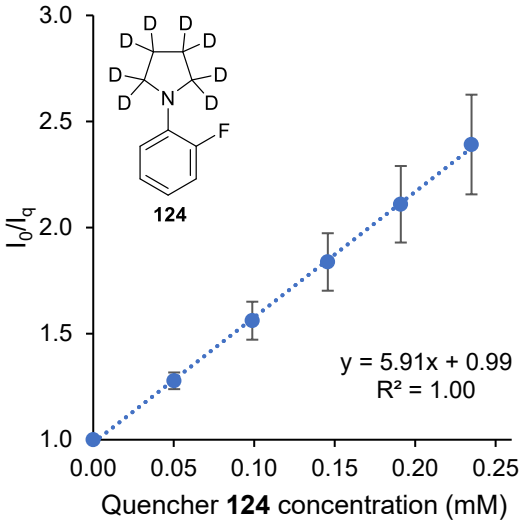

N
F
112
y = 2.62x + 1.03
R² = 0.99
I0/Iq
Quencher 112 concentration (mM)


O
N
F
113
y = 1.52x + 1.00
R² = 1.00
I0/Iq
Quencher 113 concentration (mM)


N
114
y = 7.54x + 1.03
R² = 1.00
I0/Iq
Quencher 114 concentration (mM)


N
115
y = 5.88x + 0.97
R² = 1.00
I0/Iq
Quencher 115 concentration (mM)


2.6
2.4
2.2
2.0
1.8
1.6
1.4
1.2
1.0
I_0/I_q
N
116
y = 5.30x + 0.95
R² = 0.99
0.00
0.05
0.10
0.15
0.20
0.25
Quencher **116** concentration (mM)


3.0
2.5
2.0
1.5
1.0
I_0/I_q
D
N
F
124
y = 5.91x + 0.99
R² = 1.00
0.00
0.05
0.10
0.15
0.20
0.25
Quencher **124** concentration (mM)